Radiative transfer code development. Applications to the estimation of the radiative impact of aerosols

Entwicklung eines Strahlungstransportprogramms, Anwendungen zur Abschätzung des Strahlungseinflusses von Aerosolen

DISSERTATION

zur Erlangung des akademischen Grades eines

Docteur de l'Université Pierre et Marie Curie,
Ecole Doctorale ED129, Sciences de l'environnement d'Ile de France,

und

Doktors der Naturwissenschaften
am Fachbereich für Geowissenschaften
der Freien Universität Berlin

vorgelegt von

LIONEL DOPPLER

Berlin/Paris, Mai 2013

Erstgutachter: Prof. Dr. Jürgen Fischer, FU Berlin
Zweitgutachter: Prof. Philippe Dubuisson, Université de Lille 1, Frankreich
(Drittgutachter: Prof. Dr. Andreas Macke, Universität Leipzig)

Tag der Disputation: 11. Juli 2013

Selbstständigkeitserklärung

Hiermit erkläre ich an Eides Statt, dass ich die vorliegende Arbeit selbstständig und ohne fremde Hilfe angefertigt, keine anderen als die angegebenen Quellen und Hilfsmittel benutzt und die den benutzten Quellen wörtlich oder inhaltlich entnommenen Stellen als solche kenntlich gemacht habe. Diese Arbeit hat in gleicher oder ähnlicher Form noch keiner Prüfungsbehörde vorgelegen.

Berlin, 15.05.2013

Summary

The aim of this PhD research is to contribute to a better estimation of the radiation budget of the Earth and the atmosphere by delving into the further understanding of physical phenomena of the atmosphere. The studied phenomena are the atmospheric radiative transfer and aerosols. The radiative transfer code MOMO (Matrix Operator Model) has been extended from shortwave [0.2 – 4 μm] to the full spectral range [0.2 – 100 μm] in order to obtain a versatile radiative transfer code that can be used for different radiative transfer studies (e.g. inversion of remote sensing measurements, optimization and calibration of measurement instruments and methods, estimation of radiative transfer fluxes, estimation of radiative forcings and heating rates), with different exigencies of precision and rapidity and over the full spectral range.

The extension of MOMO to the full range consisted of the integration of the emission of thermal infrared radiation by gases, aerosols and clouds into the matrix operator algorithm of the code. The extension of MOMO also required the development of a spectroscopy module for the modeling of the water vapor continuum of absorption in the thermal infrared. In MOMO, the gas transmission for spectral bands is modeled by means of a k-distribution method. This k-distribution algorithm has also been extended to the thermal infrared and now includes the gas emission of radiation.

In a second step, MOMO has been applied in a study on the contribution of aerosols to the radiation budget. This application has been carried out in 3 steps: 1) The characterization of the aerosols by means of observations on a regional scale (measurement campaign or spaceborne measurements). 2) The development of a radiative transfer scheme with radiative transfer code MOMO in its full range version. 3) The estimation of the radiative fluxes and of instant aerosol radiative forcings and heating-rates. The results of this work demonstrate the importance of the instrumental synergy of in-situ measurements and lidar remote sensing for the characterization of aerosol microscopic properties (refractive index and size distribution). The latter method was applied to aerosols in the Mediterranean basin within the measurement campaign TRAQA. The results have revealed the differences between pollution aerosols and desert dust aerosols regarding their microscopic and radiative properties. Further case studies have shown that the presence of clouds below the aerosols has a decisive influence on the sign and on the order of magnitude of aerosol direct radiative forcing.

Zusammenfassung

Das Ziel dieser Doktorarbeit ist das Verständnis von physikalischen atmosphärischen Phänomenen zu vertiefen, um eine bessere Abschätzung der Strahlungsbilanz zu erhalten. Die Phänomene, die untersucht wurden sind der Strahlungstransport in der Atmosphäre und die Aerosole. Das Strahlungstransportprogramm MOMO (Matrix-Operator Method) wurde vom kurzwelligen Spektralbereich [0.2 – 4 μm] zum gesamten Spektralbereich [0.2 – 100 μm] erweitert. Dadurch erhielten wir ein Programm, das für Strahlungstransportsimulierungen unterschiedlicher Art und ohne spektrale Einschränkung verwendet werden kann.

Die Erweiterung des Spektralbereiches MOMOs besteht in der Implementierung der Strahlungsemission von Gasen, Aerosolen und Wolken in den Matrix-Operator Algorithmus des Programms. Für die Erweiterung des Programms zum langwelligen Spektralbereich wurde auch ein spektroskopisches Modul entwickelt, um das Absorptionskontinuum von Wasserdampf im thermischen infraroten Spektralbereich zu modellieren. Innerhalb von MOMO wird die Transmission von Gasen für breite Spektralbände anhand einer sogenannten „k-Verteilung Methode“ modelliert. Des Weiteren wurde der k-Verteilungsalgorithmus MOMOs zum thermischen Infrarot erweitert, um die Strahlungsemission von Gasen zu berücksichtigen.

In dieser Arbeit wurde MOMO verwendet, um den Beitrag der Aerosole zur Strahlungsbilanz abzuschätzen. Die Studie wurde in 3 Schritten durchgeführt: 1) Die Charakterisierung der Aerosole anhand von Beobachtungen auf der regionalen Skala (aus Messkampagnen oder Satellitendaten). 2) Die Entwicklung eines Schemas zur Strahlungssimulation mit der neuen Version MOMOs als Kern. 3) Die Abschätzung der Strahlungsflüsse und des Strahlungsantriebes und der Heizrate der Aerosole. Die Ergebnisse dieser Studie zeigen wie effizient die Synergie von in-situ Messungen und LIDAR-Messungen für die Charakterisierung der mikroskopischen Eigenschaften der Aerosole ist. Diese Methode wurde innerhalb der Messkampagne TRAQA (Aerosole in der Region des Mittelmeeres) zur Datenauswertung verwendet. Die Ergebnisse zeigen große Unterschiede zwischen Verschmutzungsaerosolen und Wüstenaerosolen bezüglich ihrer mikroskopischen Eigenschaften und Strahlungseigenschaften. Weitere Fallstudien in dieser Arbeit haben gezeigt, dass Wolken unter Aerosolschichten einen entscheidenden Einfluss auf sowohl das Vorzeichen als auch den Betrag des Strahlungsantriebes der Aerosole haben.

Résumé long (Summary in French)

Les travaux de cette thèse, doivent contribuer aux améliorations des estimations du bilan radiatif de l'atmosphère, en approfondissant la compréhension de certains processus physiques. Les phénomènes étudiés sont le transfert radiatif dans l'atmosphère, et l'impact radiatif des aérosols. Le code de transfert radiatif MOMO (Matrix-Operator Model) a été étendu de la bande spectrale des courtes ondes [0.2 – 4 μm] au spectre complet des radiations solaires, terrestres et atmosphériques [0.2 - 100 μm]. Le but de cette extension est de disposer d'un outil de transfert radiatif versatile utilisable pour tous types d'études radiatives (inversion de mesures, programmation et calibration d'instruments, estimation de flux radiatifs) et sans limitation spectrale.

L'extension de MOMO au spectre complet a consisté à intégrer l'émission de radiation par les gaz, les aérosols et les nuages dans l'algorithme d'opérateurs matriciels de MOMO. L'extension de MOMO aux longues ondes a aussi nécessité le développement d'un module de spectroscopie, afin de modéliser le continuum d'absorption de la vapeur d'eau dans le domaine spectral de l'infrarouge thermique. MOMO utilise une méthode appelée « k-distribution » pour modéliser la transmission des gaz pour les larges bandes spectrales. L'algorithme de k-distribution de MOMO a lui aussi été étendu au spectre complet et inclus désormais l'émission de radiation par les gaz dans l'infrarouge thermique.

MOMO a été utilisé pour une application à l'étude de la contribution des aérosols au bilan radiatif. Cette étude a été construite en trois étapes : 1) la caractérisation des aérosols par des observations à l'échelle régionale (campagne de mesures ou satellites). 2) Le développement d'un schéma de simulations radiatives bâti autour du code MOMO. 3) L'estimation des flux radiatifs, des forçages radiatifs instantanés des aérosols et des taux de chauffages. Cette étude met en avant l'intérêt d'utiliser une synergie instrumentale mesures in-situ et lidar pour la caractérisation des propriétés microscopiques des aérosols. Cette méthode a été appliquée lors de la campagne TRAQA portant sur les aérosols du bassin méditerranéen. Les résultats montrent des différences entre les aérosols de pollution et les aérosols désertiques, en termes de propriétés microscopiques et radiatives. D'autres études de cas menées dans ce travail ont montré que la présence de couches nuageuses sous les panaches d'aérosols peut changer le signe et l'ordre de grandeur du forçage radiatif des aérosols.

Contents

1. General introduction

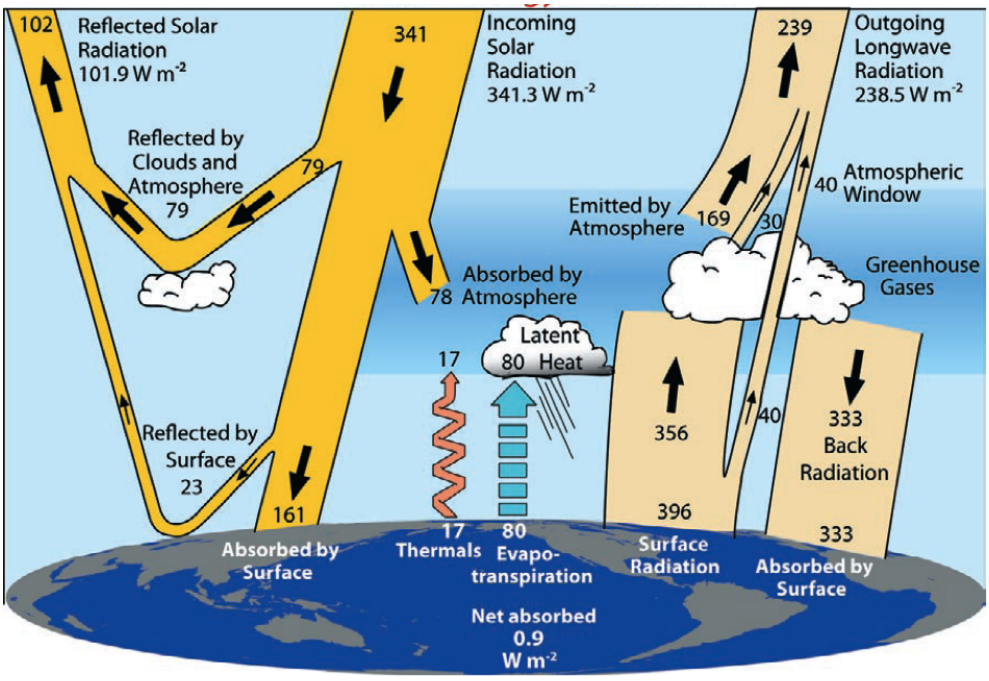

Figure 1.1.: From *Trenberth et al.* (2009) - Radiation budget of the Earth and atmosphere system. 1-D modeling of the influence of different components.

1.1. Scientific context: The Earth and atmosphere radiation budget.

The atmospheric radiative transfer is the science of all interactions of radiation with atmospheric components (gases, clouds, aerosols, Earth's surface). Radiation is the origin and the main source of energy of our atmosphere, ocean and climate system. It is thus an important purpose to estimate properly the Earth and atmosphere radiation budget. The radiation budget describes the quantity of radiation that is captured by the Earth and atmosphere system, namely: The quantity of energy that is absorbed by the Earth and by the atmosphere, the quantity of energy that is emitted by the Earth's surface and by the atmosphere, and the quantity of energy that is outgoing of the Earth and atmosphere system.

Trenberth et al. (2009) summarized the results of many models and proposed a quantification (Figure 1.1). This exercice of evaluating Earth and atmosphere radiation budget is the purpose of scientists since a century (*Stevens and Schwartz* 2012, *Trenberth et al.* 2009, *Kiehl and Trenberth* 1997, *Ramanathan et al.* 1989, *Hunt et al.* 1986, *London* 1957, *Dines* 1917). The difficulty of this exercise is that

the processes of interactions between the radiation and the Earth and atmosphere's components have to be well understood, and also, the repartition of the components in the Earth and atmosphere system must be well characterized. The method used for the radiation budget estimates consists of considering the radiation fluxes at the top of atmosphere (TOA) and at the Earth's surface. The radiation budget is split in two contributions: shortwave (solar energy) and longwave (thermal infrared radiation emitted by the Earth's surface and the atmosphere). The contributions of the diverse components are quantified with the *radiative forcings* of these components.

The quality of radiation budget estimates has considerably increased during the last decades and this for ***4*** *reasons*: *First*, the increase of the power of the calculators has allowed the computation of more parameters and thus a better accuracy. *Second*, the interactions between the radiation and the components of the Earth and atmosphere system are better understood (improvements in radiative transfer modeling). *Third*, radiation budget programs involving satellite measurements have been organized: The spaceborne instruments measure TOA fluxes at global scale. These measurements are used to validate and correct the radiative fluxes modeled by the codes. *Fourth*, remote sensing measurements, measurement campaigns and ground-based measurements have allowed improvements in the identification and in the characterization of Earth and atmosphere components.

ERB (Earth Radiation Budget study, 1975 to 1994: *Jacobowitz et al.* 1984; 1979, *Kyle et al.* 1993) and ERBE (Earth Radiation Budget Experiment, 1985 to 1989: *Barkstrom* 1984) have been the first big steps in the sake of accuracy of radiation budget estimates. The models that estimate radiative fluxes could be constraint in TOA fluxes and the contributions to global radiative fluxes have been corrected in the models. *Kiehl and Trenberth* (1997) proposed a post -ERB and -ERBE radiation budget. Their report assumes that the clouds are predominant factors for the radiation budget. *Kiehl and Trenberth* (1997) estimate of the cloud TOA forcing was - 20 Wm^{-2}. The spread for the estimations of this quantity was high: *Ramanathan et al.* (1989) found (with the help of ERBE data) an estimate of cloud radiative forcing of - 16.6 Wm^{-2} when Kiehl et al. (1994) found a value of - 19 Wm^{-2} using the same dataset. *Ardanuy et al.* (1991) found - 26.8 Wm^{-2} with ERB data and *Rossow and Zhang* (1995) found - 32.4 Wm^{-2} using ERB, ERBE data and ISCCP cloud dataset (International Satellite Cloud Climatology Project: *Rossow and Schiffer* 1991). Aerosols' effects have not been explicitly included in the calculations of *Kiehl and Trenberth* (1997) because the spatial variability of aerosols' optical properties and size distributions was to complicate to be implemented in a global-scale

model. An aerosol correction of - 3 Wm^{-2} (only for the shortwave) has been implemented, based on the estimations of *Coakley et al.* (1983).

The quantification of the radiation budget after 10 years of CERES mission (Cloud and the Earth's Radiant Energy System, 1999 to the present: *Loeb et al.* (2009), *Wielicki et al.* (1996) has been really refined. The errors in radiation budget estimates are now expected to be of the order of 5 to 10 Wm^{-2} at the TOA and 10 to 15 Wm^{-2} at the surface (*Trenberth et al.* 2009). More recently, *Kato et al.* (2012) estimated that the uncertainty on the surface radiation budget is 12 Wm^{-2}. The reasons of this refining are the improvements in all domains of the radiation budget: The CERES instruments that measure the fluxes are more precise and have more pixels than what the instruments do and had during ERBE (*Ramanathan* 2001, *Wielicki* 1996). The radiative transfer codes that are used in the radiation budget models have been improved and have better inputs: the implementation of a refined spectral database for water vapor with accurate continuum values increased the absorption by 4 to 6 Wm^{-2} (*Kim and Ramanathan* 2008). Aerosol corrections have been improved with the help of observations (*Ramanathan et al.* 2001, *Kim and Ramanathan* 2008). These observations pointed out a lack in the atmospheric absorption of 2 to 5 Wm^{-2} in the work of *Kiehl and Trenberth* 1997. Also, cloud datasets have been improved (*Rossow and Duenas* 2004, *Zang et al.* 2004) Most of all, the radiation budget quantification took advantage of a satellite remote sensing synergy: The NASA satellite Aqua, carrying two CERES instruments, is part of a fantastic satellite constellation: The A-train (fig 1.2). This constellation collocates the radiative fluxes measurements of CERES with remote sensing measurements about the features and the spatial distribution of Earth and atmosphere components (clouds, aerosols, surface emissivity and temperature). The A-Train allows the C3M-synergy (CERES, Cloudsat, CALIPSO, MODIS: *Kato et al.* 2010; 2011, *Barker et al.* 2012): CERES instruments measure the TOA fluxes (*Loeb et al.* 2009), the radar of Cloudsat (*Stephens et al.* 2002) determines the vertical distribution of the clouds, the lidar of CALIPSO (Cloud and Aerosol Lidar and Infrared Pathfinder, *Winker et al.* 2010) describes the vertical distribution of semi-transparent clouds and aerosols, and MODIS (Moderate Resolution Imaging Spectrometer: *King et al.* 1992; 2003), on board of Aqua, determines the cloud albedo and the cloud optical depth. These synergies are enforced by the use of geostationary fluxes observation: GERB on board of Meteosat (Geostationnary Earth Radiation Budget: *Harries et al.* 2005; *Allan et al.* 2007, *Slingo et al.* 2006, in mem. †); and of fluxes measurements by other spaceborne instruments: ScaRaB on board of Meteor-7 polar-orbited

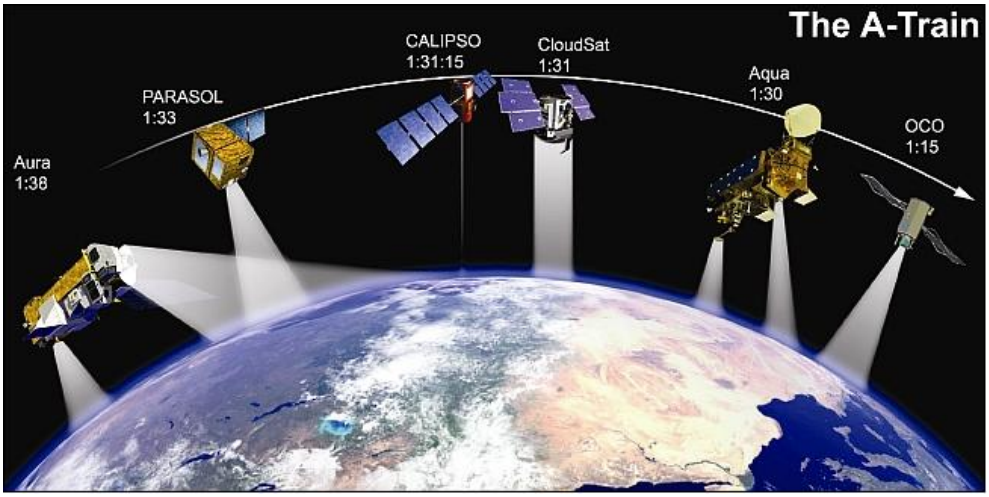

Figure 1.2.: From *eoportal (www.eoportal.com)* - Satellite Remote Sensing Synergy. The A-Train satellite constellation contains the satellites of the C3M synergy: CALIPSO, CLOUDSAT, CERES and MODIS (the two latest are both on board of Aqua).

satellite (Scanner for Radiation Budget: *Kandel et al.* 1998).

The history of radiation budget estimates points out the virtues of remote sensing measurements: The estimations of TOA fluxes have allowed to constraint the models. They also offered huge improvements in the characterization and identification of radiation budget actors. We can outline a third virtue: Remote sensing measurements allow to test the accuracy of radiative transfer code simulations and thus contributed to the improvement of radiative transfer codes. This also helps for the refining of the radiation budget estimates.

The report of *Trenberth et al.* (2009) pointed out the weak points of the recent radiation budget estimates. An important weak point is the implementation of aerosol in global estimates of radiation budget. It seems to be utopian to deliver a global aerosol model. Estimates of aerosol radiative impact with the help of many regional studies should be a more efficient approach. Another weak point is the estimate of downward longwave radiation, partly because of a poor characterization of the height of cloud bases. This point can only be improved with the help of radar measurements or measurement campaigns. Lastly, improvements could be done in the estimates of atmospheric emissions in the thermal infrared for clear air scenes. Improvements are expected from radiative transfer models especially in the domain of modeling the water vapor continuum of absorption (*Trenberth et al.* 2009, *Shine*

et al. 2012).

Other improvements are awaited: In radiative transfer modeling, using a 3-D radiative transfer code instead of a 1-D radiative transfer code can reduce the spread between instant measurements and simulations of 10 to 30 Wm^{-2} for cloudy cases (*Barker et al.* 2012). Consequences on year-averaged global fluxes have not been estimated. Also semi-direct and indirect effects of the aerosols (*Ramanathan et al.* 2001, *Haywood and Boucher* 2000, *Ackerman et al.* 2000, *Twomey* 1977; 1974, *Rosenfeld et al.* 2002, *Rosenfeld* 1999, *Albrecht* 1989) are neither fully understood nor quantified in most of radiation budget simulations.

This historical approach shows that the estimate of Earth and atmosphere radiation budget can be affined by:

1) Increasing our knowledge of the Earth and atmosphere system, namely: Promoting and multiplying the observations and measurements, and focusing on the least understood elements of the radiation budget (e.g. aerosols, interactions between aerosols and clouds, spectroscopy, regional climate and forcings).

2) Improving our capacity of simulating the radiative fluxes, forcings and radiation budget with the development of ever more precise radiative transfer codes.

The works presented in this PhD thesis placed themselves in this strategy: From a point of view of a physicist of the atmosphere, methods have been developed to understand better some Earth and atmosphere radiative phenomena (aerosol optical and radiative properties, instant aerosol radiative forcings, water vapor spectroscopy, stratification of the atmospheric optical transmission, radiative impact of aerosol and cloud vertical structures) and numerical tools have been created for the improvement of radiative transfer code MOMO (Matrix Operator Method, *Fell and Fischer* 2001).

1.2. Scientific objectives.

This PhD has been prepared in two institutes of research: In TACT (Transport Aérosol Chimie dans la Troposphère) team of LATMOS (Laboratoire Atmosphères Milieux et Observations Spatiales) at the UPMC (Université Pierre et Marie Curie) in Paris, and in the ISS (Institute for Space Sciences) of the Free University Berlin. These two institutes have different scientific cultures: TACT team is focused on the understanding of physical and chemical processes of the atmosphere and develops methods of observation. These observations are essentially active instrument observations (ground and airborne lidars, radars) and satellite remote sensing (e.g.

CALIPSO, IAISI). At the ISS, the main research activities are in the thematic of pure radiative transfer modeling (radiative transfer code modeling, spectroscopy) and inversion of satellite passive remote sensing (e.g. MERIS, MODIS, MSG) for the atmosphere, ocean and Earth's surface.

Both institutes contribute to a better understanding of radiation budget by delving into further understanding of physical atmospheric phenomena. Both institutes have an interest in estimating the radiative impact of the components of Earth and atmosphere system that they study (aerosols, clouds, water vapor, ground albedo...).

Optical observations and radiative studies are common thematic of both scientific teams. This points out a common need for both institutes: A radiative transfer code that has *two important features:*

1) The code must be *versatile*: The code must be used as a fast or precise RT code depending on the exigencies of the users. The inputs and outputs of the code should be adaptable to very different kinds of issues to simulate or to very different objectives of modeling.

2) The code must *cover the full spectral range*: The code must be able to simulate all instrument spectral channels without spectral restriction, or to model radiative phenomena at every wavelengths. The code must also be able to compute broadband radiative fluxes on the full spectral range (0.2 – 100 μm).

A versatile radiative transfer code has already been developed at the ISS and is continuously used and improved since 2 decades: It is the radiative transfer code MOMO (Matrix Operator Model, *Fischer and Grassl* 1984, *Fell and Fischer* 2001). This code was restricted to the shortwave (200 – 4000 nm). An objective of the partnership between TACT and ISS teams was to share the code MOMO between the two institutes and to extend it to the full range spectrum. This extension of MOMO to the thermal infrared was a major task of this PhD.

A second issue of this PhD has been to gather the scientific approaches of both institutes and to use the code MOMO in its new full range version for the study of the radiative impact of aerosols.

The extension of MOMO to the thermal infrared has been done with 2 objectives: First to preserve the originality of MOMO, namely its versatility and its flexibility (possibility to be applied to solve very different radiative transfer problems, possibility to adapt the precision/rapidity to the objectives of the users), and second, to implement the most modern advances in atmospheric radiative transfer modeling (spectroscopy, advanced methods for spectral band transmission and multiple scat-

tering modeling) for the sake of being a reference code regarding the precision. The main steps of MOMO's extension are the following:

- The development of a method that introduces the emission of radiation by gases, clouds and aerosols in the matrix operator method (method used in MOMO for the resolution of the radiative transfer equation with multiple scattering: *Plass et al.* 1973, *Fell and Fischer* 2001).

- The development of a spectroscopy module CGASA (Coefficient of Gas Absorption), for a precise modeling of the spectroscopy in the thermal infrared. The major difficulty of thermal infrared spectroscopy is to model properly the water vapor continuum of absorption between 8 and 12 μm (*Shine et al.* 2012, *Mlawer et al.* 2012, *Ptashnik et al.* 2011, *Clough et al.* 1989).

- The development of a method for large spectral band transmission: Spectral band transmissions are modeled in radiative transfer code with a technique named k-distribution (*Lacis and Oinas* 1991, *Fu and Liou* 1992). At the ISS, we used an advance method of k-distribution that we named non-correlated k-distribution method (*Doppler et al.* 2013a, *Bennartz and Fischer* 2000). Within this approach, we consider the stratification of the spectrum of transmission for the computation of spectral band transmission. An objective of this PhD was to adapt the k-distribution algorithm KISS (k-distribution of Institute for Space Sciences) to the thermal infrared.

The second major task of this PhD work was to study the radiative impact of aerosols. The strategy was to gather the approach of TACT (methods of observation) and of ISS (methods of radiative transfer simulations) in order to improve the knowledge about aerosols and their influence on the radiation budget. The application of radiative transfer to the estimation of the direct radiative impact of the aerosols is a current issue for scientists. Radiation budget studies could not integrate a global model of aerosols (*Kiehl and Trenberth* 1997), or they assume having uncertain estimations of the aerosol effects (*Trenberth et al.* 2009). IPCC 4th report (IPCC, 2007) points out large uncertainties in the estimation of the global aerosol direct radiative forcing: Figure SPM.2 of IPCC (2007) shows that the direct radiative forcing of the aerosols is estimated between - 0.1 Wm^{-2} and - 0.9 Wm^{-2}. This large uncertainty is due to the sensibility of aerosol radiative behavior to very variable parameters. These variable parameters are the aerosol mineral and chemical composition, the shape of the particles, their size and vertical distribution and their direct environment (ground albedo, clouds, meteorological profile). If we want to estimate the aerosol radiative forcing we need to have a precise knowledge of all these

parameters, what we do not have at a global scale.

A strategy to overcome this problem is to work at a regional scale. Measurement campaign TRAQA (Transport à longue distance et qualité de l'air) of the ChArMEx project (Chemistry and Aerosol Mediterranean Experiment) is promising advances for the aerosol characterization and the estimates of aerosol radiative impact on the climate of the Mediterranean region. The instrumental synergy (in-situ and remote sensing measurements) used in this campaign allows the application of optical closure methods (*Raut* 2008, *Raut and Chazette* 2007) for the characterization of aerosol properties. Radiative transfer simulations, on another side, point out which parameters are the most sensible for the aerosol radiative influence. The uncertainty can come from the radiative transfer method used to evaluate the radiative fluxes, from the (im)precision of the aerosol characterization (refractive index, size distribution), or from the influence of the aerosol's environment (e.g. cloud layers below aerosol plumes).

The objectives of the works about aerosols presented in this PhD were to improve the characterization of the aerosols with observation at a regional scale (measurement campaign), to develop methods of characterization (optical closure), and to compute the instant radiation budget with MOMO for 1-D case studies (1-D means along a vertical atmospheric column). These cases are precisely defined in space and time: they correspond to places and instants associated to measurements using the full instrumental synergy (in-situ and remote sensing) during the measurement campaign. Other methods must be developed for the generalization of these case studies to radiation budget estimation at larger scales of space and time. Chemical-transport models (*Skamarock et al.* 2008, *Grell et al.* 2005) will be used, as well as methods using long time satellite observations of aerosol plumes over the Mediterranean basin (lidar of CALIPSO, A-train).

1.3. Organization of the manuscript.

1.3.1. Scientific issues explored during the PhD.

During my PhD, I have developed radiative transfer tools for the radiative transfer code MOMO (Matrix Operator Model: *Fell and Fischer* 2001). I have also applied theses tools to remote sensing and radiation budget computations. Especially, I focused my work on the estimation of the direct radiative impact of the aerosols on the climate at a regional scale.

This work has been done in two main steps: (i) The extension of radiative transfer code MOMO to the thermal infrared and its application to remote sensing (ii) The development of methods for the aerosol characterization combining in-situ measurements, remote sensing and numerical tools; the development of a radiative transfer scheme for radiative budget computations; the application of these tools to the estimation of aerosol instant direct radiative forcings for case studies.

During step (i), I first focus my attention on the spectroscopy of water vapor. I developed a spectroscopy module named CGASA (Coefficient of Gas Absorption). The objective was to model properly the continuum absorption of water vapor and the absorption spectral lines. I also gave my contribution to the k-distribution module of MOMO: KISS (K-distribution of Institute for Space Sciences), by extending the non-correlated k-distribution method of *Bennartz and Fischer* (2000) to the thermal infrared. A special attention has been given to the implementation of gas emission of radiation in the k-distribution (*Doppler et al.* 2013a). I also adapted the matrix operator method used in MOMO (*Plass et al.* 1973, *Fell and Fischer* 2000) to the thermal infrared and validated the extension of MOMO (*Doppler et al.* 2013b). For each new feature described here above, I found a remote sensing application for the Infrared Imaging Radiometer (IIR, *Garnier et al.* 2012) of Cloud and Aerosol Lidar and Infrared Pathfinder Satellite Observations (CALIPSO, *Winker et al.* 2010).

During step (ii), I have taken benefit of the instrumental synergy deployed during the measurement campaign TRAQA. I developed an optical closure method. This method has allowed a characterization of the aerosols. I also developed a radiative transfer scheme with the code MOMO that can compute radiation budgets (heating rates and forcings). I have evaluated the direct radiative impact of the aerosols in different case studies. Then, I have realized a sensitivity that quantified which parameters are sensible for the aerosol direct radiative forcing. After all, I focused my work on the spatial extension of the radiation budget computations: First, along a CALIPSO track for aerosols above clouds in the Guinea Bay. This study has been done with the help of a synergy of spaceborne instruments. At the end of my work, I started to consider the generalization of the radiation budget estimations to the regional scale, for the region of the Mediterranean Basin. The first ideas are presented in the last chapter of this thesis.

1.3.2. Contents of the manuscript.

The manuscript is divided in three parts. Part I (chapters 2, 3 and 4) recalls some generalities about the radiative transfer, the radiative transfer equation (RTE) the radiative transfer codes, the spectroscopy, the k-distribution methods and the optical and radiative properties of the aerosols. Part II (chapters 5, 6 and 7) contains two articles submitted in Journal of Quantum Spectroscopy and Radiative Transfer in April and Mai 2013: *Doppler et al.* (2013a; 2013b). Part II discusses also all the developments of radiative transfer tools (MOMO, KISS, CGASA). Part III (chapters 8, 9 and 10) is devoted to the applications of radiative transfer tools for the estimation of the radiative impact of the aerosols. This part presents the works that I have done for the exploitation of the measurement campaign TRAQA, and also some results of works that I have done with others (radiative transfer code comparison AEROCOM: *Randles et al.* 2013; and a study about biomass burning aerosol above clouds for the International Radiation Symposium 2012 in Berlin: *Josset et al.* 2012).

Chapter 2 presents how radiative transfer is used in remote sensing and in radiation budget computations. The relations between measured quantities and radiative transfer mathematical concepts are displayed. The concepts of instant heating rates and radiative forcing are presented and the mathematical definitions of parameters used in the radiation budget computations are expressed. The Radiative Transfer Equation (RTE) is outlined.

Chapter 3 presents some numerical methods commonly used for the resolution of the RTE. An analysis of the different input parameters of the RTE is shown, and the methods used to determine these parameters are presented. A special attention is given to the methods used for the estimation of gas transmission: at a monochromatic scale (spectroscopy) and for wide spectral bands (k-distribution methods).

Chapter 4 recalls the basements about scattering and absorption by particles. Methods for aerosol characterization are discussed. Instruments, databases and models that can help for the characterization of aerosol features are described. The mean properties (physical, optical and radiative) of main aerosol classes are tabulated.

Chapter 5 presents the extension of MOMO to the thermal infrared spectral range and its validation. All the descriptions and discussions are in the article *Doppler et al.* 2013b. The wholeness of this submitted article is published here.

Chapter 6 discusses the spectroscopy and the development of MOMO's spectroscopy module CGASA. Applications to full range transmission spectrum of all main atmospheric gases and to full range spectral heating rates are presented.

Chapter 7 presents the new developments of KISS, the k-distribution module of MOMO. These new developments are discussed in the article *Doppler et al.* (2013a). The wholeness of this (in-revision) article is published here.

Chapter 8 deals with the optical properties of aerosols that we estimated with the help of measurement campaign TRAQA. The method of optical closure is explained, as well as the radiative transfer scheme developed for radiation budget computations. The radiative impact of aerosols is estimated for case studies taken from the TRAQA campaign.

Chapter 9 summarizes some sensible parameters for a radiative study with aerosols: the radiative transfer model and the radiative transfer scheme, the presence of clouds below aerosol plumes, and the uncertainties in the aerosol microscopic properties characterized with the TRAQA dataset in Chapter 8.

Chapter 10 explains how the radiative study of aerosols presented in Chapter 8 can be extended spatially. At a first step, this 1-dimensional study is extended to an area covering a 7500 km long spaceborne lidar track. Ideas for the extension of this study to a regional scale are proposed and discussed.

Lastly, the different conclusions of this work are highlighted. Outlook is discussed for the many perspectives that this work has opened.

Part I.

Basements

The first part of this manuscript contains 3 chapters that will give the material necessary to understand the works done in this PhD. The main concepts of radiative transfer, of remote sensing and of radiation budget are delayed and all mathematical expressions are given. The 3 chapters of Part I will also recall the state of the art of the science, regarding radiative transfer modeling and knowledge about the aerosols.

Chapter 2 is focused on the mathematical concepts of radiative transfer: The mathematical material of remote sensing and radiation budget is given and the radiative forcing and radiative heating rates are defined. The radiative transfer equation (RTE) is defined and its mathematical formulations are outlined. The RTE is the most important equation of the radiative transfer because it describes the interactions of radiation with all atmospheric components.

Chapter 3 discusses the different numerical methods that exist for the resolution of the RTE. Chapter 3 details also 2 important scientific domains of this PhD work: The spectroscopy and the k-distribution. The concepts explained in Chapter 3 will be useful for the understanding of the works presented in Part II of this manuscript.

Chapter 4 is devoted to the aerosols: aerosol physical, optical and radiative properties, and the different methods of aerosols' characterization. Chapter 3 will be useful for the understanding of the works presented in Part III of this manuscript.

2. On the Radiative Transfer Equation in remote sensing and radiation budget analysis

The radiative transfer is the basis of remote sensing observations and of radiation budget processes (Chapter 1). The objective of this chapter is to introduce the mathematical material of remote sensing and radiation budget sciences. The relation between the measured quantities in remote sensing and the concepts of radiative transfer are expressed. The different quantities (radiative forcings, heating rates) involved in radiation budget estimates are precisely defined. The mathematical descriptions of these quantities demonstrate the necessity to simulate the spectral radiance in a plane parallel atmosphere. The equation that describes the behavior of the spectral radiance in the atmosphere is the here outlined radiative transfer equation RTE.

2.1. Radiative transfer for remote sensing.

2.1.1. Generalities about Remote Sensing.

Remote sensing is the science of detecting objects or parameters per distance with a sensor technology. Remote sensing measurements can be defined in contrast to in-situ measurements. In-situ measurements consist of sampling elements of the atmosphere (e.g. air, particles, water droplets) and analyze them for a characterization of their properties. Advantages of remote sensing compared to in-situ are that remote sensing measurements are done instantaneously (the system cannot change during the time of the measurement); remote sensing measurements are done per distance so they do not disturb the measured system; and global remote sensing measurements are possible if the field of view of the instruments is wide enough (e.g. spaceborne radiometers).

Different remote sensing instruments will be presented in this thesis: Radiometers are passive instruments (passive instruments are instruments that only receive radiation) and active instruments. Active instruments send a signal and measure the radiation that comes back. The active instruments presented in this work are lidars (Light Detection and Ranging) and radars (Radio Detection and Ranging). The instruments can be carried by planes or satellites or be installed on the Earth's surface. During my PhD work, the instrument for which I have computed the most of simulations is the thermal infrared radiometer IIR (Infrared Imaging Radiometer, *Garnier et al.* 2012). IIR is on board of the satellite CALIPSO (Cloud and Aerosols Lidar and Infrared Pathfinder Satellite Observations: *Winker et al.* 2010, see also Figure 2.1.) with the lidar CALIOP (Cloud and Aerosol Lidar with

Orthogonal Polarisation: *Winker et al.* 2007), in the satellite constellation A-Train (*Stephens et al.* 2002 and Figure 1.2 of Chapter 1 of this thesis).

2.1.2. Quantities measured in Remote-Sensing.

The quantity measured by a remote-sensing instrument is the radiative energy that arrives on the sensor during a unity of time. For all kind of remote sensing instruments discussed in this thesis (lidars, radars, radiometers), the radiation that is measured comes from a given direction named direction of observation. This direction depends on the orientation of the instruments' receptor (e.g. the telescope of a lidar). We name measured radiance (in $\mathrm{W\,m^{-2}\,sr^{-1}}$) the quantity that is measured by the instrument. The measured radiance is the flux power (in W) absorbed by the sensor, divided by geometrical parameters proper to the instrument. These parameters are the azimuthal integration of the numerical aperture (the result of the integration is in sr) and the receptor's area (in $\mathrm{m^2}$). The measured radiance L_{Mes} corresponds to the spectral radiance L (in $\mathrm{W\,m^{-2}\,sr^{-1}\,nm^{-1}}$) integrated over the spectral band of the instrument's channel:

$$L_{\mathrm{Mes}} = \int_{\lambda_1}^{\lambda_2} R(\lambda) L(\lambda, \Omega) d\lambda \tag{2.1}$$

λ is the spectral wavelength; $R(\lambda)$ is the spectral response function of the instrument, defined on the spectral band $[\lambda_1, \lambda_2]$; $L(\lambda, \Omega)$ is the *spectral radiance* for the incoming direction; the incoming direction is defined with the solid angle Ω.

The *spectral response function* $R(\lambda)$ represents the spectral sensibility of the instrument. In Figure 2.2, we show the spectral response function of the three channels of IIR, and the transmission spectrum of the atmosphere within the spectral band of IIR channels.

The main difficulty in remote sensing is to estimate the desired parameter (e.g. cloud top height, aerosol optical depth, integrated water vapor profile) from a unique measured quantity, namely the measured radiance. This transformation is named *inversion* and is done by *retrieval algorithms*. The science that considers the optimization of retrieval algorithms and that makes the instrument strategy (e.g. optimization of the channels' spectral bands) is the *inverse theory* science (*Rodgers* 2000). The retrieval algorithms are based on plenty of radiative transfer simulations. The quantity that is modeled (for the instruments discussed in this work) is the spectral radiance in the spectral band of the instruments' channels.

The radiative transfer code used for these simulations is named *forward model*. Radiative transfer code MOMO has been used as forward model in many instruments' retrievals, for instance for the cloud top height retrieval with the instrument MERIS (Medium Resolution Imaging Spectrometer: *Rast* 1999): *Lindstrot et al.* (2010;2006), *Preusker and Lindstrot* (2009).

2.2. Radiative transfer for radiation budget.

2.2.1. Generalities about the radiation budget.

The *radiation budget* is the radiative energy balance of a system. In atmospheric science, this system is usually the Earth and its atmosphere, or a layer of the atmosphere. The radiation budget takes into account all the parameters that are in interaction with the atmospheric radiation: The sources of radiation (*primary sources*: solar incoming radiation, thermal infrared emission by the Earth's surface and by atmospheric constituents; *secondary sources*: the radiation reflected or scattered by the surface and by atmospheric layers); all atmospheric components (gases, clouds, aerosols), and interfaces (Earth's and ocean's surface, vegetation canopy, etc.). Within this PhD, we will compute *instant radiation budgets,* that means, the radiation budget of a 1-D column of atmosphere at a given instant (it is a radiative transfer point of view contrary to the climatologic radiation budget that is computed as a spatial averaged over the globe and a temporal average over a year). The instant radiation budget of a system is quantified by the balance of incoming and outgoing radiative energy flows (See Fig 1.1). The radiation budget is expressed in $\mathrm{W m^{-2}}$. If the instant radiation budget is computed for a layer, it is convenient to convert this quantity in temperature variation, it is then named *instant heating rate* HR, a quantity expressed in $\mathrm{K\,day^{-1}}$.

We can isolate the influence of a component on the radiation budget by computing the difference of radiation budget with and without the component. This difference is the *radiative forcing* $\Delta F_{\mathrm{component}}$ of the component (e.g. aerosol radiative forcing, clouds' radiative forcing). The radiative forcing is expressed in $\mathrm{W m^{-2}}$. In this thesis, the computed radiative forcing are *instant radiative forcings* computed from instant radiation budgets. If the instant radiative forcing is computed for a layer, we compute the difference of heating rate with and without the component, this difference is named (instant) *additional heating rate* of the component $\Delta HR_{\mathrm{component}}$ and is expressed in $\mathrm{K\,day^{-1}}$ (e.g. aerosol instant additional heating rate).

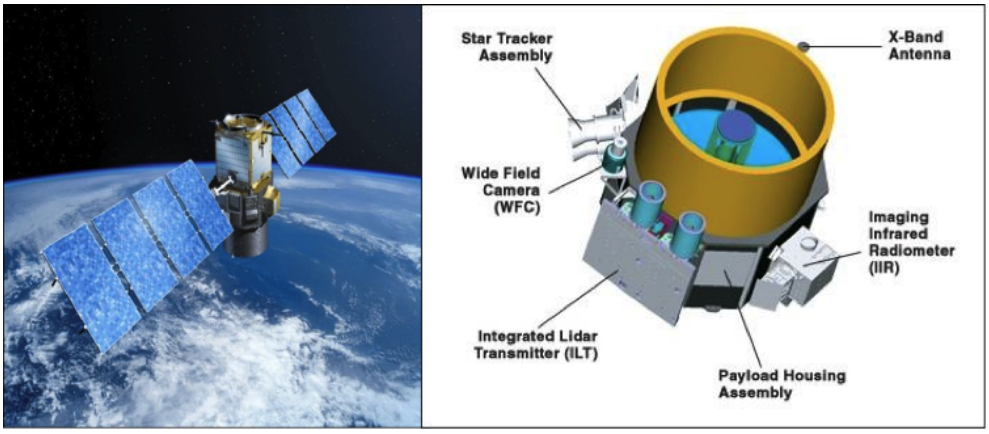

Figure 2.1.: - *From eoportal (www.eoportal.com).* Left: Artist view of satellite CALIPSO. Right: Technic view of CALIPSO platform with the IIR instrument (front right).

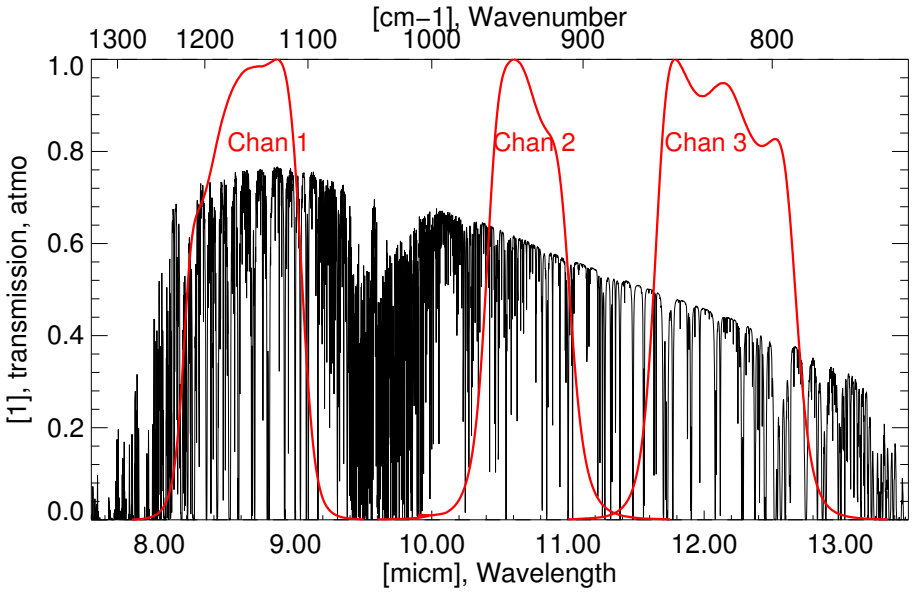

Figure 2.2.: Sensor response functions of the 3 channels of instrument IIR (red line) and transmission spectrum of a tropical standard atmosphere (black line) in the same spectral band.

2.2.2. Mathematical definition of instant radiation budget, radiative forcings and heating rates.

The (instant) *radiation budget* of a system is the difference between the incoming and the outgoing radiative energy flows coming in the system and going out of it at a given instant. If the system is an atmospheric layer or a part of the atmosphere, we are used to make a 1-D modeling with a *plane parallel atmosphere*. This approximation is correct as long as cos(SZA) is not very small (cos(SZA) > 0.14, i.e. SZA < 82°: *Petty* 2006). Thus, the incoming and outgoing flows are the vertical net fluxes F_{net} (expressed in Wm^{-2}) at the below and upper interface respectively. The *net flux* is the difference between the upward and the downward radiative *flux densities* (F_{up} and F_{down} in Wm^{-2}), going across an atmospheric level at altitude z:

$$\text{Radiation budget} = F_{\text{net}}(\text{below interface}) - F_{\text{net}}(\text{upper interface}) \tag{2.2}$$

$$F_{\text{net}}(z) = F_{\text{up}}(z) - F_{\text{down}}(z) \tag{2.3}$$

The net flux is an algebraic value. The flux density is always positive. The radiative flux F is the integration of the *spectral irradiance* I over a spectral interval:

$$F(z) = \int_{\lambda_1}^{\lambda_2} I(\lambda, z) d\lambda \tag{2.4}$$

The spectral irradiance I is the integration of the spectral radiance L over the solid angle $\Omega = 2\pi$ of a hemisphere. In the plane parallel atmosphere, we define the solid angle Ω with the azimuthal angle ϕ and the zenith angle θ:

$$I_{\text{up}}(\lambda, z) = \int_{\Omega=0}^{\pi} L(\lambda, z, \Omega) d\Omega = \int_{\phi=0}^{2\pi} \int_{\theta=0}^{\pi/2} L(\lambda, z, \theta, \phi) d\theta d\phi$$

$$I_{\text{down}}(\lambda, z) = \int_{\Omega=0}^{\pi} L(\lambda, z, \Omega) d\Omega = \int_{\phi=0}^{2\pi} \int_{\theta=-\pi/2}^{0} L(\lambda, z, \theta, \phi) d\theta d\phi \tag{2.5}$$

If we want to simulate the radiation budget, we need to simulate the spectral irradiances $I_{\text{up}}(\lambda, z)$ and $I_{\text{down}}(\lambda, z)$ at all the wanted layers of the atmosphere. Nevertheless, if the atmosphere contains scattering media, the radiative transfer code

need to consider the dispersion of the radiation in all the directions, and thus, to simulate the spectral radiance. The spectral irradiance is computed by integration of the spectral radiances over the solid angle of a hemisphere.

For the case of an atmospheric layer, we are used to convert the radiation budget in heating rate. For the conversion, we use the calorific capacity at constant pressure of the air , the gravity $g_0 = 9.81\ \mathrm{ms}^{-2}$ and the difference of pressure between the below level (P_0) and the upper level (P_1) of a layer at altitude z:

$$HR(z) = g_0/C_p \times \frac{\text{Radiation Budget}\,(z)}{P_0 - P_1} \tag{2.6}$$

2.3. The radiative transfer equation (RTE).

The discussions in previous sections have shown that for both remote sensing and radiation budget computations, it is necessary to simulate the spectral radiance L. From the spectral radiance L, we can get with trivial angular and spectral integration, all the other parameters (irradiances, radiative fluxes, radiative forcings, heating rates, measured radiances, etc.). In the present section, we will describe the behavior of the spectral radiance L in a plane parallel atmosphere. That will lead us to outline the mathematical formulations of the *radiative transfer equation* (**RTE**).

The spectral radiance $L(\lambda, s, \Omega)$, at wavelength λ, at the optical position s, and for the direction Ω is described by Schwarzschild's equation:

$$dL(\lambda, s, \Omega)/ds = -\beta_e(\lambda, s) \cdot (L(\lambda, s, \Omega) - J(\lambda, s, \Omega)) \tag{2.7}$$

β_e is the extinction coefficient (in m^{-1}) that characterizes the depletion of the light due to absorption and scattering; J is the source function.

The RTE and all the parameters that are involved are defined for a fixed wavelength λ. In order to unburden the notation, we will not write the parameter λ any more in this section.

We can decompose the source function J in two terms:

$$J(s, \Omega) = J_E(s, \Omega) + J_S(s, \Omega) \tag{2.8}$$

$J_E(s, \Omega)$ is the source of emission. J_E is the primary source due to the thermal infrared emission of radiation and is expressed in Equation 2.9:

$$J_E(s,\Omega) = (1-\omega_0(s)) \cdot B_\lambda(T(s)) \tag{2.9}$$

B_λ is the blackbody radiation. B_λ is computed with the Planck's function, knowing the temperature T of the atmospheric layer and the wavelength λ; ω_0 is the single scattering albedo. ω_0 quantifies the part of the depletion β_e that is due to the scattering (characterized by the scattering coefficient β_s), from the part due to the absorption (characterized by the absorption coefficient β_a).

Equation 2.10 summarizes the relations between β_e, β_a, β_s, and ω_0:

$$\beta_e = \beta_a + \beta_s;\ \beta_s = \omega_0 \cdot \beta_e;\ 0 < \omega_0 < 1 \tag{2.10}$$

$J_S(s,\Omega)$ is the source of scattering. J_S corresponds to the part of the radiation coming from other directions Ω' and scattered into the direction Ω . J_S is expressed in Equation 2.11:

$$J_S(s,\Omega) = \omega_0(s)/4\pi \cdot \int_{4\pi} p(s,\Omega',\Omega) \cdot L(s,\Omega')d\Omega' \tag{2.11}$$

$p(s,\Omega',\Omega)$ (in sr^{-1}) is the phase function of the layer at the position s. $p(s,\Omega',\Omega)/4\pi$ is the probability for the radiation $L(s,\Omega')$ coming from the direction Ω' to be scattered into the direction Ω.

Hence the phase function respects the following relation of normalization:

$$1/4\pi \cdot \int_{4\pi} p(s,\Omega',\Omega)d\Omega' = 1 \tag{2.12}$$

Equation 2.7 can be written as Equation 2.13 using equations 2.8, 2.9, 2.10 and 2.11:

$$dL(\tau,\Omega)/(\beta_e ds) + L(\tau,\Omega) = (1-\omega_0(s)) \cdot B_\lambda(T) + \omega_0(\tau)/4\pi \cdot \int_{4\pi} p(s,\Omega',\Omega) \cdot L(s,\Omega')d\Omega' \tag{2.13}$$

Note, that considering Equation 2.10, we can write the RTE of Equation 2.13 with the set of parameters $(\beta_s,\ \beta_a)$ instead of the set of parameters $(\beta_e,\ \omega_0)$:

$$dL(\tau,\Omega)/ds = -(\beta_a+\beta_s)\cdot L(\tau,\Omega) + \beta_a \cdot B_\lambda(T) + \beta_s/4\pi \cdot \int_{4\pi} p(s,\Omega',\Omega)\cdot L(s,\Omega')d\Omega' \tag{2.14}$$

Equations 2.13 and 2.14 are general formulations of the ***Radiative Transfer Equation*** (RTE) that must be solved by the radiative transfer codes.

Synthesis

This chapter has defined more concretely the notions of remote sensing and radiation budget. The concepts of instrument spectral response function R, radiative forcings ΔF, heating rates HR additional heating rates ΔHR have been clarified and put in equation. The quantity simulated for remote sensing applications is the spectral radiance L. For radiation budget computations, the radiative fluxes have to be computed from the irradiances I. Radiative transfer models can simulate the irradiances directly, but in most of the cases, because of the scattering, they need to simulate firstly the spectral radiance L. The spectral radiance L is thus the important parameter to simulate, both for remote sensing applications and for radiation budget estimates. The *radiative transfer equation* (**RTE**) describes the behavior of the spectral radiance in the atmosphere. The mathematical description of the RTE has been outlined in this chapter (Equations 2.13, 2.14). Simulating the spectral radiance in the atmosphere means resolving the RTE. Numerical methods for the resolution of the RTE will be presented in Chapter 3 that also presents the methods used to estimate the input parameters of the RTE.

3. Resolving the radiative transfer equation. Spectroscopy and k-distribution

Chapter 2 has outlined the main parameters of radiative transfer for remote sensing and radiation budget. The mathematical description of these parameters shows that the quantity that has to be modeled is the spectral radiance L. The *Radiative Transfer Equation* (RTE) describes the behavior of the spectral radiance L in the atmosphere. This chapter describes how to solve the RTE. Numerical methods are presented in Section 3.1. The mathematical expression of the RTE reveals a set of parameters that need to be estimated. They are the input parameters of the radiative transfer codes. These parameters are presented in section 3.2. A very important input parameter is the gas absorption coefficient. Section 3.3 explains methods used for the characterization of the gas absorption coefficient, with a monochromatic approach (spectroscopy) and a spectral band approach (k-distributions).

3.1. Numerical methods to solve the RTE.

The Radiative Transfer Equation of Equation in its general form (Equation 2.13 or 2.14) does not have an analytical solution. Many different methods to solve the RTE have been developed. Five well-known numerical methods are described here below:

- 2 Streams method / Approximation of delta of Eddington: *Toon et al.* (1989), *Joseph* (1976), *Eddington* (1916). These methods consider only the irradiance (upward and downward). They are only precise for the evaluation of the irradiances, and should not be used for simulations of radiative transfer in multiple scattering media. Nevertheless these methods are efficient for fast computations. A most advanced version (4 Streams method) is used in many radiative schemes of climate models.

- Monte Carlo methods: *Marchuk et al.* (1980), *Plass and Kattawar* (1969). These methods use a probability approach: the ways of the photons are defined individually with a random process. The process is easy to understand and to program in a code. Nevertheless it is very time consuming because of the huge quantity of photon trajectories that must be computed.

- Successive Orders of Scattering (SOS): *Deuzé et al.* (1989), *Raschke et al.* (1972): This method solves iteratively the multiple scattering, by single-scattering iterations. SOS method is accurate for multiple scattering in clouds, but fails because of a lack of convergence if the medium is not absorbing enough.

- Discrete Ordinate method (DISORT): *Stamnes* (2000; 1988), *Chandrasekhar* (1960). This method transforms the integral of the RTE (Equation 2.13

or 2.14) in a sum (on the cosines $\mu_j = \cos(\theta_j)$ of the discretized zenith angle θ_j), using a Gauss quadrature. Each discrete term μ_j is a discrete ordinate. There are $2n$ discrete ordinates. The user can choice between rapidity and accuracy by defining the value of the number n.

- Matrix operator method: *Plass et al.* (1973), *Grassl* (1978), *Olesen and Grassl* (1985). In this method, each layer of the atmosphere is divided in many very thin similar sublayers. The transmission and the reflexion of each sublayer is represented by the $N \times N$ matrices $\mathbf{T}$ and $\mathbf{R}$. N is the predefined number of discrete directions of the radiation. The sublayers are combined successively with the adding-doubling method (the method that devides the layers in millions of sublayers in order to model the multiple scattering as reflexions and transmission between and accross the sublayers) in order to compute the radiance incoming and outgoing in the complete atmospheric layer.

Only the two latest methods described here above (DISORT and Matrix Operator) are both fast and precise for radiative transfer simulations in all kinds of atmospheric media. The matrix operator method is the method used in the radiative transfer code MOMO (*Fischer and Grassl* 1984, *Fell and Fischer* 2001) for which several numerical tools have been developed during this work.

3.2. Estimation of the parameters of the RTE.

Whatever which numerical method we use, we need, for the resolution of the RTE (Equation 2.14), the knowledge of parameters β_a , β_s , p and B_λ. These parameters must be known for each layer of the atmosphere and at each wavelength λ for which the simulations are computed. These parameters are the inputs of the radiative transfer code. Their values depend on the nature of the layer (layer with particles or with gases only) and also on the radiative processes that are happening in the layer for the considered spectral interval. The possible processes are the absorption, the emission, and the scattering of radiation.

The absorption coefficient β_a can be linearly separated in two coefficients: the absorption coefficient of the gases (k) and the absorption coefficient of the particles in the layer ($\beta_{a,\mathrm{part}}$). Also, the scattering coefficient β_s can be linearly separated in two coefficients: the scattering coefficient of the gases (β_{ray}) obtained with the Rayleigh theory, and the scattering coefficient of the particles ($\beta_{s,\mathrm{part}}$). Equation 3.1 defines the absorption and scattering coefficients at the wavelength λ, for a layer at altitude z:

$$\beta_a(\lambda, z) = k(\lambda, z) + \beta_{a,\text{part}}(\lambda, z)$$

$$\beta_s(\lambda, z) = \beta_{\text{ray}}(\lambda, z) + \beta_{s,\text{part}}(\lambda, z) \tag{3.1}$$

The existing methods for the estimation of $\beta_{a,\text{part}}$ and $\beta_{s,\text{part}}$ are presented in Chapter 4. $k(\lambda, z)$ is the gas absorption at wavelength λ and altitude z. This parameter has a high spectral variability. Next section explains the methods that are used to estimate $k(\lambda, z)$.

3.3. Gas absorption coefficients.

3.3.1. Monochromatic approach: the spectroscopy.

Existence of spectral lines.

The description of the gas absorption coefficients $k(\lambda)$ (in m^{-1}) for all wavelengths λ of a spectral interval is something very complex. The quantum mechanic theory shows that the gas molecules have millions of transition lines. The wavelength λ of each line is associated to the energy E. E is the energy of the gap of the transition of the molecule between two quantum states. E is associated to λ with the Planck relation: $E = hc/\lambda$ (h is the Planck constant, c is the celerity). The molecules absorb a part of the atmospheric radiation of each wavelength λ associated to each transition line of energy gap E.

Profile of a spectral line, VCLW line profiles.

The spectral lines are not infinitely thin because of the phenomenon of *broadening*. Hence, each absorption line has to be described by a *line profile*. The main contributors to the line broadening are the Doppler and Lorentz broadening. The *Doppler broadening* is due to the random translational motions of individual molecules, due to the temperature. The spectral position of the line is thus shifted because of the Doppler effect. The Doppler broadening can be modeled with a Gaussian function. The *Lorentz broadening* is due to collisions between molecules. These collisions randomly disrupt the transitions between the quantum states and deviate the center of the spectral line. The broadening can be described by a Lorentzian function.

The Doppler and Lorentz profiles can be computed for each spectral line and depend on the temperature and on the pressure of the air. The Doppler or Lorentz profiles describe the spectral variation of the gas absorption cross section (in m^2): $\sigma(P,T)$, a function of the pressure (P) and of the temperature (T). The gas absorption coefficient $k(z)$ at altitude z and the gas absorption cross section are linked by $k(z) = \sigma(T,P) \cdot n_{\mathrm{conc}}(z)$ where n_{conc} is the gas concentration (in m^{-3}). So the gas optical depth τ is described by $\tau = \sigma \cdot n_{\mathrm{col}}$, where n_{col} is the column amount of gas (in m^{-2}).

There is a profile description that takes both Doppler and Lorentz broadenings into account. This description is name *Voigt profile* and is particularly relevant for the description of the shape of the *center of the line profile*. The *wings* of the line profile are the parts of the line profile having spectral positions that are distant from the middle of the line. In the wings, the shape of the profile should follow the Lorentz description. The Lorentz profile has an indefinite width, what the real observed line profiles has not. Hence we need to introduce a *cutoff* that define the half width of the line profile: the value of the absorption is forced to 0 for spectral positions that are further from the middle of the line than the value of the cutoff. The *Voigt Center Lorentz Wings* profile (hereafter referred to as ***VCLW*** *line profile*, Figure 3.1) considers this cutoff and is the usual description of the spectral lines: This model is a good approximation of the reality and is easy to implement in a spectroscopy computation code. Databases (HITRAN: *Rothman et al.* 2009, GEISA: *Jacquinet-Husson et al.* 2011) provide exhaustive lists of line profiles' properties for all spectral lines and for all atmospheric gases. These properties are for each line: the spectral position of the middle of the line, the line intensity and the full width at half maximum (FWHM) of the Lorentz profile associated to the line. It is thus possible, if we know the temperature, the pressure and the concentration of each gas in a layer, to compute the VCLW line profiles for all the lines of a spectral interval. By addition of all VCLW line profiles of the spectral band, we obtain the spectrum of gas absorption coefficients $k(\lambda)$ over the whole spectral band.

Water vapor continuum of absorption

For some gases in some spectral bands, the spectrum of gas absorption coefficient $k(\lambda)$ can not be described simply with the sum of the VCLW line profiles. The VCLW method leads to differences compared to the observations. For example in the spectral band [8-10 μm], for the water vapor absorption spectrum, it is obvi-

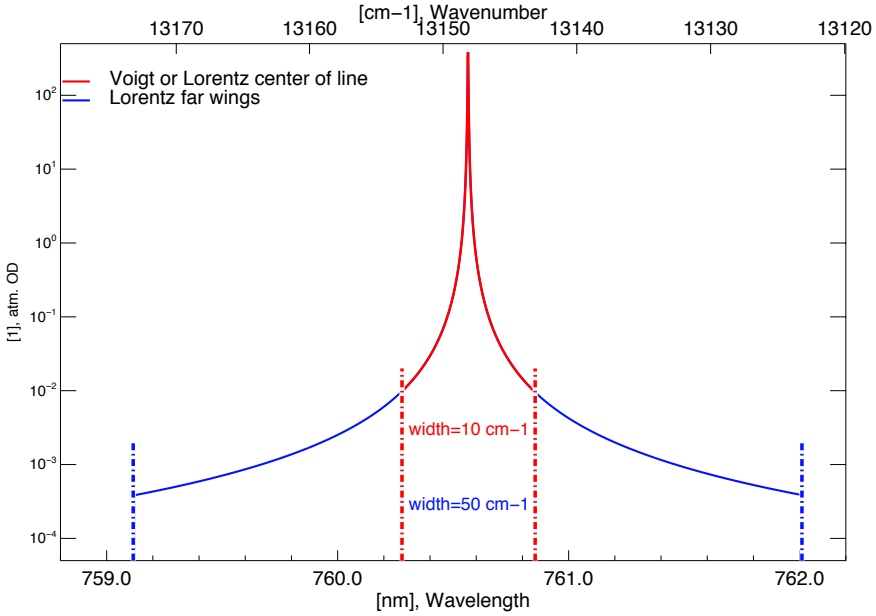

Figure 3.1.: VCLW (Voigt Center Lorentz Wings) line profile for a water vapor spectral line (here the optical depth is shown: $OD = \tau = \sigma \cdot n_{\mathrm{col}}$). The shape of the center of the line (in red) is following the Voigt profile. The shape of the wings (in blue) is following the Lorentz profile. There is a cutoff at a distance of 25 cm^{-1} from the middle of the line, so that the line profile width is not infinite.

ous that there is a continuum in addition to the line profiles. This continuum has a double origin: the dimer interaction between water vapor molecules, and the broadening of the lines due to collisions with all kind of gases. The first phenomenon is the origin of the self-continuum of absorption. The second phenomenon is the origin of the foreign-continuum of absorption (see the brilliant historical description of *Shine et al.* 2012). The self-continuum does not exist in all parts of the water vapor spectrum, but is very important in the thermal infrared. For most parts of the spectrum, the foreign continuum can be modeled by the Lorentz wings of the VCLW line profile. Nevertheless in some given spectral bands (e.g. around 900 nm or between 8 and 10 μm), the VCLW method fails because of the poor evaluation of the line profile width (the cutoffs are not appropriated). The foreign- and self-continua do not have the same dependence to water vapor amount, pressure and temperature. The values of the continua are computed with the help of tabulated coefficients. These coefficients can be found in databases: MT-CKD (Mlawer,

Tobin, Clough, Kneizys, Davies: *Clough et al.* 1989; 2005, *Mlawer et al.* 2012), CAVIAR (Continuum Absorption at Visible and Infrared wavelengths and its Atmospheric Relevance: *Ptashnik et al.* 2011). For parts of the spectrum in which the continua coefficients are used, another method than VCLW profiles must be used for the description of the centers of the lines. The computation of the appropriate line profiles and the implementation of the continua in the computation of the spectrum of $k(\lambda)$ is something challenging. Radiative transfer codes must be associated to a spectroscopy module that achieves these actions properly. Spectroscopy modules (e.g. CGASA: Coefficient of Gas Absorption, *Doppler et al.* 2013b, LBLRTM: Line by Line Radiative Transfer Model, *Clough et al.* 1992; 2005) provide accurate estimations of gas absorption coefficients $k(\lambda)$ at high spectral resolution.

3.3.2. Band approach: the k-distribution method.

The spectral variability of the gas absorption coefficient $k(\lambda)$ is very high. Spectroscopy modules need to compute $k(\lambda)$ with a high spectral resolution. Resolving the RTE at this spectral resolution would be an enormous burden regarding the computation time. For instance, the spectral band of Channel 2 of the instrument IIR is [9.5 - 11.75 μm]. For this spectral domain, a convenient spectral resolution for the computation of $k(\lambda)$ is 0.025 nm. With this resolution, there are more than 80000 spectral subintervals in the channel's spectral band. We cannot solve the RTE on 80000 intervals! We need to find a method that preserves the accuracy of the spectral transmission computation but reduces considerably the number of intervals on which the RTE will be solved.

Lacis and Oinas (1991), *Fu and Liou* (1992), and *Goody et al.* (1989) proposed a method named k-distribution method that realizes this achievement. Let a spectral band $[\lambda_1, \lambda_2]$. The gas absorption coefficient $k(\lambda)$ is computed by the spectroscopy module for N spectral subintervals. The idea of the k-distribution method is to group all the spectral subintervals having similar values $k(\lambda)$ in a bin (see example on Figure 3.2). The number n of bins is much smaller than N (for the example of Figure 3.2, n = 4 and N = 5000). The radiative transfer code must only solve the RTE for all the n bins instead of solving the RTE for each N spectral subintervals. The number of simulations can be reduced from a factor N/n varying from 10 to 20000 (1250 for the example of Figure 3.2), depending on the accuracy that the user expects.

The spectrum delivered by the spectroscopy module is an index $\{k(\lambda_j), \lambda_j\}_{j=1,\dots N}$.

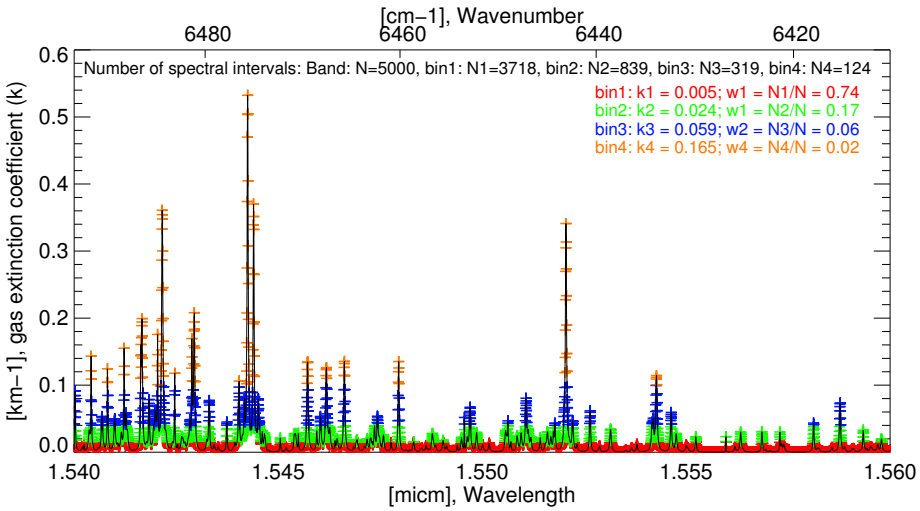

Figure 3.2.: Example of repartition of spectral subintervals in bins within *general k-distribution approach*: The spectrum of gas extinction coefficient (k) for a band is displayed (plain black line). The 5000 spectral subintervals of the spectrum are distributed in 4 groups '*bins*' of similar k value: bin 1 (red for k < 0.015); bin 2 (green for 0.015 < k < 0.04); bin 3 (blue for 0.04 < k < 0.1); bin 4 (orange for k > 0.1). The bins' extinction coefficients k_i and the bins' weight $w_i = N_i/N$ are displayed. The k-distribution $\{k_i, w_i\}_{i=1,\dots n}$ here represented is $\{(0.005; 0.024; 0.059; 0.165), (0.74; 0.17; 0.06; 0.02)\}$.

The gas absorption coefficient $k(\lambda_j)$ has been computed for each of the N wavelengths λ_j. The k-distribution replaces the index $\{k(\lambda_j), \lambda_j\}_{j=1,\dots N}$ by an index $\{k_i, w_i\}_{i=1,\dots n}$. For each bin i, a bin absorption coefficient k_i is determined. The k-distribution is an approximation, because the absorption coefficient k_i is an average of the $k(\lambda_j)$ coefficients of all spectral subintervals λ_j associated to the bin i. w_i is the bin's spectral weight, namely the part of the spectrum corresponding to the bin i. For instance, if the bin i groups the third of the spectral subintervals of $[\lambda_1, \lambda_2]$, then: $w_i = 1/3$ (see example of Figure 3.2). When the radiative transfer code solves the RTE, the value k_i replaces the parameter $k(\lambda)$ in the RTE. The RTE is solved for each bin i, and the solution is the spectral radiance L_i. The spectral radiance associated to the spectral band $[\lambda_1, \lambda_2]$ will be the weighted average: $\sum_{i=0,n} w_i \cdot L_i$.

The first difficulty for the k-distribution is that the definition of the bins must be the same for all the layers of the atmosphere. Namely, we have to group in a bin, spectral intervals that are similar regarding the gas absorption coefficient

$k(\lambda, z)$ for all the altitudes z. Spectral subintervals that have similar gas absorption values at an altitude z_A of the atmosphere do not necessarily have similar gas absorption values at another altitude z_B of the atmosphere. Different methods exist for overcoming this problem. The solution used in the k-distribution algorithm KISS (k-distribution of the Institute for Space Sciences) of radiative transfer code MOMO is presented in Chapter 7.

k-distribution are used to simulate the spectral radiance for a spectral band: with the k-distribution approach, the RTE is not applied on a monochromatic wavelength λ but on bins. A bin is associated to wavelengths having values ranging on the whole spectrum of the band. The bins' distribution is optimized to the spectral variation of the gas absorption coefficient $k(\lambda)$. Unfortunately, within a spectral band, other parameters have different spectral variability. These parameters are: the solar source of radiation, the instrument response function, the ground albedo and the blackbody radiation $B_\lambda(T)$. The three first parameters here above cited can be easily implemented by gearing the values of the weights w_i of the k-distribution (*Bennartz and Fischer* 2000). It is more difficult to implement the blackbody radiation in the k-distribution because of the double dependence of $B_\lambda(T(z))$: Dependence to altitude (z) with the temperature ($T(z)$) and dependence to wavelength (λ). The implementation of $B_\lambda(T(z))$ in the k-distribution is also the purpose of Chapter 7.

Synthesis

This chapter has been devoted to the resolution of the radiative transfer equation (RTE). Different numerical methods used to its resolution have been cited. We have outlined the parameters that play a role in the RTE (input parameters of the radiative transfer codes). One of these parameters is the gas absorption coefficient $k(\lambda)$. The way to consider the spectral variability of $k(\lambda)$ has been discussed. We have presented the concept of k-distribution. k-distribution methods allow to characterize the gas absorption for a spectral band. Other important parameters of the RTE are the parameters that characterize the scattering and the absorption by particles ($\beta_{s,\mathrm{part}}$, $\beta_{a,\mathrm{part}}$). Next chapter (Chapter 4) is entirely devoted to aerosols and particles. Experimental and modeling methods for the estimation of ($\beta_{s,\mathrm{part}}$, $\beta_{a,\mathrm{part}}$) for the cases of aerosols will be presented.

4. Aerosols: Optical properties, characterization, and radiative properties

Chapter 3 has presented how to solve the radiative transfer equation (RTE), and defined the gas parameters necessary to the resolution of the RTE. This chapter describes the particles' parameters (ω_0, p, β_{a} , β_s) necessary to the resolution of the RTE. Brief notions about aerosols are given (macroscopic parameters: ω_0, p, β_{a}, β_s, β_e, and microscopic parameters: refractive index, size distribution). The different aerosol radiative behaviors (regarding the different kinds of aerosols) are described in Section 4.1 and a table summarizes the aerosol optical, physical, lidar and radiative properties for 4 classes of aerosols. Section 4.2 presents some instrumental methods of characterization and identification of the aerosols (in-situ, and remote sensing measurements).

4.1. Optical properties of aerosols and particles.

4.1.1. Microscopic and macroscopic properties of particles.

Chapter 3 explains how to solve the radiation transfer equation (RTE). Inputs parameters are required for the resolution of the RTE. The parameters that describe the optical macroscopic properties of the particles in the layer are important parameters. They are:

- The scattering coefficient of the layer: β_s.

- The absorption coefficient of the particles of the layer: $\beta_{\mathrm{a,part}}$ (see Equation 3.9).

- The phase function: $p(\Omega, \Omega')$. The single scattering albedo (SSA): ω_0. If we have an external mixture (if the different particles do not mix together in mixed particles), then these parameters can be linearly separated per kind of constituent. Nevertheless, some rules have to be respected: Let consider 2 kinds of particles, p1 and p2 (for example aerosols and clouds) in an external mixture in a layer.

- The absorption coefficient is linear: $\beta_{\mathrm{a,part}} = \beta_{\mathrm{a,p1}} + \beta_{\mathrm{a,p2}}$

- The scattering coefficient is linear for an incoming direction Ω' to an outgoing direction Ω: $\beta_{\mathrm{s,part}} \cdot p_{\mathrm{part}}(\Omega, \Omega') = \beta_{\mathrm{s,p1}} \cdot p_{\mathrm{p1}}(\Omega, \Omega') + \beta_{\mathrm{s,p2}} \cdot p_{\mathrm{p2}}(\Omega, \Omega')$

- The scattering coefficient is linear: $\beta_{\mathrm{s,part}} = \beta_{\mathrm{s,p1}} + \beta_{\mathrm{s,p2}}$

- The SSA is not linear: $\omega_{0,\mathrm{part}} \neq \omega_{0,\mathrm{p1}} + \omega_{0,\mathrm{p2}}$

These parameters are named *macroscopic parameters* of the particles in the layer, because they describe the behavior of the whole mixture of particles with the radiation in the layer. We can distinguish the macroscopic parameters from the *microscopic parameters*. The microscopic parameters are parameters intrinsic to a kind of particle (e.g. liquid water, sulfate, black carbon, quartz). The microscopic parame-

ters are: the size distribution and the complex refractive index ($\widetilde{n} = \mathrm{Re}(\widetilde{n}) + i \cdot \mathrm{Im}(\widetilde{n})$) and the shape of the particles. The microscopic parameters describe the properties of the particles individually (particle per particle). With a Mie code, we can compute the macroscopic parameters of a kind of particle (supposed to be spherical), if we know the particle's microscopic properties. There are two possible methods to estimate the particles input parameters of the RTE:

- The *macroscopic approach*: If we know the single scattering albedo, the phase function and the extinction coefficient for each kind of particles in the layer, then the RTE can be solved directly.

- The *microscopic approach*: If we have detailed information about the chemical and mineral composition of the particles in the layer, then we can extract the size distribution of all the kinds of particles and their complex refractive index. With a Mie code, we compute the single scattering albedo, the extinction coefficient and the phase function for each kind of aerosols. Then, knowing the part of the extinction due to each component, we can solve the RTE.

The choice of the approach (microscopic or macroscopic) depends on what kind of information we have about the particles. The value of the microscopic and macroscopic parameters can be found in databases or be measured.

4.1.2. Tabulated values.

There are databases in the literature that give the properties (microscopic and macroscopic) of the aerosols. Some databases list the microscopic properties for very defined types of aerosol (with very precise mineralogical or chemical composition). Other databases are more 'atmospheric-science oriented' and give the aerosols' properties for comon classes of aerosols named mixtures. In such cases, the refractive index that is given is named effective refractive index of the mixture. We can outline 5 main classes of aerosol mixtures: The soots (or Black Carbon, BC), the organic carbon (OC), the sulfates (sulf), the sea salts (SS or marine aerosols) and the dust (or desert particles). In some areas of the atmosphere, we can find some plumes with mixing of many of these aerosols. For example, urban aerosols are mixing of BC, OC and sulfates. The mixing of the components of each category is different from one place to another; therefore, a tabulation given by a database is an approximation of what we can really observe. The parameters that are tabulated in the database are usually the complex refractive index ($\widetilde{n}$), the modal radius (R_{mod}); the standard deviation of the log-normal size distributions of the aerosols;

and the SSA (ω_0). Table 4.1 presents these values at 550 nm. The databases used for the microscopic properties given in Table 4.1 are from *Sokolik et al.* (1993) and *Volz* (1972;1973) fort the dusts. *Seinfeld and Pandis* (2006), *D'Almeida et al.* (1991), and OPAC (Optical Properties of Aerosols and Clouds): *Hess et al.* (1998) provide information for all the 4 mixtures presented in the table.

Figure 4.1 shows that the properties of the aerosols have a spectral variability (even if the spectral variability is not so high as for gas absorption coefficients). Therefore, aerosol properties cannot be considered as gray). This points out the importance of having a relative high spectral resolution for the knowledge of aerosol parameters: The values plotted are the spectrum of the refractive index (a: real part and b: imaginary part) and the SSA (c). These values are taken from OPAC database, for 4 different categories of aerosols. Note, that OPAC does not give an effective refractive index for the dust and the marines, because these mixtures are too heterogeneous in their constituents. We therefore show the spectrum of OPAC's refractive indexes for the mineral aerosol (main constituent in volume of the dusts) and the sea salt aerosol (main constituent in volume of the marines).

The main advantage of using databases is that we have information for the whole spectrum at high resolution. Nevertheless, because the tabulated mixtures are not universal but correspond to approximated mixtures, we need to constraint the tabulated values with measurements done at different wavelengths for the aerosol that we want to study specifically (see Section 4.2).

4.1.3. Aerosol radiative behavior.

The optical parameters of the aerosols have an influence on the radiative fluxes. We distinguish the scattering aerosols (if the single scattering albedo ω_0 is close to 1: $\omega_0 > 0.9$) from the absorbing aerosols ($\omega_0 < 0.85$). For scattering aerosols, the albedo effect of the aerosol will be more important than the absorbing effect and the aerosol radiative forcing should be negative in shortwave. The absorbing aerosols will absorb the radiation more than they reflect it back, thus they contributes to warm the Earth and atmosphere system. These are qualitative phenomena that depend on the aerosols' environment (above clouds or dark ocean) and on the spectral domain (shortwave or longwave). We can nevertheless outline 2 general statements:

- Absorbing aerosols have a shortwave positive radiative forcing at the TOA (if the albedo of the part of the Earth and atmosphere system above the aerosols is > 1 - SSA).

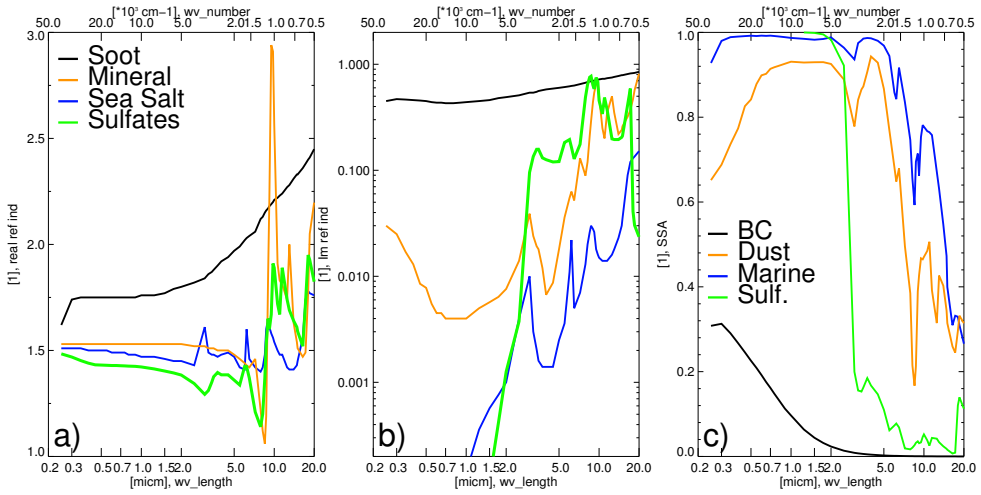

Figure 4.1.: – Spectrum of aerosol properties for 4 different categories of aerosol (from OPAC database). a) Real refractive index: Re($\widetilde{n}$); b) Imaginary refractive index: -Im($\widetilde{n}$) c) single scattering albedo: ω_0. For the following categories: Black = Black Carbon (BC); yellow = dust (mineral coarse), blue = marines (SS coarse); green = sulfates.

- Scattering aerosols have a shortwave negative forcing at the TOA (increase of the albedo effect).

Some rules of thumb can be outlined for the radiative behavior of aerosols regarding their microscopic properties (refractive indexes and size distribution):

- The imaginary part of the refractive index controls the absorption (the larger is Im($\widetilde{n}$), the larger is the absorption).

- The finer is the particle, the larger is the extinction coefficient in shortwave, and the faster the extinction coefficient vanishes when the wavelength increase (the larger is the Angström).

- Fine particles have a scattering similar to Rayleigh (p is relatively homogeneous: not much more frontscattering than backscattering).

- Coarse particles favor the backscattering (p_π at 180°), thus their lidar ratio is bigger than the one of fine particles.

Table 4.1 summarizes the microscopic properties (refractive index at 550 nm, medium size); some macroscopic parameters (lidar ratio and single scattering albedo at 550 nm); and some general radiative behaviors of 4 different classes of aerosols: BC (Black Carbon), sulfates, dust and marine aerosols (Seas Salts).

Note, that the radiative properties described in Table 4.1 are not something universal, these properties depend a lot on the environment (e.g. over clouds or dark ocean). Also, the aerosol classes that are considered can have different properties if they have different mixing (change in the aerosol composition), or with the aging of the aerosol mixture (change in size distribution) or with the relative humidity of the air (hygroscopy).

4.2. Measurements and instrumentation.

If we want to characterize the optical properties of a given aerosols, the tabulated values is not a complete source of information, because we never find in the literature a category of aerosol that corresponds exactly to the one that we observe. Therefore, it is usefull to make some measurements that allow a characterization of aerosol properties.

There are two kinds of measurements: in-situ measurements and remote sensing measurements (see definitions and descriptions in Chapter 2, Section 2.1).

4.2.1. In-situ measurements.

The in-situ measurements are done by sampling atmospheric air and particles. Analyzes of the samples allow and identification and a characterization of particles and gases. The in-situ instruments are usually on board of an aircraft that flies inside of atmospheric layers. This work will refer to 3 different in-situ instruments:

- *Nephelometer*: A nephelometer samples the air containing the particles of an atmospheric layer and estimates with an optical method the particle scattering coefficient $\beta_{\mathrm{s,part}}$ and the particle phase function integrated over the scattering angles (90°-170°). After correction, the output values are the scattering coefficient $\beta_{\mathrm{s,part}}$, and the backscattering coefficient $\beta_{\mathrm{BS,part}}$ (part of the scattering that is backscattered in all the hemisphere opposite to the incident direction). These measurements are done for 3 wavelengths (for the case of the TSI® nephelometer that we used in the TRAQA campaign): 450, 550 and 700 nm.

- *Aethalometer*: An aethalometer samples the particles of the analyzed atmospheric layer on a filter. The absorption coefficient $\beta_{\mathrm{a,part}}$ of the aerosol mixture is estimated for the wavelengths 370, 470, 520, 590, 660, 880 and 950 nm (for the case of the Magee® aethalometer that we have used during the TRAQA campaign). A weak point of the aethalometer is that its measurements are only precise if the

Class	**BC**	**Sulfates**	**Dusts**	**Marines**
Re(n) [1]	1.75 to 1.96	≈1.43	1.5 to 1.56	1.5 to 1.54
Im(n) [1]	-0,44 to -0.66	≈ -1e-8	-0.006 to -0.01	-1 to -2e-8
Size [2]	fine 0.01 to 0.02	fine 0.03 to 0.08	coarse 0.05 to 0.07/0.25 to 0.4/≈2 (diff compo)	coarse ≈0.2-/1.7 to 2.8 (diff modes)
SSA [1]	0.2 to 0.23	0.985 to 1	0.875 to 0.91	0.99 to 1
Lidar Ratio [1]	≈100	≈ 60	19 to 40	15 to 26
SW impact	Absorbing ↓albedo [3] positive forcing	Scattering ↑albedo negative forcing	Scattering and absorbing ↑albedo [4] negative forcing	Mostly scattering ↑albedo negative forcing
LW impact	insignificant	insignificant	Absorbing Positive forcing	

[1] at 550 nm; [2] Modal radius in micm; [3] Not over dark surface like ocean; [4] Not over reflexive surfaces like clouds. The forcing here presented is the TOA (top of atmosphere) radiative forcing).

Table 4.1.: Aerosol optical and radiative properties of 4 main aerosol classes

sampling is done at constant altitude (it is not recommended to make a profile of measurements).

- *PCASP: Passive Cavity Aerosol Spectrometer Probe*. The PCASP is a probe that measures the size distribution of particles having diameters ranging between 0.1 and 3 μm. The method used is a scattering inversion and the effective refractive index of the particles is pre-supposed. This is the first source of uncertainty of the PCASP measurements.

4.2.2. Remote-sensing measurements.

There are two kinds of remote sensing measurements: passive remote sensing (the instrument only measures the incoming radiation) and active remote sensing (the instrument emits a signal and measures the backscatter radiation that comes back to the instrument). The main used instrument in passive remote sensing is the spectrophotometer. A spectrophotometer is a ground-based instrument that points in direction of the sun. With a simple inversion algorithm, we can estimate the aerosol optical depth τ_{aer} (τ_{aer} is the integration of the aerosol extinction coefficient over the photon path: $d\tau = \beta_e ds$). Measurements of aerosol (τ_{aer}) or cloud (τ_{cl}) optical thickness can also be done from space (for example MODIS radiometer provides τ_{aer} and τ_{cl} at 550 nm).

Active measurements allow a ranging of atmospheric properties and a description of the heterogeneity of the concentration of particles along the atmospheric profile. There are two kinds of active remote sensing instruments: the lidars (LIDAR = Light Detection and Ranging) and the radars (RADAR = Radio Detection and Ranging). The principle is the same for both instruments: a radiation is emitted and a telescope measures the backscattered radiation. The nature of the emitted radiation is a radio-wave for the radars; for example, Cloud Profiling Radar (CPR) on board of satellite Cloudsat uses a 94 GHz nadir radiation. This radiation penetrates in dense clouds, and allows the instrument to make a cloud profile. For lidars, the radiation is a light radiation (UV, visible or near infrared). Lidars' light radiation does not penetrate in dense clouds. Lidars provide profiles of molecules (e.g. ozone, water vapor, $\mathrm{NO_2}$), aerosols, or semi transparent clouds. A description of lidar signal, lidar equation and lidar inversion algorithms is given in Appendix.

The main advantage of measurements for the estimation of aerosol properties compared to tabulated data is that measurements give the possibility to characterize the concrete mixture of aerosol that we observe, contrary to tabulated data

that are averaged properties of the main categories of aerosols. The disadvantage of the measurements is that they provide information only for few wavelengths. For a radiative study, it is necessary to know the whole spectrum of single scattering albedos, phase functions and extinction coefficients. It is thus recommended to use both measurements and databases: A method that we will use in Chapter 8 (for the case study of TRAQA campaign) consists of re-normalizing the values from the databases with the measured values obtained at the wavelengths of the instruments.

Synthesis

This Chapter has recalled the properties of the particles that are necessary for the resolution of the radiative transfer equation (RTE). The microscopic and macroscopic parameters of the aerosols have been defined. Instrumentation and literature databases have been presented. We demonstrate why they are helpful for the retrieval of aerosol parameters. The necessary tools to understand lidar, lidar measurements and lidar inversion of aerosol parameters have been recalled (in Appendix). We have briefly described the radiative behavior of the aerosols. Table 4.1 summarizes microscopic, macroscopic and radiative parameters for 4 classes of aerosols. One objective of this PhD work was to define more precisely the microscopic properties of the aerosols (the 3 first lines of Table 4.1) for the aerosol of the TRAQA campaign, and to quantify the assessments of the two latest lines of Table 4.1 about the radiative behavior of the aerosols. This has been done for case studies in Part III (chapters 8 and 9).

Part II.

FR-MOMO: Full Range high resolution 1D radiative transfer modeling

The main part of this PhD work was devoted to the development of numerical tools for the radiative transfer code MOMO (Matrix Operator Model) of the Institute for Space Sciences (Free University of Berlin). Principally, MOMO has been extended to the thermal infrared: Originally a shortwave (200 – 4000 nm) code, MOMO is now a full range radiative transfer code and covers the whole spectrum of solar, terrestrial and atmospheric radiation (0.2 – 100 μm).

All the numerical tools developed for MOMO during this PhD are presented in this part: In Chapter 5, we will see how the emission of radiation by gases, aerosols and clouds has been implemented in the matrix operator routine of the code. Validation tests are presented. These methods and results are discussed in the Article *Doppler et al.* 2013b: *Extension of radiative transfer code MOMO, Matrix-Operator Model to the thermal infrared. Clear air validation by comparison to RTTOV and application to CALIPSO-IIR.* The integrality of the article is displayed in Chapter 5 of this thesis, Section 5.2.

In Chapter 6, we will discuss the importance of spectroscopy for radiative transfer models. The spectroscopy module CGASA (Coefficients of Gas Absorption) is presented as a new development of the MOMO package. This module has been developed especially for a proper modeling of water vapor continuum of absorption in the thermal infrared. Applications of CGASA are presented in Chapter 6.

Chapter 7 is devoted to a very important module of MOMO: The k-distribution module KISS (k-distribution of the Institute for Space Sciences). The k-distribution module allows MOMO to benefit of the precision of its high-resolution spectroscopy module CGASA without that the computation time is burdened (see k-distribution description in Chapter 3). Chapter 7 explains the particularity of KISS method (not doing the correlation approximation) and describes the extension of the k-distribution method to the thermal infrared: All the methods and results are in the article *Doppler et al.* 2013a, that is entirely displayed in Section 7.3: *Improved non-correlated k-distribution methods for non-fixed instrument response function and extension to thermal infrared. Applications to satellite remote sensing.*

5. Extension of radiative transfer code MOMO to the thermal infrared

Introduction and scientific objectives.

This chapter presents the extension of radiative transfer code MOMO (Matrix Operator Model: *Fell and Fischer* 2001) to the thermal infrared. This chapter is constructed around the article *Doppler et al.* (2013b). *Doppler L, Fischer J, Carbajal-Henken C, Pelon J and Ravetta F. Extension of radiative transfer code MOMO, Matrix-Operator Model to thermal infrared. Clear air validation by comparison to RTTOV and application to CALIPSO-IIR.* Submitted in Mai 2013 to Journal of Quantum Spectroscopy and Radiative Transfer (JQSRT, Elsevier). This article is entirely displayed in Section 5.2 of this chapter.

The objectives of this chapter are:

- To recall the structure of the radiative transfer code MOMO. This is the purpose of Section 2 of the article.

- To explain the theoretical details of the extension of MOMO to the thermal infrared, especially how the adding-doubling algorithm of the matrix operator method has been adapted to the thermal infrared. These precisions are detailed in Section 3.2 of the article.

- To present a validation of the code. This validation, presented in Section 4 of the article, consists of comparisons of MOMO to an analytical solution, to another radiative transfer code (Radiative Transfer for TOV: RTTOV, *Saunders et al.* 1999a), and to measurements of a thermal infrared sensor (Imaging Infrared Radiometer: IIR, *Garnier et al.* 2012 on board of NASA's satellite CALIPSO).

5.1. Personal participation to the article Doppler et al. 2013b.

My participations to the article *Doppler et al.* 2013b have been: the whole development of the numerical tools necessary to the infrared extension, namely: The development of spectroscopy module CGASA, from the basis of the code XTRA of ISS, FU Berlin (Extinction and Transmission, *Rathke and Fischer* 2001); the extension of the k-distribution algorithm KISS (k-distribution of Institute for Space Sciences) to the thermal infrared from the basis of the shortwave k-distribution algorithm BF00 (*Bennartz and Fischer* 2000); and the implementation of the thermal infrared emission of radiation by the Earth's surface and by the atmospheric constituents within the adding doubling routine of the code MOMO.

I also managed the validation tests: simulation of the analytical solution, MOMO simulations for the comparison to RTTOV (RTTOV simulations have been done by

co-author Cintia Carbajal-Henken, ISS, FU Berlin). The MOMO simulations for the comparison to CALIPSO-IIR measurements have been done by myself; IIR measurements are delivered by the CNES (Centre National d'Etude Spatiale, French space agency) via the service ICARE (www.icare.univ-lille1.com), the cases for comparisons have been kindly selected by Thomas Deleporte (ex LATMOS, CNES). The redaction of the article has been done by myself, with help and nice reviews of co-authors.

5.2. JQSRT article: Doppler et al. 2013b (MOMO extension to the thermal infrared).

The integrality of the article submitted to Journal of Quantum Spectroscopy and Radiative Transfer (JQSRT, Elsevier) in Mai 2013, is displayed here after (22 pp.).

Extension of radiative transfer code MOMO, Matrix-Operator Model to the thermal infrared. Clear air validation by comparison to RTTOV and application to CALIPSO-IIR

Lionel Doppler[1,2,3], **Juergen Fischer**[1], **Cintia Carbajal-Henken**[1], **Jacques Pelon**[2,4], **Francois Ravetta**[2,3]

[1] Institute for Space Sciences - Free University of Berlin – Germany; [2] Laboratoire Atmosphères Milieux et Observations Spatiales (LATMOS,IPSL), Paris, France; – [3] Université Pierre et Marie Curie - Paris, France – [4] Centre Nationale de Recherche Scientifique, France

Abstract

1-D radiative transfer code MOMO (Matrix-Operator Model), has been extended from $[0.2 - 3.65\ \mu m]$ *band to the whole* $[0.2 - 100\ \mu m]$ *spectrum. MOMO can now be used for computation of full range radiation budgets (shortwave and longwave). This extension to the longwave part of the electromagnetic radiation required to consider radiative transfer processes that are features of the thermal infrared: the spectroscopy of the water vapor self-continuum absorption at* $12\ \mu m$ *and the emission of radiation by gases, aerosol, clouds and surface. MOMO's spectroscopy module, CGASA (Coefficient of Gas Absorption), has been developed for computation of gas extinction coefficients, considering continua and spectral line absorption. The spectral dependences of gas emission/absorption coefficients and of Planck's function are treated using a k-distribution. The emission of radiation is implemented in the adding-doubling process of the matrix operator method using Schwarzschild's equation. Within the layer, the Planck-function is assumed having an exponential dependence to the optical-depth. In this paper, validation tests are presented for clear air case studies: Comparisons to the analytical solution of Schwarzschild's case without scattering show an error of less than 0.07% for a realistic atmosphere with an optical depth and a blackbody temperature that decrease linearly with altitude. Comparisons to radiative transfer code RTTOV are presented for simulations of top of atmosphere brightness temperature for channels of the space-borne instrument MODIS. Results show an agreement varying from 0.1K to less than 1K depending on the channel. Finally MOMO results are compared to CALIPSO Infrared Imager Radiometer (IIR) measurements for clear air cases. A good agreement was found between computed and observed radiance: biases are smaller than 0.5 K and RMSE (Root Mean Square Error) varies between 0.4K and 0.6K depending on the channel. The extension of the code permits the utilization of MOMO as forward model for remote sensing algorithms in the full range spectrum. Another application is full range radiation budgets computations (heating rates or forcings).*

1. Introduction

This article describes the latest improvement of 1-D radiative transfer code MOMO (*Fell and Fischer, 2001,* [1]): its extension to the thermal infrared spectral band in order to cover the full spectral range of solar and terrestrial radiation: [0.2-100 μm].

The interpretations of earth observation measurements and the computations of radiation budgets, require radiative transfer simulations. These simulations have to be done by precise and fast codes. Varieties of 1-D radiative transfer codes already exist. Even so, new codes are welcome in the radiative transfer community: the more different methods to simulate a problem exist; the better is the knowledge about the way to simulate this problem. New 1-D radiative transfer codes are always invited to radiative transfer code comparisons (AEROCOM [2, 3], IPMMI [4], SPECTRE [5], ICRCCM [6]). Precise codes, as MOMO is considered to be, are especially appropriate in these experiments: they can be used as reference and evaluate the quality of the approximations done by the fast codes used in climate models.

There are plenty of radiative transfer codes, but few of them are covering the whole spectrum of wavelengths used in atmospheric research, namely $[0.2 - 100\ \mu m]$. This feature is critical: Using two different codes (one in shortwave, one in longwave) for simulations within a same study could be a source of errors. We selected a panel of five well-known 1-D radiative transfer models of the thermal infrared that cover the full range spectrum (RTTOV, Streamer, RRTM, FASDOM, and MODTRAN). References, main features, and the field of application of these models are reported in Table 1.

RTTOV (Radiative Transfer for TOVS, [7-9]) is a fast code that simulates satellite observations for a number of instruments. RTTOV simulations are also restricted to a list of satellite instrument channels and therefore cannot be used for radiation budgets computation. We selected RTTOV as a reference code for the validation of MOMO, (Section 4) because RTTOV is well tested for standard clear air atmospheric profiles.

Streamer ([10,11]) has the opposite behavior of RTTOV: Streamer can simulate the radiative transfer for bands along the full spectral range. Streamer is an efficient tool for fast radiation budget computation. Nevertheless, the width of Streamer's bands cannot be narrower than 20 cm^{-1}. Thus, Streamer cannot be used for remote sensing simulations.

RRTM (Rapid Radiative Transfer Model [12,13]) is a code developed for broad-band flux computations. RRTM is a reference code regarding the spectroscopy modeling, because RRTM uses its own line-by-line code LBLRTM (Line-by-Line Radiative Transfer Model, [12, 14, 15]). RRTM computes the fluxes for 16 broad spectral bands that cover the entire longwave spectral domain and 14 bands that cover the shortwave domain. RRTM can therefore only be used for radiation budget computations and not for remote sensing simulations.

FASDOM (Fast Calculation with Discrete Ordinate Method, [16]) and its associated codes FASRAD (Fast Calculation Radiative

Transfer) and FASAA (Fast Calculation with Absorption Approximation) are codes used originally for simulation of the channels of CALIPSO Infrared Imager Radiometer ([17]). FASDOM is an accurate and fast code. FASDOM is used for simulation of thermal infrared radiometers channels (e.g. CALIPSO-IIR, MODIS). An extension to full range radiation budgets computation is generally possible, but not recommended: FASDOM is well adapted to medium-wide satellite channels in the thermal infrared and its performances (rapidity, accuracy) are optimal for this kind of use but not for broad band flux computations.

MODTRAN (Moderate Resolution Atmospheric Transmission, [18-20]) is the only code of the here-discussed codes that can be used for both satellite remote sensing and broadband flux computations (radiation budget computations, heating rates, forcings). From a fast code at its origin, MODTRAN's precision has increased over the two last decades.

The list of codes that can be used in both shortwave and longwave, and for both remote sensing and radiation budget computations, is very limited. The extension of MOMO to the thermal infrared permits to be one of them. MOMO's main objective is to be a precise code that can be used as a reference and can test the accuracy of faster methods. Since the original version (*Fischer and Grassl, 1984,* [21]), MOMO has constantly been improved and its precision increased as well as its ability to solve new radiative transfer problems: The interaction between ocean and atmosphere has been improved ([1]), the gas transmission in the atmosphere is now simulated with an advanced k-distribution method ([22,23]), the Raman effect is taken into account ([24]), as well as the phenomenon of light polarization ([25]).

In order to fulfill the objective of high precision, we developed the high-resolution spectroscopy module CGASA (Coefficients of Gas Absorption). For the same reason, we maintain the matrix operator method ([26]) for the resolution of the RTE (Radiative Transfer Equation). This method allows precise simulations in scattering media. We adapted the matrix operator method to the thermal infrared and propose a method of implementation of the thermal emission of radiation within the matrix operator method.

Another objective of MOMO is to be used as a fast code for remote-sensing simulations. Actually, MOMO must allow a balance between rapidity and precision. It should thus be able for the user to control this balance. The use of preprocessor KISS (k-distribution of Institute for Space Sciences, [22,23]) provides this possibility: KISS is a k-distribution module ([27, 28]), namely, a tool developed to model the gas transmittance in a way that brings a considerable gain in rapidity at lowest detriment of the precision. The possibility to control the balance between rapidity and precision is enhanced by the use of a non-correlated method for the k-distribution (more details in Section 2 and in *Doppler et al, 2013,* [23]). This possibility is not given by all the codes that use the classical *correlated k-distribution* method.

The objective of this paper is to describe the extension of the radiative transfer model MOMO in the thermal infrared, and to present a validation for clear air cases. Section 2 pictures the modular structure of MOMO and each of its preprocessors. Section 3 explains the methods that have been developed and used for the MOMO extension in the thermal infrared. Section 4 presents the validation of MOMO calculations in clear air conditions: comparison to an analytical solution, comparison to another model and comparison to measurements. Discussion, conclusion and outlook are given in section 5.

2. Matrix-Operator Model MOMO: a short description

Since two decades, MOMO (**M**atrix-**O**perator **Mo**del, *Fell and Fischer*, *2001*, [1], *Fischer and Grassl, 1984* [21]) is the radiative transfer code of the ISS (Institute of Space Sciences), FUB (Free University Berlin). MOMO is a plan-parallel 1-D radiative transfer code that uses the matrix operator method (*Plass et al. 1973*, [26]). Before the here presented extension, MOMO's spectral range was limited to the solar spectral range [0.2-4 μm]. MOMO has a modular structure (see Figure 1). MOMO's modules can be used independently: one can only compute the spectroscopy with CGASA or only solve the Radiative Transfer Equation (RTE) with preprocessor MOMO. The modules can also be used in chain for a complete radiative transfer simulation.

The main module of MOMO is the preprocessor **MOMO@MOMO.** It is a Fortran code that solves the RTE and computes the radiation fluxes (spectral radiances, spectral irradiances, actinic fluxes) at all levels of the atmosphere that the user prescribed. The method used for the resolution of the RTE is the matrix operator method (*Plass et al, 1973* [26]). This is one of the most precise methods for the RTE resolution, especially in scattering media. The precision of matrix operator method is comparable to the precision of the DISORT method (Discrete ordinate method, [29-31]). DISORT is used in FASDOM, RRTM and in the precise versions of MODTRAN and Streamer. DISORT and matrix operator methods are much more precise than 2 Streams method ([32]) that Streamer and MODTRAN only use for simulations of non-scattering atmospheres. Details about the matrix operator method used in MOMO are given in *Fell and Fischer, 2001* [1]. In Subsection 3.2 of this paper, we explain how we extended the method in longwave by including the emission of radiation in the matrix operator algorithm.

For the RTE resolution, MOMO@MOMO needs input information. An important input is the transmission of the different layers of the atmosphere. Gas transmission is computed by the spectroscopy preprocessor **CGASA** (**C**oefficients of **Gas A**bsorption). CGASA was newly developed for the thermal infrared simulations. CGASA computes the absorption coefficients of all the gases and for all the layers that the user prescribed. CGASA uses line information from HITRAN 2008 database [33], and continua information from MT-CKD 2.4 [14,34]. Details about CGASA are given in subsection 3.1. The RTE is then solved monochromatically for each spectral subinterval with MOMO@MOMO.

Radiative transfer computations are usually performed for large spectral bands, which usually cover hundreds or thousands of individual absorption lines. Simulating the radiative transfer for a band requires calculations for each of the many spectral monochromatic subintervals. In the case of MODIS (Moderate Resolution Imaging Spectrometer, [35]) channel 32 (12 μm, $\tilde{\nu} \in [815; 850\ \mathrm{cm}^{-1}]$), the width of the band is $\Delta_{\tilde{\nu}} = 35\ \mathrm{cm}^{-1}$. At this wavenumber, a precise simulation of the gas extinction coefficients requires N = 42042 spectral subintervals. This value is obtained by N=$N_{\mathrm{Sch}}/5$; $N_{\mathrm{Sch}} = 5\times10^{6}\Delta_{\tilde{\nu}}/\bar{\tilde{\nu}}$, where $\Delta_{\tilde{\nu}}$ is the spectral width in cm^{-1}, and $\bar{\tilde{\nu}}$ is the mean wavenumber of the interval in cm^{-1} (*F. Schreier, 2011* [36]). For most of the applications there is no reason to solve the RTE with MOMO@MOMO for 42042 subintervals. However, we compute the gas extinction coefficients with CGASA for these 42042 subintervals, and use a k-distribution method, namely preprocessor **KISS** (k-distribution of Institute for Space Sciences) to reduce the number of intervals on which the preprocessor MOMO will solve the RTE. The k-distribution (*Lacis and Oinas, 1991* [27], *Fu and Liou, 1992* [28]) is a tool developed to model the gas transmittance in a way that brings a considerable gain in rapidity to the fewest detriment of the precision: Some k-intervals named *bins* are associated to groups of spectral subintervals in which the values of the gas transmission are similar. The number of *bins* is much reduced compared to the number of spectral subintervals. The advantage of the k-distribution is that we only need one resolution of the RTE per *bin* and no more per spectral subinterval. The possibility of controlling the balance between rapidity and precision is facilitated by the use of a non-correlated method for the k-

distribution (*Doppler et al, 2013,* [23], *Bennartz and Fischer, 2000* [22]). With this method, we really have the relation: the larger is the number of *bins* defined by the k-distribution the more accurate is the result, but the longer is the computation.

Another important input for MOMO@MOMO preprocessor is the knowledge of the optical properties of the particles (aerosols, clouds). This information is computed with the module **SCA**: SCA is a preprocessor that uses a Mie code (following the scheme of *Wiscombe, 1980* [37]) to compute the normalized extinction coefficients of the particles, their single scattering albedos and their phase functions. Inputs of SCA are the size distributions and refractive indexes of the particles. These parameters are usually taken from databases (e.g. OPAC (*Hess et al, 1998* [38]) or from values obtained from measurement campaigns.

CGASA and MOMO@MOMO need the knowledge of the vertical distribution of gas and particles and the vertical profile of temperature and pressure. The module VTP provides this major information. VTP is therefore the first module of MOMO's chain. In input of VTP, the user has to describe the altitude levels in which the fluxes will be computed by MOMO. VTP interpolates the (P, T, conc.)-profiles from user-selected AFGL-ACP (Air Force Geophysics Laboratory – Atmospheric Constituents Profiles, [39]) standard profiles or from a provided radio sounding. VTP outputs are vertical profiles of temperature, pressure, gas concentrations and particle distributions at a suitable format for the preprocessors CGASA and MOMO.

3. Radiative transfer in thermal infrared

3.1. Spectroscopy: CGASA preprocessor

In many bands of the shortwave spectrum, gas absorption coefficients can be described by the Voigt Center and Lorentz Wings profiles of spectral lines (here after referred to as VCLW, see Figure 2a). This description of the gas absorption coefficients is valid if the absorption coefficient is only composed of lines and do not contain any absorption continuum. This approximation is not valid in most parts of the thermal infrared spectrum because of the importance in strength and in spectral width of the water vapor absorption continuum (*Shine et al, 2012* [40]).

The spectroscopy preprocessor CGASA has been developed for the computation of gas absorption spectra, also for spectral regions in which there is continua absorption. CGASA is an improved version of FUB's code XTRA (*Rathke and Fischer, 2000* [41]). CGASA takes lines information from HITRAN 2008 ([33]), and computes the continuum values with MT-CKD 2.4 coefficients (*Clough et al, 1989* [34], *Mlawer et al, 2012* [14]). In parts of the spectrum where MT-CKD provides non-zero values for the continuum, CGASA method for line modeling is the same as LBLRTM's one (*Clough et al, 1992* [15], *Clough et al, 2005* [12]. It is necessary to follow LBLRTM method because MT-CKD coefficients of the continua are consistent with LBLRTM definition of "local lines": The aim of the definition of MT-CKD coefficients is that the sum (continuum computed with MT-CKD) + (local line computed with LBLRTM) = entire absorption coefficient (cont+line) of the gas specie.

The method that we used and those results exactly fit LBLRTM results is the following: The line profile is divided in 4 areas (Figure 2): The center of the profile "center of line" has a width of 64 times the FWHM (Full Width at Half Maximum). This center is divided in two parts: The top of the center of line and the basement (see Figure 2b). The two other areas are the left wing and the right wing. The method consists in putting in the "local line", only the upper part of the center of line (center of line – basement), and computing the rest (basement + wings) with the MT-CKD coefficients as a "continuum". This procedure of line computing that we name *64FWHM* allows CGASA to have similar results as LBLRTM for parts of the spectrum with continuum absorption. For example, simulations of MODIS Channel 31 at 11 µm (a spectral region in which the water vapor self-continuum is important) by CGASA and LBLRTM have a good agreement: 0.8 % RMSE (Root Mean Square Error) for the total atmospheric optical depth (Fig 3a) and 0.002 (no unit) for the total atmospheric transmission (Fig 3b). Qualitatively, this agreement is visible on Figure 3c: all details of the lines of the optical depth are in perfect agreement. Note that 64FWHM method is the best one to fit LBLRTM results, because LBLRTM line profiles are described using a fast convolution algorithm of functions. These functions of convolution are defined on intervals centered on the center of line, and having a width of $2^n \times FWHM;\ n = \{1,2,3,4\}$ (*Clough and Kneizys, 1979,* [42]). For cases with MT-CKD values of zero, we do not apply 64FWHM method. We there model the lines' profiles using the conventional VCLW profiles with fixed cutoffs (Figure 2a): The center of the line profile (width = 10 cm^{-1}) is computed with a Voigt profile, and the "far wings" (left and right of the line center) are computed with a Lorentz profile. A cutoff value of 10 cm^{-1} (25 cm^{-1} for water vapor) is applied: line profile's optical depths for wavelengths that are further from the center of the line than the cutoff value are considered as null. Note that this cutoff also exists in the 64FWHM method and in LBLRTM ([14, 34]).

3.2. Radiative transfer equation: Monochromatic case

Preprocessor MOMO (MOMO@MOMO on Figure 1) solves the radiative transfer equation. The method used is the matrix operator method coupled with the adding-doubling method (*Fell and Fischer 2001*, [1], *Plass et al. 1973,* [26]). That means that MOMO is based on the interaction principle (§3 and figure 1 of [1]): For a layer between optical abscissa τ_0 and τ_1 (Figure 4), diffuse radiation (L_0^-) emerging, e.g. from the upper boundary at τ_0 consists of reflected downward radiation ($\mathcal{R}_{01}L'^{+}_{0}$), transmitted upward radiation ($\mathcal{T}_{10}L'^{-}_{1}$) and upward radiation produced ($\mathcal{J}_{10}^-$) inside the layer [τ_0, τ_1]:

$$L_0^- = \mathcal{R}_{01}L'^{+}_{0} + \mathcal{T}_{10}L'^{-}_{1} + \mathcal{J}_{10}^- \quad (1)$$

L_0^-, L'^{+}_{0}, L'^{-}_{1} and $\mathcal{J}_{10}^-$ are vectors of p elements; $\mathcal{R}_{01}$ and $\mathcal{T}_{10}$ are $p \times p$ matrixes. p is the number of radiation directions that are considered (incoming and emerging, see Figure 4).

In shortwave, there is no primary source of radiation within an atmospheric layer, ignoring Raman scattering, which only has to be considered in high spectral resolution simulations. Thus, $\mathcal{J}_{10}^-$ consists only on the radiation produced by upward scattering within the layer. In thermal infrared there is radiation emission within a layer, following Planck's law. $\mathcal{J}_{10}^-$ can be separated in two terms: $\mathcal{J}_{D,10}^-$, the inside upward scattered radiation and $\mathcal{J}_{E,10}^-$, the upward thermal-emitted radiation.

$$\mathcal{J}_{10}^- = \mathcal{J}_{D,10}^- + \mathcal{J}_{E,10}^- \quad (2)$$

For sake of simplicity, we consider that the layer is not a scattering medium. In order to evaluate $\mathcal{J}_{E,10}^-$, we apply the Schwarzschild's equation to the radiation produced by thermal emission only in this pure-absorbing/emitting medium:

$$\mu_k \frac{\partial L_{E,k}{}^-(\tau_a)}{\partial \tau_a} = -L_{E,k}^-(\tau_a) + \mathfrak{B}(T) \quad (3)$$

- $L_{E,k}{}^-$ is the component of the upward spectral radiance associated to the direction of zenithal angle θ_k.
- $\mathfrak{B}(T)$ is the Planck function at temperature T that characterizes the thermal emission at τ_a.
- μ_k is the cosine of angle θ_k: $\mu_k = \cos(\theta_k)$
- τ_a is the absorption optical depth ($\tau_a = 0$ at τ_1 and $\tau_a = \tau_{abs10}$ at τ_0).
- τ_{abs10} is the absorption optical depth of the layer:

$$\tau_{abs10} = \tau_{abs,gas10} + (1 - \omega_{o,aer})\tau_{aer10} + (1 - \omega_{o,cl})\tau_{cl10} \quad (4)$$

- τ_{abs10} is the absorption optical depth of the layer.
- $\tau_{abs,gas10}$ is the gas absorption optical depth of the layer (computed with CGASA)
- τ_{aer10} is the optical depth of the aerosol in the layer

- τ_{cl10} is the optical depth of the clouds in the layer
- $\omega_{o,\mathrm{aer}}$ and $\omega_{o,\mathrm{cl}}$ are the single-scattering albedos of aerosols and clouds respectively (computed with preprocessor SCA).

Rewriting Schwarzschild's equation E3 as E5, allows to derive an expression of an emerging radiance as E6:

$$\mu_k \frac{\partial (L_k^-(\tau_a)\exp(\tau_a/\mu_k))}{\partial \tau_a} = \mathfrak{B}(T)\exp(\tau_a/\mu_k) \quad (5)$$

$$\begin{cases} L_k^-(\tau_{\mathrm{abs10}})\exp(\tau_{\mathrm{abs10}}/\mu_k) - L_k^-(0) = \frac{1}{\mu_k}\int_0^{\tau_{\mathrm{abs10}}} \mathfrak{B}(T(\tau_a))\exp(\tau_a/\mu_k)\mathrm{d}\tau_a \\ L_k^-(0) = 0 \\ L_k^-(\tau_{\mathrm{abs10}}) = J^-_{E10,k} \end{cases} \quad (6)$$

If the temperature T is homogeneous in the layer $[\tau_0, \tau_1]$, $\mathfrak{B}(T)$ is homogeneous within the layer: $\mathfrak{B}(T) = b_{10}$, and:

$$\mathcal{J}^-_{E10,k} = b_{10}(1 - \exp(-\tau_{\mathrm{abs10}})) \quad (7)$$

Usually, the temperature is not homogeneous within $[\tau_0, \tau_1]$. The method followed in this case is the one of *Dubuisson et al 2005,* [16] in the code FASDOM: The Planck function is supposed varying exponentially with the optical depth within the layer: This is a consequence of the Absorption Approximation described by *Fu et al, 1997* [43]. Other methods ([13] for DISORT or *H. Grassl, 1978,* [44] and *Olesen and Grassl, 1985,* [45] for the matrix operator method in thermal infrared) consider that the Planck function varies linearly with the optical depth.

We consider that within the layer, the Planck function is exponential to the absorption optical depth τ_a (τ_a= 0 at τ_1 and τ_a= τ_{abs10} at τ_0):

$$\begin{cases} \mathfrak{B}(T(\tau_a)) = b_0\exp(-\beta\tau_a) \\ \beta = \frac{1}{\tau_{\mathrm{abs10}}}\ln(\frac{b_0}{b_1}) \end{cases} \quad (8)$$

b_0 and b_1 are the blackbody radiances computed with Planck function for the temperature at level 0 and level 1, respectively. β (no unit) characterizes the logarithmical variation of the blackbody radiation within a layer. In this case, E9 is the formulation of E6:

$$J_{\mathrm{E10},k}\exp(\tau_{\mathrm{abs10}}/\mu_k) = \frac{b_0}{\mu_k}\int_0^{\tau_{\mathrm{abs10}}} \exp((-\beta + 1/\mu_k)\tau_a)\,\mathrm{d}\tau_a \quad (9)$$

$$J_{\mathrm{E10},k}\exp(\tau_{\mathrm{abs10}}/\mu_k) = \frac{-b_0}{\beta\mu_k - 1}(\exp((-\beta + 1/\mu_k)\tau_{\mathrm{abs10}}) - 1)$$

$$J_{\mathrm{E10},k} = \frac{b_0\exp(-\tau_{\mathrm{abs10}}/\mu_k) - b_0\exp(-\beta\tau_{\mathrm{abs10}})}{\beta\mu_k - 1}$$

$$J_{\mathrm{E10},k} = \frac{b_0\exp(-\tau_{\mathrm{abs10}}/\mu_k) - b_1}{\beta\mu_k - 1} \quad (10)$$

This method can only be applied if the medium is purely absorbing. For scattering media, MOMO uses the adding-doubling method: The layer is divided in 2^q sublayers. The value of q is defined considering the scattering optical depth (τ_{scat}) of the layer (the larger is τ_{scat}, the larger is q). The interaction principle is applied in each sublayer. Each sublayer is considered as purely absorbing (no scattering inside of it). The scattering is computed by the reflections between the sublayers (single scattering albedos and phase function are taken into account in the values of the coefficients of $\mathcal{R}_{nn-1}$ and $\mathcal{T}_{nn-1}$). This method permits the simulation of multi-scattering (more details in [1]).

A source matrix $\mathcal{J}^-_{Enn-1}$ is implemented in each sublayer in order to consider the thermal emission of radiation. The coefficients of $\mathcal{J}^-_{Enn-1}$ are adapted from E10 to a sublayer $[\tau_{n-1}, \tau_n]$:

$$J_{\mathrm{Enn-1},k} = \frac{b_0\exp(-\tau_{\mathrm{abs,nn-1}}/\mu_k) - b_1}{\beta\mu_k - 1} \quad (11)$$

with: $\tau_{\mathrm{abs,nn-1}} = \frac{\tau_{\mathrm{abs,whole\ layer}}}{2^q}$

4. Validation of MOMO in the thermal infrared

We validate the extension of MOMO for the thermal infrared. In this paper we focus on the validation of the contribution of gas emissions; we will thus focus on clear air and perform three comparisons: to an analytical solution (Subsection 4.1), to RTTOV simulations for MODIS channels (Subsection 4.2), and to CALIPSO-IIR observations (Subsection 4.3).

4.1. Analytical solution: Schwarzschild's equation

Within this subsection, we validate MOMO's monochromatic method in the thermal infrared, namely, the matrix operator method combined to adding-doubling and the exponential-in-optical-depth dependence of Planck function for the emission of radiation (Subsection 3.2.).

In the thermal infrared, for a purely absorbing/emitting medium (without scattering), the radiative transfer is described by Schwarzschild's equation [46]:

$$\mu_k \frac{\partial L_k}{\partial \tau} = -L_k + \mathfrak{B}(T(\tau)) \quad (12)$$

We consider a vertical profile of temperature in which the Planck function decreases linearly with τ between $\tau = 0$ and $\tau = \tau_1$. This profile is plotted in Figure 5: The atmosphere's optical depth increases linearly with altitude (in km) between 0 km ($\tau = 0$) and 8 km ($\tau_1 = 0.5$). The Y-axis scale shown at the left is the altitude and the Y-axis scale shown at the right is the optical depth. The X-axis shows the blackbody radiance (top) and the temperature (bottom). The profile of blackbody radiances at λ = 11 μm is plotted in blue for the corresponding temperatures of emission; the temperature profile is plotted in red. (E13) describes the evolution of blackbody radiation $\mathfrak{B}$ with respect to the optical depth τ:

$$\mathfrak{B}(\tau) = b_0 - \frac{b_0 - b_1}{\tau_1}\cdot\tau \quad (13)$$

L_0 is the value of the upward radiance emitted by the ground:

$$L_k(0) = L_0 = b_0 \quad (14)$$

(E15) is the solution of (E12) using (E13) and (E14):

$$L_k(\tau_1) = b_1 + \mu_k\frac{b_0 - b_1}{\tau_1}\cdot(1 - \exp\left(-\frac{\tau_1}{\mu_k}\right)) \quad (15)$$

Analytical computation has been done for 5 different observation angles (θ_k): 0°, 13°, 30°, 60° and 75°. The same computations have been done with MOMO for the atmospheric profile as given in Figure 5. This atmosphere has been parameterized for MOMO computations with a description in 20 layers. Table 4a presents the results for top of atmosphere spectral radiance of MOMO (column 3) and for the analytical solution (column 2). The observation angle is given in column 1. Column 4 shows the difference in percent between the simulated values (MOMO) and the exact ones (analytical solution). Differences never exceed 0.07 %, even for large observation angles. That means that 20 layers are sufficient for MOMO to make a precise monochromatic computation in this clear atmosphere case. This validates the in-layer description of radiative transfer described in Subsection 3.2 (matrix operator combined to adding-doubling method with the use of a Planck function that has an exponential dependence to the optical depth within the layers). As a comparison, Table 4b presents results of MOMO with an atmosphere parameterized with only 5 layers. One can see that even if the results are close to the analytical solution (differences below 0.25%), the departure to the analytical solution is slightly larger than it was for the case of the atmosphere described with 20 layers. However, the computation is faster. That points to the fact, that in thermal infrared radiative transfer the vertical resolution of the input temperature profile determines the accuracy of the results.

4.2 Validation by comparison to RTTOV.

RTTOV (Radiative Transfer for TOVS) [7-9] is a fast radiative transfer model for nadir viewing passive infrared and microwave satellite instruments. For a given atmospheric profile (temperature, gas concentration, particle vertical distribution) and a given ground emissivity and temperature, RTTOV simulates the top of atmosphere upward radiance corresponding to a selection of satellite instrument channels.

RTTOV relies on a set of *predictors* [47]. These predictors are parameters (functions of geophysical quantities) that vary as functions of variable parameters' departures from reference

profiles. These main variable parameters are: water vapor, ozone concentration and temperature profile. *Regression coefficients* are computed using a convolution of the channel spectral response and the monochromatic transmittances computed with a LBL (line-by-line) code. The regression coefficients are thus channel specific. The regression coefficients characterize how the layer optical depths and the layer transmittances vary with the variation of the variable parameters. The predictors are considered in the regression coefficients' computation. Hence, the same regression coefficients can be used to compute transmittances given any input atmospheric profile. If a set of regression coefficients exists for a given instrument channel, then RTTOV can compute very fast the transmittances and the top of atmosphere spectral radiances for this instrument channel and for different atmospheric profiles.

For the validation of MOMO's ability to simulate radiative transfer in the thermal infrared, we selected six satellite instrument channels within the spectral range between 8 and 14,5 μm and compared MOMO simulations to RTTOV's ones for the top of atmosphere radiance. This spectral interval is of special interest for a validation experiment because the Planck function has its maximum values around 10 μm for atmospheric temperatures (200-300 K). Also, the self-continuum water vapor absorption is relatively important in this spectral interval (see Figure 6). The six selected satellite channels are MODIS channels 29, 30, 31, 32, 33 and 35 corresponding to central wavelengths of 8.55, 9.73, 11.03, 12.02, 13.335 and 13.935 μm ([35]) respectively. Figure 6 shows the atmospheric transmission spectrum (bottom) for the $[8 - 14.5\ \mu m]$ band, and the detailed transmission spectra of all active gases within this spectral interval, namely CH4, N2O, O3, CO2 and H2O (upper panels). The instrument functions of the 6 selected MODIS channels are plotted in red on each spectrum.

The version of RTTOV that has been used is RTTOV 9.3 [48, 49]. Predictors of RTTOV version 7 [50, 51] have been used to compute the regression coefficients for the MODIS channels [52]. RTTOV takes line information from HITRAN-1996 ([53]) and water vapor continuum information from CKD2.1 [34].

Input data for the simulations are the mid-latitude summer standard vertical atmosphere [39] for temperature, water vapor and ozone vertical profile. Surface temperature is 294.2 K and emissivity is 1. CO2, N2O and CH4 concentrations are taken vertically constant in ppmv, with the same ground values as the ones used for the computation of RTTOV-7 regression coefficients, namely [CO2] = 396 ppmv, [N2O] = 321.8 ppmb, [CH4] = 181.4 ppmb (P. Brunel personal communication).

Figure 7 shows, for each MODIS channel, MOMO (blue) and RTTOV (red) top of atmosphere (TOA) spectral radiance (in $mW/m^2/sr/cm^{-1}$) with respect to the Zenithal Observation Angle θ_k (ZOA in °). Under each figure the MOMO-RTTOV differences are plotted (TOA spectral radiance computed with MOMO minus TOA spectral radiance computed with RTTOV) with respect to θ_k (purple line). For θ_k = 0°, the radiance has been converted to brightness temperature (B_T), and the results are displayed in Table 5. The brightness temperature differences ($B_T(\mathrm{MOMO}) - B_T(\mathrm{RTTOV})$) are reported in column 4.

Figure 7 and Table 5 show that there is a good agreement between the two codes: qualitatively, it is visible in Figure 7 that MOMO (blue) and RTTOV (red) have the same ZOA dependence. Moreover, MOMO and RTTOV curves are always very close to each other. This finding is confirmed by the quantification shown in Table 5: The brightness temperature difference for the nadir observation direction (θ_k = 0°) never exceeds 1 K.

For MODIS channels 29 and 31, only one significant absorber, namely water vapor (see Figure 6), contributes to the gas transmission; this is thus a simple issue for both models. That might be the reason why the difference in B_T between MOMO and RTTOV is below 0.1 K for these two channels. This result can be considered as very good, regarding the difficulty to reproduce the same experiment for both codes.

For the MODIS channels 32 and 33 the differences between the two codes are slightly larger but do not exceed 0.5 K, which is still satisfying. These channels are slightly more difficult to simulate than channels 29 and 31, because in addition to water vapor, CO_2 absorption and emission have to be taken into account in the radiative transfer computation.

For MODIS channels 30 and 35 the radiances of MOMO and RTTOV at TOA are close to each other: between 1 and 2 $mW\ m^{-2}sr^{-1}cm$ (purple line). The corresponding brightness temperature differences are slightly smaller than 1 K (Table 5). The agreement between the two codes is acceptable for the chosen cases. In addition to water vapor, ozone's amount is relevant within the spectral range of MODIS channel 30, and carbon dioxide in channel 35 (Figure 6). Both gases do not have the same vertical distribution as water vapor. While CO2 is generally assumed to be related to the atmospheric density profile, the maximum of ozone is located in the stratosphere, where the temperature profile is less linear. For the model inter-comparison both models resolve the upper troposphere between 5 km and the mid-latitude tropopause ($\sim$ 12 km) with only 7 layers. This means that the vertical temperature profile decreases in steps of 7 K in this domain. This feature is less important for water vapor, which is mainly located in the boundary layer, but for O_3 and CO_2, it matters. The differences in the characterization of the in-layer blackbody radiance of both models might be responsible for the bias between the results of the different models (see sections 3.2 and 4.1). Further on, the estimation of the ozone absorption lines is more challenging, since the pressure broadening of the absorption lines is much weaker in the stratosphere than in the troposphere where most of the atmospheric gases are located. However, the MOMO spectroscopic code CGASA (subsection 3.1) resolves the absorption lines at all atmospheric levels with sufficient details. Also, CGASA takes line information from the latest HITRAN version (HITRAN-2008, [33]), while RTTOV-7 spectroscopy code, GENL2 ([54]) is based on HITRAN-96 ([53]). This also is a source of uncertainties.

The difficulty of the ozone spectroscopy's simulation in the thermal infrared is put forward in ISSWG (IASI Sounder Science Working Group) line-by-line inter-comparison experiment ([55]): Figure 8 of [55] shows that radiances computed with the help of different line-by-line codes all differ from each other (differences between the code can reach 1 or 2 K) in the spectral region near 1050 cm^{-1}. Figure 6 of [55] shows that no code is in agreement with the observations in this spectral region. This problem is also visible in RTTOV documentation: In Figure 19 of [49], one can see that due to the spectroscopy, an error of 1 K is possible in the ozone spectral region near 1050 cm^{-1}.

Despite these small differences, we can assess that MOMO and RTTOV are in good agreement in the $[8 - 14.5\ \mu m]$ spectral domain.

4.3. Validation by comparison to observations: CALIPSO-IIR thermal infrared channels.

In order to achieve the validation of the code, we further compare MOMO simulations to CALIPSO-IIR measurements. IIR (Imaging Infrared Radiometer, *Garnier et al, 2012* [17]) is a thermal infrared radiometer developed by the CNES (Centre National d'Etudes Spatial). IIR is on board the NASA-CNES satellite CALIPSO (Cloud and Aerosol Lidar and Infrared Pathfinder Satellite Observations, [56]). CALIPSO-IIR has three large-band channels ($\simeq$ 2 μm wide) in the thermal infrared. The central wavelengths of the channels are at 8.65, 10.6 and 12.05 μm. Figure 8 (bottom) presents the transmission spectrum of a tropical atmosphere in CALIPSO-IIR spectral range (7.5 – 13.5 μm). CALIPSO-IIR channels' response functions are plotted in red (C1, C2, C3). The details of the

spectroscopy (CO_2, O_3, N_2O and CH_4) are plotted on the top of the figure. CALIPSO-IIR is used to study the microphysics of aerosol and semi-transparent clouds ([57]). The Second Level Processing for IR Signal, (SPIRS, [17]) is used for the inversions. CALIPSO-IIR observed radiances are obtainable on the ICARE website (ICARE, Cloud-Aerosol-Water-Radiation-Interactions [58]). For each IIR measurement, a simulated radiance is calculated for clear air or dense low clouds using the fast and operational version FASAA of FASDOM (*Dubuisson et al, 2005*, [16]) radiative transfer code for non scattering atmosphere, hereafter referred to as *op-IIR*. FASAA/FASDOM is the code used in the SPIRS algorithm. Input meteorological data for the computations of simulated radiance are GEOS-5 data from Global Modeling and Assimilation Office (GMAO) at NASA GSFC (Goddard Space Flight Center, [59]). GEOS-5 atmospheric profiles include information (ozone, water vapor, temperature profiles) at time intervals of 6 hours on a spatial grid of 540×361 (longitude×latitude and for 36 atmospheric layers. GEOS-5 provides also 2D surface temperature information at time intervals of 4 hours.

In order to make the comparison with MOMO, we selected all clear air cases, over the Pacific Ocean in the tropics between the 1st and the 20th September 2011. We selected 1300 cases where the SST (Sea-Surface Temperature) is between 299.2 K and 300.2 K.

For the selected cases, we extracted time, longitude and latitude, to interpolate, the atmospheric profile and ground from GEO-5, which are needed as input parameters of MOMO.

First, we computed all absorption lines within the CALIPSO-IIR spectral range with CGASA (Figure 8). This time-consuming computation is done only once, for the tropical standard atmosphere ([39]). The resolution of the spectroscopy computation is 0.001 cm^{-1}. In a second step KISS (see Section 2) estimates N_{bin} *bins* (k-distribution intervals) for which the preprocessor MOMO will solve the RTE. KISS produces 4 $N_{lay} \times N_{bin}$ matrixes (N_{lay} = 36 is the number of layers used in GEOS-5 atmospheric parameterization) with the optical depths of the tropical atmosphere for each *bin* and each layer. There is one matrix per molecular absorber, namely: H_2O (lines+foreign continuum only), mixed-gases (CO_2, N_2O, CH_4), ozone and H_2O self-continuum. For each of the 1300 cases MOMO reads the four matrixes and extended them from the tropical standard profile to the profile associated to the observed case, by applying the ratios of the actual and the atmospheric reference model, here the tropical standard profile. This approach has only the disadvantage that the line broadening due to pressure and temperature is fixed to the tropical profile. Thus, H_2O (lines+foreign continuum), mixed-gases and ozone matrixes are extended linearly with the gases amount but H_2O (self continuum) matrix is extended using a quadratic water vapor amount dependence of the extinction coefficient (the absorption optical depth of the water vapor self continuum has a quadratic water vapor amount dependence, [34]). MOMO solves the RTE for the considered case and for each *bin*, using the extended matrixes. Hence, MOMO has to solve N_{bin} times the RTE per case and per channel. Outputs are TOA spectral radiances and brightness temperatures for each of the 1300 cases and for each of the three channels.

Figure 9a shows the brightness temperature observed by CALIPSO-IIR (green), the simulated brightness temperature BT_{calc}(op-IIR) simulated by *op-IIR* (red) and the brightness temperature BT_{calc}(MOMO) simulated by MOMO (blue). The agreement between simulated and observed brightness temperatures is qualitatively good. The observations seem to be closer to MOMO simulations than to *op-IIR* ones, principally for Channel 1. Figure 9b shows the differences between calculated and observed brightness temperatures: $BT_{calc} - BT_{obs}$. RMSE (Root Mean Square Error): $RMSE = \sqrt{\overline{(BT_{calc} - BT_{obs})^2}}$, and the bias: $bias = \overline{BT_{calc} - BT_{obs}}$ are displayed as well and summarized in Table 6, columns 3 and 4. Table 6 and Figure 9b confirm the good agreement between simulations and measurements. MOMO results are slightly closer to the observations than *op-IIR* results are, especially for Channel 1 (0.45 K). MOMO and *op*-IIR results are similar for other channels (there is a change of the sign of the difference for Channel 3).

Agreement between MOMO simulations and the observations are satisfying: differences are for all channels below 0.7 K regarding RMSE and below 0.5 K regarding the bias. Nevertheless, these differences are larger than the intrinsic 1-σ noise of the instrument (*Garnier et al, 2012,* [17]). Instrument noise values are reported in column 4 of Table 6. Instrument biases for IIR are expected to be smaller than 0.5 K after careful in-lab calibration (CNES report, [17 and herein]). Comparisons with MODIS brightness temperatures in equivalent channels give an unexpected difference of less than 0.3 K and a drift smaller than 0.1 K [60]. Significant differences between simulated temperature and moisture and true atmosphere features can induce the differences between observed and simulated values.

A small difference in temperature, ozone or water vapor profiles between the real profile and the analysis profile interpolated for the simulations' inputs (that does not capture all atmospheric variability) can easily lead to 0.5 to 1 K of difference in the brightness temperature. This problem is visible on Figure 9a for the 200 points close to the point 1100 (see X-Axe): For all three channels, MOMO and *op-IIR* brightness temperatures have constant values, nevertheless, observed brightness temperature (green) increases. Our interpretation is that the simulation uses the same atmospheric profile even if in the reality, the temperature profile becomes warmer or the water vapor amount is decreasing along the track. The result is that the observed brightness temperature increases by 2 K for the three channels within the 200 points interval. At the opposite, the simulated brightness temperature stays at the mean value on this interval. Figure 10 shows scatter plots of the distribution of BT_{TOA} (computed) in function of BT_{TOA} (observed). In left figures, BT_{TOA} (computed) are obtained with *op-IIR* (left) and for right ones, with MOMO. The colors of the points of the scatter plot characterize the IWV (Integrated Water Vapor) column in mm. This shows how complex the experiment is: a large sample of water vapor contents has been taken into account (1300 points with IWV ranging between 20 and 50 mm). Qualitatively, the observed and corresponding brightness temperatures are well distributed along lines parallel to the bisector (y=x line). It is important to notice that the observed biases with respect to 1:1 ideal behavior are not depending on IWVP: Larger or lower IWV contents do not seem to affect the agreement between BT_{TOA} (observed) and BT_{TOA} (computed). However the bias is different in the three channels and smaller at 10.6 µm (Channel 2). This is satisfying for both radiative transfer codes because the difficulty in modeling the water vapor absorption continuum in this spectral range could lead to errors in the BT_{TOA}(computed). Thus, the scatter plots proves that the continuum is well simulated. The biases are larger when there are a lot of absorption lines in the spectrum (channel 1 and 3, see spectrum on Figure 8). Both radiative transfer codes agree very well for channel 2 and 3,. For channel 1, MOMO has a bias (0.44 K) twice smaller than the bias of *op-IIR* (0.87 K), and a RMSE of 0.6 K for 1 K with *op-IIR*. This gain in precision is balanced by a computational cost: we used 244 *bins* for MOMO computations (Table 6, column 2) while *op-IIR* uses less than 20 (P. Dubuisson, personal communication). Channel 1 is the most difficult to be modeled. The simulation of Channel 1 requires computations for water vapor lines and continuum absorption, as well as ozone absorption (See Figure 8).

As already mentioned in section 4.2, the radiative transfer is difficult to simulate when the atmosphere owns 2 absorbers in the spectral band, and when both absorbers have 2 different absorption spectra and 2 different vertical distributions (ozone and water

vapor). The k-distribution method, as used in *op-IIR*, is based on the *correlation approximation*, which assumes that the absorption spectrum of different layers of the atmosphere are correlated. This *correlated-k* method is not the most suitable for precise radiative transfer simulation for such kind of atmospheric configuration (West et al., [61]), because ozone and water vapor spectra are very different. On another side, non-correlated k-distribution methods that MOMO uses with KISS (see Section 2), do not make this approximation and are expected being more accurate for the resolution of such kind of problem by increasing the number of *bins*. This can be the reason of MOMO's advantage in precision for the simulation of channel 1. For channel 2 and 3, where there is more or less only water vapor as active absorber, MOMO and *op-IIR* have similar performances.

MOMO's performances for CALIPSO channels' simulation are qualitatively good. Quantitatively, RMSE between MOMO simulations and IIR observations remain longer than instrumental noise but smaller than the experiment incertitude. We name experiment incertitude, errors due to the lack of capacity of reproducing exactly the atmospheric profile needed in input of the simulations. This comparison to observations shows also that MOMO results are at least as good as (when not better than) the results obtained with the validated *op-IIR* code (*Dubuisson et al, 2005,* [16]). This experiment validates MOMO's ability to simulate radiative transfer in the thermal infrared and its use in remote sensing inversion algorithms.

5. Conclusions

We have extended the matrix operator code MOMO from the shortwave to the thermal infrared. Validation experiments have been done for clear air cases: comparisons to analytical solutions, comparisons to simulation of the remote sensing radiative transfer code RTTOV and comparison to CALIPSO-IIR observations. The following conclusions can be drawn from the model validation:
1) The method used to integrate the emission of radiation in the matrix operator method showed a good accuracy for monochromatic test (differences < 0.07 % to analytical solution).
2) Tests for wider spectral bands on MODIS thermal infrared channels showed that MOMO and RTTOV are in good agreement (differences vary from 0.1 K to 1 K depending on the MODIS channel that is considered).
3) The spectroscopy of water vapor in the thermal infrared computed with CGASA with the 64FWHM method is in good agreement with LBLRTM, which is a reference for the water vapor spectroscopy within the spectral intervals of the thermal infrared absorption self continuum. *RMSE*(CGASA, LBLRTM) = 0.0002 for the water vapor transmission within the spectral band of MODIS 31.
4) Small differences (< 1 K at the top-of-atmosphere brightness temperature) exist for some channels in the comparison of MOMO to RTTOV for MODIS thermal infrared channels. We attribute them to differences in modeling the spectroscopy of ozone at 9.6 µm, and to the fact that the RTTOV spectroscopy database is older (HITRAN-96 instead of HITRAN-2008) for MODIS channels.
5) Within the comparison to CALIPSO-IIR observations, on a large panel of clear air cases (1300 cases) for very different atmospheric conditions (IWV column varying between 20 and 50 mm), differences between MOMO and the observations have RMSE values of 0.57 K, 0.43 K, and 0.61 K for the top-of-atmosphere brightness temperatures. This is larger than the instrument noise (≈ 0.12 K), but it stays within the uncertainty limits that are due to the difficulty to get accurate atmospheric temperature and gas concentration profiles as required inputs of the simulations.

This paper presented the validation for clear air cases of the new developments in MOMO. These developments have been focused on thermal infrared continua and the implementations of the emission of radiation in the adding-doubling process of the matrix operator method. The new version of MOMO does not propose changes for the scattering part, which has been validated in the shortwave (Fell and Fischer, 2001, [1]). The validation in a scattering medium will be the topic of future works: A comparison of MOMO and RTTOV simulations to observations of aerosol loaded and cloudy atmospheres is under progress.

The matrix operator method is an efficient tool to solve the radiative transfer equation in scattering media. The extension of MOMO enables plenty of applications for new remote sensing approaches and for radiation budgets computations.

Acknowledgements

We thank the DAAD (Deutscher Akademischer Austauschdienst) for funding the travels of principal author between the French (LATMOS, UPMC) and German (ISS, FU Berlin) institute. We nicely thank Thomas Deleporte (LATMOS, CNES) for his help for the selection of CALIPSO-IIR cases for which we have compared MOMO to observations. GMAO (GEOS-5) and CALIPSO data have been taken from ICARE database. (http://www.icare.univ-lille1.fr/). We want to thank ICARE's team for their help in the database handling. Lastly, we thank the French space agency CNES for the IIR data of the CALIPSO mission.

References

[1] Fell F, Fischer J. Numerical simulation of the light field in the atmosphere-ocean system using the matrix-operator method, J Quant Spectrosc and Radiat Transfer 2001;69:351–88.

[2] Randles CA, Kinne S, Myhre G, et al. Intercomparison of shortwave radiative transfer schemes in global aerosol modeling: results from the AeroCom Radiative Transfer Experiment. Atm Chem Phys 2013;3(5):1-74.

[3] Halthore RN, Crisp D, Schwartz SE, et al. Intercomparison of shortwave radiative transfer codes and measurements. J Geophys Res 2005;110(D11):1984-2012.

[4] Bais, AF, Madronich S, Crawford J, et al: International Photolysis Frequency Measurement and Model Intercomparison (IPMMI): Spectral actinic solar flux measurements and modeling. J Geophys Res 2003;108(D16):8543-63.

[5] Ellingson RG, Wiscombe WJ. The Spectral Radiance Experiment (SPECTRE): Project description and sample results. Bull Am Met Soc 1996;77:1967-85.

[6] Ellingson RG, Ellis J, Fels S. The inter-comparison of radiation codes used in climate models: long wave results. J Geophys Res 1991;96(D5):8929-53.

[7] Saunders RW, Matricardi M, Brunel P. A fast radiative transfer model for assimilation of satellite radiance observations – RTTOV-5. ECMWF Tech Memo 1999;282.

[8] Saunders RW, Matricardi M, Brunel P. An Improved Fast Radiative Transfer Model for Assimilation of Satellite Radiance Observations. Quart J Royal Meteorol Soc 1999;125:1407-1425.

[9] Eyre JR. A fast radiative transfer model for satellite sounding systems. ECMWF Tech Memo 1991;176.

[10] Key JR: Streamer User's Guide, version 3.0. Coop Inst for Met Sat Stud, Univ of Wisconsin, USA, 2002;70pp.

[11] Key J, Schweiger AJ. Tools for atmospheric radiative transfer: Streamer and FluxNet. Comput Geosc 1998;24:443–51.

[12] Clough SA, Shephard MW, Mlawer EJ, Delamere JS, Iacono MJ, Cady-Pereira K, Boukabara S, Brown PD. Atmospheric radiative transfer modeling: a summary of the AER codes, Short Communication. J Quant Spectrosc Radiat Transfer 2005;91:233–44.

[13] Mlawer EJ, Taubman SJ, Brown PD, Iacono MJ, Clough SA. Radiative transfer for inhomogeneous atmospheres: RRTM, a validated correlated-k model for the longwave. J Geophys Res 1997;102(D14):16663-82.

[14] Mlawer EJ, Payne VH, Moncet JL, Delamere JS, Alvarado MJ, Tobin DC. Development and recent evaluation of the MT_CKD model of continuum absorption. Phil. Trans R Soc 2012;A370:2520-56.

[15] Clough SA, Iacono MJ, Moncet JL. Line-by-line calculation of atmospheric fluxes and cooling rates: Application to water vapor. J Geophys Res 1992;97:15761-85.

[16] Dubuisson P, Giraud V, Chomette O, Chepfer H, Pelon J. Fast Radiative transfer modeling for infrared imaging radiometry. J Quant Spectrosc Radiat Transfer 2005;95:201–20.

[17] Garnier A, Pelon J, Dubuisson P, Faivre M, Chomette O, Pascal P, Kratz DP. Retrieval of Cloud Properties Using CALIPSO Imaging Infrared Radiometer. Part I: Effective Emissivity and Optical Depth. J App Met and Clim 2012;51:1407-25.

[18] Berk A, Anderson GP, Acharya PK, Shettle EP. MODTRAN 5.2.1 User's Manual. SSI-AFRL 2011;69pp.

[19] Berk A, Bernstein LS, Anderson GP, Acharya PK, Robertson DC, Chetwynd JH, Adler-Golden SM. MODTRAN Cloud and Multiple Scattering Upgrades with Application to AVIRIS. Remote Sens Environ 1998;65:367-75.

[20] Berk A, Bernstein LS, Robertson DC. MODTRAN: A Moderate Resolution Model for LOWTRAN 7. GL-TR-89-0122, Geophysics Directorate, Phillips Laboratory, Hanscom, 1989.

[21] Fischer J, Grassl H. Radiative transfer in an atmosphere-ocean system: an azimuthally dependent matrix-operator approach. Applied Optics 1984;23(7):1031-39.

[22] Bennartz R, Fischer J. A modified k-distribution approach applied to narrow band water vapour and oxygen absorption estimates in the near infrared. J Quant Spectrosc Radiat Transfer 2000;66:539–53.

[23] Doppler L, Preusker R, Bennartz R, Fischer J. k-bin and k-IR: Improved non-correlated k-distribution methods for non-fixed instrument response function and extension to thermal infrared. Applications to satellite remote sensing. J of Quant Rad Transfer 2013; in press.

[24] von Bismarck J, Fischer J. An Examination of Errors in Computed Water-leaving Radiances Due to a Simplified Treatment of Water Raman Scattering Effects. IRS Proceeding 2012.

[25] Hollstein A, Fischer J. Radiative transfer solutions for coupled atmosphere ocean systems using the matrix operator technique. J Quant Spectrosc Radiat Transfer 2012;113:536-548.

[26] Plass G, Kattawar G, Catchings F. Matrix-operator theory of radiative transfer. 1: Rayleigh scattering. Applied Optics 1973;12(2):314-29.

[27] Lacis AA, Oinas V. Nongray Gaseous Absorption, Thermal Emission, and Multiple Scattering in Vertically Inhomogeneous Atmospheres. J of Geophys Res 1991;96(D5): 9027-63.

[28] Fu Q, Liou KN: On the Correlated k-Distribution Method for Radiative Transfer in Nonhomogeneous Atmospheres. J Atm Sc 1992;49(22):2139-56.

[29] Stamnes K, Tsay SC, Laszlo I. DISORT, a General-Purpose Fortran Program for Discrete-Ordinate-Method Radiative Transfer in Scattering and Emmiting Layered Media: Documentation of Methodology (version 1.1.). Goddard Flight Space Center 2000.

[30] Stamnes K, Tsay SC, Wiscombe W, Jayaweera K. Numerically stable algorithm for discrete-ordinate-method radiative transfer in multiple scattering and emitting layered media. Applied Optics 1988;27(12).

[31] Chandrasekar S. Radiative Transfer. Dover New York Inc, 1960;393pp.

[32] Toon OB, McKay CP, Ackerman TP. Rapid calculation of radiative heating rates and photodissociation rates in inhomogeneous multiple scattering atmospheres. J of Geophys Res 1989;94(D13):16287-301.

[33] Rothman LS, Gordon IE, et al. The HITRAN 2008 molecular spectroscopic database. J of Quant Spectrosc and Radiat Transfer 2009;110(9–10):533-72.

[34] Clough SA, Kneizys FX, Davies RW. Line Shape and the Water Vapor Continuum. Atmos Res 1989;23:229-41.

[35] King MD, Kaufman YJ, Menzel WP, Tanré D. Remote Sensing of Cloud, Aerosol, and Water Vapor Properties from the Moderate Resolution Imaging Spectrometer (MODIS). IEEE Transac on Geosc and Rem Sens 1992;30(1).

[36] Schreier F. Optimized implementations of rational approximations for the Voigt and complex error function. J Quant Spectrosc Radiat Transfer 2011;112:1010-25.

[37] Wiscombe WJ. Improve Mie Scattering Algorithm. Applied Optics 1980;19(9):1505:09.

[38] Hess M, Koepke P, Schult I. Optical Properties of Aerosols and Clouds: The Software Package OPAC. Bull Am Met Soc 1998;79(5):831-44.

[39] Anderson GP, Clough SA, Kneizys FX, Chetwynd JH, Shettle EP. AFGL Atmospheric Constituent Profiles (0-120km). AFGL-TR-86-0110, Env Res Papers 1986;984:1-43.

[40] Shine KP, Ptashnik IV, Raedel G. The Water Vapour Continuum: Brief History and Recents Developments. Surv Geophys 2012;33:535-55.

[41] Rathke C, Fischer J. Retrieval of cloud microphysical properties from thermal infrared observations by a fast iterative radiance fitting method. J Atmos Ocean Technol 2000;17:1509-24.

[42] Clough SA, Kneizys FX. Convolution algorithm for the Lorentz function. Applied Optics 1979;18(13):2329-33.

[43] Fu Q, Liou KN, Cribb MC, Charlock TP, Grossman A. Multiple Scattering Parameterization in Thermal Infrared Radiative Transfer. J of Atm Sciences 1997;54:2799-2812.

[44] Grassl H. Strahlung in Getruebten Atmosphaeren und in Wolken. Hamburger Geophysikalische Einzelschriften 1978;A(37):136pp.

[45] Olesen FS, Grassl H. Cloud detection and classification over oceans at night with NOAA-7. Int J Remote Sensing 1985;6(8):1435-44.

[46] Petty GW. A First Course in Atmospheric Radiation. Second Edition. Sundog Publishing 2006;458pp.

[47] Matricardi M, Chevallier F, Tjemkes S. An improved general fast radiative transfer model for the assimilation of radiance observations. ECMWF Tech Memo 345, 2001.

[48] Saunders R, Matricardi M, Geer A. RTTOV-9 Users Guide. MWPSAF-MO-UD-016, 2010.

[49] Saunders R, Matricardi M, Geer A, Rayer P, Embury O, Merchant C. RTTOV-9 Science and Validation Report. NWPSAF-MO-TV-020, 2010.

[50] Saunders R. RTTOV-7 Users Guide. EUMETSAT 2012.

[51] Saunders R, Andersson E, Brunel P, Chevallier F, Deblonde G, English S, Matricardi S, Rayer P, Sherlock V. RTTOV-7 Science and Validation Report. EUMETSAT 2002.

[52] http://research.metoffice.gov.uk/research/interproj/nwpsaf/rtm/rttov9_coefficients.html

[53] Rothman LS, Rinsland CP, Goldman A, Massie ST, et al. The HITRAN Molecular Spectroscopic Database and HAWKS (HITRAN Atmospheric Workstation): 1996 Edition. J Quant Spectrosc and Radiat Transfer 1998;60:665-710.

[54] Edwards DP. GENLN2: A general line-by-line atmospheric transmittance and radiance model. Version 3.0: Description and users guide. NCAR Tech Note 1992.

[55] Tjemkes SA, Patterson T, Rizzi R, Shephard MW, et al. The ISSWG line-by-line inter-comparison experiment, J Quant Spectrosc Radiat Transfer 2003;77:433-53.

[56] Winker DM, Pelon J, Coakley JA, et al. The CALIPSO Mission, A Global 3D View of Aerosols and Clouds. Bull of Am Met Soc 2010;91(9):1211-29.

[57] Dubuisson P, Giraud V, Pelon J, Cadet B, Yang P. Sensitivity of thermal infrared radiation at the top of the atmosphere and the surface to ice cloud microphysics. J Appl Meteor Climatol 2008;47:2545-60.

[58] http://www.icare.univ-lille1.fr

[59] (http://gmao.gsfc.nasa.gov/) Global Modelling and Assimilation Office, Annual Report & Research Highlights, 2011-2012, NASA Goddard Space Flight Center, 2012

[60] Scott NA, Garnier A, Pelon J, et al. Assessing Calipso IIR radiance accuracy via stand-alone validation and a GEO/LEO inter-calibration approach using MODIS/Aqua and SEVIRI/MSG, GSICS Quartely 2009; 3(3), 3-5.

[61] West R, Goody R, Chen L, Crisp D. The correlated-k method and related methods for broadband radiation calculations. J Quant Spectrosc Radiat Transfer 2010;111:1672-73.

[62] Wiscombe WJ, Evans JW. Exponential-sum fitting of radiative transmission functions. J Comp Phys 1977;24:416-444.

Table and Figure Captions

Table 1: List of the acronyms used in the article

Table 2: List of well-known radiative transfer codes
Column 1: Name of the code. Column 2: Principal references. Column 3: method used to solve the RTE. Column 4: Method used to compute the spectroscopy and to compute the transmittance. Column 5: Domain of application of the model.

Table 3: List of mathematical symbols used in this article.

Table 4: Results of the comparison with analytical solution (Schwarzschild's equation).
Column 1: observation angle. Column 2: spectral radiance computed with the analytical solution. Column 3: Top of atmosphere spectral radiance computed with MOMO. Column 4: Difference in % between analytical solution and MOMO.
4a) Case of an atmosphere parameterized with 20 layers in input of MOMO.
4b) Case of an atmosphere parameterized with 5 layers in input of MOMO.

Table 5: Results of the comparison RTTOV/MOMO
Column 1: Channel. Column 2: TOA-BT (Top of atmosphere Brightness Temperature), MOMO. Column 3: TOA-BT, RTTOV. Column 4: Difference MOMO-RTTOV in K

Table 6: Comparison MOMO to CALIPSO-IIR observations and operational algorithm simulations (op-IIR).
Column 2: Number of bins of the k-distribution used by MOMO for the computation. Column 3: RMSE (Root Mean Square Error) on the Brightness Temperature difference (BT_{diff} = BT(computed – BT observed). Colum 4: Bias between computed brightness temperatures and observed ones. Column 5: Instrument noise as given by the CNES and Garnier et al 2012 [17]. Instrument biases are larger (expected to be < 0.5 K). For columns 3,4 and 6, values for MOMO are without brackets and values for op-IIR are in brackets.

Figure 1: Modular structure of MOMO
Green boxes: in green: modules (preprocessors), in black after the arrows: outputs of the preprocessor. Dotted blue boxes: databases used for the inputs.

Figure 2: Spectroscopy methods
2a) CVLW (Voigt Center Lorentz Wings) method used by CGASA for the case where MT-CKD 2.4. has null values. Red hyperbole: Voigt profile of an absorption line (within a band of width $\Delta\tilde{\nu} = 10$ cm^{-1} centered on the center of the line). Blue hyperbole: Lorentz profile used for the wings of the line. There is a cutoff at ± 25 cm^{-1} from the center of the line: for wavenumbers further from the center of the line than the cutoff limits, we force to 0 the value of the line profile of absorption.

2a) Method used by CGASA for the case where MT-CKD 2.4. has non-null values. Hyperbole: Voigt profile of an absorption line. Rectangle:

the basement delimited in the area centered on the center of the line and with a width of 64 times the FWHM (Full Width at Half Maximum) of the line profile.

Figure 3: Agreement LBLRTM/CGASA for water vapor spectroscopy within MODIS 31 channel.
3a) Water vapor transmission within MODIS 31 channel. In red: Spectral response function of MODIS 31. In blue: water vapor transmission computed by CGASA, in orange (dashed): water vapor transmission computed by LBLRTM. RMSE = Root Mean Square Error of transmission(CGSA)-transmission(LBLRTM).
3b) Water vapor absorption OD (optical depth) within MODIS 31 channel. In blue: water vapor OD computed by CGASA, in orange (dashed): water vapor OD computed by LBLRTM. RMSE = Root Mean Square Error of OD(CGSA)-OD(LBLRTM) in percent (RMSE*100).
3c) Zoom on a 80 nm wide band for the water vapor spectrum. In blue: water vapor OD computed by CGASA, in orange (dashed): water vapor OD computed by LBLRTM.

Figure 4: The interaction principle.
Reproduction of Figure 1 of Fell and Fischer 2001, [1]: "Diffuse light emerging, e.g. from the upper boundary at τ_0 consists of reflected downward light, transmitted upward light and upward light produced inside the layer $[\tau_{0,}\tau_1]$: $L_0^- = \mathcal{R}_{01}L_0'^+ + \mathcal{T}_{10}L_1'^- + \mathcal{J}_{10}^-$"

Figure 5: description of the vertical profile of atmosphere used for the comparison of MOMO to analytical solution (Subsec. 4.1.).
Y-axis: Left: altitude in km, right: optical thickness.
X-axis: Top: Blackbody radiance (blue curve), bottom: Temperature (red curve)

Figure 6: Transmission spectrum with MODIS response instrument response functions. From bottom to top: All gases, water vapor, CO_2, ozone, N_2O, methane. In red: MODIS channels response functions.

Figure 7: Results of the comparison of MOMO to RTTOV, for 6 MODIS channels.
Red curve: Top of atmosphere spectral radiance computed by RTTOV, blue curve: Top of atmosphere spectral radiance computed by MOMO. Purple curve: Spectral radiance difference (also in mW $m^{-2}sr^{-1}$cm): MOMO-RTTOV.

Figure 8: Transmission spectrum in MOMO-IIR bands

Figure 9: Results of the comparison MOMO to CALIPSO-IIR observations.
9a) Top of atmosphere brightness temperature (BT_{TOA}) observed by CALIPSO-IIR (green), computed with MOMO (blue), computed by SPIRS operational code (BT_{calc}(op-IIR) in red) for CALIPSO channel 1, 2 and 3 (from top to bottom).
9b) Difference BT_{TOA} computed – BT_{TOA} observed (in blue, BTTOA computed is the one computed by MOMO, in red BT_{TOA} computed is the one computed by SPIRS operational code), for CALIPSO channel 1, 2 and 3 (from top to bottom). RMSE (Root Mean Square Error) and mean_bias (medium bias) are displayed.

Figure 10: Scatter plots of brightness temperature computed vs brightness temperature observed, influence of the integrated water vapor (IWV) dependence.
x-y distributions. y: BT_{TOA}(computed) , Brightness Temperature computed. x: BT_{TOA}(observed) Brightness Temperature observed. From top to bottom: channel 1, channel 2 and channel 3. Left: BT_{TOA}(computed) is computed with SPIRS operational algorithm *op-IIR*. Right: BT_{TOA}(computed) is computed with MOMO. Colors represent the value of the IWV (Integrated Water Vapor) Column. Green line: bisector (y=x line). Red line (hidden under the bisector): Linear regression ($y = a \times x$, where a is the slope computed by the linear regression). The value of the slope is displayed on the graphs. Purple line: line parallel to the linear regression shifted from the bias (its value is also displayed on the graph) between computed and observed values ($y = x + bias$).

Table 1

Acronym	*Full description*
ACP	**A**tmospheric **C**onstituent **P**rofiles
AEROCOM	**Aero**sol **Com**munity
AFGL	**A**ir **F**orce **G**eophysics **L**aboratory
CALIPSO	**C**loud-**A**erosol **L**idar and **I**nfrared **P**athfinder **S**atellite **O**bservations
CGASA	**C**oefficients of **Gas A**bsorption
CKD	**C**lough, **K**neizys and **D**avies
CNES	**C**entre **N**ational d'**E**tudes **S**patiales (French Space Agency)
CNRS	**C**entre **N**ational de **R**echerche **S**cientifique
DISORT	**Dis**crete **Or**dina**t**e method
EOS	**E**arth **O**bserving **S**ystem
ESFT	**E**xponential **S**um **F**itting of **T**ransmission
FASAA	**Fas**t Calculation with **A**pproximation **A**bsorption
FASDOM	**Fas**t Calculation with **D**iscrete **O**rdinate **M**ethod
FASRAD	**Fas**t Calculation **Rad**iative Transfer Code
FUB	**F**reie **U**niversitaet **B**erlin
FWHM	**F**ull **W**idth at **H**alf **M**aximum
GMAO	Global Modeling and Assimilation Office
GSFC	(NASA) Goddard Space Flight Center
HITRAN	**Hi**gh Resolution **Tran**smission
IASI	**I**nfrared **A**tmospheric **S**ounding **I**nterferometer
ICARE	Cloud Aerosol Water Radiation Interactions
ICRCCM	**I**nter-**C**omparison of **R**adiation **C**odes used in **C**limate **M**odels: long wave results
IIR	**I**maging **I**nfrared **R**adiometer
IPMMI	**I**nternational **P**hotolysis Frequency **M**easurement and **M**odel **I**ntercomparison
IPSL	Institut Pierre Simon Laplace
ISS	**I**nstitut für **S**pace **S**ciences
ISSWG	**I**ASI **S**ounder **S**cience **W**orking **G**roup
IWV	**I**ntegrated **W**ater **V**apor
KISS	**k**-distribution of Institute for Space Sciences
LATMOS	**L**aboratoire **A**tmosphere **M**ilieux et **O**bservations **S**patiales
LBLDOM	**L**ine-**b**y-**L**ine **D**iscrete **O**rdinate **M**ethod
LBLRTM	**L**ine-**b**y-**L**ine **R**adiative **T**ransfer **M**odel
MODIS	**Mod**erate **R**esolution **I**maging **S**pectrometer
MODTRAN	**Mod**erate Resolution Atmospheric **Tran**smission
MOMO	**M**atrix-**O**perator **Mo**del
MT-CKD	**M**lawer, **T**obin, **C**lough, **K**neizys, and **D**avies
NASA	**N**ational **A**eronautics and **S**pace **A**dministration
OPAC	**O**ptical **P**roperties of **A**erosol and **C**louds
RMSE	**R**oot **M**ean **S**quare **E**rror
RRTM	**R**apid **R**adiative **T**ransfer **M**odel
RTE	**R**adiative **T**ransfer **E**quation
RTTOV	**R**adiative **T**ransfer for **TOV**S
SPECTRE	**Spect**ral **R**adiance **E**xperiment
SPIRS	**S**econd **L**evel **P**rocessing for **IR S**ignals
SST	**S**ea-**S**urface **T**emperature
TIROS	**T**elevision **I**nfra**r**ed **O**bservation **S**atellite
TOVS	**TIROS O**perational **V**ertical **S**ounder
UPMC	**U**niversité **P**ierre et **M**arie **C**urie
XTRA	**Ex**tended Line-by-Line Atmospheric **T**ransmittance and **R**adiance **A**lgorithm
ZOA	**Z**enithal **O**bservation **A**ngle
VCLW	**V**oigt **C**enter **L**orentz **L**ines

Table 2

Code	Ref	Method	Absorption method	Application
RTTOV	*[7, 8] Saunders et al, 1999a;b*	Predictors	LBL[2] external code (eg GENL2, LBLRTM), channel reg coeff	Remote sensing (fast code)
Streamer	*[11] Key and Schweiger, 1998*	2 Streams, DISORT[1]	LBL computation then ESFT	Radiation budget (fast code)
MODTRAN	*[20] Berk et al, 1989*	2 Streams, DISORT	Statistical band model, k-distribution	Radiation budget, remote sensing
RRTM	*[13] Mlawer et al, 1997*	DISORT	LBL own code LBLRTM, k-distribution method	Radiation budget (GCM[4])
FASDOM	*[16] Dubuisson et al, 2005*	DISORT	LBL ext code XXX, k-distribution	Remote sensing (fast code)
MOMO	*[1] Fell and Fischer, 2001*	matrix operator	LBL own code CGASA, k-distribution	Remote sensing, Radiation budget (precise code)

[1] Discrete Ordinates method, [2] Line-by-line, [3] Exponential Sum Fitting of Transmission, [62], [4]Global Climate Model.

Table 3

Symbol	***Description and unit***
L	Spectral Radiance, [W.m^{-2}μm^{-1}sr^{-1}] or [mW.m^{-2}cm.sr^{-1}]
T	Temperature. [K]
$\mathfrak{B}$	Spectral blackbody radiance, [W.m^{-2}μm^{-1}sr^{-1}] or [mW.m^{-2}cm.sr^{-1}]
$bias$	$bias(A,B) = \overline{A-B}$
$RMSE$	Root Mean Square Error: $RMSE(A,B) = \sqrt{\overline{(A-B)^2}}$, [unit of A and B]
τ	Optical depth, [1]
λ	Wavelength, [m] (commonly [nm] or [μm])
θ	Observation angle, [°]
μ	Inv(airmass): $\mu = \cos\theta$, [1]
$\mathcal{R}$	Reflection operator (matrix)
$\mathcal{T}$	Transmission operator (matrix)
$\mathcal{J}$	Source operator (vector), [W.m^{-2}μm^{-1}sr^{-1}] or [mW.m^{-2}cm.sr^{-1}]
ω_o	Single-scattering albedo, [1]
$\tilde{\nu}$	Wavenumber: $\tilde{\nu} = 1/\lambda$, [m^{-1}] (commonly [cm^{-1}])

Table 4

a)

θ_k	$L_k(\tau_1)$, Analytic	$L_k(\tau_1)$, MOMO	[%], diff
0°	7.761	7.756	0.064
12.8°	7.739	7.734	0.065
30°	7.630	7.626	0.052
59°	7.070	7.066	0.057
75°	6.038	6.035	0.050

b)

θ_k	$L_k(\tau_1)$, Analytic	$L_k(\tau_1)$, MOMO	[%], diff
0°	7.761	7.751	0.129
12.8°	7.739	7.729	0.131
30°	7.630	7.620	0.138
59°	7.070	7.058	0.171
75°	6.038	6.023	0.248

Table 5

Channel	[K], B_T(MOMO)	[K], B_T(RTTOV)	[K], ΔB_T
MODIS 29	289.595	289.729	- 0.134
MODIS 30	267.997	267.001	0.996
MODIS 31	292.335	292.272	0.063
MODIS 32	290.943	291.363	-0.420
MODIS 33	269.710	269.484	0.226
MODIS 35	248.01	247.056	0.954

Table 6

Channel	N_{bin}	RMSE MOMO (op. IIR)	Bias MOMO (op. IIR)	Instrument noise
1	244	0.57 K (0.96 K)	0.44 K (0.87 K)	0.09 K
2	130	0.43 K (0.46 K)	0.12 K (0.07 K)	0.14 K
3	97	0.61 K (0.69 K)	0.30 K (-0.33K)	0.11 K

Figure 1:

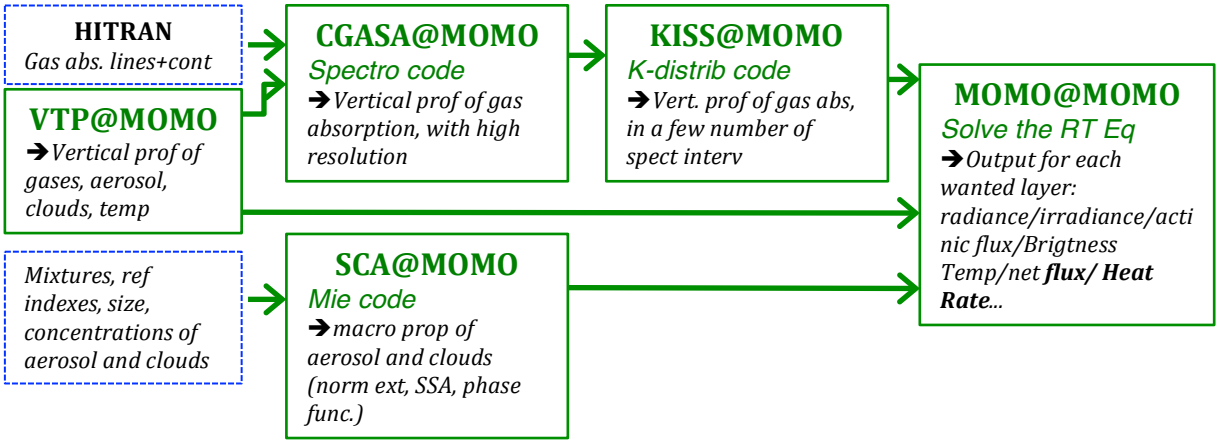
HITRAN
Gas abs. lines+cont
VTP@MOMO
➔Vertical prof of gases, aerosol, clouds, temp
Mixtures, ref indexes, size, concentrations of aerosol and clouds
CGASA@MOMO
Spectro code
➔Vertical prof of gas absorption, with high resolution
SCA@MOMO
Mie code
➔macro prop of aerosol and clouds (norm ext, SSA, phase func.)
KISS@MOMO
K-distrib code
➔Vert. prof of gas abs, in a few number of spect interv
MOMO@MOMO
Solve the RT Eq
➔Output for each wanted layer: radiance/irradiance/actinic flux/Brigtness Temp/net flux/ Heat Rate...

Figure 2:

a)

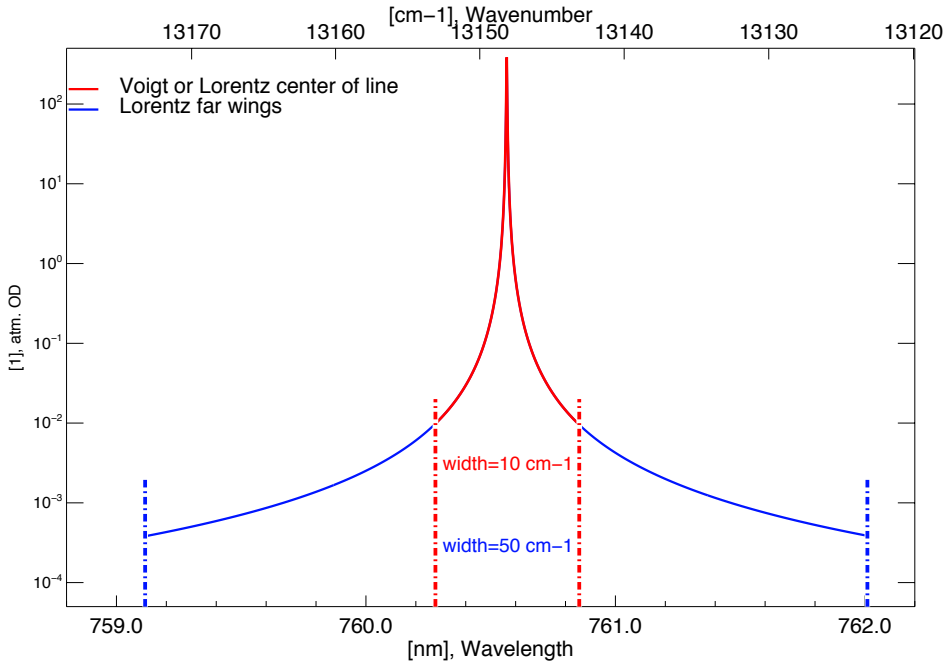
[cm−1], Wavenumber
13170
13160
13150
13140
13130
13120
Voigt or Lorentz center of line
Lorentz far wings
[1], atm. OD
width=10 cm−1
width=50 cm−1
759.0
760.0
761.0
762.0
[nm], Wavelength

b)

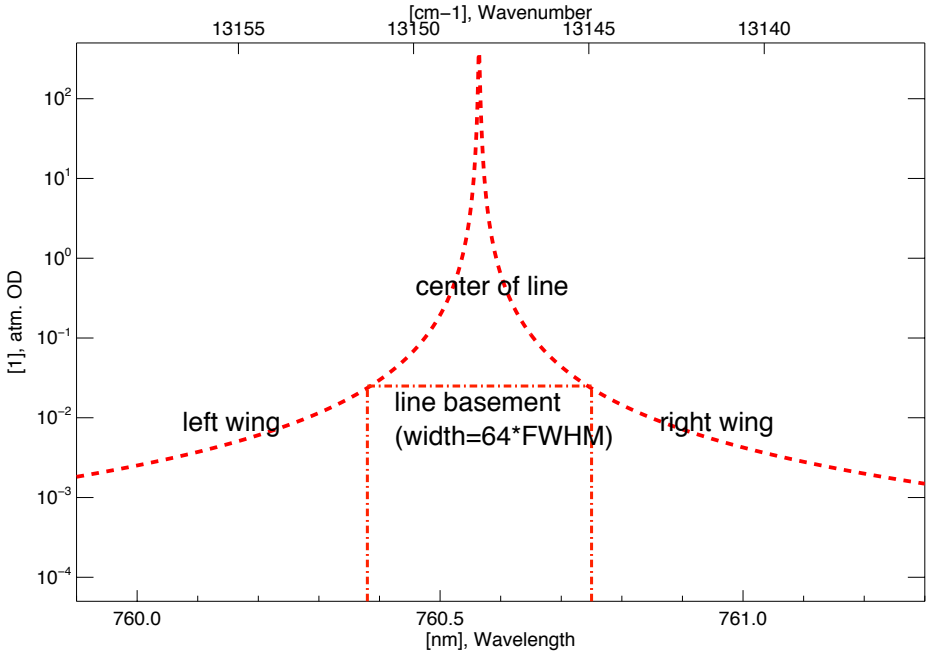
[cm−1], Wavenumber
13155
13150
13145
13140
[1], atm. OD
center of line
left wing
line basement
(width=64*FWHM)
right wing
760.0
760.5
761.0
[nm], Wavelength

Figure 3:

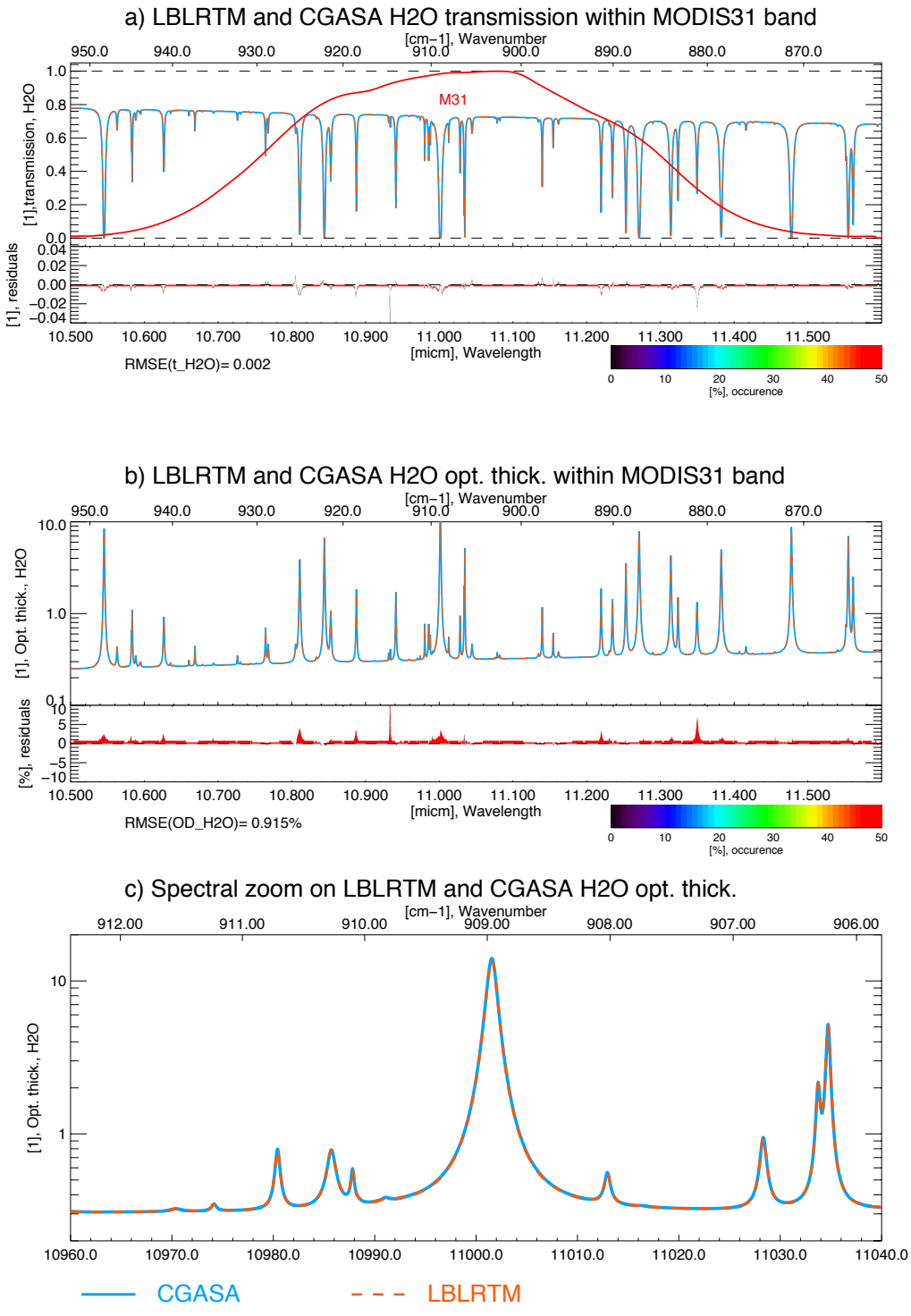
a) LBLRTM and CGASA H2O transmission within MODIS31 band
[cm−1], Wavenumber
950.0 940.0 930.0 920.0 910.0 900.0 890.0 880.0 870.0
[1],transmission, H2O
M31
[1], residuals
10.500 10.600 10.700 10.800 10.900 11.000 11.100 11.200 11.300 11.400 11.500
[micm], Wavelength
RMSE(t_H2O)= 0.002
0 10 20 30 40 50
[%], occurence
b) LBLRTM and CGASA H2O opt. thick. within MODIS31 band
[cm−1], Wavenumber
950.0 940.0 930.0 920.0 910.0 900.0 890.0 880.0 870.0
[1], Opt. thick., H2O
[%], residuals
10.500 10.600 10.700 10.800 10.900 11.000 11.100 11.200 11.300 11.400 11.500
[micm], Wavelength
RMSE(OD_H2O)= 0.915%
0 10 20 30 40 50
[%], occurence
c) Spectral zoom on LBLRTM and CGASA H2O opt. thick.
[cm−1], Wavenumber
912.00 911.00 910.00 909.00 908.00 907.00 906.00
[1], Opt. thick., H2O
10960.0 10970.0 10980.0 10990.0 11000.0 11010.0 11020.0 11030.0 11040.0
CGASA
LBLRTM

Figure 4:

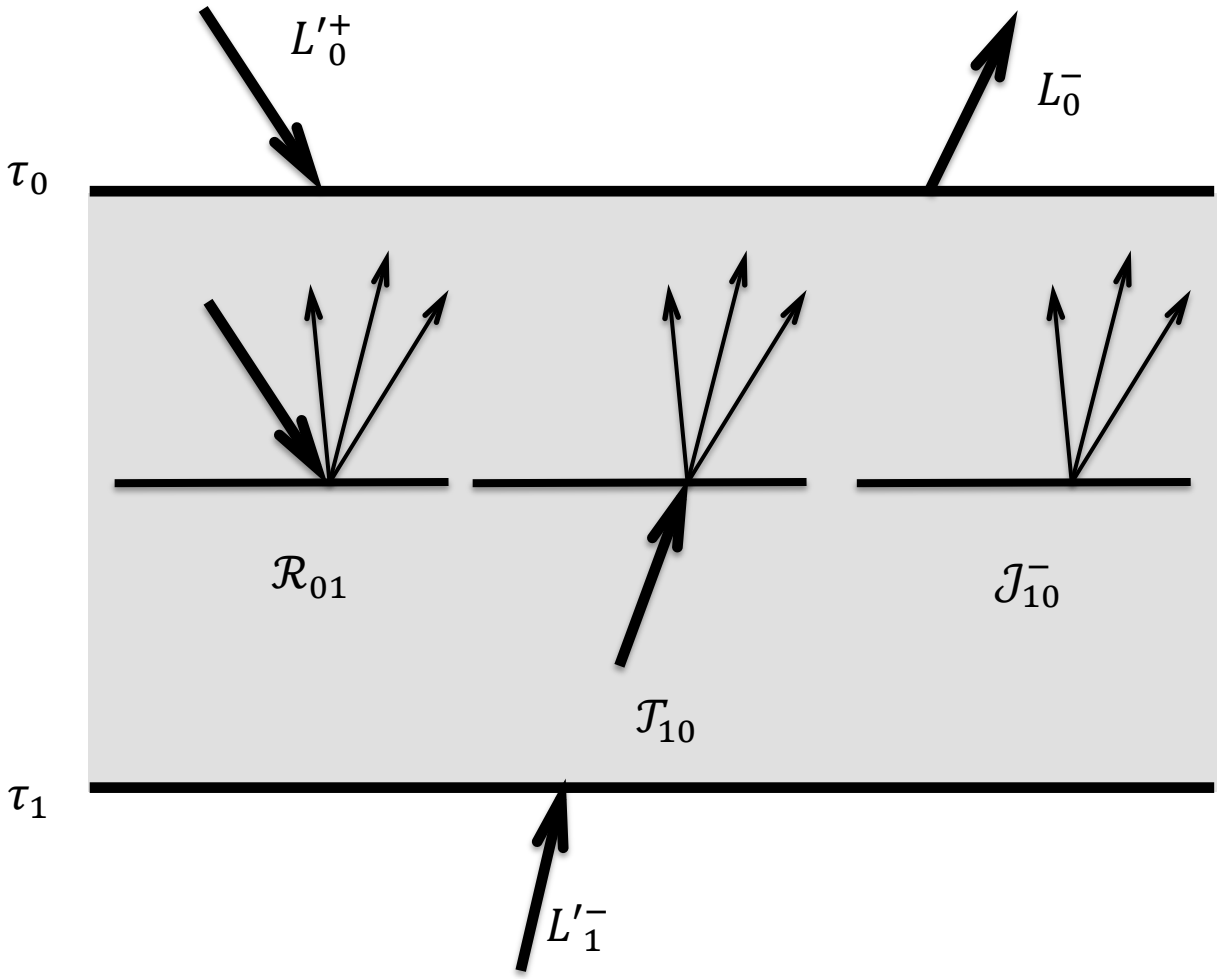

Figure 5:

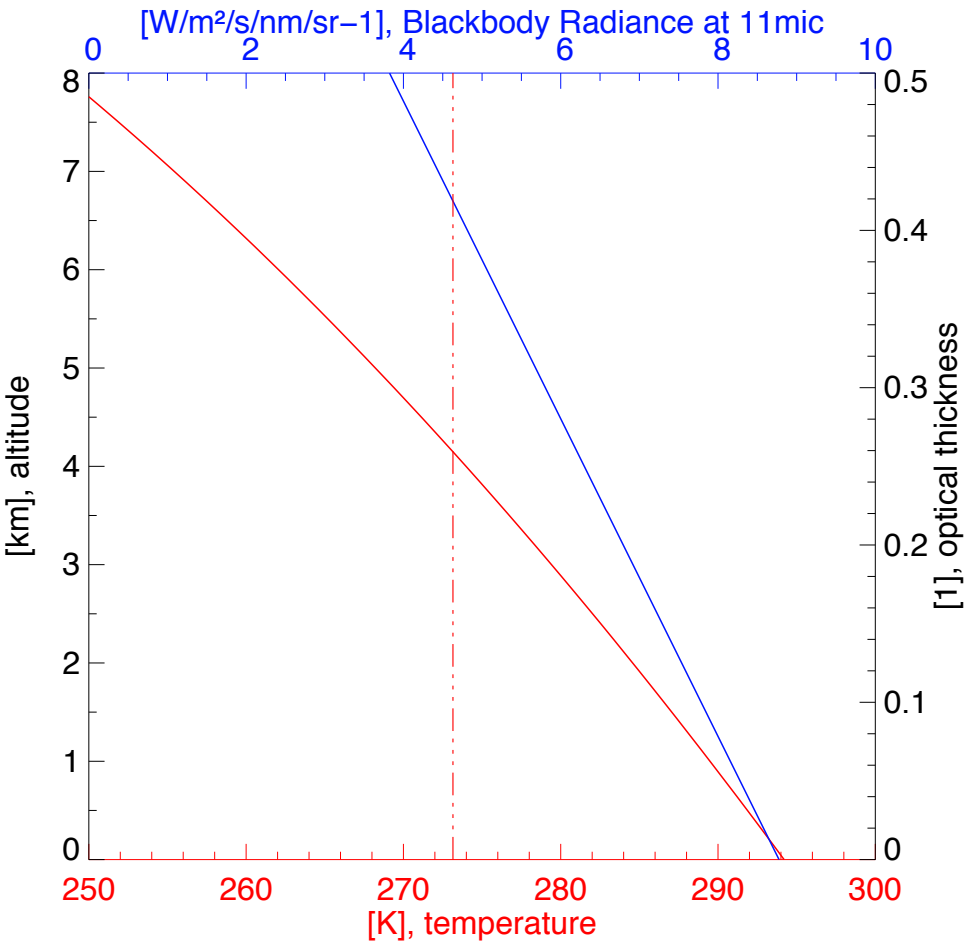
[W/m²/s/nm/sr−1], Blackbody Radiance at 11mic
0
2
4
6
8
10
8
7
6
5
4
3
2
1
0
[km], altitude
0.5
0.4
0.3
0.2
0.1
0
[1], optical thickness
250
260
270
280
290
300
[K], temperature

Figure 6:

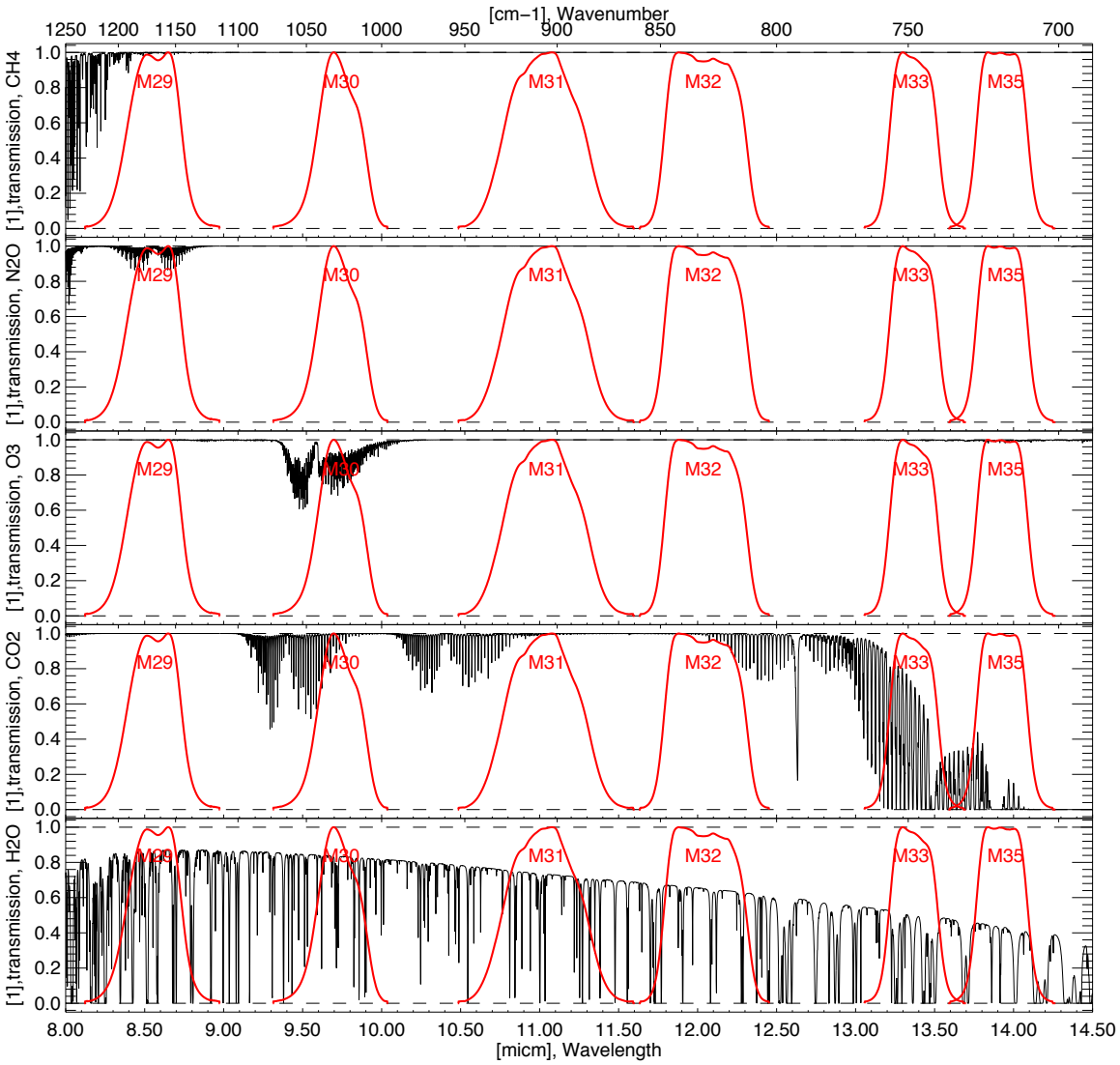
[cm−1], Wavenumber
1250 1200 1150 1100 1050 1000 950 900 850 800 750 700
[1],transmission, CH4
[1],transmission, N2O
[1],transmission, O3
[1],transmission, CO2
[1],transmission, H2O
M29
M30
M31
M32
M33
M35
8.00 8.50 9.00 9.50 10.00 10.50 11.00 11.50 12.00 12.50 13.00 13.50 14.00 14.50
[micm], Wavelength

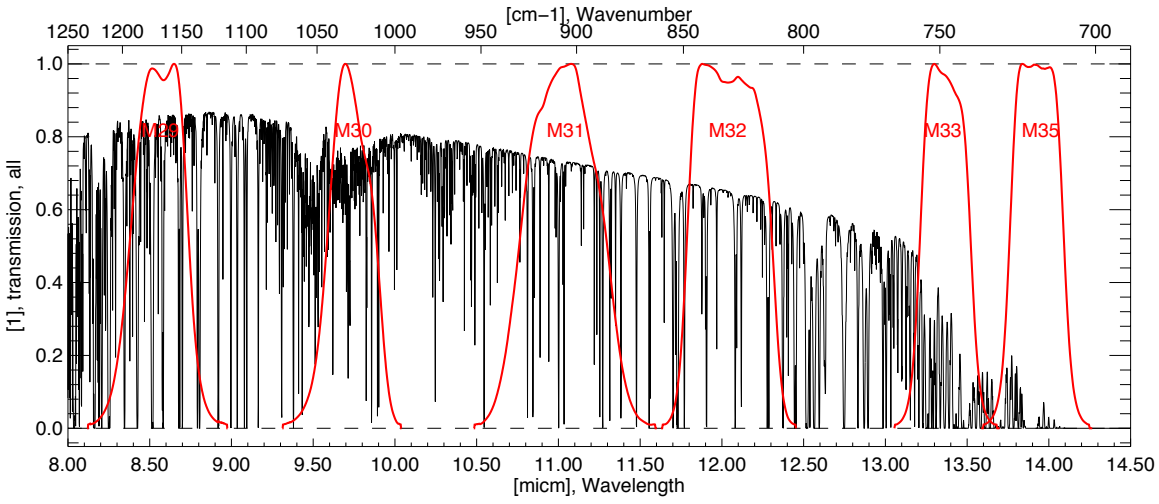
[cm−1], Wavenumber
1250 1200 1150 1100 1050 1000 950 900 850 800 750 700
[1], transmission, all
M29
M30
M31
M32
M33
M35
8.00 8.50 9.00 9.50 10.00 10.50 11.00 11.50 12.00 12.50 13.00 13.50 14.00 14.50
[micm], Wavelength

Figure 7:

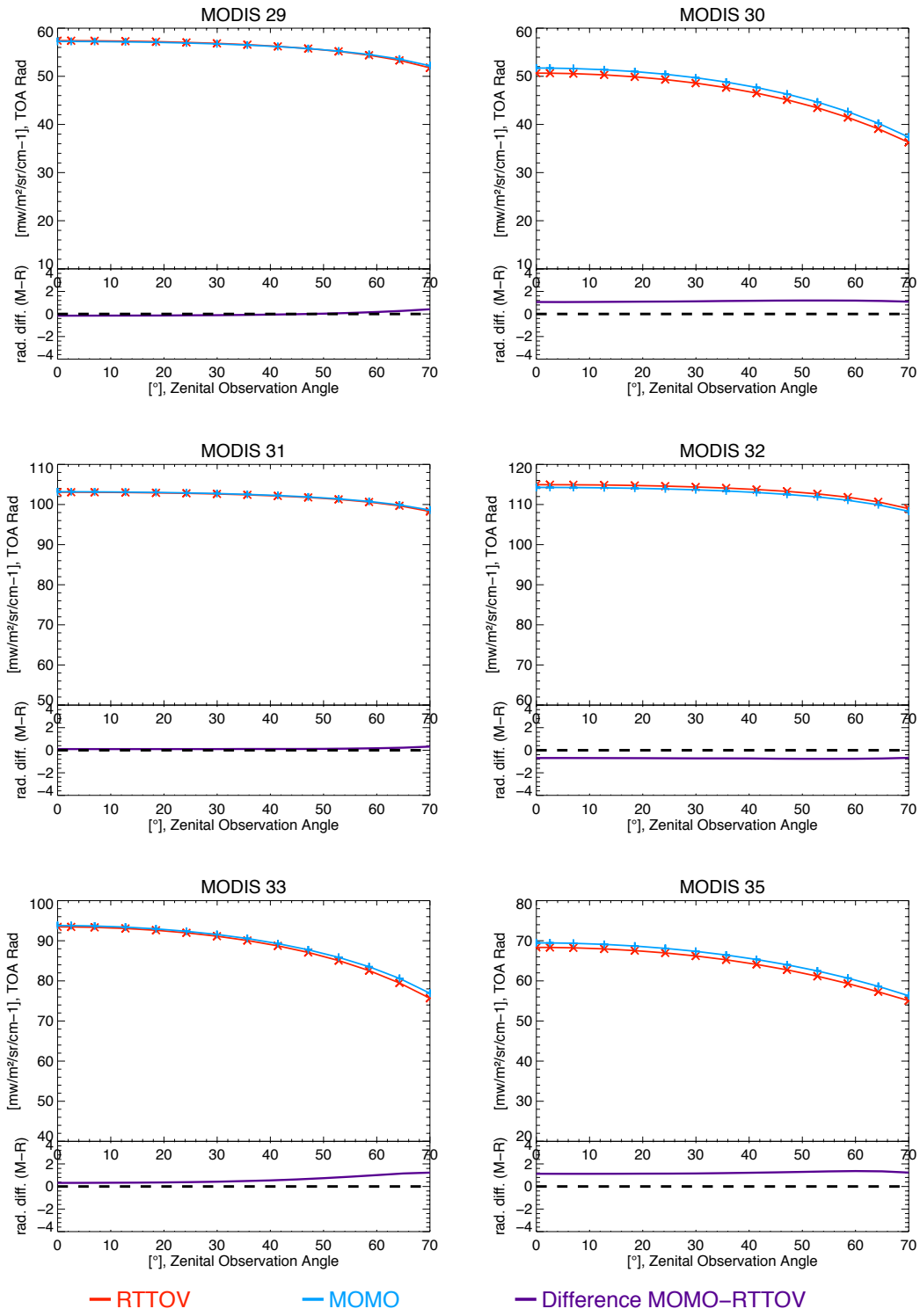
MODIS 29
MODIS 30
MODIS 31
MODIS 32
MODIS 33
MODIS 35
[mw/m²/sr/cm−1], TOA Rad
rad. diff. (M−R)
[°], Zenital Observation Angle
RTTOV
MOMO
Difference MOMO−RTTOV

Figure 8:

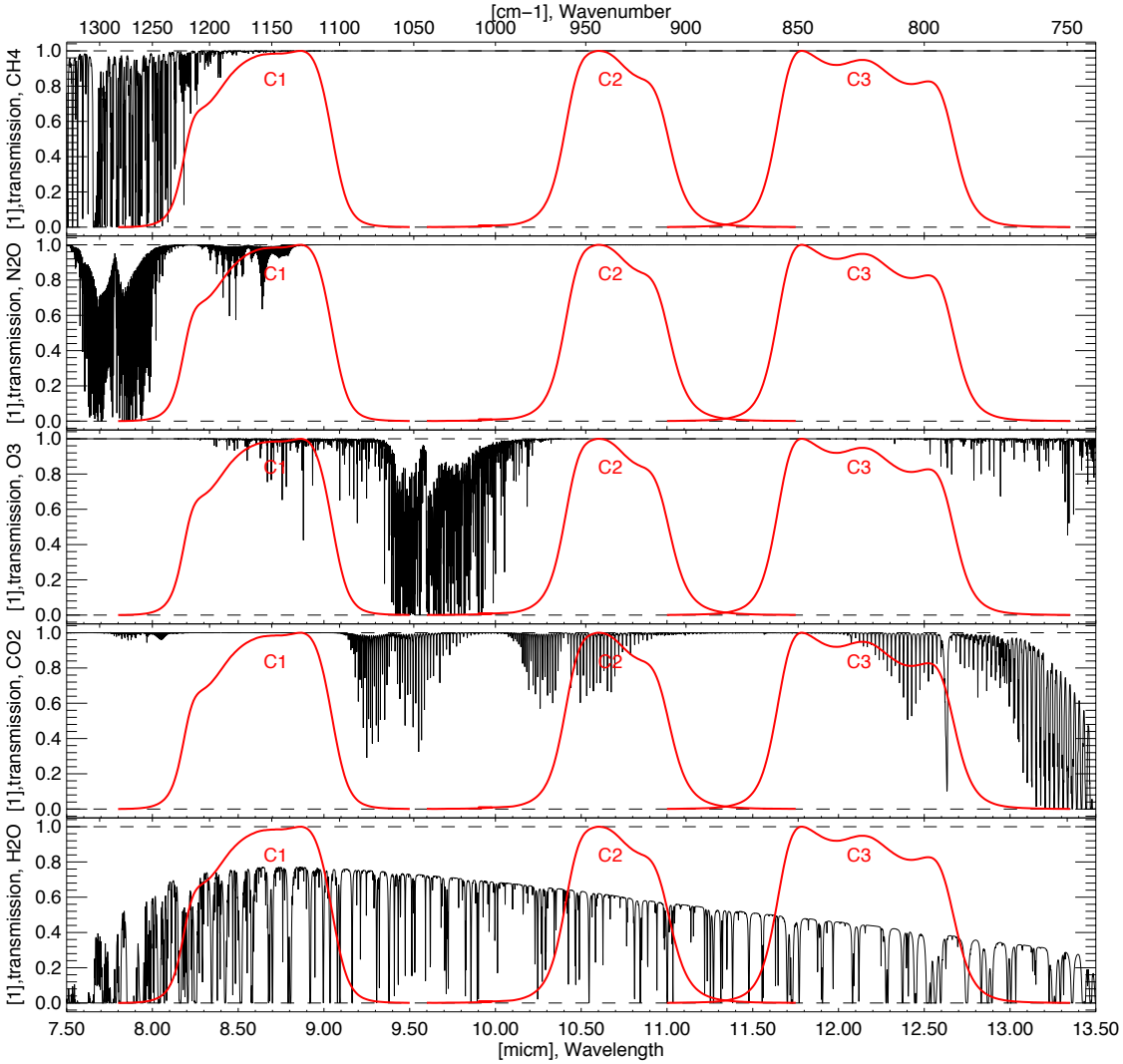
[cm−1], Wavenumber
1300 1250 1200 1150 1100 1050 1000 950 900 850 800 750
[1],transmission, CH4
[1],transmission, N2O
[1],transmission, O3
[1],transmission, CO2
[1],transmission, H2O
C1
C2
C3
7.50 8.00 8.50 9.00 9.50 10.00 10.50 11.00 11.50 12.00 12.50 13.00 13.50
[micm], Wavelength

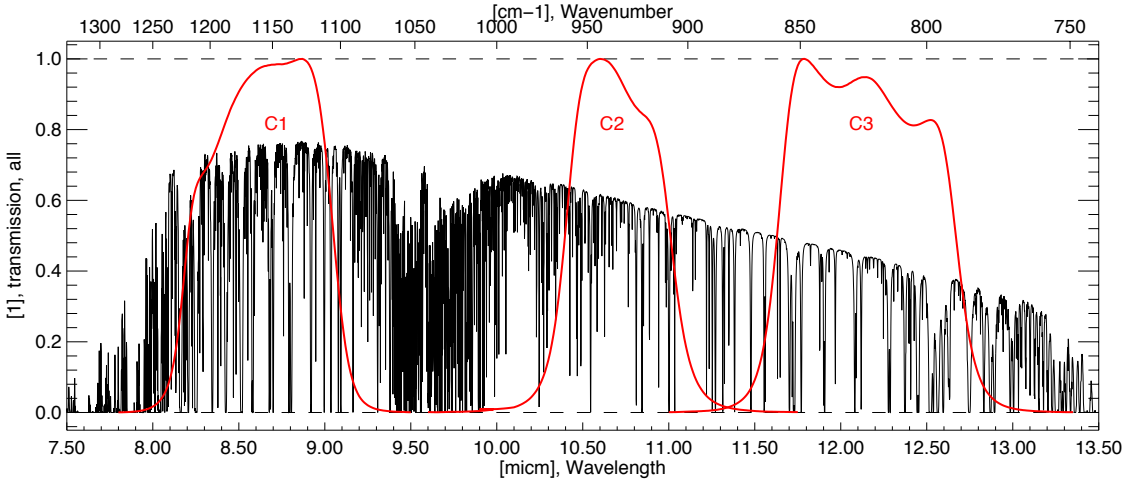
[cm−1], Wavenumber
1300 1250 1200 1150 1100 1050 1000 950 900 850 800 750
[1], transmission, all
C1
C2
C3
7.50 8.00 8.50 9.00 9.50 10.00 10.50 11.00 11.50 12.00 12.50 13.00 13.50
[micm], Wavelength

Figure 9:

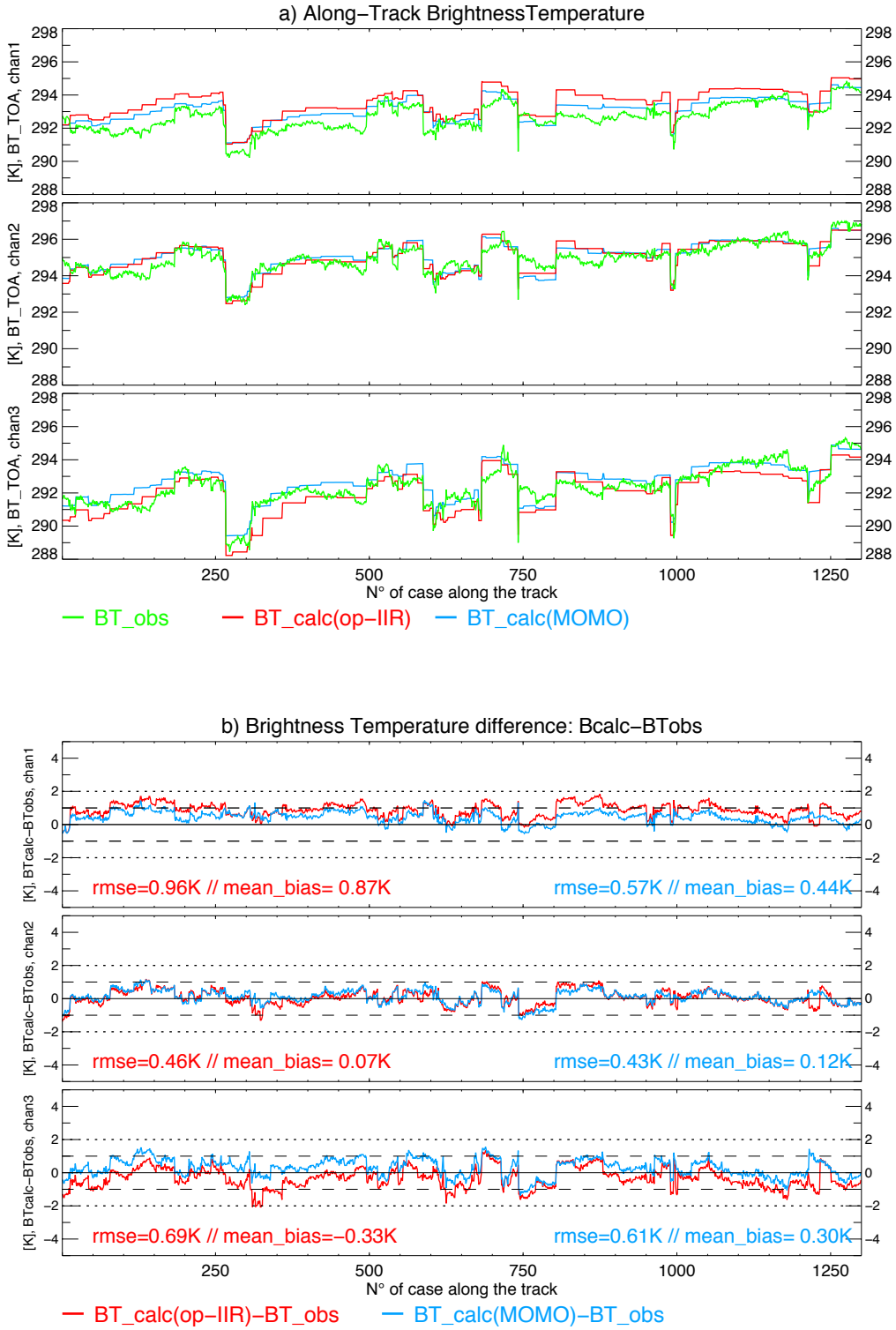
a) Along−Track BrightnessTemperature
[K], BT_TOA, chan1
[K], BT_TOA, chan2
[K], BT_TOA, chan3
N° of case along the track
BT_obs
BT_calc(op−IIR)
BT_calc(MOMO)
b) Brightness Temperature difference: Bcalc−BTobs
[K], BTcalc−BTobs, chan1
[K], BTcalc−BTobs, chan2
[K], BTcalc−BTobs, chan3
rmse=0.96K // mean_bias= 0.87K
rmse=0.57K // mean_bias= 0.44K
rmse=0.46K // mean_bias= 0.07K
rmse=0.43K // mean_bias= 0.12K
rmse=0.69K // mean_bias=−0.33K
rmse=0.61K // mean_bias= 0.30K
N° of case along the track
BT_calc(op−IIR)−BT_obs
BT_calc(MOMO)−BT_obs

Figure 10:

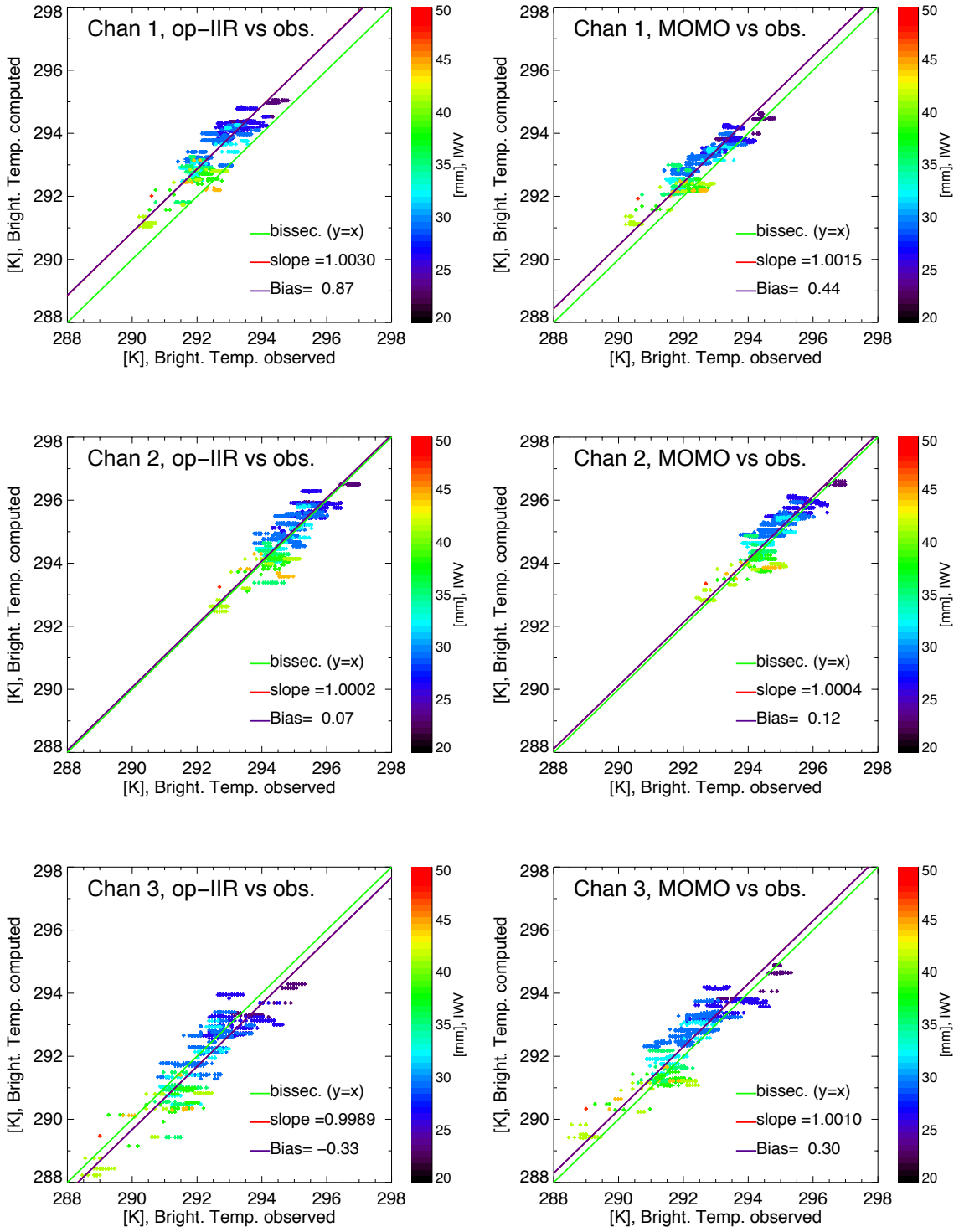
Chan 1, op–IIR vs obs.
bissec. (y=x)
slope =1.0030
Bias= 0.87
Chan 1, MOMO vs obs.
bissec. (y=x)
slope =1.0015
Bias= 0.44
Chan 2, op–IIR vs obs.
bissec. (y=x)
slope =1.0002
Bias= 0.07
Chan 2, MOMO vs obs.
bissec. (y=x)
slope =1.0004
Bias= 0.12
Chan 3, op–IIR vs obs.
bissec. (y=x)
slope =0.9989
Bias= −0.33
Chan 3, MOMO vs obs.
bissec. (y=x)
slope =1.0010
Bias= 0.30
[K], Bright. Temp. computed
[K], Bright. Temp. observed
[mm], IWV
288
290
292
294
296
298
20
25
30
35
40
45
50

Summary and outlook.

The radiative transfer code MOMO has been extended to the thermal infrared and a complete validation process has been done. As shown in the article *Doppler et al.* 2013b, the validation of the code for clear air cases is conclusive. An outlook will be to realize some validations for simulations of radiative transfer in atmospheres with clouds and aerosols. Also, we could deal with the simulation of the channels of IIR in depth: A code-comparison experiment with MOMO, FASDOM (Fast Radiative Transfer with Discrete Ordinate Method: *Dubuisson et al.* 2005; 2008), RTTOV, and the operative algorithm of the instrument IIR is in project. This experiment will consist of simulating the radiative transfer for the three IIR channels in media with low dense clouds, semi transparent clouds and aerosols. Inter-channels brightness temperature differences should also be compared.

The article also presented developments of radiative transfer tools for spectroscopy (see Section 3.1 of the article with the description of CGASA), and for gas transmission for large spectral bands (k-distribution algorithm KISS: Section 3.3 of the article). The motivation of these developments, the technical details and the validations of these tools are discussed in the two next chapters.

6. Spectroscopy module CGASA

Introduction and scientific objectives.

The spectroscopy is a key element of radiative transfer simulations. Fine spectroscopy simulations are required for the quantification of greenhouse gases' effects: Large band models are not relevant for the estimation of the atmosphere warming with the increase of gas amounts (e.g. CO_2 and global warming). Also, remote sensing inversion algorithms need precise spectroscopy simulations (see Lindstrot et al. 2012, with my personal contribution in Subsection 4.3 of the article). Spectroscopy studies are also necessary for instrument developers who need a good knowledge of the transmission spectrum of the atmosphere in order to determine the spectral position of the response function of their instruments (e.g. laser beam of a lidar, spectral band of a radiometer).

The spectroscopy of water vapor is an important source of mistakes in global radiation budget estimations. Improvements in the description of lines and continua leaded to an increase of 3 to 6 $\mathrm{W\,m^{-2}}$ in the estimation of the total atmospheric absorption (*Kim and Ramanathan* 2008). The water vapor continuum of absorption is a critical parameter. In the thermal infrared, the self-continuum contributes to the major part of the water vapor absorption (see Figure 6.1). Also the foreign-continuum has a non negligible contribution: the foreign continuum leads to an enhancement of 25 % of the cooling rate in the upper troposphere compared to cases where the spectral lines alone are computed (*Shine et al.* 2012, *Clough et al.* 1992). For a radiative transfer code like MOMO, that expects to be a precise code, it was necessary to develop a spectroscopy module that can compute all kinds of gas absorption coefficients properly. This module is named CGASA (Coefficient of Gas Absorption: *Doppler et al.* 2013b).

The objectives of this chapter are:

- To present the spectroscopy module CGASA (Coefficient of Gas Absorption) of the radiative transfer code MOMO.

- To discuss the method used for the simulation of water vapor lines and continua.

- To present some applications of the spectroscopy code CGASA: Full range spectrum computations for atmospheric transmission and for vertical profile of spectral heating and cooling rates.

6.1. Coefficient of Gas Extinction: CGASA.

CGASA, Coefficients of Gas Absorption (*Doppler et al.* 2013b) is the spectroscopy module of MOMO. CGASA is presented in Subsection 3.1 of the article *Doppler et al.* 2013b displayed in Chapter 5 of this thesis.

The development of CGASA was an important issue of this PhD. It was a part of the developments necessary to the extension of MOMO to the thermal infrared. CGASA is an adaptation of thermal infrared spectroscopy scheme XTRA (Extinction and Transmission: *Rathke and Fischer* 2000). The main improvement of CGASA is the parameterization of water vapor spectroscopy: The continua of absorption are parameterized with the MT-CKD 2.4 coefficients (*Clough and al.* 2005; 1992; 1989; *Mlawer et al.* 2012; see description in Chapter 3 of this thesis). The line profiles are described with the same method as LBLRTM (Line By Line Radiative Transfer Model, *Clough et al.* 1992; 2005), for the spectral location for which the values of MT-CKD continuum coefficients are not null. As explained in Section 3.1 of the article *Doppler et al.* (2013b) presented in Chapter 5, LBLRTM method leads to underestimation of the value of the gas absorption, for part of the spectrum where the MT-CKD continuum coefficients are null. For these parts of the spectrum, the choice make in CGASA is to estimate the line profiles with the VCLW (Voigt Center Lorentz Wings) method presented in Chapter 3, Figure 3.1 of this thesis.

6.2. Applications of CGASA.

6.2.1. Full range spectrum of gases' transmission.

This subsection presents the full-range (0.2 – 100 μm) spectrum of transmission for the 8 most important gases in atmospheric radiative transfer, namely H_2O (water vapor), CO_2 (carbon dioxide), O_3 (ozone), N_2O (nitrous oxyde), CO (carbon monoxide), CH_4 (methane), and O_2 (dioxygen). The spectral range has been split in two parts: [0.2 – 20 μm] represented in Figure 6.1, and [1 – 100 μm] represented in Figure 6.2. This study allows a qualitative control of the results of the spectroscopy module, and provides us a map of the spectrum of the atmospheric gas transmission. It is interesting to have look on this spectral map and to recognize which constituent play a role in which spectral band. For example, ozone has an important influence between 200 and 700 nm because of its continuum of absorption. At 765 nm, we recognize the famous O_2-A band of dioxygen, used for cloud top height

retrievals (*Preusker and Lindstrot* 2009, *Lindstrot et al.* 20010; 2009; 2006). From 0.8 to 8 μm, the transmission spectrum is controlled by water vapor lines (and to a lesser extend, by the water vapor foreign continuum of absorption). We recognize the thermal infrared self-continuum of water vapor between 8 and 12 μm. Between 9.5 and 10 μm, the ozone plays again a major role, by absorbing the radiation in the upper part of the atmosphere (see next subsection). Between 13 and 17 μm, there is the so famous (because of the debate on climate change) large CO_2 absorption of radiation, responsible of the greenhouse effect increased by CO_2 anthropogenic emissions. The atmospheric transmission spectrum in the far infrared is something more boring because the water vapor absorption puts the whole atmospheric transmission to 0. Nevertheless, in the far infrared, spectral variations happen for the gas absorption in the upper part of the atmosphere, this can be seen on the spectrum of vertical profile of heating and cooling rates presented in the next subsection.

6.2.2. Full range spectrum of Spectral heating rates.

The here-presented study is in the thematic of radiation budget estimations. With a spectroscopy module like CGASA and a radiative transfer code like MOMO, it is possible to compute the vertical profile of heating or cooling rates for small spectral bands, all along the [0.2 – 70 μm] spectrum. Figure 6.3 represents the spectrum of vertical profile of radiative heating rates for the shortwave part (the source of radiation is the sun; the solar zenith angle is taken at 30°; the Earth's surface is supposed having an albedo of 0 for all the wavelengths, thus the whole radiation that reaches the ground is absorbed by the surface). Figure 6.4 represents the spectrum of vertical profile of cooling rates (cooling rate = - heating rate) for the thermal and far infrared spectrum. The sources of radiation are the atmospheric molecules. The ground is supposed to have an emissivity of 0, in order to focus only on the vertical profile of absorption and emission by atmospheric molecules. The figures 6.3 and 6.4 have to be compared to the transmission spectrum of each gas presented in figures 6.1 and 6.2. This study is similar to the one done by *Clough et al.* 1992 for the development of spectroscopy and line-by-line code LBLRTM. This comparison allows to understand the spectral variation of heating or cooling rates at the different altitudes and to understand which gas is responsible of the heating or cooling rates variations.

In Figure 6.3, we recognize the ozone absorption in the stratosphere between

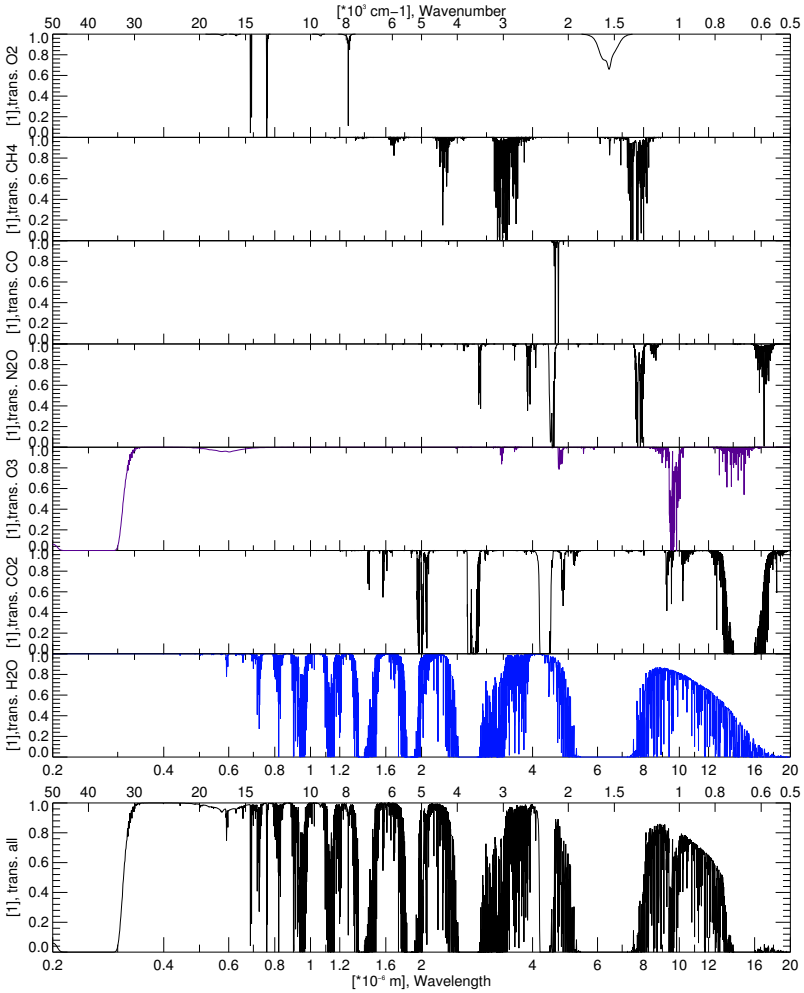

Figure 6.1.: [0.2 – 20 μm] Transmission spectrum of a mid-latitude summer standard atmosphere (picture under). The isolated transmissions of the different gases are also shown in the upper figures: From bottom to top: water vapor (H_2O), carbon dioxide (CO_2), ozone (O_3), nitrous oxide (N_2O), carbon monoxide (CO), methane (CH_4), and dioxygen (O_2). These spectra have been computed with CGASA, using HITRAN 2008 and MT-CKD 2.4 continua's coefficients.

200 and 350 nm and then again between 450 and 700 nm. For the rest of the spectrum, the water vapor seems to have the main influence on the radiation budget in shortwave. We recognize water vapor influence not only by recognizing the main water vapor bands of absorption (by comparison to Figure 6.1), but also, because the vertical distribution of water vapor in the atmosphere is localized at lower altitudes than the vertical distribution of other gases. At 1.5, 1.9 and 2.7 μm, the maximum of heating rates (thus the absorption) are positioned in the middle troposphere. These local maximum of heating rates can be attributed to CO_2 and CH_4. We also observe that the larger is the wavelength, the smaller is the heating rate in the right half part of Figure 6.3. The reason of this phenomenon is that the power of the solar source is vanishing from the thermal infrared (before 1 μm) to the longwave boundary (4 μm).

Figure 6.4 shows the spectrum of the vertical profile of cooling rates from 4 μm to 70 μm. The highest values of cooling rates on this picture are in the spectral band [7 - 14 μm], because in this spectral band, the Planck's function that controls the blackbody radiation is the highest for atmospheric temperatures. We recognize the large water vapor cooling rates at low altitudes in the [8 – 13 μm] band. The ozone has a large influence on stratospheric cooling rates around 9.5 μm and again around 15 μm. At these wavelenghs, just below the stratospheric ozone, there are the only regions of positive heating rates of Figure 6.4: The gases in the high troposphere absorb the radiation emitted by the stratospheric ozone more than they self emit radiation. Between 14 and 20 μm, the maximum of the spectral cooling rates is in the middle troposphere; this proves that the cooling rate of this spectral region is due more to N_2O and CO_2 than to H_2O. Spectral cooling rates in the very far infrared (near 60 μm) do not have large values because for wavelengths larger than 15 μm, the source (Planck function) is vanishing when the wavelength increases.

Summary and outlook.

The spectroscopy module CGASA is not only a necessary tool for MOMO, it offers also interesting analysis (full range transmission spectrum, full range spectrum of vertical heating and cooling rates). CGASA has been validated within the article *Doppler et al.* (2013b) (Section 3.1 of the article) displayed in Chapter 5 (Section 5.2). The validation is done for the water vapor transmission and optical depth within the continuum band. The validation has been done by comparison to LBLRTM, the spectroscopy code that is the reference for the spectral regions of

water vapor continuum.

Outlook for CGASA development are: a validation of the VCLW method for other bands than the [8 – 12 μm] and for other gases than H_2O. This validation can be done by comparison to measurements by spaceborne spectrometers (e.g. SCHIAMACHY on board of former ESA satellite ENVISAT, or IASI on board of EUMETSAT satellite MetOp). For some wavelengths and some gases, the Voigt profile (and thus the VCLW method) should not be appropriated. This is for example the case for O_2 spectroscopy near the O_2-A band. Other parameterizations exist (considering line mixing and collision-induced absorption: *Tran and Hartmann* 2008) and should be implemented in CGASA.

Regarding the applications of CGASA, there are plenty of possibilities: It is for instance possible to compute the spectrum of vertical additional heating rates due to the increase of the amount of one constituent (for instance of + 20 % of CO_2). Such studies could help to understand and quantify the greenhouse effect and the anthropogenic climate change.

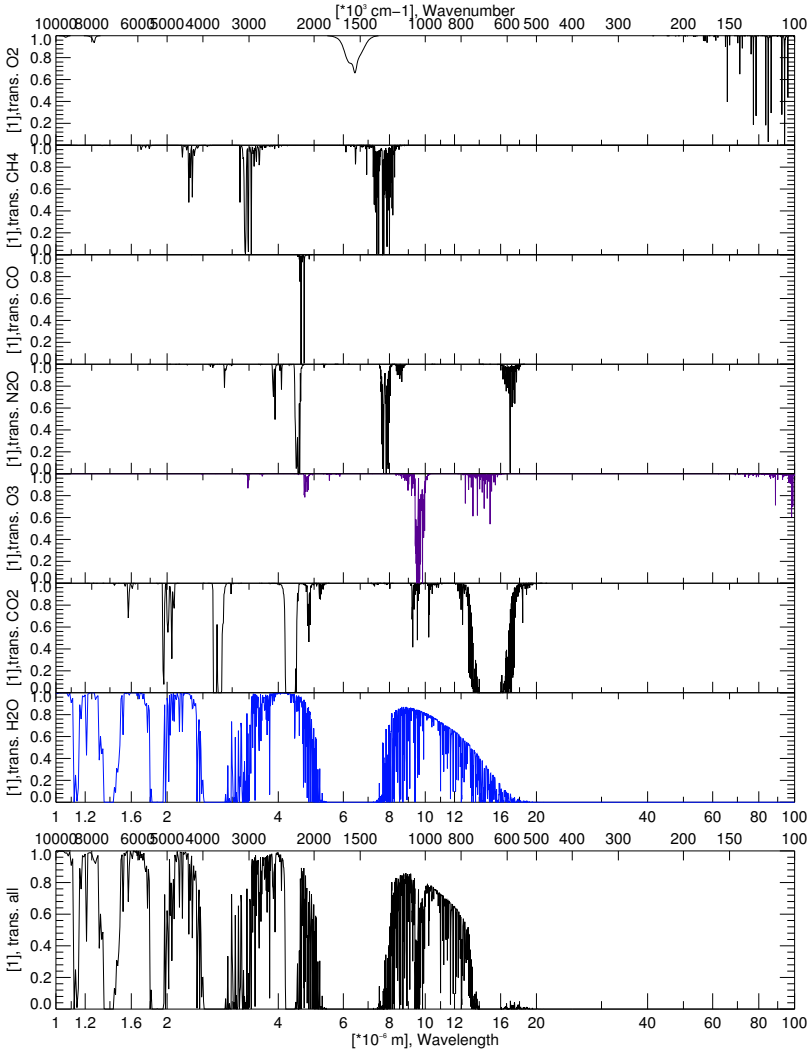

Figure 6.2.: [1 – 100 μm] transmission spectrum of a mid-latitude summer standard atmosphere. Computed with CGASA with the same spectral databases as the one used for Figure 6.1.

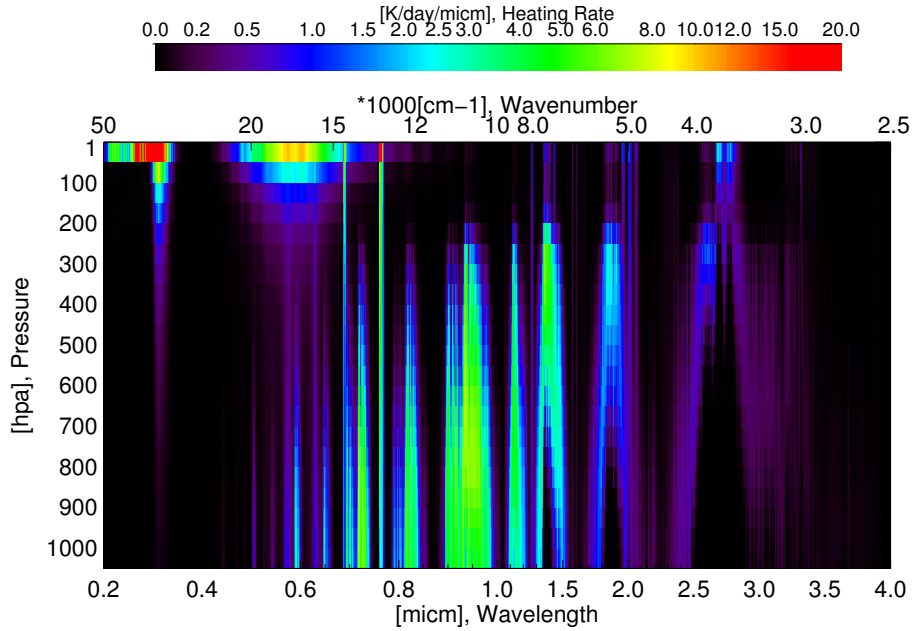

Figure 6.3.: [0.2 – 4 μm] spectrum of vertical profile of radiative heating rates in clear air atmosphere for a mid-latitude summer standard atmospheric profile. Computed with CGASA and MOMO.

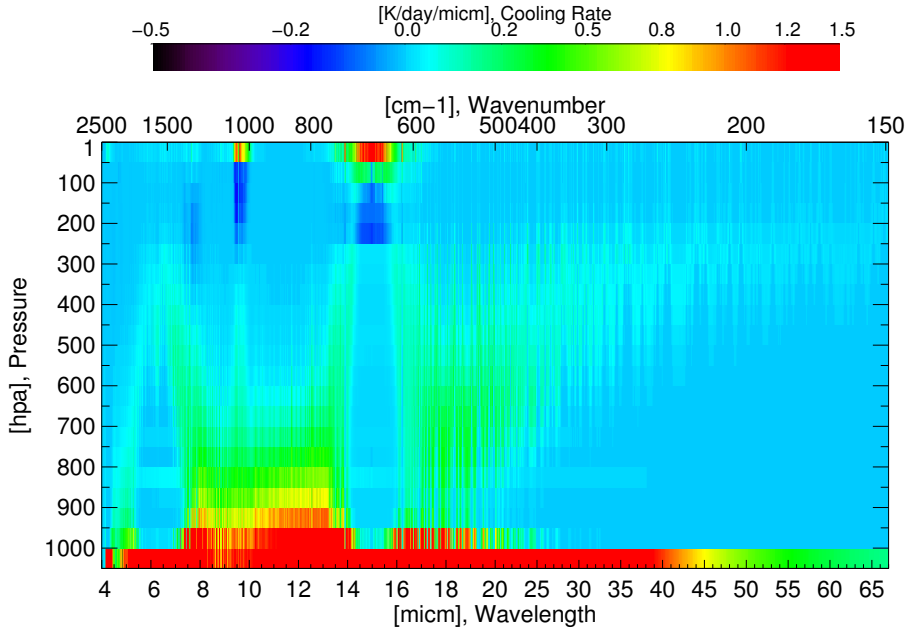

Figure 6.4.: [4 – 70 μm] spectrum of vertical profile of radiative cooling rate in clear sky for a mid-latitude summer standard atmospheric profile. Computed with CGASA and MOMO.

7. Combining high resolution and large band computations: k-distribution module KISS

Introduction and scientific objectives.

As explained in Chapter 3 (Section 3.3.2) of this thesis, k-distribution methods are necessary for the simulation of radiative transfer for spectral bands. The k-distribution allows to reduce the computation time and to preserve the precision of an accurate high-resolution spectroscopy parameterization. At the Institute for Space Sciences (ISS) of FU-Berlin, with MOMO's k-distribution module KISS (k-distribution of Institute for Space Sciences), we use a k-distribution method that is different from the classic one: The k-distribution method of KISS is a *non-correlated k-distribution method* (*Bennartz and Fischer* 2000, *West et al.* 1989). This method has the particularity to avoid the *correlation approximation* (an approximation that assumes the spectra of different layers of the atmosphere being correlated). The limitations of k-distribution methods using the correlation approximation have been described by *Doppler et al.* (2013a), *West et al.* (2010), and *Bennartz and Fischer* (2000). The main problem is that the error due to the correlation approximation cannot be controlled. Therefore, within correlated k-distribution methods (k-distribution methods using the correlation approximation) it is not possible to have a balance between rapidity and precision by increasing the number of bins (see definitions in Chapter 3, Section 3). This balance is possible with non-correlated k-distribution methods. A challenge of the extension of radiative transfer code MOMO to the thermal infrared was to succeed in extending the non-correlated k-distribution method of KISS to the thermal infrared. The main difficulty was to implement the blackbody radiation in the k-distribution. This has been done with the so-called k-IR method presented in *Doppler et al.* (2013a).

This chapter presents the extension of MOMO's k-distribution module KISS (k-distribution of Institute for Space Sciences) to the thermal infrared. The main developments of the module KISS are discussed in the article *Doppler et al.* (2013a): *Doppler L, Preusker R, Bennartz R, and Fischer J. k-bin and k-IR: Improved non-correlated k-distribution methods for non-fixed instrument response function and extension to thermal infrared. Applications to satellite remote sensing. J of Quant Spect and Rad Transfer 2013; in revision.* Submitted in April 2013 to Journal of Quantum Spectroscopy and Radiative Transfer (JQSRT, Elsevier) and in revision in Mai 2013. This article is entirely displayed in Section 7.2 of this chapter.

The objectives of this chapter are:

- To recall the particularity of the k-distribution method used in KISS. This method is named non-correlated k-distribution and is described in Section 2 of the

article (referred to as BF00 method: *Bennartz and Fischer* 2000).

- To explain the theoretical details of the extension of the non-correlated k-distribution method to the thermal infrared, especially the implementation of the blackbody radiation for the emission of radiation by gases (k-IR method). This is the purpose of Subsection 3.1 and 3.2 of the article.

- To present the validation of the infrared extension of KISS. This validation, presented in Subsection 3.3 of the article, consists of simulations of CALIPSO-IIR (*Garnier et al.* 2012) Channel 3. The top-of-atmosphere brightness temperature is simulated with a reference line-by-line case, and the result is compared to simulations done with k-distribution method of KISS.

7.1. Personnal participation to Doppler et al. 2013a.

My participations to *Doppler et al.* (2013a) are: The development of the bin-averaged method used to implement the blackbody radiation in the k-distribution (k-IR method presented in Section 3 of the article). The validation test of k-IR compared to line-by-line simulations for CALIPSO-IIR channel 3 (Subsection 3.3 of the article) has been done by myself. The k-bin method, for non-fixed spectral response function (Section 4 of the article) has been found by co-authors Ralf Bennartz and René Preusker, who have also realized the application to OCO-2. Section 2 that recalls the principle of the non-correlated k-distribution method has been entirely written by myself. Section 3 about the k-IR method and the appendixes have also been written by myself. Rene Preusker (ISS, FU Berlin) and Ralf Bennartz (AOS University of Wisconsin) have written the Section 4. Introduction, and Conclusion (sections 1 and 5) have been written by all 4 co-authors. The gathering in one article of the contributions of each author has been managed by myself, with helpful reviews and advice of my co-authors.

7.2. JQSRT article: Doppler et al. 2013a (non-correlated k-distributin module KISS extended to the thermal infrared).

The integrality of the article submitted to Journal of Quantum Spectroscopy and Radiative Transfer (JQSRT, Elsevier) in April 2013 and accepted for revisions in Mai 2013, is displayed here after (19 pp.).

k-bin and k-IR: Improved non-correlated k-distribution methods for non-fixed instrument response function and extension to thermal infrared. Applications to satellite remote sensing.

Lionel Doppler[1,2], Rene Preusker[1], Ralf Bennartz[3], Juergen Fischer[1]

[1] Institute for Space Sciences - Free University of Berlin – Germany; [2] LATMOS, IPSL - Université Pierre et Marie Curie - Paris, France; [3] Atmospheric and Oceanic Sciences - University of Wisconsin –Madison, USA

Abstract

Non-correlated k-distribution methods are efficient tools for radiation transfer simulations of layered atmosphere with variable gas absorption. Non-correlated k-distribution methods optimize the k-distribution for all the atmospheric layers, instead of applying the correlation approximation. This difference of method, compared to correlated k-distribution methods leads to a loss of rapidity but to a gain of precision. Particularly, non-correlated k-distribution methods permit a balance between rapidity and precision by decreasing or increasing the number of bins (spectroscopically similar k-distribution intervals). Within this article, we recapitulate the main principles of non-correlated k-distribution methods and present two improvements: k-IR method, which is an adaptation of non-correlated k-distribution method to the thermal infrared, and k-bin that allows the user to simulate narrow-band satellite channels with a non-fixed spectral response function. k-IR permits a modeling of the absorption and emission by gases, even if the spectral variability of the Planck function is completely different from the spectral variability of absorption/emission coefficients. This is achieved by associating to each bin (spectroscopically similar k-distribution interval), a pre-computed value of the bin-averaged blackbody radiance. Within this paper we outline k-IR and apply it for the simulation of Channel 3 ($12.05\ \mu m$*) of the Imaging Infrared Radiometer (IIR) aboard the CALIPSO satellite. Results show that the accuracy steadily increases with an increasing number of bins. In doing so, we can reach the instrument precision. k-bin, otherwise, is a more stringent approach of the k-distribution. The major difference between a conventional k-distribution and k-bin is, that for a given spectral interval no assumption about the shape of the sensor weighting function has to be incorporated a-priori. For a given spectral interval, any sensor response function can be constructed from a set of radiative transfer simulations. This requires somewhat different constraints in the way the sub-division in bins is performed, namely we must ensure that not only the band-averaged transmission is resembled to high accuracy, but also the transmission in each bin. Within this paper we outline k-bin method and apply it to high-resolution spectroscopic simulations in the oxygen A-band. k-bin allows for a representation of any channel (with a resolution of* 0.04 *nm or lower) within the oxygen A-band with an accuracy of* 0.2 *% or better with less than 600 simulations. This corresponds for the Orbiting Carbon Observatory-2 (OCO-2) to a computational cost of 0.6 simulations per channel.*

1. Introduction

High spectral resolution or large band remote sensing observations require fast radiative transfer models that include gas absorption. For many applications, monochromatic simulations are not feasible because of time constraints. Common ways to significantly reduce the computational costs are to represent each satellite channel by a set of monochromatic simulations. These monochromatic simulations are afterwards weighted in order to account for the sensitivity of the channel. Typically, in the visible and near infrared, and dependent to the variability of gas absorption within the channel, between 3 and 20 monochromatic simulations suffice for an accurate simulation of a high- to mid-resolution channel of a given sensor.

Different methods exist to find the optimum number of monochromatic simulations needed to represent a given channel of a satellite instrument. Methods such as optimal spectral sampling (OSS, *Moncet et al.* [1]) provide similar capabilities as those cited above. An important limiting case is reached, if only one simulation is used for each channel. For this particular case, the band averaged effective transmission can be calculated analytically for each channel's spectral weighting function. This approach is taken for example in OPTRAN (*Kleespies et al.* [2]), RTTOV (*Saunders et al.* [3,4]) and other fast infrared models (*Sherlock et al.* [5]). It can be shown that for the case of a non-scattering atmosphere the analytical effective transmission perfectly fits the true band averaged transmission. For scattering atmospheres arbitrary photon paths do not allow the use of these approaches; we will prefer k-distribution methods. *Fu and Liou 1992* [6], *Lacis and Oinas 1991* [7] and *Goody et al. 1989* [8] derived the first correlated k-distribution (from here on referred to as *ckdist*) methods. A new approach of k-distribution is presented by *West et al, 1990* [9] with the

so-called Spectral Mapping Transformation (here after referred to as SMT) and later by *Bennartz and Fischer 2000* [10]. The method of *Bennartz and Fischer 2000*, is our reference and will be here after referred to as *BF00*. This here after referred to as *non-correlated k-distribution approach*, consists in applying the k-distribution method without doing the correlation approximation. We recapitulate the *non-correlated k-distribution* approach main principles in Section 2 and we explain why this method overcomes some of the weaknesses of the ckdist methods and we will show that the *non-correlated k-distribution* methods allow for more accurate simulations. Until this article, BF00 method was restricted to the shortwave band (UV, visible and near infrared) and to channels with fixed spectral response functions.

In the middle-infrared band, the most efficient methods for the simulation of atmospheric radiation are *ckdist* methods [6-8]. Even after nice improvements for satellite bands simulation (*Kratz* [11], *Dubuisson et al.* [12]) or for heating-rates computations (*Mlawer et al.* [13]), two problems remain: 1) The assimilation of blackbody radiation and its non-gray nature in the k-distribution. We provide in Subsection 3.2 a method named *k-IR* that overcomes this problem. 2) The relative accuracy of *ckdist* methods for the cases of atmospheres having a complex vertical gas distribution or in spectral bands and for atmospheres presenting overlapping spectra. We demonstrate in Subsection 3.3, that contrary to *ckdist* methods, we can, with *k-IR,* mitigate these problems by increasing the number of bins (i.e. increasing the computational cost). In Section 4, we present a validation of the *k-IR* method: we compare simulations done with the help of *k-IR* to line-by-line simulations for a middle-infrared wide-band sensor: Channel 3 of Imaging Infrared Radiometer (IIR, *Garnier et al.* [14]) of Cloud and Aerosol Lidar and Imager Pathfinder Satellite Observation (CALIPSO, *Winker et al.* [15]).

A general feature of all the above outlined approaches is that they simulate each channel individually. The computational cost of these approaches is therefore proportional to the number of channels times the average number of spectral intervals needed to represent those channels. Within Section 4 of this paper we take a fundamentally different approach in that we simulate entire absorption bands and reconstruct the radiances for each channel afterwards, from the simulations that represent the entire spectral band. This we call the *k-bin* method. As shown below, this approach significantly reduces the number of necessary simulations for a given sensor. For a sensor like the Orbiting Carbon Observatory-2 (OCO-2, [16,17]) with about 1000 channels within the oxygen A-band this approach reduces the computational costs to simulate all 1000 channels from about 10000 simulations to about 600, as shown in Subsection 4.3.

Section 2 of this article presents the non-correlated k-distribution methods and the general approach of BF00. *K-IR*, BF00's extension to the thermal infrared (with the assimilation of gas emission of radiation) is presented in Section 3; a validation of *k-IR* has been done along the simulation of a *CALIPSO-IIR* channel. Section 4 outlines the *k-bin* method, and its application of this method to the oxygen A-band. Conclusions are delivered in Section 5.

2. Non-correlated k-distribution methods, general BF00 approach.

2.1. Correlated and non-correlated k-distribution methods.

Most of the k-distribution methods are using the *correlation approximation* ([6,7,11-13]). The correlation approximation consists in assuming that the gas absorption spectra of the different layers of the atmosphere are correlated to the gas absorption spectrum of a *reference layer*. The correlation approximation allows very fast radiative transfer simulations: if the spectra of all the layers of the atmosphere are correlated, then the k-distribution that has been found and tested for a reference layer can be applied to all the layers of the atmosphere and therefore, there is not need to define a large number of *bins* (spectroscopically similar intervals of the k-distribution). The resolution of the radiative transfer equation will thus be fast.

The correlation approximation can be wrong for the cases of *overlapping band* (*Goody and Yung, 1989,* [18]): if within a spectral interval, the gas absorption spectrum of a layer *A* is completely different from the gas absorption spectrum of a layer *B* (for example for a spectral band near 10 µm if layer *A* is near the ground with a high amount of water vapor and layer *B* is in the stratosphere with a high amount of ozone). [18] warn about the use of (implicit: *correlated*-) k-distributions in this overlapping band context. For such cases, the most advanced *ckdist* methods use *overlapping coefficients* (e.g. [13]). This solution diminishes the problem, and improves the accuracy of *ckdist* methods. But that does not ensure that the k-distribution is appropriated for the modeling of all the atmospheric layers.

We referred to as *non-correlated k-distribution* methods, the k-distribution methods that do not make the correlated approximation. This approach is not very widespread. *West et al, 1990* [9] along the SMT method, were the first who introduce this concept. SMT is also known as SMART (Spectral Mapping Atmospheric Radiative Transfer Model [19, 20]). Ten years after, *Bennartz and Fischer* 2000, [10] presented BF00 that is a slightly different method.

Instead of doing the correlation approximation, non-correlated k-distribution methods test the validity of the k-distribution not only at a reference layer but also at each layer of the atmosphere. This precaution guaranties the accuracy of the k-distribution method also for overlap bands.

Another feature of non-correlated k-distribution methods is that they permit a balance between computation speed and accuracy: A k-distribution with a larger number of bins is more precise. This feature is not guaranteed by *ckdist* methods: *West et al. 2010,* [21] already pointed out that *ckdist* methods do no ensure that the correct value for a radiation parameter can be approached simply by increasing the number of bins. In Subsection 3.3, we show with the application of *k-IR* (thermal infrared extension of BF00) to Channel 3 of *CALIPSO-IIR* radiometer that the accuracy of BF00 increases with the number of bins.

Non-correlated k-distribution methods like SMT and BF00 can easily be adapted to simulations of the gas transmission for instrument channels with a non-fixed spectral response function. The adaptation of SMT to such instrument response function is obvious. BF00, which uses a different algorithm, needed a special extension for non-fixed spectral response function. We developed this extension and named it *k-bin.* We present *k-bin* in Section 3 of this article.

2.2. Different non-correlated k-distribution methods.

Non-correlated k-distribution methods are rather unusual in the radiative transfer community. BF00 and SMT are at our knowledge the only ones. BF00 and SMT have some similarities: they pay high attention to define a mapping that suits to all the atmospheric layers, instead of doing the correlated approximation. The credit for this idea is to be given to *West et al, 1990,* [9] who introduce it in the SMT method. Excluded this general principle, BF00 and SMT are different methods; the mapping for instance is not similarly done. We detailed in Appendix 1, the procedures used by BF00 and all the steps of BF00's k-distribution

algorithm. We highlight here some major differences between SMT and BF00:
- In BF00, the user controls the accuracy of the k-distribution with criteria (the thresholds) about not only the gas transmission of all the layers but also about the whole atmosphere gas transmission.
- In BF00, the parameter that is mapped is not the gas absorption spectral coefficient $k(\nu)$ of a layer *l* but a coefficient $k^*(\nu)$ that considers both the gas absorption of the layer *l* and the gas absorption of the whole atmosphere (see description of *procedure a* in Appendix 1)
- The basis of non-correlated k-distribution method is that one unique mapping is defined for all the layers. The way to define this mapping is completely different between SMT and BF00: BF00 find a different mapping (what we here refer to as 'mapping' is the bins' distribution named *index* in the algorithm description in Appendix 1) for each different layer. After it, a special procedure (*procedure b* in Appendix 1) derives a common index from all the different layers' indexes. SMT on the other hand, keep the same index from the starting layer to the last layer mapped and improve step by step this index for each time that a new layer is mapped ([9]).
- SMT controls that the departure of the $k(\nu)$ coefficients to the bin absorption coefficient k_i within each bin *i,* is always below a predefined limit Δk. So a test is done for each spectral subinterval ν. On the other hand, BF00 increases the number of bins until the k-distribution satisfies some *threshold tests*. These thresholds tests are done for the whole band transmissions and not for each wavenumber subinterval individually. So BF00 criterion may be less stringent then SMT. Theoretically, BF00's *k*-distribution should have fewer bins than SMT's *k*-distribution.

2.3. Mathematical description of the general method of BF00.

Before we discuss the two improvements *k-IR* and *k-bin*, we recapitulate briefly the mathematical description of BF00. The details about parameters notations and equations can be found in *Bennartz and Fischer 2000*, [10].

The basic idea behind all k-distribution methods is that the band-averaged transmission in a spectral interval with variable gas absorption within a homogeneous layer can be approximated by:

$$T(L) = 1/(\nu_1 - \nu_0)\int_{\nu_0}^{\nu_1} R(\nu)\cdot \exp(-k(\nu)\cdot L)\,d\nu \approx \sum_{i=1}^{N} w_i \cdot \exp(-k_i \cdot L) = \check{T}(L) \quad (1)$$

Where ν is the wavenumber, L is the path length through the absorbing medium, $T(L)$ is the transmission, $R(\nu)$ is the sensor's response function and $k(\nu)$ is the spectrally variable absorption coefficient. $\check{T}(L)$ is the transmission resconstructed with the k-distribution. This k-distribution defines *N* bins, and affects to each bin *i* a weight w_i and an absorption coefficient $k_{i,l}$ (there is one absorption coefficient per bin *i* and per atmospheric layer *l*).

k-distribution and other approaches, such as OSS [1], use different methods to minimize the total transmission's error $\Delta T(L)$ (defined in Equation (2)) by finding an optimal combination of $\{N, k_{i=1,\dots N}, w_{i=1,\dots N}\}$ for each channel.

$$\Delta T(L) = \check{T}(L) - T(L) \quad (2)$$

Each term (k_i, w_i) of the combination is named *bin*. Each bin represents a certain non-continuous subinterval within the spectral range covered by $R(\nu)$, in which the optical properties are similar. For example, if the satellite channel to 60 % covers an absorption-free spectral interval, then there would be a k-distribution term with $\{k_i = 0.0, w_i = 0.6\}$. The actual spectral location of the absorption-free areas can be neglected. It could be a continuous wavenumber interval, or it could be several absorption-free areas spaced between various absorption lines. Note, that strictly speaking other spectrally variable boundary conditions, such as the solar constant or surface albedo, have to be part of the integral in Equation (1). In a sake of simplicity, these are neglected in this paper. For the complete description of the treatment of these parameters, refer to [10].

3. BF00 method extended to thermal infrared: *k-IR.*

3.1. General k-distribution approach in thermal infrared: the k-IR method.

We developed *k-IR* method in order to introduce the emission of radiation by gases in the non-correlated k-distribution method BF00. This permits the use of BF00 for thermal infrared spectral bands simulations. We keep the notations of [10] recalled in Subsection 2.3. The spectral response function is fixed. Thus, the error $\Delta T(L)$ in the transmission $T(L)$ due to the k-distribution $\{N, k_{i=1,\dots N}, w_{i=1,\dots N}\}$ can be computed for the whole band and is defined in Equation (2).

In the thermal infrared, in addition to the gas absorption, the emission of radiation has to be taken into account. The spectral radiance $\mathfrak{L}(L)$ along the path L for the band $[\nu_0, \nu_1]$ is governed by Schwarzschild's Equation:

$$\mathfrak{L}(L) = \frac{1}{\nu_1 - \nu_0 \int_{\nu_0}^{\nu_1} R(\nu)\cdot \mathfrak{L}_\nu(0)} \cdot t(\nu, L)\,d\nu + 1/(\nu_1 - \nu_0)\int_{\nu_0}^{\nu_1} R(\nu)\cdot B(\nu,\theta)\cdot \varepsilon(\nu, L)\,d\nu \quad (3)$$

Where, $B(\nu,\theta)$ is the blackbody radiance at temperature θ. $t(\nu, L)$ and $\varepsilon(\nu, L)$ are the transmission and the emissivity at wavenumber ν along pathlength L:

$$t(\nu, L) = \exp(-k(\nu)\cdot L); \qquad \varepsilon(\nu, L) = 1 - \exp(-k(\nu)\cdot L) \quad (4)$$

The definition of band transmission $T(L)$ is the one of Equation (1) (Subsection 2.2). The band emissivity $E(L)$ is defined in the same way as $T(L)$ in Equation (5):

$$\begin{cases} T(L) = 1/(\nu_1 - \nu_0)\int_{\nu_0}^{\nu_1} R(\nu)\cdot t(\nu, L)\,d\nu = 1/(\nu_1 - \nu_0)\int_{\nu_0}^{\nu_1} R(\nu)\cdot \exp(-k(\nu)\cdot L)\,d\nu \\ E(L) = 1/(\nu_1 - \nu_0)\int_{\nu_0}^{\nu_1} R(\nu)\cdot \varepsilon(\nu, L)\,d\nu = 1/(\nu_1 - \nu_0)\int_{\nu_0}^{\nu_1} R(\nu)\cdot (1 - \exp(-k(\nu)\cdot L))\,d\nu \end{cases} \quad (5)$$

The challenge for k-distributions applied in the thermal infrared is to produce a k-distribution which can accurately model $T(L)$, $E(L)$ and, simultaneously, the blackbody radiation $B(\nu,\theta)$. The solution used for the introduction of $B(\nu,\theta)$ in the k-distribution is detailed in Subsection 3.2. $\check{T}(L)$ is the approximation of $T(L)$ (see Equation (1)) using the k-distribution. We also define $\check{E}(L)$, the k-distribution approximation of $E(L)$:

$$\begin{cases} \check{T}(L) = \sum_{i=1}^{N} w_i \cdot \check{T}_i(L) = \sum_{i=1}^{N} w_i \cdot \exp(-k_i \cdot L) \\ \check{E}(L) = \sum_{i=1}^{N} w_i \cdot \check{E}_i(L) = \sum_{i=1}^{N} w_i \cdot (1 - \exp(-k_i \cdot L)) \end{cases} \quad (6)$$

Where $\check{T}_i(L)$ and $\check{E}_i(L)$ are the approximate transmission and emissivity of a bin *i* of the k-distribution.

We define also $\Delta T(L,\nu)_i$ and $\Delta E(L,\nu)_i$, the errors in transmission and emission within each spectral subinterval ν:

$$\begin{cases} \Delta T(L,\nu)_i = \check{T}_i(L) - R(\nu)\cdot t(\nu, L) \\ \Delta E(L,\nu)_i = \check{E}_i(L) - R(\nu)\cdot \varepsilon(\nu, L) \end{cases} \quad (7)$$

$\overline{\Delta T}_i(L)$ and $\overline{\Delta E}_i(L)$ are the errors in transmission and in emission averaged over the bin *i*:

$$\begin{cases} \overline{\Delta\tilde{T}}_i(L) = \tilde{T}_i(L) - 1/w_i \cdot \int_{\Delta_{\gamma:i}} R(\nu) \cdot t(\nu, L) d\nu = 1/w_i \cdot \int_{\Delta_{\gamma:i}} \Delta T(L,\nu)_i \, d\nu \\ \overline{\Delta E}_i(L) = \tilde{E}_i(L) - 1/w_i \cdot \int_{\Delta_{\gamma:i}} R(\nu) \cdot \varepsilon(\nu, L) d\nu = 1/w_i \cdot \int_{\Delta_{\gamma:i}} \Delta E(L,\nu)_i d\nu \end{cases} \quad (8)$$

The errors in the total band emission and transmission are the *whole band errors* $\Delta T(L)$ and $\Delta E(L)$:

$$\begin{cases} \Delta T(L) = \tilde{T}(L) - T(L) = \sum_i^N w_i \cdot \overline{\Delta T}_i(L) = \sum_i^N \int_{\Delta_{\nu:i}} \Delta T(L,\nu)_i \, d\nu \\ \Delta E(L) = \tilde{E}(L) - E(L) = \sum_i^N w_i \cdot \overline{\Delta E}_i(L) = \sum_i^N \int_{\Delta_{\nu:i}} \Delta E(L,\nu)_i \, d\nu \end{cases} \quad (9)$$

It is trivial to understand that $\Delta E(L) = \Delta T(L)$. Nevertheless, $\Delta E(L)/E(L) \neq \Delta T(L)/T(L)$. Therefore, we have to control separately the relative errors in transmission and in emission. The process used to build the k-distribution finds an optimal combination $\{N, k_{i=1,\dots N}, w_{i=1,\dots N}\}$ to approximate the transmission $T(L)$ and the emission $E(L)$ in each layer of the atmosphere. Contrary to *ckdist* methods, BF00 method allows for an increase in the number N of bins in order to reach arbitrary, predefined accuracy criteria. Within BF00 method, these criteria are $\Delta T/T \leq \%_T$ for each layer, and $\Delta T/T \leq \%_{T\text{tot}}$ for the whole atmosphere transmission. $\%_T$, $\%_{T\text{tot}}$ are *thresholds* given by the user as input parameters. *k-IR* is the extension of BF00 to the thermal infrared. We thus also want to control how the k-distribution approximate the emission. We therefore add a criterion about the emission: $\Delta E/E \leq \%_E$ for each layer. *k-IR* has thus to valid 3 thresholds tests: $\%_T$, $\%_E$, $\%_{T\text{tot}}$. The thresholds tests that are required for each different methods of BF00 are recapitulated in Table 1. If the relative errors are larger than these thresholds, the mapping process will define a new k-distribution with a larger number of bins. Thus, the new k-distribution will be more accurate (see algorithm description in Appendix 1).

Table 1: Recapitulation of the thresholds used in the different methods:

Method	General BF00 method and *k-bin*	*k-IR*
Thresholds	$\lvert\Delta T(\text{layer},\lambda)_i/t(\lambda,\text{layer})\rvert \leq \%_T$ $\lvert\Delta T(\text{layer},\lambda)_i/t(\lambda,\text{atmo})\rvert \leq \%_{T\text{tot}}$	$\lvert\Delta T/T(\text{layer})\rvert \leq \%_T$ $\lvert\Delta T/T(\text{atmo})\rvert \leq \%_{T\text{tot}}$ $\lvert\Delta E/E(\text{layer})\rvert \leq \%_E$

3.2. Introduction of the blackbody radiance in the k-distribution within k-IR method.

Introducing the emission by the gases ($\varepsilon(\nu, L) \cdot B(\nu, \theta)$) in the k-distribution suppose to consider not only the emission and transmission of the gases ($\varepsilon(\nu, L)$ and $t(\nu, L)$), but also the blackbody radiance at the temperature of the different atmospheric layers : $B(\nu, \theta)$. $B(\nu, \theta)$ depends not only to wavenumber ν, but also to temperature θ. Thus, $B(\nu, \theta)$ has a different value at each atmospheric layer. Thus, $B(\nu, \theta)$ cannot be treated with the same method as the method used to treat the sensor's response function $R(\nu)$ or the solar constant $S(\nu)$ in [10]. Different solutions have been proposed in the literature. The basic idea [7,8,11] is to consider the blackbody radiance as gray within the considered band. This approximation is acceptable only if the spectral band is very narrow, which is rarely the case for the channels of thermal infrared sensors. For example, Channel 3 of *CALIPSO-IIR* has a sensor response function that covers the [750; 900 cm^{-1}] band. The averaged value at fixed temperature of $B(\nu, \theta)$ within the band interval is $B_{\text{mean}} = 1/(\nu_1 - \nu_0) \int_{\nu_0}^{\nu_1} B(\nu, \theta) \, d\nu$. We note $\%_B$, the variation in % of blackbody radiance within the band at a fixed temperature: $\%_B = (B_{\max} - B_{\min})/B_{\text{mean}}$. For *CALIPSO-IIR* Channel 3, for $\theta = 280$ K, $\%_B = 12.4$ %. This large variability convinces us that the blackbody radiance cannot be considered as gray within every spectral band of a thermal infrared instrument channel. To overcome this problem, the band can be divided into many narrow bands (*Kratz* [11]) This solution diminishes the problem but does not overcome it (within the smaller spectral intervals, the blackbody radiation still has a spectral variability).

Another solution, also suggested by *Kratz* [11], is a Planck-weighting method (*Chou et al.* [22]): The optical depth of each layer is weighted with the value of $B(\nu, \theta)$ for this layer. This method is efficient to characterize the emission, but less efficient when the transmission and the emission are both treated within the same k-distribution.

The method proposed by *Mlawer et al.* [13] is the most advanced one: it computes for each layer and for each bin *i*, the average (over all wavenumbers associated to the bin) blackbody radiance $\bar{B}_i$. The main advantage of this method is that the bins are defined as groups of wavenumbers having similar absorption/emission coefficients: Within a bin *i*, $\varepsilon(\nu) \approx \varepsilon_i$. So the value of the radiance emitted within the considered bin ($(\overline{\varepsilon B})_i$) can be approximated as follows: $(\overline{\varepsilon B})_i \approx \varepsilon_i \overline{(B)}_i$ without producing a large error.

The *k-IR* method is similar to [13]: In order to include the blackbody radiance in the k-distribution, we define a bin-averaged blackbody radiance $\bar{B}_i$ for every bin *i*:

$$\bar{B}_i(\theta) = 1/(w_i(\nu_1 - \nu_0)) \cdot \int_{\Delta_{\lambda:i}} R(\nu) \cdot B(\nu, \theta) \, d\nu \quad (10)$$

We use the parameter $\bar{B}_i$ for the estimation of the error due to the k-distribution approximation in the in-layer emitted radiance $\mathfrak{L}_E(L)$ within $\bar{B}_i$ method. The spectral radiance $\mathfrak{L}(L)$ of Schwarzschild's Equation (Equation (3)) can be divided in two terms ($\mathfrak{L}_T$: *transmitted radiance* and $\mathfrak{L}_E$: *emitted radiance*):

$$\mathfrak{L}(L) = \mathfrak{L}_T(L) + \mathfrak{L}_E(L) \quad (11)$$

The error $\Delta\mathfrak{L}_E$ in emitted radiance $\mathfrak{L}_E$ caused by the bin decomposition within the *k-IR* method is evaluated in the Appendix 2. Equation (A13) shows that the error in $\mathfrak{L}_E$ is a combination of the two parameters $\Delta(BE)_i$ and $\overline{\Delta\tilde{E}}_i(L)$. These two parameters are both combinations of $\Delta E(L,\nu)_i$ (defined in Equation (7)). Hence, the smaller is $\overline{\Delta\tilde{E}}_i(L)$, the smaller is also $\Delta\mathfrak{L}_E(L)$. A *bin* groups the spectral subintervals that have similar values of $t(\nu, L)$ and $\varepsilon(\nu, L)$. Thus, $\Delta E(L,\nu)_i$ have values that are controlled by the number of bins (the more bins there are, the smaller is the variability of $E(L,\nu)$ inside of each bin *i*, thus the smaller are the $\Delta E(L,\nu)_i$) . This is the reason why the introduction of the parameter $\bar{B}_i$ contributes to the control of the errors: $\bar{B}_i$ is defined in a way that all the errors are due to errors in inside-bin parameters like $\Delta E(L,\nu)_i$.

k-IR goes two steps further than [13] and many *ckdist* methods regarding the precision. Firstly, contrary to [13], *k-IR* does not have a restricted number of bins: Within the *k-IR* method, a larger number of bins leads to a lower $\Delta E(L,\nu)_i$. Secondly, because $\Delta E(L)$ and $\Delta BE(L)$ are highly correlated with $\Delta E(L)/E(L)$, we decided to control the parameters $\Delta E(L)$ and $\Delta BE(L)$, by checking that $\Delta E(L)/E(L)$ is below a *threshold* ($\%_E$) (see Table 1). This control is done for each layer. There is also a layer transmission threshold ($\%_T$) and a total atmospheric transmission threshold ($\%_{T\text{tot}}$). *ckdist* methods at the contrary, assume that the transmission (and emission) spectra of the layers of the atmosphere are correlated to the transmission (and emission) spectrum of a reference layer. This assumption can introduce uncontrolled errors. The feature that the accuracy of the k-distribution increases with the number of bins is possible, because *k-IR* is not a *ckdist* method, as we already discussed in Subsection 2.1. Because of that, ckdist methods usually proceed as follows: a balance between a-priori accuracy and speed is established and the number of bins is fixed (for example [13] fix

the number of bins to 16). In non-correlated k-distribution methods, the mapping process constructs the k-distribution by testing its accuracy for all the layers in transmission and in emission. Here, increasing the number of bins in order to enhance the accuracy is not only possible but also necessary. This feature is validated in Subsection 3.3, by application of *k-IR* to the simulation of Channel 3 of *CALIPSO-IIR* instrument.

Within the *k-IR* method, the bin-averaged blackbody radiance ($\bar{B}_i$) is computed after the bin-wavenumber mapping. $\bar{B}_i(\theta)$ is computed for 2000 temperatures between 0 K and 430 K and stored (the interval of temperature is wide, so that *k-IR* can be applied to very warm atmospheres or to the very cold part of the upper atmosphere). A radiative transfer routine (in our case, the code MOMO, Matrix Operator Model [23]) reads this data, and, knowing the temperature θ of each atmospheric layer, interpolates for each bin the blackbody radiance corresponding to the temperature θ. That allows for possibility (so do [12] and [13]) of using the computed k-distribution for different atmospheres having different temperature profiles.

3.3. Validation of k-IR method by simulation of a CALIPSO-IIR thermal infrared channel.

We simulate the top-of-atmosphere spectral radiance ($\mathfrak{L}_{TOA}$ in W m^{-2}sr^{-1}µm^{-1}) for the channel 3 of the Imaging Infrared Radiometer (*IIR*, *Garnier et al.* [14]) of Cloud and Aerosol Lidar and Imager Pathfinder Satellite Observation (*CALIPSO*, Winker et al. [15]). The channel response function (Figure 1) is centered on 12.05 µm (830 cm^{-1}) and is 2250 nm (150 cm^{-1}) wide. This width corresponds to all the part of the spectrum where the instrument function is not null. We must thus simulate a band that is much wider than the half width at half maximum (~1000 nm, i.e. 70 cm^{-1} for this channel, [14]). We make the simulation for a Mid-Latitude Summer (MLS) standard atmosphere (*McClatchey et a.l* [24]). We compute the gas transmission line-by-line with the code C-GASA of the Freie Universitaet Berlin. C-GASA (Coefficients of Gas Absorption) is an adaptation of the code XTRA (*Rathke and Fischer,* [25]). Its spectroscopic references are HITRAN-2008 (*Rothmann et al.,* [26]) for the lines, and MT-CKD 2.4 (*Clough et al.* [27, 28]) for water vapor and CO_2 continua in the thermal infrared. The transmission atmospheric spectrum (Figure 1) shows that the water vapor continuum is prominent in this band (bottom spectrum of the picture of the top). Optical depths of the different gases are computed at a 0.1 nm ($\approx$ 0.01 cm^{-1}) spectral resolution. With this resolution, each absorption line is described with at least 10 values of the optical depth computed with C-GASA. 22500 spectral subintervals cover the whole band.

We generated many different cases using the *k-IR* method. These cases are listed in Table 2. The differences between these cases are the user-set accuracies, i.e. the value of the user-defined thresholds in in-layer transmission and emissivity errors ($\%_T$, $\%_{\mathrm{Ttot}}$ and $\%_E$) that must not be exceeded. $\%_{\mathrm{Ttot}}$ is always set to be 5 times more stringent than $\%_T$. The more stringent are the thresholds, the more bins are found by the k-distribution. For example, a fit of the band with an accuracy of $\%_{\mathrm{Ttot}} = 5$ % for the whole atmosphere transmittance and of $\%_T = 25$ % for the in-layer transmittance and $\%_E = 5$ % of the in-layer emission is achieved with 935 bins (see Table 2, case 6). The top-of-atmosphere upward spectral radiance observed at a 0° viewing angle is $\mathfrak{L}_{TOA} =$ 7.549 W m^{-2} sr^{-1}µm^{-1}. This corresponds to a brightness temperature $BT_{TOA} = 288.889$ K. The reference value (line by line *LBL* method in Table 2, case 1) is $BT_{\mathrm{TOA,ref}} = 288.988$ K. Thus, the *Error* in the top-of-atmosphere nadir brightness temperature BT_{TOA} is 0.099 K. This is better than the announced instrument precision for the channel 3 of the *CALIPSO-IIR* (*intrinsic 1-sigma noise* = 0.11 K, [14]).

Results of Table 2 are presented in Figure 2. The values of BT_{TOA} simulated with different k-distributions (that all have different number of bins) are plotted as a function of the number of bins. The dashed line represents the reference value (BT_{TOA}(LBL)). Dotted lines are the limits of the *1-sigma noise* of the instrument (BT_{TOA}(LBL) $\pm$ 0.11 K). There is an inverse X-axis at the top of the figure. This axis shows the value of the factor f_{ECO-CT}. This is the factor of economy in computation time: $f_{ECO-CT} = N_{\mathrm{LBL}}/N_{\mathrm{kdist}}$. N_{kdist} is the number of bins of the k-distribution and N_{LBL} is the number of simulations that have to be done when we do not use the k-distribution method ($N_{\mathrm{LBL}} = 22500$). This figure shows that the error due to *k-IR* method is below the instrumental noise if the k-distribution gives more than 900 bins (i.e. $f_{ECO-CT} = 25$). We conclude that *k-IR* method achieve very high precision and however reduce the computation time with a factor f_{ECO-CT} between 10 and 100. Most of all, Figure 2 proves that contrary to correlated k-distribution methods, *k-IR* method permits a balance between speed and accuracy, because the more bins are mapped by the k-distribution, the more accurate is the result.

Results of Table 2 and Figure 2 are obtained with nadir simulations for non-scattering media, hence the airmass was always equal to 1. Even for nadir instruments simulations, we need to know if the results are still correct for larger airmasses because, in a scattered medium, the light's direction can change and the light can go across aerosol and clouds with other angles before going back in the nadir direction. This is the reason why we simulate also $\mathfrak{L}_{TOA}$(kdist,α) for different airmasses (characterized by the viewing angle α). We compare $\mathfrak{L}_{TOA}$(kdist,α) to the reference $\mathfrak{L}_{TOA}$(LBL,α). We define an error in %:
Error(α) = $|(\mathfrak{L}_{TOA}(\mathrm{kdist},\alpha) - \mathfrak{L}_{TOA}(\mathrm{LBL},\alpha))/\mathfrak{L}_{TOA}(\mathrm{LBL},\alpha)|$

Cases in bold from Table 2 are plotted for different values of α. Figure 3 shows (for the cases in bold in Table 2) the error (in %) in $\mathfrak{L}_{TOA}$, depending to α. For all cases except the case (50%/50%) threshold, the error is below 0.2 % for all the viewing angles. The difference of accuracy between the case (50%/50%) and the other cases is due to the fact that the (50%/50%) case has really less bins than the other cases (13 bins compared to more than 400 bins). This high precision is achieved because the tests done for the mapping of the k-distribution are very strict (combination of thresholds tests of the in-layer emission and transmission for all the layers, and for different airmasses).

Table 2: The different cases discussed in Subsection 3.3. *Threshold* refers to the user-defined threshold for the whole atmosphere transmission error (before slash value) and threshold designed to the in-layer emissivity for each layer (after slash value). BT_{TOA} (in K) is the top-of-atmosphere equivalent brightness temperature. BT_{TOA} is obtained by converting $\mathfrak{L}_{TOA}$ (the top-of-atmosphere nadir spectral radiance in W m^{-2}sr^{-1}μm^{-1} simulated for *CALIPSO-IIR* Channel 3). *Error* refers to the error (in K) between BT_{TOA}computed with the different k-distributions and BT_{TOA}obtained with the LBL (line-by-line) method:

Case	Threshold [$\%_{Ttot}/\%_E$]	bins	BT_{TOA} [K]	Error [K]
1	LBL	*22500*	*288.988*	*0* (reference)
2	***1/1***	***3099***	***288.972***	***-0.017***
3	***0.5/0.5***	***2668***	***289.016***	***-0.027***
4	*1/2*	*2495*	*288.959*	*-0.030*
5	*0.5/5*	*1202*	*288.881*	*-0.107*
6	***5/5***	***935***	***288.889***	***-0.099***

7	*1/10*	*505*	*288.845*	*-0.143*
8	***10/10***	***471***	***288.878***	***-0.110***
9	*2/20*	*190*	*288.773*	*-0.215*
10	*5/50*	*77*	*289.033*	*0.044*
11	*10/50*	*66*	*288.970*	*-0.019*
12	***50/50***	***13***	***288.596***	***-0.392***
13	no/no	*1*	*285.563*	*-3.425*

4. k-bin: An improvement of BF00 for instrument channels with a non-fixed spectral response function.

4.1. The k-bin method for an absorption band.

The *k-bin* method is conceptually different from the general non correlated k-distribution method in that the sensor's spectral response function $R(\nu)$ is not a-priori considered. Initially, the entire spectral band $[\nu_1, \nu_2]$ is subjected to a k-distribution analysis. This is equal to setting the spectral response $R(\nu)$ function in the integral in Equation (1) to:

$$\mathrm{R}(\nu) = 1 \text{ for } \nu_1 \leq \nu \leq \nu_2 \text{ and } \mathrm{R}(\nu) = 0 \text{ otherwise} \qquad (12)$$

This is conceptually not new and would basically also be done, if, instead of a satellite channel, atmospheric heating rates within the spectral interval are calculated. However, because we wish to simulate high-resolution channels with this method, the errors in the approximation in Equation (1) have to be treated more carefully. In particular, a global minimization of the error in $T(L)$ in the approximation in Equation (1) is insufficient. Rather, each single k-distribution interval $i = 1, \dots, N$ has to be ensured to be below a certain minimum error. We therefore minimize the error:

$$\Delta T(L, \nu_i) = \int_{\Delta\gamma_i} \exp\left(-k(\gamma) \cdot L\right) \cdot \delta(\gamma^*) d\gamma - \exp\left(-k_i \cdot L\right); \quad \forall i, \gamma^* \qquad (13)$$

The new variable γ is associated to the wavenumber coordinate ν. There is a bijective mapping between ν and γ with $F(\nu) = \gamma;\ F^{-1}(\gamma) = \nu$. This function is called *index function* and maps from wavenumber space into Γ-space, in which the wavenumbers are sorted in order of increasing gas absorption coefficient k (refer to [10] for details). Equation (13) ensures that for each wavenumber within the *i*-th *k-bin* interval the maximum error falls below a certain user-defined threshold.

The minimization of $\Delta T(L, \nu_i)$ of Equation (13) is done iteratively following the scheme given in Figure 4. In the example shown in Figure 4; initially 3 *k-bi*n intervals are used to describe the spectral interval (upper left). For all three intervals the error in transmission is calculated at high resolution using Equation (13) (Figure 4, lower left). Since the maximum error occurs in the first interval, this interval is then split in two. This action results in two new *k-bin* intervals, as well as retaining two of the originals *k-bin* intervals. In each iteration step, the method to derive the new weights and absorption coefficients for the two new split intervals is the one of BF00 ([10]). The iterative method is performed until the relative error $|\Delta T/T(L, \nu)_i|$, for all intervals $i = 1, \dots, N$ and all ν, is below threshold $\%_T$ (see Table 1). The iterative method is also performed for all layers' transmissions and for the total transmission of the atmosphere.

Compared to the traditional k-distribution approaches (except SMT, [9]) this method offers the advantage that not only the band-averaged transmission is well represented but also the transmission for each *k-bin* interval $i = 1, \dots, N$. Note, that this is not necessarily the case if only the band-averaged transmission is optimized. An interval with small contribution to the total transmission ($w_i \to 0$) might have high errors that do not contribute much to the band-averaged error. If a narrow-band channel covers only this interval, it will also exhibit high errors. The maximum error allowed for each *k-bin* interval can be relaxed for very spectrally small *k-bin* intervals. Since small intervals do not contribute strongly to the total transmission, their maximum allowable error can be weighted by a factor $\Delta\nu_{\mathrm{sensor}}/w_i$ which is the ratio between the width of the sensors spectral response function $R(\nu)$ and the spectral width of the *k-bin* interval. If a *k-bin* interval is a factor of one hundred smaller than the spectral response function, its contribution will be at maximum 0.01 and thus an error in this particular interval will only contribute with at maximum a factor of 0.01 to the total error in transmission. Note, that this weighting is independent to the strength of the absorption in the spectral subintervals associated to the considered *k-bin* interval: The strength of the absorption is only quantified by the extinction coefficients k_i given to the *kbin* interval, not by the weight w_i.

4.2. Derivation of weights for channels within the selected band

With the *k-bin* method outlined in previous subsection we have derived a set of $\{N, k_{i=1,\dots N}, w_{i=1,\dots N}, F(\nu), F^{-1}(\gamma)\}$ that allows to represent the spectral band $[\nu_1, \nu_2]$. In this subsection we outline the method that generates results for arbitrary satellite channels within this spectral band. Given the above *k-bin* results and a satellite response function $R(\nu)$ we only need to know how much each *k-bin* interval $i = 1, \dots, N$ contributes to the total spectral response of the channel. This fraction can be calculated in a straightforward manner by:

$$\widetilde{w}_i = \int_{\Delta\gamma:i} R\left(F^{-1}(\gamma)\right) d\gamma \qquad (14)$$

The new weights $\widetilde{w}_i$ constitute the weighting of a channel with filter function $R(\nu)$ in the *k-bin*. For example the top-of-atmosphere spectral radiances of this channel can be constructed via:

$$\widetilde{\mathfrak{L}} = \sum_{i=1}^{N} \widetilde{w}_i \cdot \widetilde{\mathfrak{L}}_i \qquad (15)$$

Where $\widetilde{\mathfrak{L}}$ is the spectral radiance (in W $\mathrm{m^{-2}sr^{-1}\mu^{-1}}$) of the channel under consideration and the $\widetilde{\mathfrak{L}}_i$ are results of radiative transfer simulations for the $i = 1, \dots, N$ *k-bin* intervals. For example if one particular channel is fully within one *k-bin* interval (e.g. an absorption-free channel), the corresponding $\widetilde{w}_i = 1$. From this consideration it is obvious that not only the broadband transmission but also the transmission within each *k-bin* interval has to be accurate. In the next subsection, we apply this method to simulations of the oxygen A-band.

4.3. Application to high-resolution oxygen A-band simulations

Within this subsection we apply, as an example, the *k-bin* method to the oxygen A-band. We wish to simulate the channel response of the forthcoming OCO-2 sensor. OCO-2 is an instrument that observes backscattered solar radiation within the oxygen A-band, and the two carbon dioxide absorption bands around 1.6 μm and 2.06 μm. OCO's spectral resolving power in the oxygen A-band will be about 17000, leading to a spectral half-width of roughly 0.04 nm for each individual channel. The spectral range between 758 nm and 772 nm will therefore be covered by roughly 350 channels (or more if the interval is oversampled). At this early stage of OCO-2's design, neither the actual spectral response functions nor the center wavelengths of the channels are accurately known. We therefore assume Gaussian spectral response functions with the above half-width of 0.04 nm and an equal spacing of 0.04 nm over the entire spectral band. For the purpose of this study we simulated the transmittances in the whole OCO O_2-A band spectral

interval using the HITRAN 2008 spectroscopic database (*Rothman et al.* [26]) for an U.S Standard Atmosphere (*McClatchey et al.* [24]) subdivided into 23 layers. The high-resolution spectrum as well as the same spectrum seen with *OCO-2-like filter functions* is shown in Figure 5. We then generated four different cases using the above outlined *k-bin* method (see Table3). The difference between the four different cases is the value of the user-defined threshold $\%_T$ in transmittance error that must not be exceeded. We applied more stringent criteria for the whole atmosphere transmission than for the in-layer transmission. With increasing accuracy, the *k-bin* method produces more sub-intervals (*bins*) in order to fulfill the more stringent requirements. As can be seen from Table 3, a fit of the entire band with an accuracy of 5 % is achieved with 136 k-distribution terms. Note, that the resulting accuracy is actually better than 5 % since the in-layer transmission for each layer is optimized too. For a user-defined threshold of $\%_T = 0.5$ %, the whole atmosphere transmission error is already below 0.2 % for each of the intervals. Note, that the values given in Table 3 refer to the maximum errors found in individual *k-bin* intervals and not in reconstructed channels. Any channel within the oxygen-A band can now be reconstructed from Equation (15) using an appropriated set of weights $\widetilde{w}_i$. The resulting error of any reconstructed channel will thus be a weighted average over the individual errors of the *k-bin* intervals. Those errors are discussed subsequently.

Weights $\widetilde{w}_i$ were generated for each of the 340 *OCO-2-like* channels according to Subsection 4.2. The transmittances of each channel could then be constructed by the transmittances of the *k-bin* intervals from Equation (15) and compared to the 'true' transmission in each channel. We did this comparison for variable relative absorber masses between 0.25 and 8. This is useful in order to validate the k-distribution for scattering media in which the angle of the photon path always changes, hence the k-distribution has to be valid for many different airmasses. An absorber mass of 1 corresponds to one vertical pass through the atmosphere, whereas an absorber mass of 8 corresponds to a pass through the atmosphere at a zenith angle of 82.8 °. Note, that a relative absorber mass < 1 can exist if the pass does not go across the whole atmosphere. Figure 6 shows the error in whole atmosphere transmission for the four cases with respect to relative absorber mass. The error is defined as the maximum error found in all 340 channels for each absorber mass. As can be seen from Figure 6, the error for Case 3 (0.5 % accuracy) and Case 4 (0.1 % accuracy) are everywhere below 0.2 %, regardless of the relative absorber mass. Figure 7 shows the maximum error in transmission over all different absorber masses for each layer and all 340 channels. This error is generally also within the range smaller than ± 0.25 % with a few exceptions for channels in areas with step gradients in the spectral absorption coefficient.

Finally we would like to relate the errors derived here to OCO-2 instrument characteristics. In the oxygen A-band OCO-2 will have a signal-to-noise ratio of roughly 350 (Crisp, D., pers. comm.). This translates to first order to a transmission uncertainty of $1/350$ ($\times$ 100 %) $=$ 0.29 %. Cases 3 and 4 thus produce uncertainties below the instrument noise. Note, that by using more stringent thresholds the error of the *k-bin* method can be further reduced.

Another factor that might affect the accuracy of OCO-2 simulations are slight spectral mislocations of its channels. These spectral mislocations can in principle be corrected in orbit. However the maximum achievable accuracy depends to the width of the channel itself. We assume here, that the center position of each channel is known to within 0.001 nm. Figure 8 shows the impact of such an uncertainty on the whole atmosphere transmission at a relative absorber mass of 1. The error due to uncertainties in OCO's spectral calibration would in this case be in the order of 1 % and thus a factor of 5 larger than the errors introduced by the *k-bin* in Case 3.

Table 3: The four different cases discussed in Subsection 3.3. *Threshold* refers to the user-defined threshold for the whole atmosphere transmission error. The values in brackets refer to the additional threshold applied to the in-layer transmission for each layer. The maximum error refers to the maximum error in the whole atmosphere transmission in each of the *k-bin* intervals:

Case	Threshold $[\%_{T\mathrm{tot}}/(\%_T)]$	bins	Max. Errors [%]
1	*5.0/(50.0)*	*136*	*1.8*
2	*1.0/(10.0)*	*375*	*0.3*
3	*0.5/(5.0)*	*561*	*0.2*
4	*0.1/(1.0)*	*1557*	*0.06*

5. Conclusions

We present two improvements for non-correlated k-distribution methods: *k-IR* that extends BF00 method (*Bennartz and Fischer, 2000,* [10]) to thermal infrared simulations, and *k-bin* that extends BF00 to simulations of instrument channels with non-fixed spectral response functions.

k-IR solves the problem of modeling both gas transmission an emission of radiation by the use of a *bin-averaged blackbody radiance* for each bin and for various temperatures. The accuracy of transmission and of emission for every layer is evaluated. Contrary to correlated k-distribution methods, a balance between accuracy and computation speed can be established: the more bins, the more accuracy. This feature is validated along an application of *k-IR* to *CALIPSO-IIR* instrument: We have simulated the top-of-atmosphere equivalent brightness temperature for Channel 3 of *CALIPSO-IIR*. We reach a 0.5 K precision for this value for k-distribution with 13 bins, a 0.2 K precision with 200 bins and a 0.11 K precision (instrument accuracy) is reached with 900 bins. This method leads to longer computation time than correlated k-distribution ([11-13]), but results in better accuracy. Results for different viewing angles are also satisfying and show that even for higher airmasses, the precision of the top-of-atmosphere spectral radiance is better than 0.2 %, if enough bins are used. This allows the use of *k-IR* method to model gas absorption and emission also in scattering media.

k-bin method has been developed to optimally perform radiative transfer simulations over wide spectral bands. This method presents many advantages. Firstly, the radiative transfer within a given absorption band can be completely solved using a set of *N k-bin* intervals. Once the corresponding *N* radiative transfer simulations are performed, all satellite channels within this absorption band can be reconstructed as a weighted average over the *N* simulation results. In the case discussed here, we can re-construct every OCO-2 channel in the oxygen A-band with accuracy better than the sensor noise with only less than 600 simulations. For a sensor with 1000 channels, the numerical cost to simulate each channel would thus be 0.6 simulations per channel. Secondly, if the spectral response function of a sensor varies in time (e.g. due to thermal variations) these variations can be accounted for without new simulations by re-deriving the weights for the new spectral response function. Also, any other sensor with a channel covering the absorption band can be simulated by just deriving new weights. Thirdly,

because *k-bin* is a non-correlated k-distribution method, the trade-off between accuracy and speed is tunable. If more accurate simulations are needed, the *k-bin* has to be performed with a lower user-defined accuracy threshold. The *k-bin* technique can in principle be applied to any sensor and spectral region. The more different channels there are to be simulated, the more effective the *k-bin* method will be.

Acknowledgments

This work was partly funded by NASA via grant NNG-05GE57G. The authors would like to thank Mark Kulie, Rasmus Linsdstrot, Cintia Carbajal-Henken, Jacques Pelon, and Francois Ravetta for their helpful comments.

APPENDIX 1: Algorithm of BF00 method

A1.1) Procedures

a) Mapping and indexing of the layer A_j

- *Input:* Gas absorption spectrum of the layer A_j : $k_{A_j}(\nu)$, number of wanted bins N_j, gas absorption spectrum of the total atmosphere: $k_{tot}(\nu)$.
- *Output:* The index of the layer A_j with N_j bins: index(A_j, N_j)

We define a *layer and atmosphere absorption coefficient* $k^*(\nu)$ (Equation 8 of [10]). This coefficient is a pondered average of $k_{A_j}(\nu)$ and $k_{tot}(\nu)$. The introduction of parameter $k^*(\nu)$ is a particularity of BF00. The use of this parameter permits to optimize the k-distribution for both layer A_j and the whole atmosphere.

We note N_j, the wanted number of bins for the k-distribution of layer A_j. We map the extinction coefficient k^*; to this purpose, the function k^* is sorted in ascending order.

We define N_j k-intervals named *bins*. Each bin i has the same width in k (Δk_i): $\Delta k_i = k^*_{max}/N_j, \forall i$; $k^*_{max} = \max(k^*(\nu), \nu \in \Delta\nu)$.

We store an index of the spectrum. In the index, each wavenumber ν is labeled with the number of bin i to which ν is associated. The index is proper to the layer A_j and to the number of bins N_j; we write it: index(A_j, N_j). This process is the *inverse mapping*.

b) Combine indexing and definition of the k-distribution for the common index.

- *Input*: indexes index(A_j, N_j) for all p already indexed layers.
- *Output*: 1) the common index index(p,N) with N bins that combines all the indexes of all p layers that have already been indexed; 2) the k-distribution (N, $k_{i,l}$, w_i) associated to index(p,N) with bins absorption coefficients ($k_{i,l}$) and bins weights (w_i).

Because the spectra of all the layers are not necessarily correlated, the indexes of the p already indexed layers A_1, …, A_p are not necessarily the same. It is nevertheless necessary to have a common index for all the layers.

We thus use a program that groups the indexes together: the aim is to find a *common index* that has the minimum number of bins, but that respects the bin separations of all the indexes index(A_1, N_1), …, index(A_p, N_p). This means: wavenumbers that are not labeled with the same bin in one of the p indexes should be labeled with a different bin in the common index. N is the number of bins of the common index. We necessarily have: $N > \max(N_j)_{j=\{1,\dots,p\}}$. The common index is written: index(p,N).

We derive the k-distribution (N,$k_{i,l}$, w_i) from the common index. The bins absorption coefficients $k_{i,l}$ are computed for every layer l of the atmosphere and for each of the N bin i of the common index index(p,N). The values of the weights w_i are common to all the layers and computed with the method develop in [10].

c) Threshold test for the transmission of a layer l of the atmosphere

Within this procedure, we check if the k-distribution is accurate for the transmission of a given layer l: we evaluate the relative difference between the real transmission of layer l and the approximated transmission of this layer. The approximated transmission is the transmission of layer l evaluated with the k-distribution (N, $k_{i,l}$, w_i). The relative difference has to be below a threshold given by the user: $\%T_{lay}$. If this condition is not respected, then the k-distribution has to be improved for this layer.

d) Threshold test for the transmission of the whole atmosphere

Within this procedure, we check if the k-distribution is accurate for the whole atmosphere transmission: we evaluate the relative difference between the real transmission of the whole atmosphere and the approximated transmission of the whole atmosphere. The approximated transmission is the whole atmosphere transmission evaluated with the k-distribution (N, $k_{i,l}$, w_i). The relative difference has to be below a threshold given by the user: $\%T_{tot}$. If this condition is not respected, then the k-distribution has to be improved, and we have to find which layer is the worst indexed.

A1.2) Chronology of the algorithm

(i) We select a reference layer that we name A_1.
(ii) We start with a number of wanted bins N_1=2. We index the spectrum of A_1 with procedure a). We obtain the index of A_1: index(A_1, N_1).
(iii) We derive a k-distribution with procedure 2). We test if this k-distribution succeeds in modeling the transmission of the layer A_1: We apply the layer threshold test of procedure c) at layer A_1. If the k-distribution fails to the test, then
(iv) we improve the k-distribution by finding a new index for layer A_1, with more bins: we apply procedure a) with $N_1 = N_1 + 1$; then
(v) we derive the new k-distribution with procedure b) and redo the threshold test of procedure c).
We repeat the actions *(iv)*, *(v)* until the k-distribution succeeds at threshold test c).
When the threshold test is validated:
(vi) We control if the k-distribution succeeds in modeling the other atmospheric layers: We apply the procedure c) to all the atmospheric layers. If the test c) is validated for all the layers then we go to *(ix)*. If there is a layer for which test c) fails then this layer is named A_2 and we define $N_2 = 2$ and
(vii) we find the index of the spectrum of layer A_2 (index(A_2, N_2)) with procedure a),
(viii) and we then find a common index index(p=2,N) and a common k-distribution with procedure b). We apply the threshold test c) to layer A_2. We repeat steps *(vii)* and *(viii)* with $N_2 = N_2 + 1$; until the k-distribution succeeds in test c) for A_2. We go back to step *(vi)* in order to test the new k-distribution for other atmospheric layers. Of course if other layers have to be optimized with procedure a), then, in steps (vii) and (viii), we replace the names (A_2, N_2, p=2) by (A_3, N_3, p=3), then by (A_4, N_4, p=4), etc…
(ix) After the k-distribution method has succeeded in threshold test c) for all the atmospheric layers, we test if the k-distribution satisfies the demand of the user regarding the whole atmospheric transmission: we apply threshold test d). If the k-distribution succeeds in threshold test d) then we go to *(xi)*. If it does not succeed:
(x) We refine the k-distribution by re-indexing one of the layer A_j, with more bins ($N_j = N_j + 1$) with procedure a), we find a new common index and a new k-distribution with procedure b), and we test with procedure d) the ability of the k-distribution to model the whole atmosphere transmission with procedure d). We repeat all the actions since *(x)* until the k-distribution succeeds in test d).
(xi) The k-distribution algorithm is finished with success; we keep this k-distribution and store it.

APPENDIX 2. Expression of $\Delta\mathfrak{L}_E(L)$, the error in emitted Radiance $\mathfrak{L}_E(L)$.

For the sake of simplicity, we consider a rectangular spectral sensor function ($R(\nu) = 1$ over the whole band), but the method can be generalized to every sensor spectral response function.
We express the bin-averaged blackbody radiance $\bar{B}_i$ of Equation (10) with the feature $R(\nu) = 1$:

$$\bar{B}_i(\theta) = \frac{1}{w_i(\nu_1-\nu_0)} \cdot \int_{\Delta_{\nu:i}} B(\nu,\theta)\, d\nu \quad \text{(A1)}$$

Equation (11) separates the spectral radiance $\mathfrak{L}(L)$ of Schwarzschild's Equation (Equation (3)) in two terms ($\mathfrak{L}_T$: *transferred radiance* and $\mathfrak{L}_E$: *emitted radiance*):

$$\mathfrak{L}(L) = \mathfrak{L}_T(L) + \mathfrak{L}_E(L) \quad \text{(A2)}$$

With:

$$\begin{cases} \mathfrak{L}_T(L) = 1/(\nu_1-\nu_0)\int_{\nu_0}^{\nu_1} \mathfrak{L}_\nu(0)\cdot T(\nu)\, d\nu = \sum_i^N w_i \cdot \mathfrak{L}_i(0)\cdot[\exp(-k_i\cdot L) + \overline{\Delta T}_i(L)] \\ \mathfrak{L}_E(L) = 1/(\nu_1-\nu_0)\int_{\nu_0}^{\nu_1} B(\nu,\theta)\cdot(1-\exp(-k(\nu)\cdot L))\, d\nu = \sum_i^N \mathfrak{L}_{E,i}(L) + \Delta\mathfrak{L}_E(L) \end{cases} \quad \text{(A3)}$$

We introduce the bin decomposition for $\mathfrak{L}_E$. We obtain (A4) by applying this decomposition to (A3):

$$\begin{cases} \mathfrak{L}_E(L) = \sum_i^N \mathfrak{L}_{E,i}(L) \\ \mathfrak{L}_{E,i}(L) = 1/(\nu_1-\nu_0)\cdot\int_{\Delta_{\nu:i}} B(\nu,\theta)\cdot\varepsilon(\nu,L)d\nu \end{cases} \quad \text{(A4)}$$

$\breve{\mathfrak{L}}_E(L)$ is the reconstruction of $\mathfrak{L}_E(L)$ with the k-distribution. $\Delta\mathfrak{L}_E(L)$ is the difference between the real $\mathfrak{L}_E(L)$ and its reconstructed value with the k-distribution:

$$\begin{cases} \Delta\mathfrak{L}_E(L) = \breve{\mathfrak{L}}_E(L) - \mathfrak{L}_E(L) \\ \breve{\mathfrak{L}}_E(L) = \sum_i^N \breve{\mathfrak{L}}_{E,i}(L) \end{cases} \quad \text{(A5)}$$

With:

$$\breve{\mathfrak{L}}_{E,i}(L) = \bar{B}_i \cdot \breve{E}_i(L) \quad \text{(A6)}$$

We define $\Delta B_i(\nu)$, the difference between $\bar{B}_i(\theta)$ and $B(\nu,\theta)$, in the same way as for T and E in Equation (7):

$$B(\nu) = \bar{B}_i + \Delta B_i(B(\nu,\theta)) \quad \text{(A7)}$$

Per definition of $\bar{B}_i$, the value of $\overline{\Delta B}_i$ that is the bin-averaged difference between $B(\nu,\theta)$ and $\bar{B}_i(\theta)$ is zero:

$$\overline{\Delta B}_i = \frac{1}{w_i(\nu_1-\nu_0)} \cdot \int_{\Delta_{\nu:i}} \Delta B_i(\nu) d\nu = 0 \quad \text{(A8)}$$

We define $\overline{\Delta(\breve{B}\breve{E})}_i$:

$$\overline{\Delta(\breve{B}\breve{E})}_i = \frac{-1}{w_i(\nu_1-\nu_0)} \cdot \int_{\Delta_{\nu:i}} \Delta B_i(\nu)\cdot\Delta E(L,\nu)_i d\nu \quad \text{(A9)}$$

The expression of $\mathfrak{L}_{E,i}$ is derived from equations (A4), (A1), (7) and (A7):

$$\mathfrak{L}_{E,i}(L) = 1/(\nu_1-\nu_0)\cdot\int_{\Delta_{\nu:i}} (\bar{B}_i - \Delta B_i(\nu)(\breve{E}_i - \Delta E(L,\nu)_i)d\nu \quad \text{(A10)}$$

(A10) simplifies to (A11) using (A9), (A8), (8) and (A7):

$$\mathfrak{L}_{E,i}(L) = w_i \cdot \left(\bar{B}_i \cdot \breve{E}_i - \breve{E}_i \cdot \overline{\Delta B}_i - \bar{B}_i \cdot \overline{\Delta E}_i + \overline{\Delta(BE)}_i\right) \quad \text{(A11)}$$

Hence, using (A6) and (A8):

$$\begin{cases} \mathfrak{L}_{E,i}(L) = \breve{\mathfrak{L}}_{E,i}(L) - w_i \cdot \left(0 - \bar{B}_i \cdot \overline{\Delta E}_i + \overline{\Delta(\breve{B}\breve{E})}_i\right) \\ \mathfrak{L}_E(L) = \sum_i^N w_i \cdot \breve{\mathfrak{L}}_{E,i}(L) - \sum_i^N w_i \cdot \bar{B}_i \cdot \overline{\Delta E}_i(L) + \sum_i^N w_i \cdot \overline{\Delta(\breve{B}\breve{E})}_i \end{cases} \quad \text{(A12)}$$

The error $\Delta\mathfrak{L}_E(L)$ in the emitted radiance $\mathfrak{L}_E(L)$ is detailed in (A13):

$$\begin{cases} \Delta\mathfrak{L}_E(L) = \sum_i^N w_i \cdot \bar{B}_i \cdot \overline{\Delta\breve{E}}_i(L) + \sum_i^N w_i \cdot \overline{\Delta(\breve{B}\breve{E})}_i\,(L) \\ \overline{\Delta\breve{E}}_i(L) = \frac{1}{w_i} \cdot \int_{\Delta_{\nu:i}} \Delta E(L,\nu)_i d\nu \\ \overline{\Delta(\breve{B}\breve{E})}_i = \frac{-1}{w_i(\nu_1-\nu_0)} \cdot \int_{\Delta_{\nu:i}} \Delta \mathrm{B}_i(\nu)\cdot\Delta E(L,\nu)_i d\nu \end{cases} \quad \text{(A13)}$$

References

[1] Moncet J, Uymin G, Snell HE. Atmospheric radiance modeling using the Optimal Spectral Sampling (OSS) method. SPIE Defense and Security Symposium Conference 2004;5425-37.

[2] Kleespies T, van Delst P, McMillin L, Derber J. Atmospheric Transmittance of an Absorbing Gas. 6. OPTRAN Status Report and Introduction to the NESDIS/NCEP Community Radiative Transfer Model. Appl Opt 2004;43:3103-3109.

[3] Saunders RW, Matricardi M, Brunel P. A fast radiative transfer model for assimilation of satellite radiance observations – RTTOV-5. Tech. Memo. 282: ECMWF; 1999.

[4] Saunders RW, Matricardi M, Brunel P. An Improved Fast Radiative Transfer Model for Assimilation of Satellite Radiance Observations. Quart J Royal Met Soc 1999;125:1407-1425.

[5] Sherlock V, Collard A, Hannon S, Saunders R. The Gastropod fast radiative transfer model for advanced infrared sounders and characterization of its errors for radiance assimilation. J of App Met 2003;42(12):1731-1747.

[6] Fu Q, Liou KN. On the Correlated k-Distribution Method for Radiative Transfer in Nonhomogeneous Atmospheres. J Atm Sci 1992; 49(22):2139-2156.

[7] Lacis AA, Oinas V. Nongray Gaseous Absorption, Thermal Emission, and Multiple Scattering in Vertically Inhomogeneous Atmospheres. J Geophys Res 1991;96(D5):9027-9063.

[8] Goody R, West R, Chen L, Crisp D. The correlated-k method for radiation calculations in nonhomogeneous atmospheres. J of Quant Spectrosc and Radiat Transfer 1989;42(6):539-550.

[9] West R, Crisp D, Chen L. Mapping transformations for broadband atmospheric radiation calculations. J Quant Spectrosc and Radiat Transfer 1990;43(3):191-199.

[10] Bennartz R, Fischer J. A modified k-distribution approach applied to narrow band water vapour and oxygen absorption estimates in the near infrared. J Quant Spectrosc and Radiat Transfer 2000;66:539–553.

[11] Kratz DP. The correlated k-distribution technique as applied to the AVHRR channels, J of Quant Spectrosc and Radiat Transfer 1995;53(5), 501-517.

[12] Dubuisson P, Giraud V, Chomette O, Chepfer H, Pelon J. Fast Radiative transfer modeling for infrared imaging radiometry. J Quant Spectrosc and Radiat Transfer 2005;95:201–220.

[13] Mlawer EJ, Taubman SJ, Brown PD, Iacono MJ, Clough SA. Radiative transfer for inhomogeneous atmospheres: RRTM, a validated correlated-k model for the longwave. J Geophys Res 1997;102(D14):16663-16682.

[14] Garnier A, Pelon J, Dubuisson P, Faivre M, Chomette O, Pascal N, Kratz DP. Retrieval of Cloud Properties Using CALIPSO Imaging Infrared Radiometer. Part I: Effective Emissivity and Optical Depth. J App Met and Clim 2012;51:1407-1425.

[15] Winker DM, Pelon J, Coakley JA et al. The CALIPSO Mission, A Global 3D View of Aerosols and Clouds. Bull of Am Met Soc 2010;91(9):1211-1229.

[16] Crisp D, Johnson C. The orbiting carbon observatory mission, Acta Astronautica 2005;56(1-2):193-197.

[17] Boesch H, Baker D, Connor B, Crisp D, Miller C. Global Characterization of CO_2 Column Retrievals from Shortwave-Infrared Satellite Observations of the Orbiting Carbon Observatory-2 Mission. Remote Sensing 2011;3(2):270-304.

[18] Goody RM, Yung YL. Atmospheric Radiation, Theoretical Basis. Oxford University Press. Second Edition, 1989; 519pp. Subsection 4.8.3 (176:177).

[19] Meadows VS, Crisp D, Ground-based near-infrared observations of the Venus nightside: The thermal structure and water abundance near the surface.J of Geoph Research 1996;101(E2): 4595-622.

[20] Crisp, D. Absorption of Sunlight by Water Vapor in Cloudy Conditions: A Partial Explaination for the Cloud Absorption Anomaly. Geophys Res Lett 1997;24:571–4.

[21] West R, Goody R, Chen L, Crisp D. The correlated-k method and related methods for broadband radiation calculations. J Quant Spectrosc and Radiat Transfer 2010;111:1672-1673.

[22] Chou MD, Ridgway WL, Yan NMH. One-parameter scaling and exponential-sum fitting for water vapor and co2 infrared transmission functions. J Atmos Sci 1993; 50:2294–2303.

[23] Fell F, Fischer J. Numerical simulation of the light field in the atmosphere-ocean system using the matrix-operator method. J Quant Spectrosc and Radiat Transfer 2001;69:351–388.

[24] McClatchey RA, Fenn RW, Shelby JEA, Voltz FE, Garing JS. Optical properties of the atmosphere. Res Paper AFCRF-72-0497, Hanscom Air Force Base, Bedford, MA; 1972.

[25] Rathke C, Fischer J. Retrieval of cloud microphysical properties from thermal infrared observations by a fast iterative radiance fitting method. J Atmos Ocean Technol 2000;17:1509-1524.

[26] Rothman LS, Gordon IE, et al. The HITRAN 2008 molecular spectroscopic database. J Quant Spect and Radiat Transfer 2009;110(9–10):533-572.

[27] Clough SA, Kneizys FX, Davies RW. Line Shape and the Water Vapor Continuum. Atmos Res 1989;23:229-241.
[28] Clough SA, Shephard MW, Mlawer EJ, Delamere JS, Iacono MJ, Cady-Pereira K, Boukabara S, Brown PD. Atmospheric radiative transfer modeling: a summary of the AER codes, Short Communication. J Quant Spectrosc and Radiat Transfer 2005; 91:233–244.

Figure 1: The atmospheric transmission in the spectral subinterval of the *CALIPSO-IIR*, channel 3 for a Mid-latitude Summer Standard atmosphere. The shown transmission are: all gases (bottom) and specific transmissions of different species (top). The different species whose transmissions are shown are from bottom to top: water vapor self continuum only, water vapor (local lines + self continuum + foreign continuum), carbon dioxyde and ozone. The response function of Channel 3 of the instrument *CALIPSO-IIR* is drawn with a thicker line (IIR-3). The underlying spectroscopic databases are HITRAN-2008 andthe MT-CKD 2.4 water-vapor continuum:

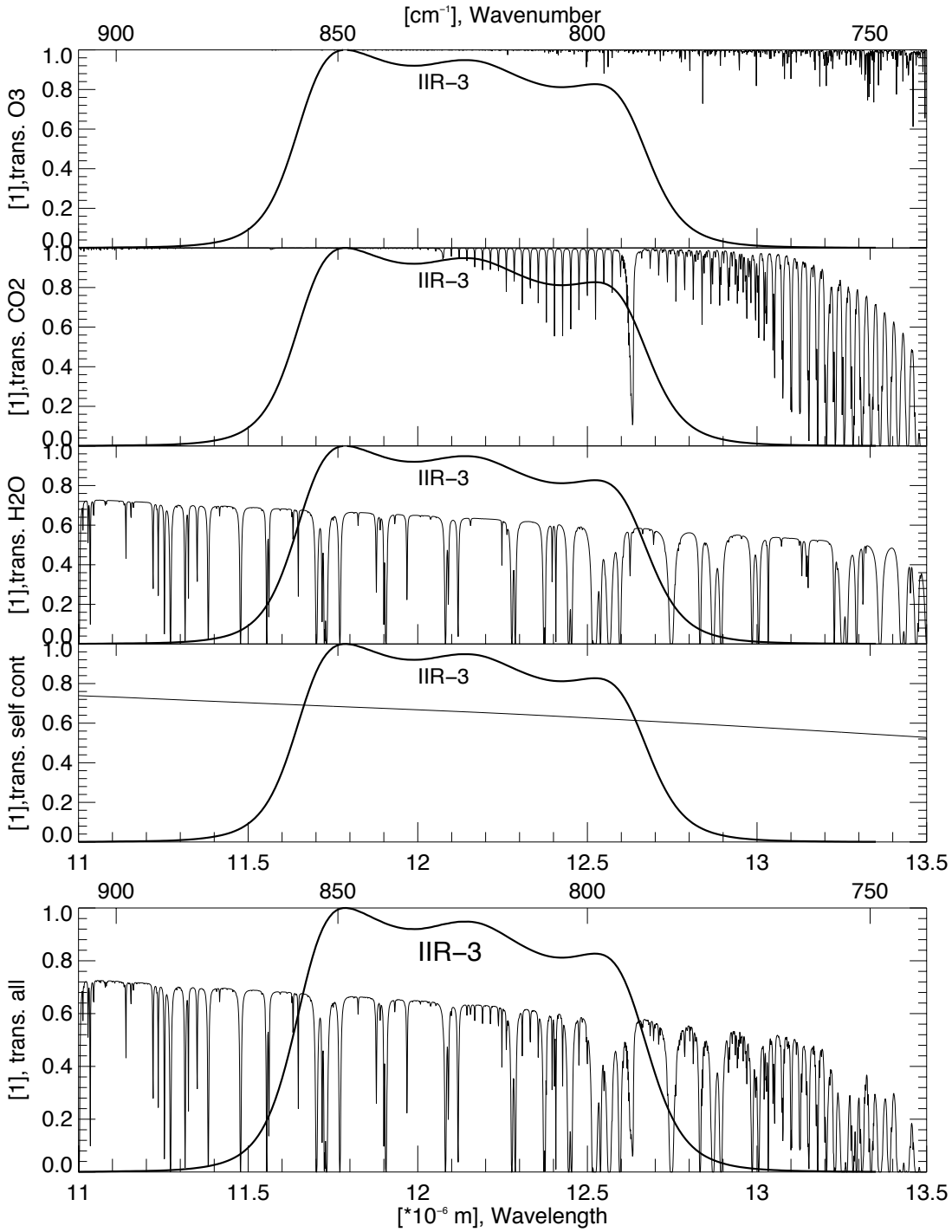

Figure 2: Value of BT_{TOA} (top-of-atmosphere equivalent brightness temperature) as a function of number of *bins* (intervals created by the k-distribution). Upper axis shows the time economy factor $f_{eco\text{-}CT}$ (number of intervals needed by the line-by-line method divided by the number of bins of the k-distribution):

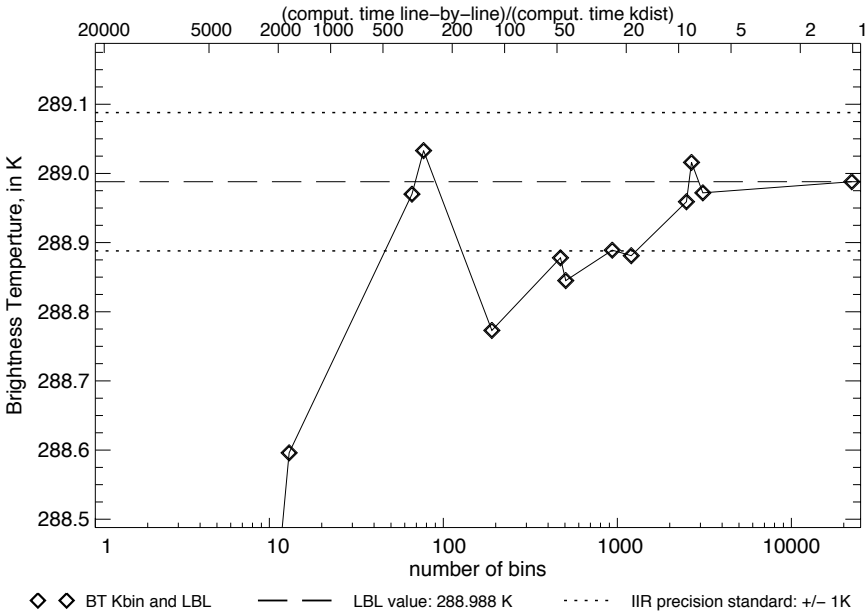

Figure 3: Error due to the *k-IR* technique as a function of space-borne instrument viewing angle (α) for five different user-defined accuracy thresholds (cases in bold in Table 2). Errors are in percent of the upper spectral radiances obtained with the LBL method (% ofΩ_{TOA}(LBL,α)):

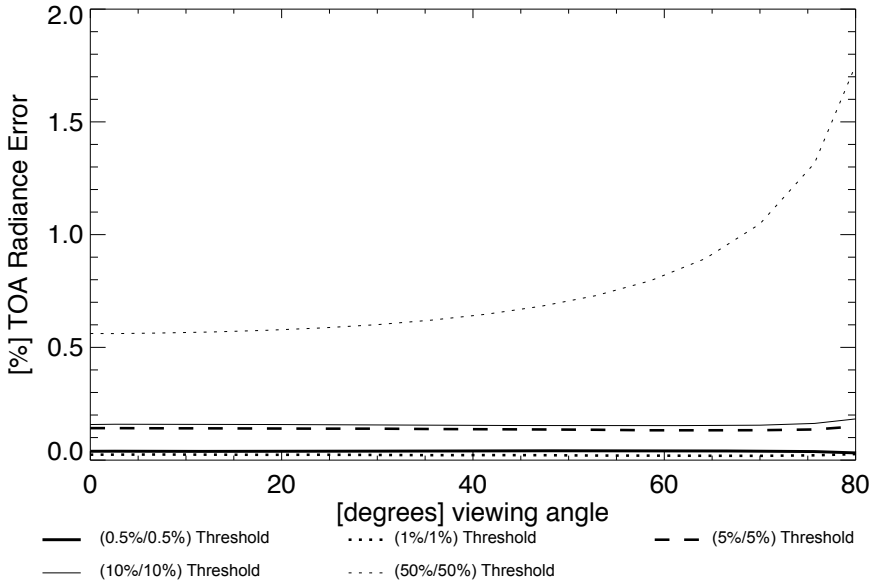

Figure 4: Schematic representation of the *k-bin* approach. The broadband wavenumber interval is initially subdivided into *N k-bin* intervals (here *N* = 3). The interval with the highest error in transmission compared to monochromatic transmittances is subdivided into two intervals. The process is then iteratively repeated until all transmittance errors fall below a user-defined threshold:

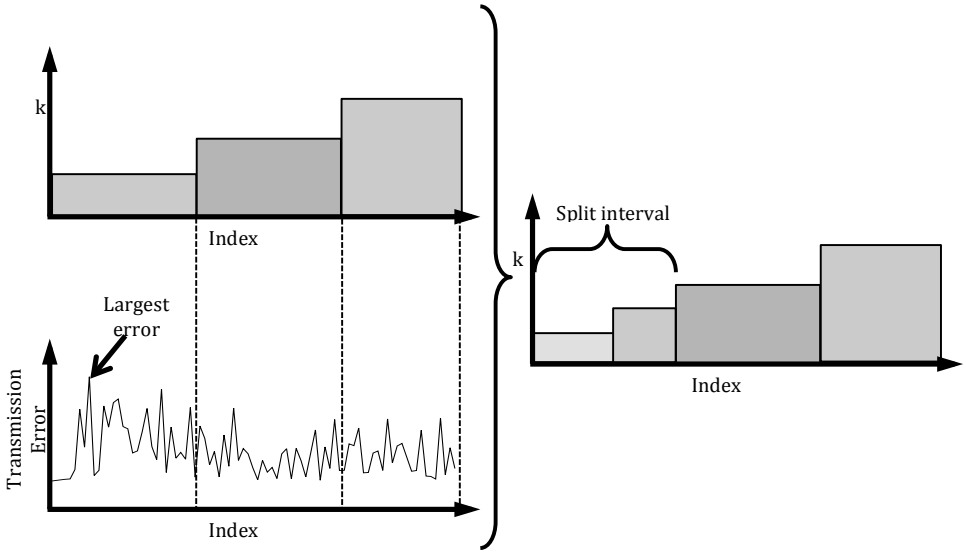

Figure 5: The atmospheric transmittance in the oxygen A-band for a U.S. Standard atmosphere. The upper panel shows the transmittance at a wavelength resolution of *0.00025* nm. The lower panel shows the transmittance at OCO2's spectral resolution of roughly *0.04* nm. The underlying spectroscopic database is HITRAN-2008:

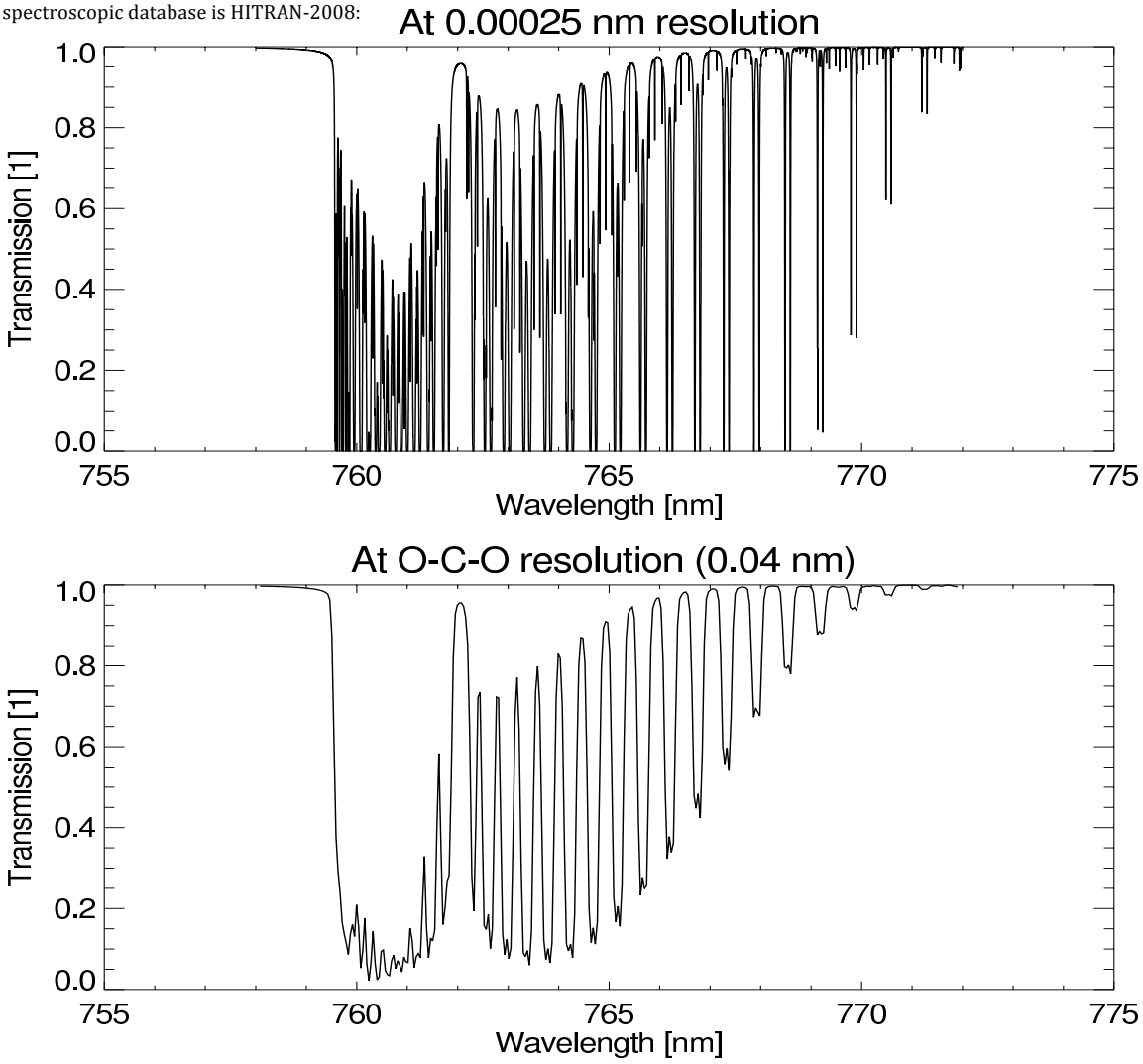

Figure 6: Error due to the *k-bin* technique as a function of relative absorber mass for four different user-defined accuracy thresholds. The errors shown here are the maximum errors out of the *340* OCO-2 channels covering the oxygen A-band:

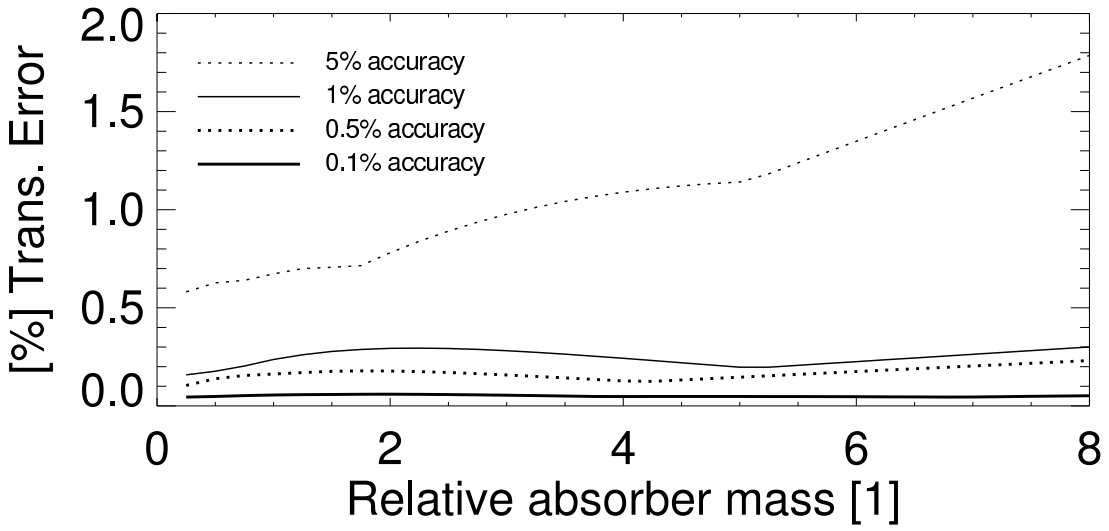

Figure 7: In-layer transmittance errors for all *23* modeled layers and all *340* OCO-2 channels. The error shown here is the maximum error over all absorber masses between *0.25* and *8* and for a user-defined accuracy threshold of *0.5* % whole atmosphere transmission (case 3):

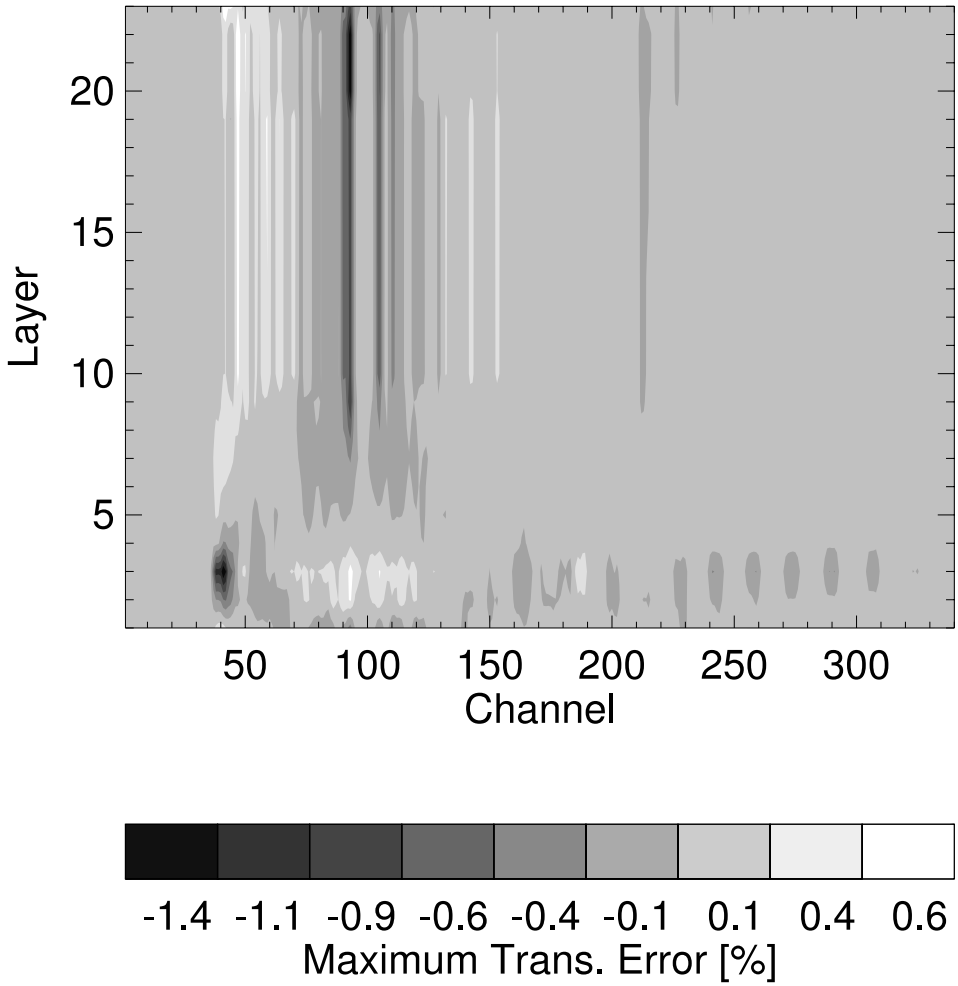

Figure 8: Uncertainty in the whole atmosphere transmission due to an assumed uncertainty of 0.001 nm in the spectral position of the different OCO-2 channels:

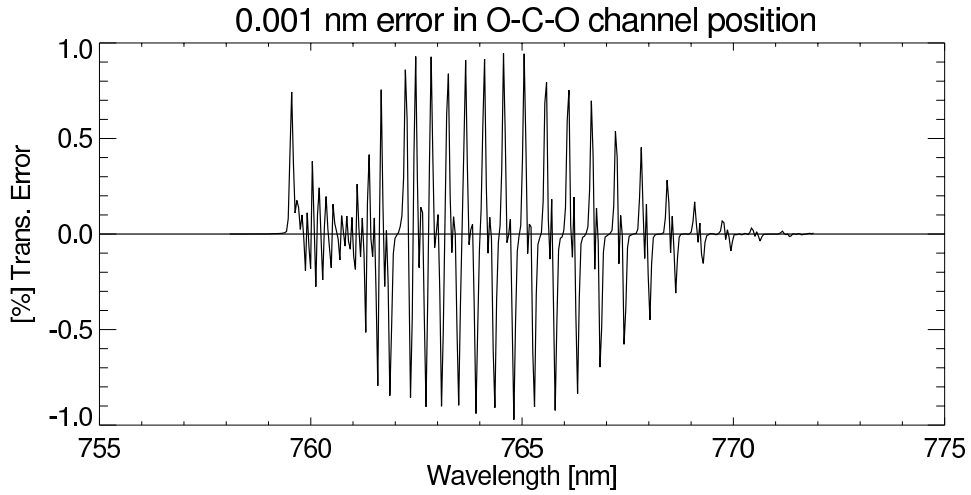

Summary and outlook.

The k-IR method presented in *Doppler et al.* (2013a) succeeds in implementing the blackbody radiation in the k-distribution scheme. Thus the k-distribution module KISS can be used in the thermal infrared. Figure 2 of the article *Doppler et al.* (2013a) published here above demonstrates that within k-IR method, a balance is possible between accuracy and rapidity by increasing or decreasing the number of bins of the k-distribution. This feature is not always validated for correlated k-distribution methods.

The k-distribution module KISS can reach high accuracy or be fast, but rarely both. This is the weakness of using a non-correlated k-distribution algorithm. Up to now, with KISS, the user fixed his exigencies about the accuracy in transmission and emission with thresholds (see article) and the k-distribution increased the number of bins in order to find a suitable k-distribution that fulfills these exigencies. A future outlook is to develop a fast non-correlated k-distribution method: an algorithm that found the most accurate k-distribution (bins' definition) for a fixed number of bins imposed by the user. This exiting outlook could be a way for KISS to challenge the rapidity of faster methods like correlated k-distributions (*Dubuisson et al.* 2005, *Mlawer et al.* 1997), with the lowest limitation on the precision.

Summary of Part II.

Radiative transfer code MOMO has been successfully extended to thermal infrared within this PhD work. MOMO covers now the full spectral range [0.2 – 100 μm].

This extension concerned 3 modules of the MOMO package: The spectroscopy module CGASA has been built, in order to simulate properly the water vapor spectroscopy in the thermal infrared: The aim was to overcome the difficulty of modeling the water vapor continuum of absorption. The k-distribution module KISS has been adapted and a method has been found to implement the blackbody radiation in the k-distribution method. The numerical routine of adding-doubling of the matrix operator method has also been adapted and includes now the emission of radiation by gases, aerosols and clouds.

Validation tests presented in the 2 articles displayed in sections 5.2 and 7.2 (*Doppler et al.* 2013b; 2013a) show convincing results. This allows radiative transfer code MOMO (with its modules CGASA and KISS) to be used as a precise code in the thermal infrared.

There is still outlook potential for numerical developments of MOMO: Within this PhD work, we delve into the spectroscopy of water vapor. Other gases require the same attentions: for example O_2, CO_2 and O_3. Validations with comparison to IASI measurements should be done. The rapidity of the code can be improved by developing a non-correlated k-distribution method for KISS that does not define so many bins. Also, validations of MOMO for radiative simulations for scattering media in thermal infrared spectral regions are planned.

The field of applications of the full range radiative transfer code MOMO is wide: from remote sensing simulations in the thermal infrared to radiation budget computations. In the following Part (Part III, chapters 8, 9, 10), we will show several studies about the aerosol impact on the radiation budget. The full range fluxes (and aerosol radiative forcings, and aerosol additional heating rates) presented in Part III have all been computed with the radiative transfer code MOMO used in its brand new full range version.

Part III.

Applications to the estimate of aerosol direct radiative forcings.

In Part II of this thesis, the developments of numerical tools of radiative transfer have been presented. These new tools allow broadband shortwave and longwave radiative transfer simulations with the radiative transfer code MOMO.

In this part of the thesis, we will discuss some methods, involving MOMO simulations that allow to estimate the influence of aerosols on the radiation budget. The strategy that we followed is to estimate the radiative impact of the aerosols at a regional scale. Chapter 8 presents two case studies with the dataset of the measurement campaign TRAQA. This dataset allows, thanks to a synergy of lidar and in-situ measurements, to characterize the aerosols and to estimate the aerosol radiative forcings for isolated cases. Chapter 9 is devoted to a sensibility study: the sensibility of the aerosol radiative forcings to aerosol size distribution, and to the value of the aerosol refractive index is simulated. The AEROCOM radiative transfer models comparison experiment to which MOMO took part is presented. This experiment has quantified how the radiative transfer scheme can influence the estimates of aerosol radiative forcing. Lastly, the sensibility of absorbing aerosol radiative forcings to the presence of clouds below aerosol plumes is analyzed within a theoretically study. In Chapter 10, we will discuss how to extend spatially and temporally the aerosol radiative forcing studies. A case study is presented; this case study estimates the aerosol radiative forcings for biomass burning aerosols above low dense clouds, in the Guinea bay. It is a 1-D case study extended spatially in one direction: Many 1-D cases are analyzed all along a spaceborne lidar track, with the help of spaceborne instruments' synergy. Outlook is presented for an extension of the estimates of aerosol radiative impact to a regional scale: The aim is to estimate the aerosol radiative impact on the climate of the Mediterranean region. Two methods are proposed: one using a mesoscale model, and another method, using A-train data and especially the spaceborne lidar CALIOP for a better characterization of the spatial distribution of aerosol plumes and their temporal evolution.

8. Optical properties and radiative impact of aerosols: A case study for TRAQA campaign

The main message of Chapter 4 (Part I) of this thesis is that a good characterization of the aerosols is required, if we want to estimate the aerosol radiative impact. The measurement campaign TRAQA (Transport à longue distance et qualité de l'air) deployed a synergy between in-situ and remote sensing measurements. This synergy facilitates the aerosols' characterization (chemical, physical and optical properties). In the current chapter, the method and the results for two case studies are presented. The studied cases are aerosol vertical profiles for two measurements' flights during the TRAQA campaign. The first part of the study is devoted to the aerosol characterization with a method named optical closure. The second part of the study realizes the computation of the radiation fluxes and the estimation of the radiative impact of the aerosols (heating rates, forcings). The objectives of this chapter are:

- To present briefly the measurement campaign TRAQA and the two cases that are studied.

- To characterize two different kinds of aerosol (Saharan dust and pollution from the Pô Valley) with their microscopic properties (size distribution and refractive indexes).

- To estimate the radiative impact of these two kinds of aerosol by simulating the forcings and aerosol additional heating rates for the two studied cases.

Many approximations have been done in this case study. There are all mentioned in the text, and numerated. In Section 8.5, all the approximations are recalled and their validity are discussed.

8.1. The measurement campaign TRAQA.

TRAQA (Transport à longue distance et Qualité de l'air) is a measurement campaign. This campaign is part of the long-term experiment ChArMEx (Chemistry Aerosol Mediterranean Experiment) of the project MISTRALS (Mediterranean Integrated Studies at Regional And Local Scales).

This campaign involved more than 60 hours of aircraft flights between the 20th of June and the 11th of July 2012. The flights have been done in the North-West part of the Mediterranean Basin (see map of the flights in Figure 8.1). The campaign involved a synergy between LIDAR and in-situ measurements. The airborne LIDAR is LNG2 (LEANDRE Nouvelle Generation 2, LEANDRE = Lidars aéroportés pour l'Etude des Aérosols, des Nuages, de la Dynamique, du Rayonnement et du cycle de l'Eau). LNG2 has 3 spectral channels: 355 nm, 532 nm, and 1064 nm. The 355

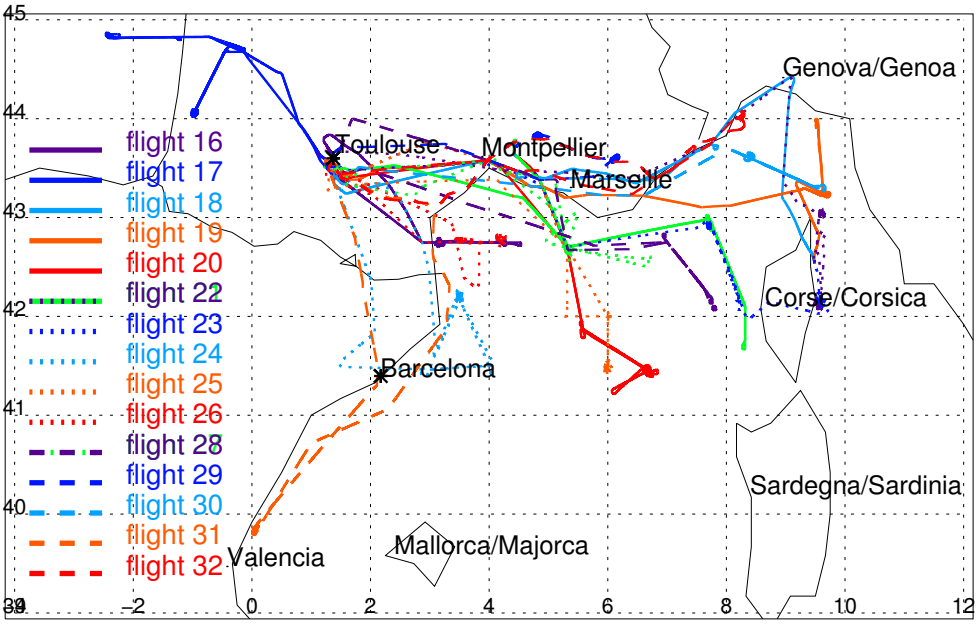

Figure 8.1.: Map of the 32 flights of the TRAQA campaign.

nm channel is split in two (normal signal and signal on the perpendicular direction of polarization). LNG2 is on board of the aircraft ATR-42 of SAFIRE (Service des Avions Français Instrumentés pour la Recherche en Environement). LNG2 can be put in nadir or in zenith position of observation.

The in-situ instruments are part of the AVIRAD sampling system (in-situ measurements instruments constellation of the institute LISA: Laboratoire Interuniversitaire des Systèmes Atmosphériques). The instruments used for this work are:

- A TSI® nephelometer that provides scattering and backscattering coefficients at 450, 550 and 700 nm for vertical soundings.

- A Magee® aethalometer that provides the absorption coefficient at 370, 470, 520, 590, 660, 880, 950 nm for constant altitude sampling.

- A PCASP instrument (Passive Cavity Aerosol Spectrometer Probe) that provides measurements of the size distribution of the aerosols.

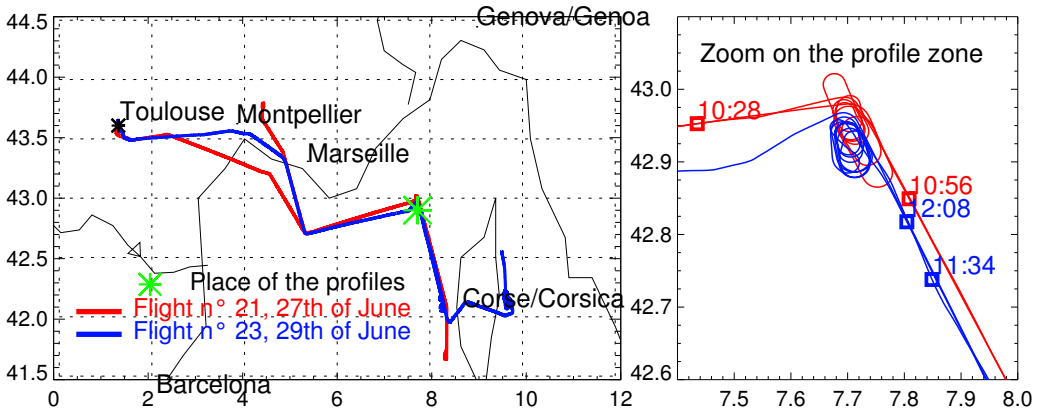

Figure 8.2.: Map of the flights 21 and 23 for the case studies (left). Zoom on the hippodrome descent for the sounding of the vertical profile (right). Squares on the picture of the right give the location and time of the lidar measurements before and after the in-situ soundings.

8.2. Case studies with pollution and dust aerosols.

During flight 21 (27th June 2012) and flight 23 (29th June 2012), a sounding in an hippodrome descent took place. The place of the sounding was exactly the same for the two flights: somewhere over the sea between Marseille and the Corsica (Figure 8.2).

Two plumes have been sampled. In the plume of Flight 21 there is a different aerosol composition as in the plume of Flight 23. During Flight 21, observed aerosols were mostly pollution aerosols coming from the Pô Valley (so the conclusions of trajectory studies). The pollution aerosol layer was below 1 km of altitude (see Figure 8.3, left). During Flight 23, observed aerosols were mostly Saharan dust aerosols. The plume was between 2 and 4 km of altitude. The objective of the work presented in this chapter is to characterize the optical properties of these two kinds of aerosol in order to have solid inputs for a radiative study, with MOMO simulations (Section 8.4). These inputs are: a spectrum of the refractive index of the aerosols and their size distribution. A way to obtain this information is to realize an optical closure with a synergy of lidar and in-situ measurements.

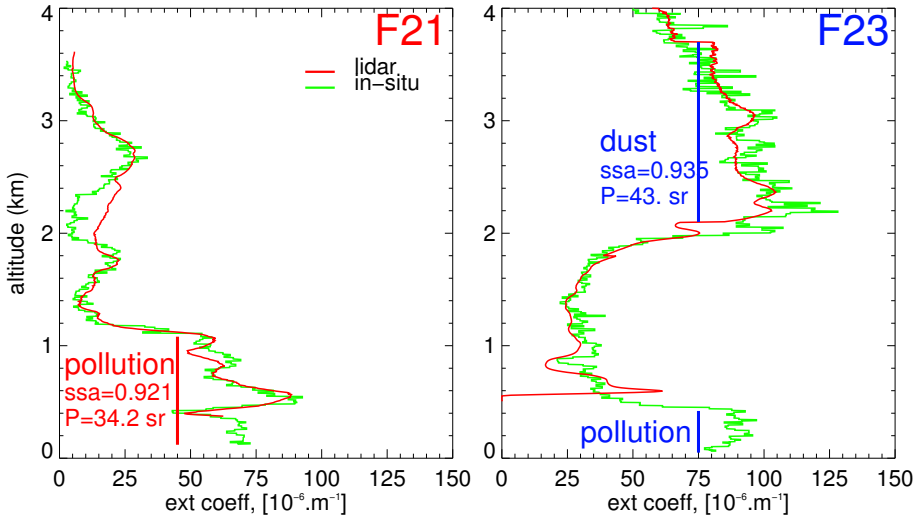

Figure 8.3.: Extinction coefficient profile during the vertical sounding of flight 21 (left) and flight 23 (right). Green line represents the extinction coefficient obtained with in-situ measurements and red line the extinction coefficient obtained with a lidar inversion algorithm.

8.3. Aerosol microscopic properties' characterization with optical closure method.

A method named optical closure is applied. This method allows to combine the information given by the lidar measurements (attenuated beta β_{att} profile, see Appendix) to the information provided by the in-situ measurements (scattering coefficient profile, single scattering albedo of the aerosol layers, size distribution). The final goal is to extract the refractive indexes of the aerosols for the 6 wavelengths of the aethalometer (370, 470, 520, 590, 660, 880, 950 nm) and for the lidar wavelength (532 nm). The parameters used for the optical closure are the lidar ratio P, the single scattering albedo ω_0 and the size distribution of the aerosols $N(R_{\text{mod}})$.

8.3.1. Determination of the lidar ratio *P*: LIExI method.

As described in Appendix, the inputs of the lidar inversion algorithm can be the profile of extinction coefficient and the profile of β_{att}, and the outputs can be the profiles of β_{180} and of lidar ratio P. Figure 8.4 summarizes the method used to determine the lidar ratio with the use of nephelometer, aethalometer and lidar measurements. We named this method LIExI (Lidar Inversion with Extinction coefficient in Input).

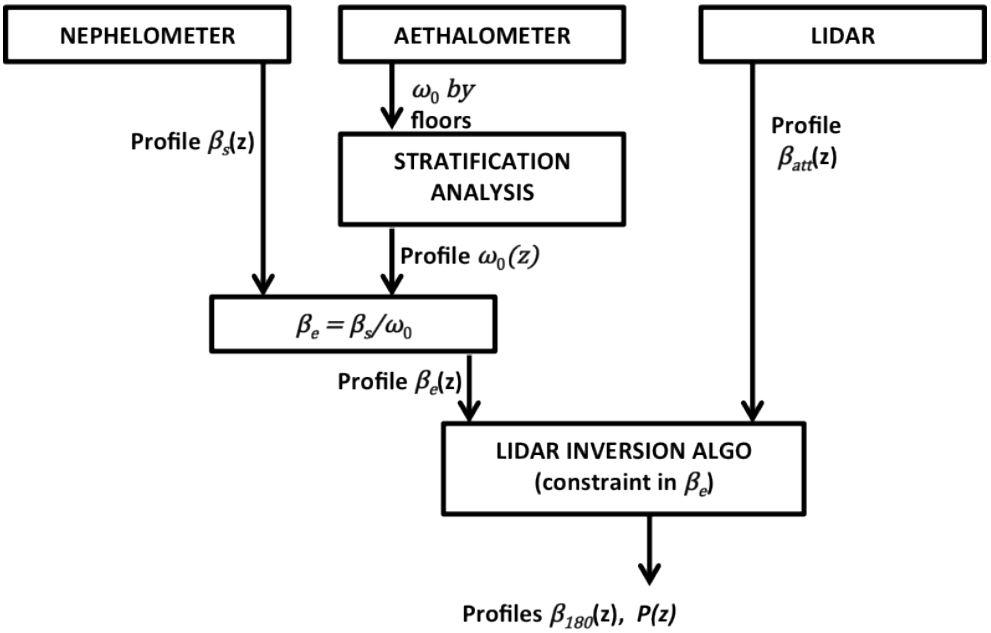

Figure 8.4.: LIExI (Lidar Inversion with Extinction Coefficient in Input) method for the estimate of the profile of lidar ratio $P(z)$.

This method works as follows:

The profile of β_{att} is a measurement of the lidar. The profile of extinction coefficient β_{e} is obtained with the profile of scattering coefficient β_{s} (obtain with the nephelometer for the wavelengths 450, 550 and 700 nm and interpolated to the lidar wavelength: 532 nm) and with the single scattering albedo ω_0 (obtained for the 6 wavelengths of the aethalometer and interpolated to 532 nm). A first approximation (Approximation 1) is that the interpolation of these parameters is valid. A second approximation is that the single scattering albedo ω_0 (measured with the absorption coefficient for some strategic layers of the profile) is homogeneous in a thick layer of the atmosphere (that means that there are 2 or 3 layers in the vertical profile that are homogeneous in ω_0 : Approximation 2). The lidar inversion algorithm can be constraint in extinction coefficient and give the lidar ratio P in output.

8.3.2. Optical closure method used to obtain the refractive index with a 2-D dichotomy on the values of SSA and lidar ratio.

Both lidar ratio and single scattering albedo SSA are parameters that depend on the complex refractive index $\widetilde{n}$ and on the size distribution$N(R_{\mathrm{mod}})$. Because we know the size distribution $N(R_{\mathrm{mod}})$ of the aerosol, a Mie code can, with these inputs (refractive index), compute the phase function $p(\theta', \theta)$ and the single scattering albedo ω_0 of the aerosol. With p and ω_0, we can compute the lidar ratio ($P = 1/(\omega_0 \cdot p_\pi);\ p_\pi = p(\theta, \theta + \pi)$, see Equation 10.6 in Appendix). The inverse method is more challenging: obtaining the refractive index $\widetilde{n}$, knowing the SSA, P and the size distribution. It is nevertheless possible to do it with an inversion process. The inversion process consists of running many Mie code computations for a set of pre-supposed values of the refractive index and realizing a 2-D dichotomy process. The method is explained in Figure 8.5 and works as follows: We presuppose a sample of 200 refractive indexes (10 different values of the imaginary part of the refractive index $\mathrm{Im}(\widetilde{n})$ and 20 different values of the real part of the refractive index Re($\widetilde{n}$)). We know the size distribution thanks to the PCASP data. With a Mie code (here the Mie code of the preprocessor SCA of the radiative transfer code MOMO, based on the Mie description of *Wiscombe* 1980), we compute the phase function, the SSA and the value of P. We make a scatter plot with P in y-axe and SSA in x-axe (see Figure 8.6). We define a criterion of closeness for the computed values of P and SSA compared to the real values of P and SSA of the aerosol: The points of the scatter plot that are close enough in SSA and P (namely, that respect the user defined closeness criterion) are in the red rectangle of Figure 8.6 (left graph). On the right graph of Figure 8.6, the computed points are also put on another scatter plot, where Re($\widetilde{n}$) are the x values and Im($\widetilde{n}$) are the y values. The points contained in the red rectangle of the left graph are plotted in red on the right graph. The 2-D dichotomy consists of only selecting the ranges of Re($\widetilde{n}$) and Im($\widetilde{n}$) that give the red points; and defining a new sample of 200 couples of (Re($\widetilde{n}$), Im($\widetilde{n}$)) that are contained in these ranges. This action is represented with the loop on the right of Figure 8.5. The sample of (Re($\widetilde{n}$), Im($\widetilde{n}$)) values is affined compared to the initial sample. A run with the Mie code is done again and the dichotomy analysis is achieved in order to reduce one more time the possible ranges of Re($\widetilde{n}$) and Im($\widetilde{n}$). By iteration, a precise estimate of Re($\widetilde{n}$) and Im($\widetilde{n}$) is possible.

For this case study, the results are:

- For dust aerosols of flight 23, $\mathrm{Re}(\widetilde{n}) = 1.506 \pm 0.005$; $\mathrm{Im}(\widetilde{n}) = 0.0023 \pm 0.0002$.

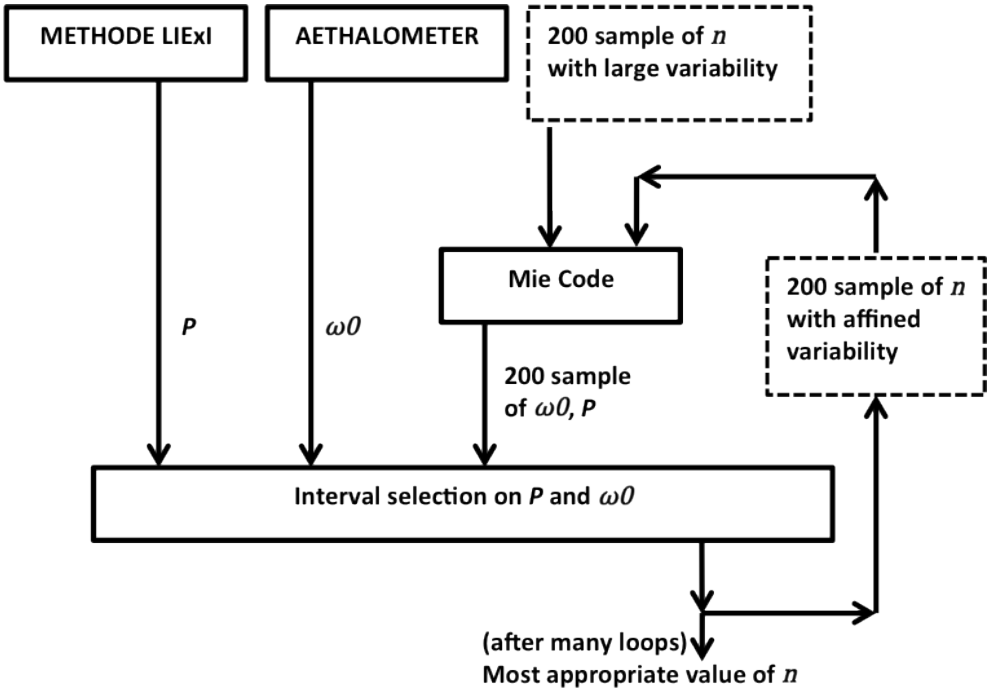

Figure 8.5.: Optical closure method: obtaining the refractive index (real and imaginary part) with a 2-D Dichotomy on the value of the SSA and of the lidar ratio.

- For pollution aerosols of flight 21, $\mathrm{Re}(\widetilde{n}) = 1.65 \pm 0.1$; $\mathrm{Im}(\widetilde{n}) = 0.013 \pm 0.002$.

Note, that a third approximation has been done: Dust particles have been treated with a Mie code, even if they are not spherical particles (Approximation 3).

This 2-D dichotomy method for the optical closure allows to estimate the values of Re($\widetilde{n}$) and Im($\widetilde{n}$) at 532 nm for the aerosols. This is a first step for the characterization of the aerosol, but it is not enough for a radiative study. The radiative study requires a full range spectrum of Re($\widetilde{n}$) and Im($\widetilde{n}$). This method of radiative closure is not well used in the literature. *Raut and Chazette* 2007 did something similar, but with two 1-D dichotomies (instead of one 2-D dichotomy like here): a first dichotomy Re($\widetilde{n}$) <-> β_s/N (N is the total number of particles) and a second dichotomy Im($\widetilde{n}$) <-> SSA. For *Raut and Chazette* 2007, the value of the lidar ratio is only used to control this inversion. In a further work, *Raut and Chazette* 2008 discussed the benefit of a 2-D dichotomy for the inversion of the aerosol refractive index: A 1-D dichotomy do not necessary allow to isolate the sample of Re($\widetilde{n}$) and

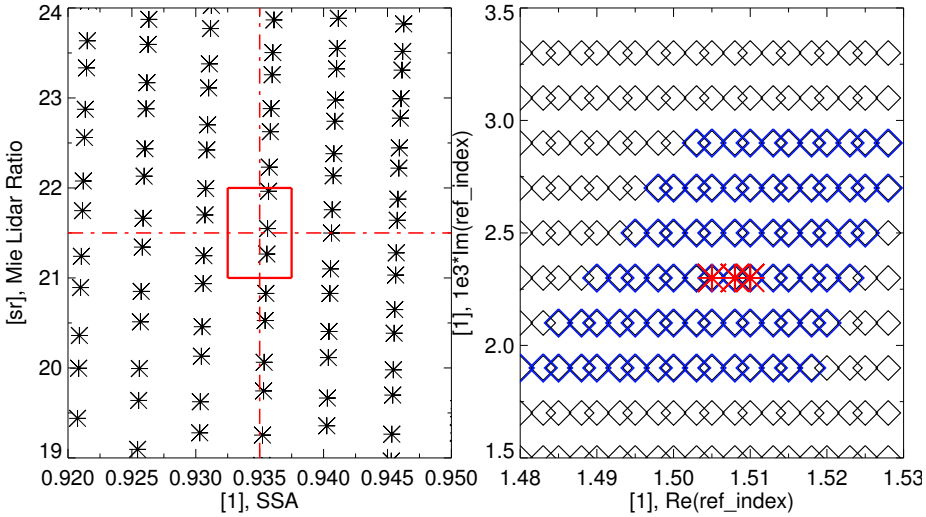

Figure 8.6.: 2-D dichotomy for the estimation of Re($\widetilde{n}$) and Im($\widetilde{n}$) with the values of P and SSA. Left graph: Scatter plot in (SSA, P). Each plot corresponds to an (Re($\widetilde{n}$), Im($\widetilde{n}$)) combination that gives in output of the Mie code a (SSA, P) combination. Right graph: Scatter plot in (Re($\widetilde{n}$), Im($\widetilde{n}$)). The blue diamonds are the points that figure on the left graph; the red stars are the points that figure in the red rectangle of the left graph.

Im($\widetilde{n}$) that leads to the nearest values of SSA and P.

We only have lidar information at one wavelength (532 nm). So, the optical closure described here above can only be done for 532 nm. However, the aethalometer provides values of the SSA for 6 other wavelengths. Literature information indicates that the real refractive index does not have spectral variations between 350 and 1000 nm (See OPAC values for different aerosol classes on Figure 8.7.). We make a new approximation (Approximation 4): The value of Re($\widetilde{n}$) found with the optical closure at 532 nm is the same as the values of Re($\widetilde{n}$) for the 6 wavelengths of the aethalometer (370, 470, 520, 590, 660, 880, and 950 nm). For these 6 wavelengths, we realize a simplified optical closure: In Figure 8.5, we replace the sample of 200 values of $\widetilde{n}$, by a sample of 10 values of Im($\widetilde{n}$). The Value of Re($\widetilde{n}$) is fixed (it is the one of 532 nm). Then, we make a 1-D dichotomy: the variable parameter in input of the Mie code is Im($\widetilde{n}$), and the output parameter of control is the SSA. With this technique, we can estimate the values of Im($\widetilde{n}$) for the 6 wavelengths of the aethalometer. There are reported on Figure 8.7 with the blue crosses (for the dust of Flight 23) and with the red crosses (for the pollution aerosol of Flight 21). This method (extracting Im($\widetilde{n}$), supposing Re($\widetilde{n}$)) is similar to the method of *Takamura et*

al. 1994, with a difference: we used the SSA instead of the lidar ratio for the output parameter of the 1-D dichotomy.

As Figure 8.7 shows, the values of the refractive index obtained do not correspond exactly to the values of a tabulated category of OPAC (Optical Properties of Aerosols and Clouds, *Hess et al.* 1998). This is not a surprise: The aerosol mixtures of TRAQA campaign are mixtures of different aerosols present in the layers. Therefore, the TRAQA-dust is not the OPAC-mineral, but a mixture dominated by mineral aerosols (the spectral variation is the same as the OPAC mineral category, but there is a factor of difference for the imaginary part of the refractive index). For pollution aerosol, the characterization of the mixture is difficult, because pollution aerosol is a mixing of soot (black carbon), sulfates and other organic aerosols. Because the real part of the refractive index of the TRAQA-pollution aerosol has a high value, we suppose that there is a large soot amount. This soot amount is balanced with a scattering aerosol; this can explain the high values of the SSA. Because of the mixing of the aerosols, it is more appropriate to talk about *effective refractive index* of the mixture instead of 'refractive index' only for the description of the parameter inverted with this optical closure.

The instrumental synergy allowed a nice characterization of the optical properties of the aerosols: The refractive index (real and imaginary parts) is estimated at 7 shortwave wavelengths. The PCASP measurements (constrained with the values of the refractive index) provided the size distribution of the aerosol. A radiative study is now possible. This radiative study will allow to estimate the additional heating rates of the aerosols and their radiative forcings. This is the purpose of the next section.

8.4. Radiative study: differences between pollution aerosol and dust aerosol.

8.4.1. Radiative scheme.

The radiative study is done with the radiative transfer code MOMO of the FU Berlin (Matrix Operator Model: *Fischer and Grassl* 1986, *Fell and Fischer* 2001, *Doppler et al.* 2013b). Thanks to the thermal infrared extension (Part II, chapters 5, 6, 7), MOMO can compute spectral radiances, spectral irradiances and thus, radiative fluxes, radiative heating rates and forcings, for the full spectral range [0.2 – 100 μm].

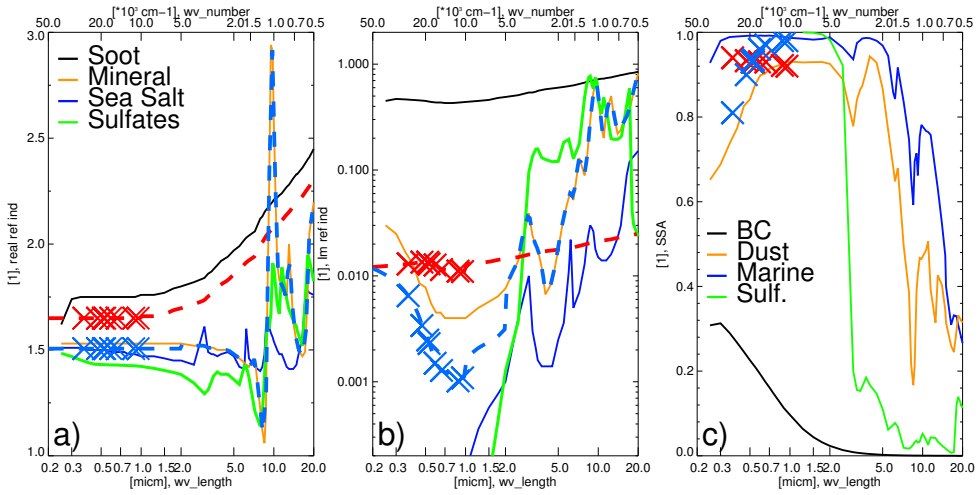

Figure 8.7.: Spectrum of the aerosol refractive indexes: a) real part Re($\widetilde{n}$), and b) imaginary part Im($\widetilde{n}$). The colored curves are the OPAC standard aerosol mixtures. The blue and red crosses are the values obtained with the optical closure for dust aerosol of flight 23 (blue) and pollution aerosol of flight 21 (red). The red and blue dashed lines correspond to the spectral interpolations and the longwave extensions of the refractive indexes Re($\widetilde{n}$) and Im($\widetilde{n}$) to the whole [0.2 – 20 μm] spectrum.

MOMO is a radiative transfer code that computes the spectral radiances or irradiances monochromatically. Thus, the radiative transfer scheme has to define the spectral intervals that have to be simulated by MOMO. These spectral intervals have to cover the whole spectrum (for this study, the [0.2 – 20 μm] spectrum). The spectral intervals must have a spectral resolution that is high enough to take into account the spectral variation of the different parameters. Thanks to the k-distribution module (KISS: *Doppler et al.* 2013a, *Bennartz and Fischer* 2000, see Figure 8.8), the high spectral variability of the gas absorption coefficient is not a problem: We can define large bands and nonetheless the spectral variability of gas absorption coefficient is considered. It is the same for the spectral variability of the source of radiations (solar for the shortwave and Planck's function for the thermal infrared). Other non-gray parameters are not implemented in the k-distribution: these parameters are the Rayleigh scattering and the aerosol optical properties. The spectral intervals of the radiative scheme have to be defined in consequence: The spectral width of the bands is very narrow in UV and visible, spectral regions in which the Rayleigh scattering and the aerosol optical properties have high spectral

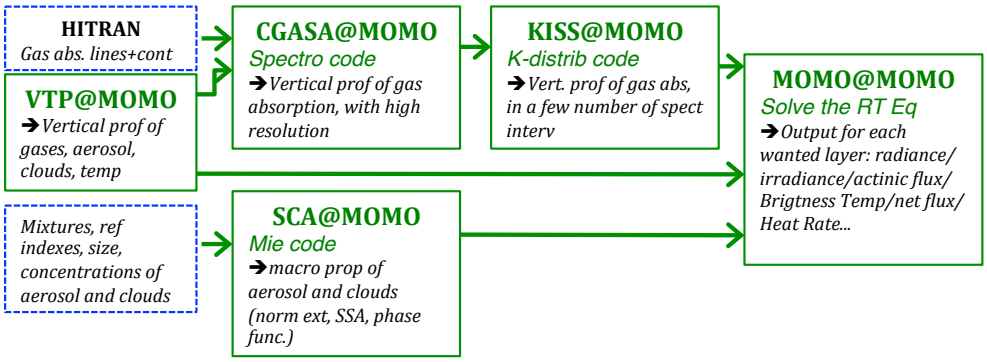

Figure 8.8.: – From *Doppler et al.* 2013b (Figure 1). Schematic view (inputs, outputs, preprocessors) of the structure of radiative transfer code MOMO.

variations.

The width of the bands of the radiative scheme with respect to the wavelength are presented in the table below:

Spectral Region	Width of the bands
200 - 300 nm	1 nm
300 - 400 nm	2 nm
400 - 500 nm	5 nm
500 - 600 nm	10 nm
600 - 800 nm	20 nm
800 - 2000 nm	50 nm
2 - 4 μm	100 nm
4 - 8 μm	250 nm
8 - 14 μm	500 nm
14 - 20 μm	1000 nm

Therefore, the radiative scheme owns 268 spectral bands (234 in shortwave: [200 – 4000 nm] and 34 in longwave: [4 – 20 μm]).

It is necessary to know the spectrum of the refractive indexes of the aerosols. The study of Section 8.3 only provides these values for 7 wavelengths in shortwave. We thus need to extend this information to the whole spectrum. For the wavelengths below 1000 nm, we have enough points of measurements for a spectral interpolation (Approximation 6). For the values over 1000 nm, we do not have any measurements, and we are constraint to take the values of the nearest OPAC category and trust them. This leads to a new approximation (Approximation 6): For the wavelengths above 1 μm, we take the values of the refractive index of the soot aerosols (black

plain line in Figure 8.6) of OPAC category for the pollution aerosol (red dashed line); we take the radiative index of the OPAC mineral aerosols (yellow plain line) for the dust aerosol (blue dashed line).

The vertical distribution of the aerosols given in input of MOMO is the profile of extinction coefficient at reference wavelength (532 nm) taken from in-situ measurements (plotted in green in Figure 8.3). Regarding the aerosol microscopic properties, we assume that for Flight 21, the layers above 2 km contain dust aerosol only (small amount) and the layers below 2 km contain pollution aerosol only (large amount). For Flight 23, we assume that the upper layers (above 1 km of altitude) contain dust aerosols only (large amount) and that the layers below 1 km contain pollution aerosols only (small amount). The ground surface is supposed to be a dark ocean, with a gray albedo of 0 in shortwave, and a gray surface emissivity of 0.98 in longwave. The ocean surface temperature is supposed to be 288.2 K. The water vapor, gas concentration and temperature profile is taken from the US standard atmosphere (*Anderson et al.* 1986).

8.4.2. Results: Heating rates, radiative forcings and radiative forcing efficiencies.

Figure 8.9 shows the vertical profile of instant aerosol additional radiative heating rate for a SZA (solar zenith angle) of 30°. Flight 21 is represented on the left and Flight 23 on the right. The green dashed line is the shortwave radiative heating rate. The blue dashed line is the longwave radiative heating rate. The net (shortwave + longwave) radiative heating rate is in plain red line. TOA (Top of Atmosphere), surface and atmospheric aerosol radiative forcings for shortwave, longwave and net are displayed above the graphs. These are instant radiative forcings for SZA = 30°.

The main difference between the two cases is that for Flight 21 there are 20 % of dust aerosol and 80 % of pollution aerosol. To the opposite, for Flight 23, there are 80 % of dust and 20 % of pollution. Also, the total aerosol optical depth (AOD) is higher for the case of flight 23 (AOD = 0.283) than for flight 21 (AOD = 0.117). The consequence is that there are larger values of heating rates and forcing for the case of flight 23 (e.g. total shortwave radiative forcing is 18 Wm^{-2} for case 23 and 6.2 Wm^{-2} for case 21). The difference of aerosol type plays a large role for longwave heating rate and radiative forcing: For the case with high pollution amount (Flight 21), the values of the longwave forcings are much smaller (0.5, 1.1, -0.6 Wm^{-2}) than

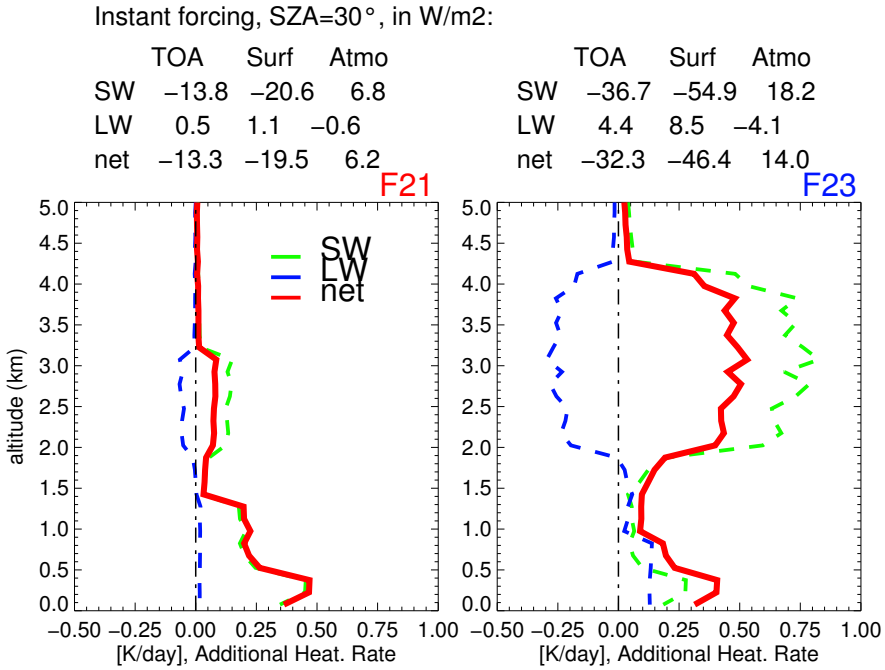

Figure 8.9.: Vertical profile of aerosol additional radiative heating rates and aerosol direct radiative forcing for the case of Flight 21 (left) and of Flight 23 (right). Instant values computed for SZA = 30°. Radiative forcings in Wm^{-2} are displayed above the graph.

the values obtained for the case of high dust amount (Flight 23: 4.4, 8.5, -4.1 Wm^{-2}). This is due to the fact that dust aerosol is a coarser aerosol than the pollution one (the Angström is less small), and the value of the refractive index is larger for the dust in longwave. Thus, dust aerosol absorbs and emits radiation in longwave what pollution aerosols does not. The forcing efficiency (aerosol radiative forcing divided by AOD) is expressed in the table here below (in Wm^{-2}). These values are consistent with the values reported in the literature for similar SZA (*Perrone et al.* 2012, Di *Biagio et al.* 2010; 2009; *Di Sarra et al.* 2011 and references herein).

Case	F21	F23
TOA SW	-117.9	-129.7
TOA LW	4.27	15.55
Surf SW	176.1	194.0
Surf LW	9.4	29.3
Atmo SW	58.1	64.3
Atmo LW	-5.13	-14.5

8.4.3. Spectral analysis of radiative forcing for dust and pollution.

In order to understand the difference between dust aerosol and pollution aerosol regarding their radiative impact, we computed two artificial cases: We give in input for both cases the same vertical profile of aerosols, and the same total AOD (0.2 at 532 nm). The only difference is that for one case, there is pollution aerosol only, and for the other case, dust aerosol only. We show on Figure 8.10, the spectral aerosol radiative forcings of the aerosol in $\mathrm{Wm}^{-2}\mu\mathrm{m}^{-1}$. Red lines represent the pollution aerosol and blue lines represent the dust aerosol. TOA, surface and atmosphere spectral radiative forcings are plotted.

This figure allows to understand the results found in subsection 8.4.2: In contrary to pollution aerosol, dust aerosol has a non-negligible radiative forcing in the thermal infrared (longwave). This radiative impact of dust aerosols in longwave is due not only to the absorption and emmission, but also to the scattering (*Dufresne et al.* 2002). Pollution aerosol has a higher radiative forcing in the shortwave, but for wavelengths larger than 1 μm its radiative influence is insignificant. These observations show that the knowledge of optical properties of the pollution aerosol is only mandatory for UV, solar and near IR spectral ranges. Dust aerosol, on another side, has a radiative impact all along the spectrum and its optical properties have to be known from 0.2 to 2 μm and from 7 to 15 μm.

8.5. Discussion of the approximations done in this study.

Approximation 1: *We can interpolate the values of the scattering coefficient from the three wavelength of the nephelometer (450, 550, 700 nm) to the lidar wavelength (532 nm).*

Discussion: In general, 3 wavelengths is something few for an interpolation. But here, very qualitatively speaking, because 532 nm (the lidar wavelength) is close to 550 nm (one of the wavelengths of the nephelometer), the error done with the interpolation should not be excessive.

Aproximation 2: *The aerosol vertical profile can be divided in 2 or 3 layers having homogeneous lidar ratio, single scattering albedo, and aerosol microscopic properties (size distribution, refractive index).*

Discussion: The consequence of the dynamic of the atmosphere is that the aerosols of a same kind and origin are spatially distributed in plumes. In a 1-D

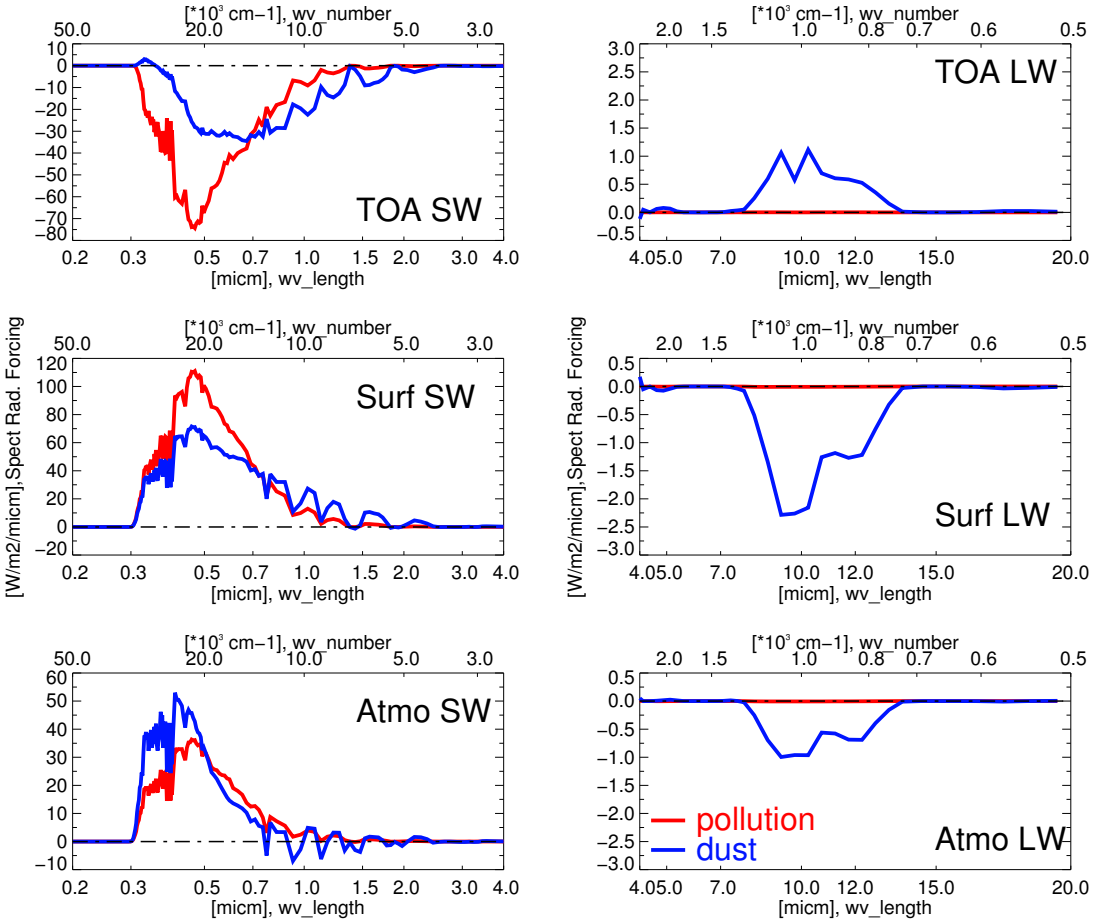

Figure 8.10.: Spectral distribution of the radiative forcing for theoretical vertical distribution of pure pollution aerosol (red), and pure dust aerosol (blue) with an AOD of 0.2 at 532 nm. Left figures are for shortwave and right figures for longwave. Top figures represent the TOA radiative forcing; middle, the surface radiative forcing; and bottom the atmosphere radiative forcing. The values have been computed for SZA = 30°.

model, that means that the aerosols of a same kind (composition, size distribution, optical properties) are grouped in layers. If the layers' vertical positions are well defined, it is therefore correct to assume that the optical properties of the aerosols are homogeneous in each layer.

Approximation 3: *We simulate the dust particles with a Mie code even if there are not spherical particles.*

Discussion: Dust particles are not spherical (*Volten et al.* 2001). This has an influence on the relation between microscopic (size distribution, refractive index) and macroscopic (SSA, lidar ratio, phase functions) properties of the aerosols, that cannot be computed by a Mie code without doing some mistakes. For non-spherical particles, other numerical methods than Mie code exist to compute (SSA, p, P) from (size distribution, refractive index). *Mishchenko* 2000 summarized all the existing methods. The most famous one is the T-matrixes method (*Waterman* 1965). More modern alternatives exist (e.g. Ray tracing approximation: *Macke et al.* 1995).

The values of the phase function for the large backscattering directions are especially different for non-spherical particles if they are computed with a Mie code or an exact method. Errors due to the spherical approximation can reach 50 % (*Raut* 2008) for the phase function at 180° (p_π), thus for the lidar ratio. *Dubovic et al.* 2006 show that the 'Mie-error-ratio' p_π(computed with Mie method)/p_π(exact) is between 1.5 and 2.5 depending on the orientation of the dust aerosol particles. For the optical closure of this study, for the dust aerosol, we search with the 2-D dichotomy, not the lidar ratio $P = 43$ sr obtained with the LIExI method but a Mie lidar ratio: $P_{\mathrm{mie}} = P/2$ (supposing the ratio due to the Mie error equal to 2). The value of the real index of refraction is the only parameter that could have an error of more 20% due to the uncertainty on the estimate of the Mie-error-ratio.

Approximation 4: *The real refractive index of the aerosols is supposed to be spectrally constant on the [350 – 1000 nm] interval.*

Discussion: This approximation is verified for each tabulated class of aerosols. There is no database in the literature that says the contrary. This is not the principal a source of errors in this study (see sensitivity study in Chapter 9).

Approximation 5: *The refractive index of the aerosols can be interpolated from the dataset {370, 470, 520, 532, 590, 660, 880, 950 nm} to the whole [200 – 1000 nm] spectral range.*

Discussion: The panel of wavelengths is complete enough to make a solid interpolation. Maybe only the values between 200 nm and 370 nm will have larger differences compared to the reallity, because we need to extrapolate for this interval.

Approximation 6: *For the [1 – 20 μm] spectrum: We assign the values of the refractive index of the soot aerosol of OPAC database to the pollution aerosol of Flight 21; and the refractive index of the mineral aerosol of OPAC database to the dust aerosol of Flight 23.*

Discussion: This approximation is questionable: The refractive indexes estimated in shortwave with the optical closure, are rather different from the refractive indexes of the OPAC categories. There is therefore no reason that the refractive indexes of the TRAQA aerosols in longwave fit the OPAC refractive indexes. A sensibility study of the sensitivity on the radiative forcings to the imaginary refractive index over 1 μm is presented in Chapter 9. Nevertheless, Figure 8.10 shows that this approximation has a radiative consequence only for dust aerosol: Pollution aerosol does not have any radiative influence for wavelengths larger than 1 μm.

Another phenomenon that has not been discussed is the hygroscopy: Aerosol absorbs water vapor and this changes their microscopic properties (size distribution, refractive indexes). Also, because the analysis of the in-situ instruments are not done in the same conditions of humidity and temperature as in the layers, the results of the measurements (size distribution for example) differ sometimes from the reality (*Ferrare* 1998, *Hänel* 1976, *Raut and Chazette* 2007). These effects have not been taken into account in this study, but the sensibility study about the aerosol size presented in Chapter 9, will allow to quantify the possible errors that this approximation could cause.

Synthesis and conclusions of the case study.

We have developed a method of optical closure that allows to characterize the aerosols. This method is based on the synergy between in-situ measurements (nephelometer, aethalometer, PCASP instrument for the size distribution), and lidar measurements. The result of the optical closure is the estimation of the refractive index of the aerosols at 7 wavelengths in UV, visible and near infrared. This allowed the characterization of 2 kinds of aerosols for a case study during the TRAQA campaign. These aerosols are: pollution aerosol of the Pô Valley and dust aerosol transported at continental distance from the Sahara.

With the help of literature databases, we extended these properties to the whole spectrum, and realized a radiative study. The results of the radiative study are the vertical profile of radiative heating rates for two cases during the TRAQA cam-

paign. The main differences between these two cases are due to the predominance of the pollution aerosol for the first case (Flight 21), and the predominance of the dust aerosol for the second case (Flight 23). The results are not surprising: the dust aerosols have a spectral signature in longwave that is visible on the radiative heating rates profiles and in the estimation of the longwave direct radiative forcings. A theoretical study points out the spectral influence of pollution aerosol of the Pô Valley and dust aerosol on the radiative forcing. This study shows that pollution aerosol has a strong radiative impact between 0.2 and 1 μm, and no impact at all wavelengths larger than 1 μm. Dust aerosol on the contrary has a radiative impact from 0.2 to 2 μm, and between 7 and 12 μm.

This study has used a lot of approximations that have been discussed but not yet quantified (some of them will be quantified in next chapter). This discussion about the approximations points out that the radiative impact of the aerosols depends on many parameters. It is important to be able to estimate the sensitivity of the radiative forcing to these parameters. This sensitivity study will be presented in the first section of next chapter: The sensitivity of the radiative forcings to aerosol size distribution and to the values of the real and imaginary part of the refractive index will be discussed.

The study presented in this chapter has been done in collaboration with Claudia Di Biagio (Laboratoire Interuniversitaire de Sciences Atmospheriques: LISA). I kindly thank Claudia for providing the nephelometer and PCASP data (SSA, nephelometer extinction coefficient and aerosol size distributions). The method presented in this chapter will be applied to other pollution aerosols observed during TRAQA (e.g. pollution aerosols from Barcelona and Marseille urban areas).

9. Uncertainties in the estimates of aerosol radiative forcings: A sensitivity study.

In this chapter we explore some sources of uncertainties on the estimation of the radiative impact of the aerosols. In a first step, we will discuss how the radiative transfer scheme can lead to errors in the estimates of aerosol radiative forcing: We will analyze the conclusion of AEROCOM radiative transfer code intercomparison experiment, to which MOMO took part. Section 9.2 shows the results of tests about the sensibility of aerosol instant radiative forcings for the two cases presented in case study of Chapter 8. The sensibility on the aerosol radiative forcings to the aerosol refractive indexes (real and imaginary part) and to the aerosol size distribution are quantified. In Section 9.3, we will discuss how the presence of clouds below aerosol layers can influence the TOA aerosol radiative forcing.

9.1. Sensitivity to the radiative transfer code and scheme: AEROCOM experiment.

9.1.1. Aerosol Model Intercomparison Initiatiative (AEROCOM).

AEROCOM (Aerosol Model Intercomparison Initiative) is a project that strives for a better understanding of the aerosols contribution to the global radiation budget. AEROCOM organized many experiments of models' comparisons. The purpose of each experiment is to isolate a precise parameter and to estimate the uncertainty due to this parameter on the aerosol global radiative forcing. For example, *Textor et al.* 2006 were focused on the characterization of aerosol life cycles; *Kinne et al.* 2006 point out the importance of the initial assessment of optical properties of aerosols on global models; *Koch et al.* 2009 were specialized in the black carbon implementation in global model; and *Huneeus et al.* 2011 compared the dust global models.

9.1.2. Article *Randles et al.* 2013, an AEROCOM experiment that compares radiative transfer schemes.

The experiment presented by *Randles et al.* 2013, is focused on the influence of the radiative transfer scheme on the estimate of shortwave aerosol radiative forcing. *Randles et al.* experiment is the continuity of former studies: *Halthore et al.* 2005, *Fouquart et al.* 1991. 31 different radiative transfer codes took part in the experiment and MOMO was one of them. Many simple simulations have been proposed: Clear air computations (top of atmosphere and bottom of atmosphere integrated

fluxes) and computations with aerosols (with a given Angström, SSA and geometric factor) should be achieved for two solar zenith angles (SZA = 30° and 75°) and two kinds of atmospheres (subarctic winter SAW and tropical). The radiative fluxes and the aerosol radiative forcings obtained with the 31 different codes have been compared. The fluxes are reported at two spectral bands: SW broadband (200 – 4000 nm) and UV-Visible (200 – 700 nm). Two types of aerosols are considered: scattering aerosols (SSA = 1) and absorbing aerosols (SSA = 0.8).

9.1.3. Personal contribution to the article and MOMO performances.

This experiment was totally in the thematic of this PhD work: Improving the understanding of the radiation budget by improving the radiative transfer simulations. Therefore, a part of this PhD work was devoted to take part to the experiment of *Randles et al.* 2013. Radiative transfer simulations of the experiments have been done by myself for MOMO (code number 31 in the article) as well as the redaction of the code's description (Appendix A28, page 2375 in the article).

MOMO succeeded in having results close to the reference codes of the experiment, namely the line-by-line codes GENLN2-LBL using DISORT methods with 16 streams and RFMD using DISORT with 4 streams.

The values computed by MOMO for SZA = 75° of the broadband downward direct fluxes at the surface were wrong when the article has been submitted. This problem has been solved in a post-experiment simulation, using the most advanced version of CGASA for the spectroscopy computing and a high-resolution solar irradiance model (*Kurucz* 2005). However, for UV-Vis band, or for both bands and SZA = 30°, MOMO is in the standard deviation band of the models' dispersion, and always in the group of codes containing the reference codes. That means that MOMO does not create any systematic bias in this experiment.

The performances of MOMO for SZA = 30° and for the SW broadband [200 - 4000 nm] case of the downward fluxes are summarized in Table 9.1. The experiment (type of atmosphere and of aerosol) is described in the first column. The value of the downward flux computed by MOMO is presented in the second column. The bias in % (third column) between MOMO and the average of the fluxes (only for the group of accurate results) can be compared to the standard deviation in % of the group of accurate results (fourth column).

9.1.4. Conclusions about the influence of the radiation scheme on aerosol radiative forcing estimates.

This study has demonstrated that the dispersion between the codes in SW broadband and not in UV-Vis band is stronger for the tropical atmosphere than for the SAW atmosphere. Difference between codes can reach 6%. The interpretation is that the water vapor is not treated equally by all the codes. This reinforces the idea that water vapor modeling is a crucial parameter for radiation budget computations. For clear air, the largest intermodal flux differences observed in the experiment is for the downward diffuse fluxes. For aerosol cases, the largest inter-models differences occur for TOA radiative forcing for the case of scattering aerosols and low SZA (The diversity between the models is 15 %). The method used to model the multiple scattering is in cause. Two-streams models fail for these cases. This demonstrate the necessity to use an advanced radiative transfer code for simulations in scattering media.

The conclusion of this study is that the radiation scheme's improvement is a necessary (even if not sufficient) step for good estimates of aerosol radiative forcing. Errors in the radiative transfer scheme can lead to 6 % errors on the fluxes estimates for clear air cases (essentially due to the modeling of water vapor and clear air scattering) and to 15 % errors for media with scattering aerosols. Nevertheless, for aerosol radiative forcing, other parameters are very important, e.g. the aerosol parameterization due to its characterization (*Boucher et al.* 1998). This is the purpose of next section.

9.2. Sensitivity to the microscopic properties of aerosols characterized within TRAQA campaign.

Within the case study of Chapter 8 we estimated the aerosol radiative forcings. This radiative study, needed aerosol microscopic properties as input of the radiative transfer code MOMO. These microscopic properties are the aerosol size distribution and the aerosol refractive index (real and imaginary part: Re($\widetilde{n}$) and Im($\widetilde{n}$)). Within this section, we quantify the impact on the values of the radiative forcings due to a large error in the estimate of the microscopic properties of the aerosols: We realize a sensitivity study for the aerosol radiative forcings to aerosol size distribution and to aerosol refractive index.

Experiment	Flux MOMO (Wm^{-2})	Bias MOMO-Avg (%)	Std dev all accurate (%)
No aer TROP	906.1	0.5	1.2
No aer SAW	998	0.2	1.4
Abs TROP	891.6	0.5	1.2
Abs SAW	983	0.3	1.5
Scat TROP	853.3	0.6	1.3
Scat SAW	942.7	0.4	1.5

Table 9.1.: Summary of MOMO performances for SZA = 30° in AEROCOM experiment (*Randles et al.* 2013). For surface downward fluxes, broadband ([200 - 4000 nm]. *Avg* is the average of the more accurate fluxes of the experiment. *Std deviation* is the standard deviation of all the more accurate fluxes of the experiment. *TROP* = tropical atmosphere, *SAW* = Subarctic winter atmosphere. *No aer* = without aerosols, *abs* = with absorbing aerosols, *scat* = with scattering aerosols

9.2.1. Sensitivity to aerosol size.

We compute the radiative forcings of Figure 8.9, and compare the radiative forcings to radiative forcings computed for an aerosol having the same values of refractive index but a twice larger modal radius. For the sensitivity study, the factor of change in the particle size should be large enough to observe a difference compared to the original case, but small enough so that the aerosol stays in the same class (fine particles should not become coarse particles); therefore, we choose to take a factor of 2. Histograms of figures 9.1, 9.2, 9.3, and 9.4 show the radiative forcings for the initial case presented in chapter 8 (blue bars) and for twice larger aerosols in radius (red bars). Doubling the radius of the aerosol does not significantly change the TOA shortwave radiative forcing of the pollution aerosol (see results for flight 21 on Figure 9.1 left) but consequently reduces the TOA shortwave radiative cooling of dust aerosols (see results for flight 23 on Figure 9.1 right). The relative difference on TOA longwave radiative forcing (Figure 9.2) is significant (+ 90 % for flight 21 and + 80 % for flight 23), but the absolute difference is not large for case 21. An interpretation of this last observation is that doubling the aerosol radius keeps the pollution aerosol (80 % of the aerosols of case 21) in a small particle category (thus an aerosol with no radiative impact in longwave), and the differences observed on the TOA longwave forcing for case 21 are only attributed to dust aerosols. Dust aerosols are already coarse particles before the size doubling, and doubling their size makes them absorbing and emitting more radiation in longwave. The same

comments and analysis can be done for the atmospheric longwave radiative cooling shown in Figure 9.4. Figure 9.3 shows that doubling the radius of the pollution aerosols does not change the absorption of the aerosols in shortwave (see atmosphere radiative forcing of Flight 21, on Figure 9.3, left). On the opposite, dust aerosol seems to have a different behavior when the particles are twice larger in radius (the atmospheric absorption is increased of 50 % for the case of Flight 23).

9.2.2. Sensitivity to real part of aerosol effective refractive index: Re($\widetilde{n}$).

We make varying the real part of aerosol effective refractive index. The variation is an increase of 0.1 of Re($\widetilde{n}$). The value of 0.1 corresponds to the maximum spectral variation that we can observe in OPAC for all categories of aerosols in the [0.3 -3 μm] spectrum range. A change in the real part of the refractive indexes (Re($\widetilde{n}$) = Re($\widetilde{n}$) + 0.1) does not lead to large changes in the radiative forcing (compare blue bars to green bars on the figures): Only the shortwave TOA radiative forcing is changed by more than 5 % if the real part of the refractive index is increased of 0.1, and this is only the case for Flight 23 (see Figure 9.1, right) that is a case with a large dust aerosols amount. These results justify the choice of Approximation 4 of Chapter 8: even if the real part of the refractive index is not gray in UV and visible as suggested in Chapter 8, the impact on the aerosol radiative forcings of a variation of Re($\widetilde{n}$) value is not something significant.

9.2.3. Sensitivity to imaginary part of aerosol effective refractive index of: Im($\widetilde{n}$).

We make varying the imaginary part of aerosol effective refractive index. The variation is a doubling of Im($\widetilde{n}$). It corresponds to the maximal error that we can do by approximating Im($\widetilde{n}$) of observed aerosol with tabulated values for the spectral domains in which we do not have any measurements (see Chapter 8). A change in the imaginary part of the refractive index (Im($\widetilde{n}$) = 2$\times$Im($\widetilde{n}$)) leads to large differences for the TOA longwave radiative forcings (compare blue bars to purple bars on figures 9.2 and 9.4). Doubling Im($\widetilde{n}$) for pollution aerosols does not make pollution aerosols absorbing and emitting in longwave but the dust aerosols (also present in a small amount during case 21) absorb and emit more if Im($\widetilde{n}$) is doubled and the TOA radiative warming is increased for both cases 21 and 23 (Figure 9.2). We have the same interpretation for atmosphere longwave radiative cooling (Figure 9.4). The atmosphere shortwave radiative warming (Figure 9.3) is increased by more than 40

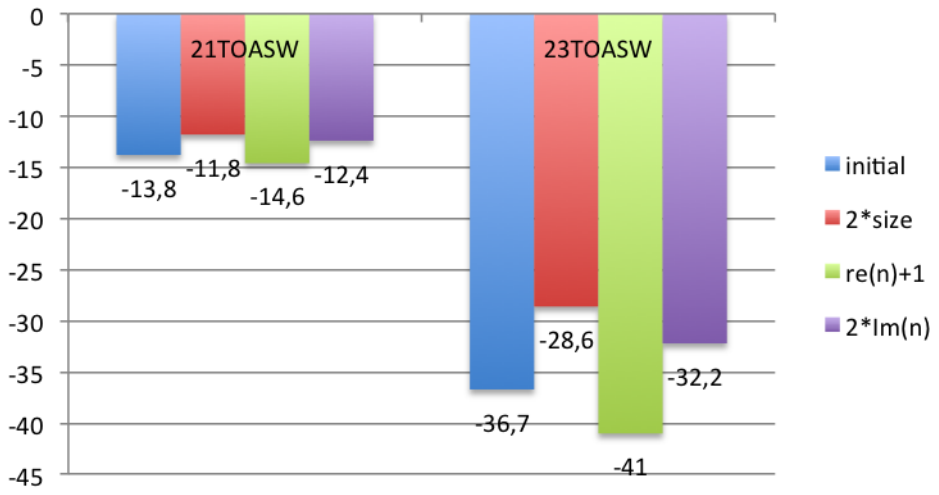

Figure 9.1.: Sensitivity study for the TOA shortwave radiative forcing. All values are in $\mathrm{W m^{-2}}$. Left, case of Flight 21; right, case of Flight 23. Blue, forcing with initial (from Chapter 8) composition; red, forcing for a size distribution with twice coarser (in radius) aerosols; green, forcing for a Re($\widetilde{n}$) increased of 1; purple, forcing for a twice larger Im($\widetilde{n}$).

% for both cases 21 and 23, when Im($\widetilde{n}$) is doubled. Both kinds of aerosol (pollution and dust) are concerned by the change in atmosphere shortwave radiative forcing due to the doubling of Im($\widetilde{n}$). This is not a surprise, because the larger is Im($\widetilde{n}$), the larger is the aerosols' absorption, and therefore the larger is the atmospheric absorption.

9.2.4. Conclusions of the sensitivity study to aerosol characterization.

The sensitivity study presented in this section shows that a significant change (doubling the modal radius) in the size distribution, leads to a significant change of the radiative forcings for both cases (case 21 and case 23), but only because of the influence of the size for dust aerosol. The radiative forcings of pollution aerosol does not seem to be influenced by the doubling of the modal radius.

The real part of the refractive index is not a critical parameter: An increase of 0.1 of Re($\widetilde{n}$) does not lead to significant changes on the radiative forcings especially in shortwave. This put in perspective the importance of the Approximation 4 of Chapter 8: *'the real part of the refractive index is supposed gray between 0.2 and 1 μm'*. Even if this approximation is wrong, the consequences on the radiative forcings

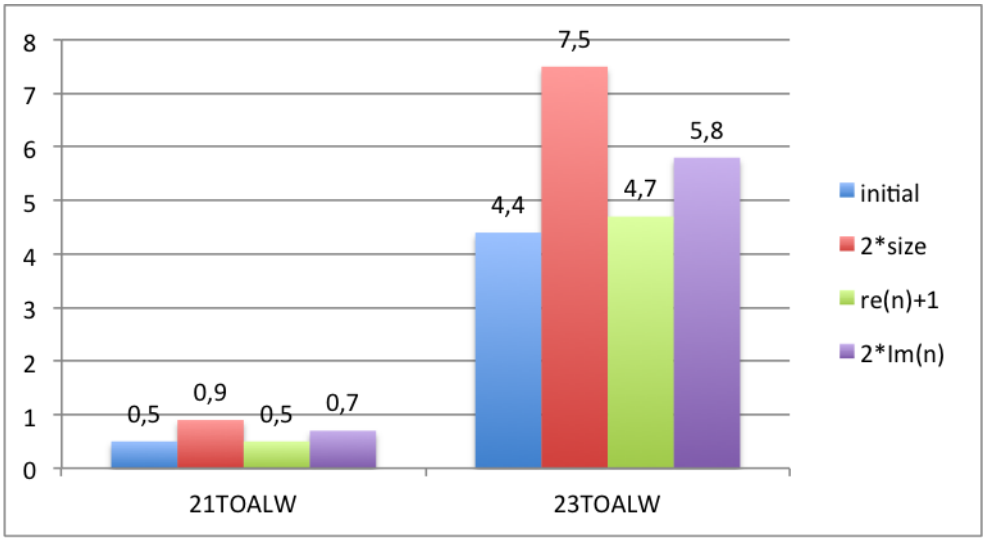

Figure 9.2.: Sensitivity study for the TOA longwave radiative forcing. Values in Wm^{-2}.

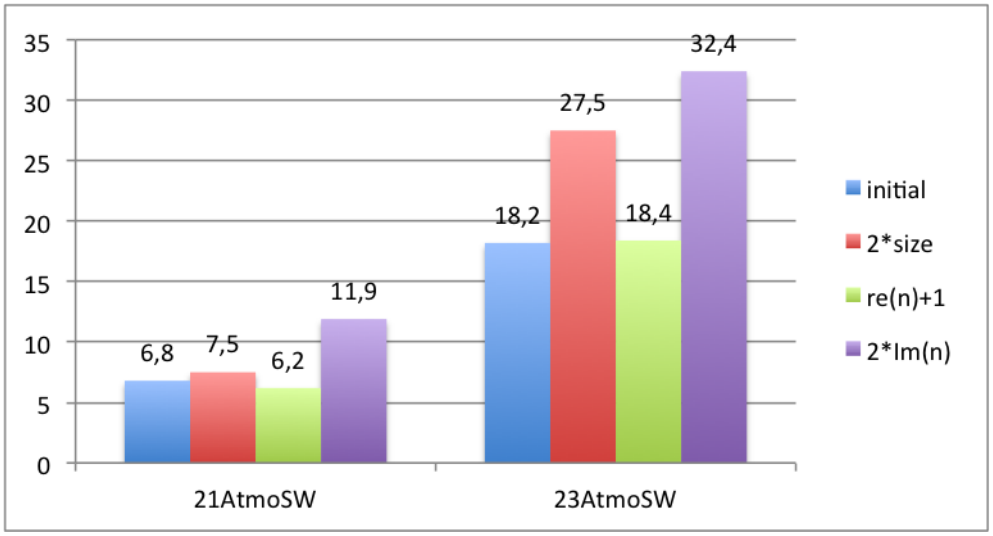

Figure 9.3.: Sensitivity study for the atmosphere shortwave radiative forcing. Values in Wm^{-2}.

are limited.

The imaginary part of the refractive index has a high influence on the aerosol absorption; thus, the TOA and atmosphere longwave radiative forcings are significantly increased when we double $\mathrm{Im}(\widetilde{n})$. Also the atmosphere shortwave radiative forcing is increased, because the aerosol absorbs much more radiation when $\mathrm{Im}(\widetilde{n})$

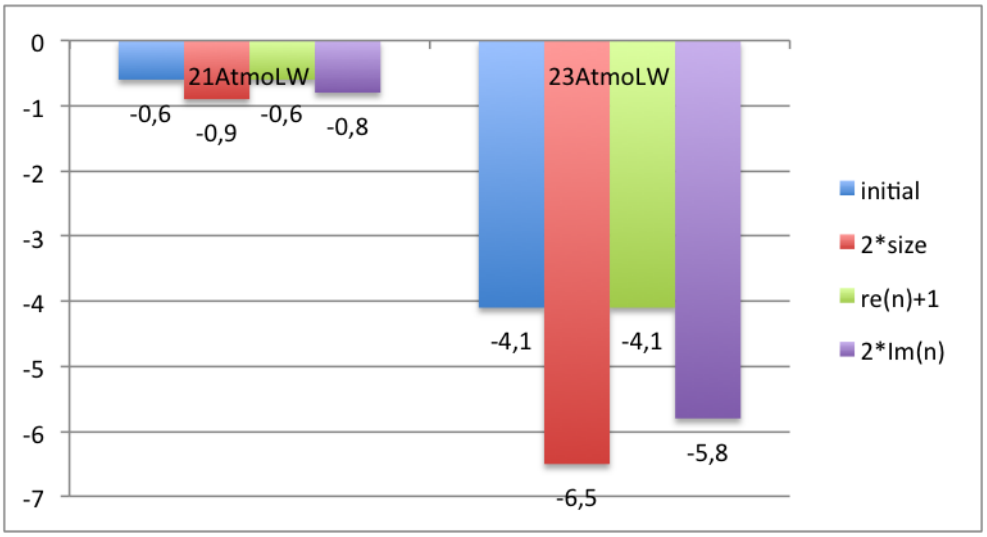

Figure 9.4.: Sensitivity study for the atmosphere longwave radiative forcing. Values in $\mathrm{W m^{-2}}$.

is doubled.

These results bring information about which parameters have do be estimated precisely during the measurement campaigns: We should pay more attention to the retrieval of Im($\widetilde{n}$) than for Re($\widetilde{n}$). Uncertainties on the estimation of the size distribution for pollution aerosols do not have any impact on the radiative study, contrary to the cases with dust aerosols, for which precision about the size distribution is a necessary condition of an accurate radiative study. A precise aerosol parameterization takes also the environment of the aerosols into account. Next section will answer the question: How clouds can change the radiative forcing of absorbing aerosols?

9.3. Sensitivity to the aerosol environment: aerosol plumes above clouds.

9.3.1. Absorbing aerosols above clouds.

In this section, we study the radiative influence of clouds below absorbing aerosols. The considered aerosol is very absorbing: It is an aerosol built as a mixture of 3 OPAC categories: a mix of water soluble (21.4 % in particles' quantity), insoluble (0.12 %) and soot (78.6%). This mixture is what we expect biomass burning aerosol

to be. The altitude of the plumes containing this type of aerosol is usually high enough (at least 1.5 – 2 km of altitude) to be above the low clouds layers. A computation with the Mie code of preprocessor SCA of MOMO gives the associated phase function and SSA, and the normalized extinction coefficient ext_{norm} (see Equation 9.1).

$$ext_{\mathrm{norm}}(\lambda) = \beta_e(\lambda)/\beta_e(\lambda_{\mathrm{ref}} = 550\,\mathrm{nm}) \tag{9.1}$$

From the phase function, we can compute the asymmetry parameter g that characterizes the relative importance of the front to back scattering (see Equation 9.2).

$$g = \int_{\theta=0}^{\theta=\pi} p(\theta, 0) \cdot sin(\theta)\, d\theta \tag{9.2}$$

SSA, ext_{norm} and g for the whole [0.2 – 20 μm] spectrum are displayed in Figure 9.5. One can see that the aerosol that is studied does not have any significant radiative impact for wavelengths larger than 2 μm (ext_{norm} vanishes when lambda increases). Also, this aerosol is really absorbing (the SSA is between 0.6 and 0.75 in the spectral interval 0.2 – 2 μm).

Aerosols (even absorbing ones) over ocean have a negative radiative forcing at the TOA. This is because aerosols do not only absorb the radiation, but also scatter a part of it back to the TOA. Thus, the presence of aerosols increases the albedo of the Earth and atmosphere system. If under the aerosol plumes there is a surface that is more reflecting or scattering than the aerosols, the problem is different. This is the case for low dense clouds below aerosol plumes (*Haywood and Shine* 1997, *Haywood and Boucher* 2000). Low clouds scatter much more the radiation than aerosols do. Thus, the albedo of the Earth and atmosphere system with low dense clouds is higher when there is no aerosol than when there are high absorbing aerosol plumes, like biomass burning aerosols. In the following subsection, we will quantify the TOA aerosol radiative forcing for different aerosol and cloud optical depths.

9.3.2. Sensitivity to AOD and COD.

We realize a theoretically study with a cloud layer between 0.5 and 1.5 km of altitude and an aerosol layer between 1.5 and 3.5 km. We compare the TOA aerosol radiative forcings for different AOD (Aerosol Optical Depth) varying between 0.05

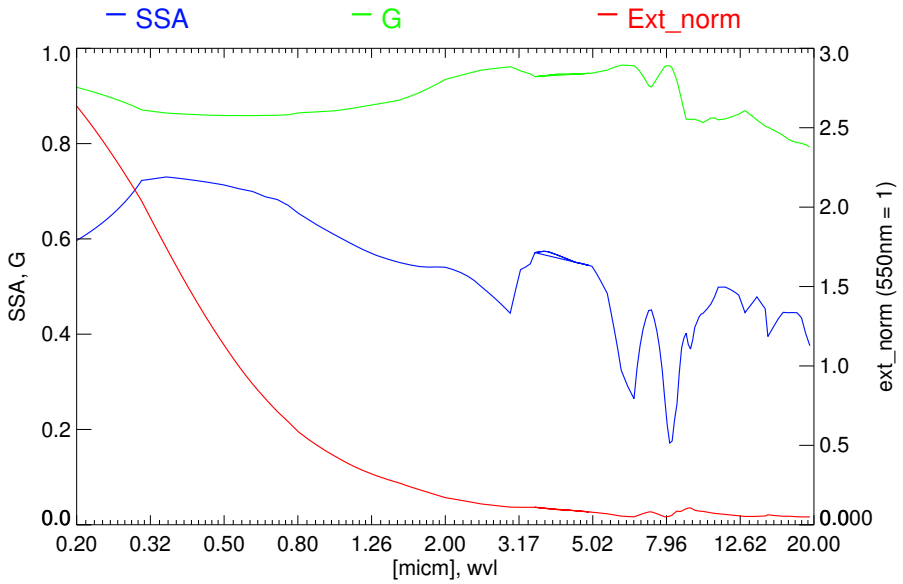

Figure 9.5.: Spectrum of the macroscopic properties of the aerosol used for the study 'aerosol above clouds' and for the case study of Guinea Bay aerosols (Chapter 10). Blue line: Single scattering albedo (SSA). Green line: asymmetry factor (g). Red line (y axis is on the right): Normalized extinction coefficient ext_{norm} (Ext_norm).

and 0.2 and different COD (Cloud Optical Depth) varying between 0 and 9. Figure 9.6 shows the results for the shortwave aerosol radiative forcing (instant radiative forcing for SZA = 30°) and Figure 9.7 shows the results for aerosol longwave radiative forcing. Longwave radiative forcing is insignificant compared to shortwave radiative forcing. This is not a surprise, knowing the nature of the aerosol (biomass burning aerosol). The fact that this aerosol does not have a longwave radiative impact was already quantified with its low ext_{norm} coefficient for wavelengths larger than 2 μm (Figure 9.5). Figure 9.6 summarizes the sensibility of TOA radiative forcing of absorbing aerosols to the presence of low cloud layers: Without clouds (COD = 0, left column): The aerosol has a negative radiative forcing and the strength of the forcing increases with the AOD. When there are some clouds below the aerosol plume (COD different from 0), the aerosol has a positive radiative forcing. The higher is the AOD the higher is the radiative forcing, because aerosols absorb more the radiation. The higher is the cloud optical depth, the higher is the aerosol ra-

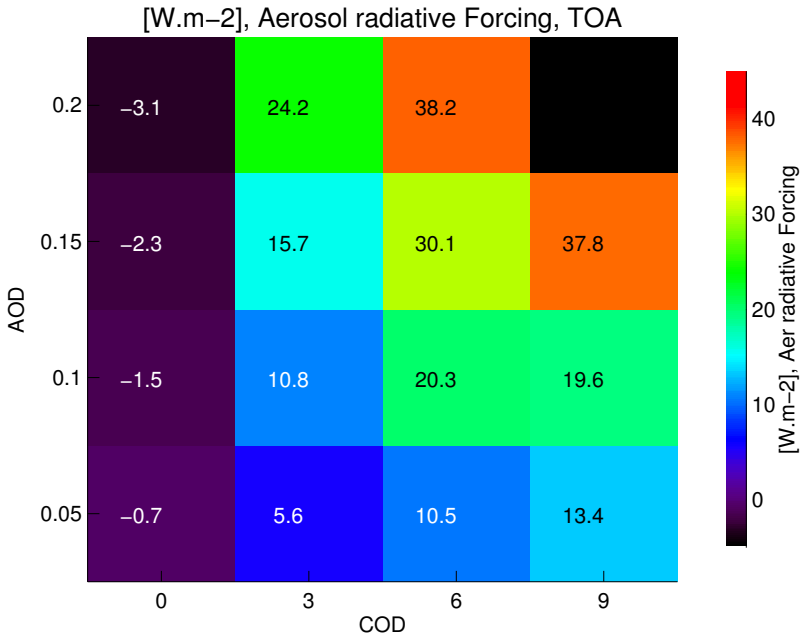

Figure 9.6.: Shortwave TOA radiative forcing of absorbing aerosols above clouds for different COD and AOD.

diative warming, because the clouds reflected more radiation in the direction of the atmospheric layer and aerosols can absorb this reflected radiation. Without clouds, the TOA radiative cooling of the aerosols varies from 0.7 to 3.1 Wm^{-2} for an AOD varying between 0.05 and 0.2. With clouds, the TOA radiative warming varies from 5.6 to 38.2 Wm^{-2} for COD varying between 3 and 9 and AOD varying between 0.05 and 0.2.

Synthesis and outlook

Within this chapter, we analyzed different sources of uncertainty for aerosol radiative forcings. These sources of uncertainty are: The size distribution, the values of the refractive index (real part and imaginary part) put in input of the radiative transfer model (RT model); the RT model itself and the RT scheme used by the RT model; and the presence of low clouds below the aerosol plumes. The uncertainties have been quantified: The size of the particles is a critical parameter for dust aerosol. The real part of the refractive index $\mathrm{Re}(\widetilde{n})$ has a minor influence (for a

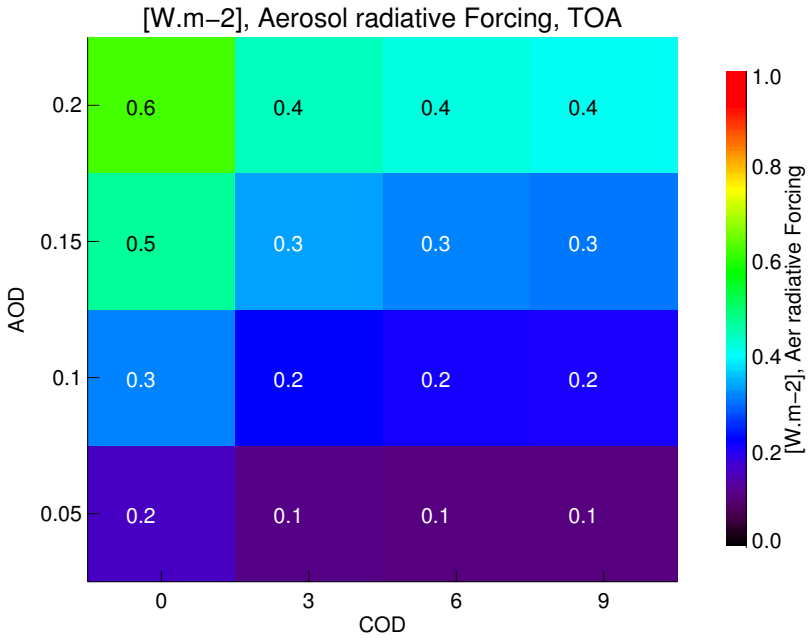

Figure 9.7.: Longwave TOA radiative forcing of absorbing aerosols above clouds for different COD and AOD.

slight ± 0.1 variation of $\mathrm{Re}(\widetilde{n})$) on the aerosol radiative forcing. The imaginary part of the radiative index $\mathrm{Im}(\widetilde{n})$ is the parameter of influence for the aerosol absorption, thus, the atmosphere aerosol radiative forcing is sensible to this parameter.

Differences on the forcing due to the use of different radiation transfer schemes can reach 15 % (so the AEROCOM experiment). MOMO's performances (except for the spectroscopy / solar constant problem for SZA = 75°) in the AEROCOM experiment has proofed its ability to simulate the broadband shortwave radiative forcing for absorbing and scattering aerosols.

The theoretical experiment of Section 9.3 shows that the radiative forcing of absorbing aerosols is really sensible to the presence of low clouds above the aerosol plumes (the presence of low clouds changes the sign of the TOA radiative forcing of the aerosols) and to the value of the cloud optical depth.

Other parameters could be test for a sensitivity study of aerosol radiative forcing: Surface albedo, aerosol hygroscopy, aerosol mixing with other kinds of aerosols, aerosol shape and orientation... These can be the topic of further researches. During this chapter we focused on the parameters that are supposed to be uncertain

within the case studies that we presented.

10. Spatialisation of the radiative study

The case study presented in Chapter 8 is done for a 1-D profile of the atmosphere. As explained in the introduction, one finality of this work is to estimate the radiative impact of the aerosols at a regional scale. The 1-D radiative studies must be therefore extended to larger spatial areas. Section 10.1 will present a first step of this extension with a study of the radiative impact of the aerosols along a 7500 km long lidar track. Within this case study, the additional radiative heating rates of the aerosols and the aerosol radiative forcings are estimated along the track of the lidar CALIOP on board of CALIPSO satellite in the Guinea Bay in summer 2007. In a second step (Section 10.2), we will discuss how to extend the radiative study to a regional scale, for a whole region like the Mediterranean basin.

10.1. Extended 1-D radiative study: absorbing aerosols above clouds along A-train track in the Guinea bay.

10.1.1. Scientific objectives: absorbing aerosols above clouds in the Guinea Bay.

We study the radiative effect (direct radiative forcing and vertical profile of additional heating rates) of absorbing aerosol above liquid water clouds in the Gulf of Guinea. The radiative transfer code used for this study is Matrix Operator Model (MOMO) and the dataset given in input of MOMO is obtained with a synergy between A-train instruments. The aim of this study is to estimate the radiative impact of the aerosols, not only limited to a 1-D column (like in case study of Chapter 8), but for many 1-D columns all along the track of CALIPSO's lidar CALIOP. Hence, many different cloud and aerosol vertical distributions are observed and the radiative fluxes are computed for all these different configurations. The case study presented here is localized in a CALIOP track in the Guinea Gulf, between latitude - 30° and + 5°, on the 11th of August 2007. The aerosol that is observed is a biomass-burning aerosol in a plume overlying the low clouds layers.

10.1.2. Synergy of spaceborne instruments.

An instrumental synergy is used to provide the whole input material: The instrument MODIS (Moderate Resolution Imaging Sopectrometer) of NASA satellite Aqua provides the total COD, for wavelength $\lambda = 550$ nm; the lidar CALIOP (Cloud-Aerosol Lidar with Orthogonal Polarization) on board of NASA-CNES satel-

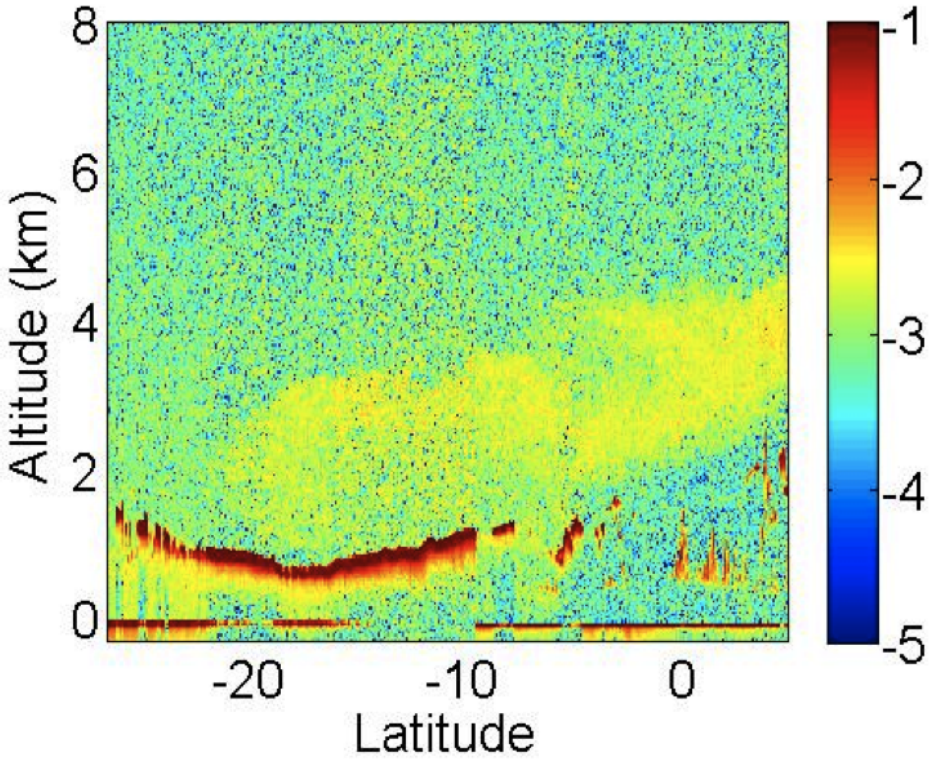

Figure 10.1.: From D. Josset - Aerosol (and cloud) vertical profile of extinction coefficient. Obtained with spaceborne lidar CALIOP on board of satellite CALIPSO. Colorbar: Aerosol extinction coefficient (in km^{-1}).

lite CALIPSO (Cloud and Aerosol Lidar and Infrared Pathfinder Satellite Observation) provides the aerosol extinction coefficient at $\lambda = 532$ nm, over the clouds (*Hu et al.* 2007) or over the ocean (*Josset et al.* 2008). The vertical profile of aerosol extinction coefficient along the whole CALIOP track is plotted on Figure 10.1. The cloud vertical distribution is provided by the radar CPR (Cloud Profiling Radar) on board of Cloudsat satellite.

The main advantage of this synergy is that all the data are collocated and quasi synchronized because all the instruments that are used are on board of satellites of the A-Train constellation (see Figure 1.2 in Chapter 1). This case study allows to apply to a real case the theoretical study of Section 9.3 that has estimated the TOA radiative forcing for a set of AOD and COD.

10.1.3. Radiative transfer parameterization.

The aerosol mixture is the same as the one presented in the theoretical study of Section 9.3: a model of biomass burning aerosols mixing different OPAC aerosol classes: water soluble (21.4 % in particles' quantity), insoluble (0.12 %) and soot (78.6%). The spectrum of macroscopic properties (SSA, g and ext_norm) is displayed on Figure 9.5. Cloud microscopic properties are taken from OPAC maritime cumulus category. Water vapor, gases, ozone, and temperature vertical profile are taken from GMAO data (Global Modeling and Assimilation Office of NASA Goddard Space Flight Center). The radiative transfer scheme divides the 0.2 – 20 μm spectrum in 121 shortwave (0.2 – 5 μm) intervals, with a lot of narrow bands for UV and visible in order to model properly the Rayleigh scattering; and 85 longwave (3.5 – 20 μm) intervals. The spectroscopy module CGASA was used to compute the gas absorption coefficients, and the fluxes have been computed with the radiation transfer code MOMO (*Doppler et al.* 2013b, *Fell and Fischer* 2001, *Fischer and Grassl* 1986), with the use of non-correlated k-distribution module KISS (*Doppler et al.* 2013a, *Bennartz and Fischer* 2000). The area of the study is the CALIOP lidar track, and covers a latitude range from 30° South to 5 ° North. We divided this spatial zone in 35 intervals, each covering an area from a latitude length of 1° (around 200 km).

10.1.4. Radiative heating rates and forcings of aerosols along the A-train track.

The radiative transfer code MOMO computes the aerosol additional heating rates and the TOA aerosol direct radiative forcing for each spatial zone. Figure 10.2 shows the vertical profile of aerosol additional radiative heating rates for the whole area of the lidar track. The results shown are the net (longwave + shortwave) heating rates. If we compare the inputs (extinction coefficient) presented in Figure 10.1 and the output (heating rates) presented in Figure 10.2, one can see that the aerosol additional heating rate is positive within the aerosol layers (this is not a surprise, because the aerosols are very absorbing: SSA < 0.75). We also see that the aerosols have a cooling effect in the cloud layers. This could conduct to an increase of the cloud mass by condensation and thus produce a semi-direct effect of the aerosols (change on the radiation budget of some atmospheric layers because of a change of the cloud mass due to evaporation or condensation of clouds because of an aerosol direct radiative warming or cooling: *Ackerman et al.* 2000).

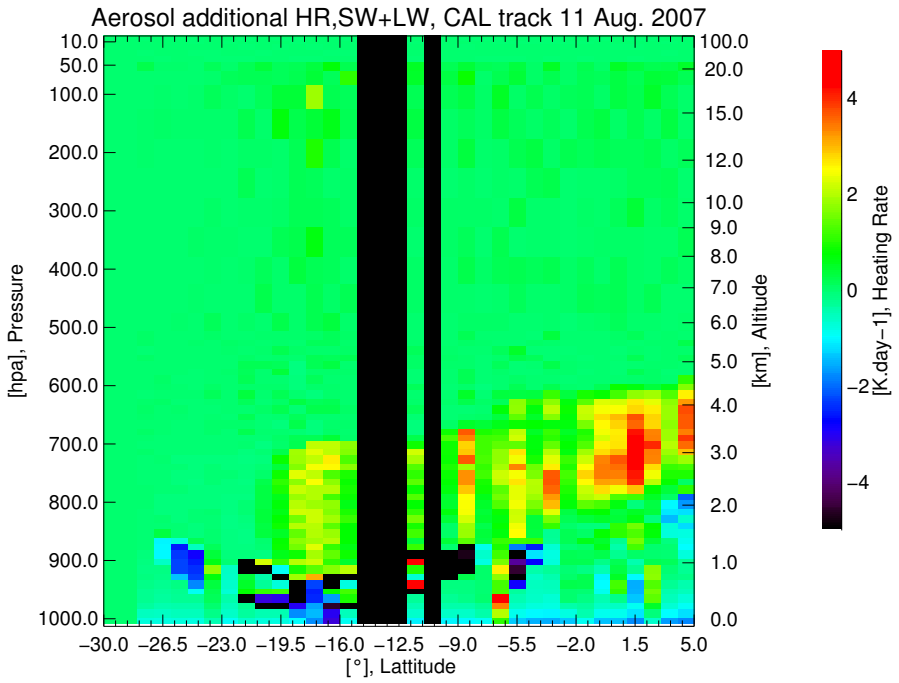

Figure 10.2.: Vertical profile of aerosol additional radiative heating rates, computed with MOMO. Displayed values are instant heating rates, for SZA = 30°.

The aerosol radiative effect is more visible if we analyze the aerosol TOA radiative forcing. Figure 10.3 shows (in red) the TOA radiative forcing for each 1° of latitude portion of the lidar track. The COD (in blue) and the AOD (in black) are also plotted. The results presented on Figure 10.3 quantifies for real case what was theoretically studied in Section 9.3 (Figure 9.6 and 9.7): The value of the aerosol TOA radiative forcing can be larger than 30 Wm^{-2} if there is a cloud with a large COD (COD > 10) below the aerosol plume. Without dense clouds below the aerosol plume (COD < 6) the aerosol radiative forcing is negative.

10.1.5. Discussion.

Thanks to the instrumental synergy provided by the A-Train, we could make a radiative study at a 2-D scale on an area covering a range of 35° of latitude in the Guinea Bay. This approach allows simulations fore a larger variety of cases than what we did within the 1-D approaches presented for the TRAQA campaign

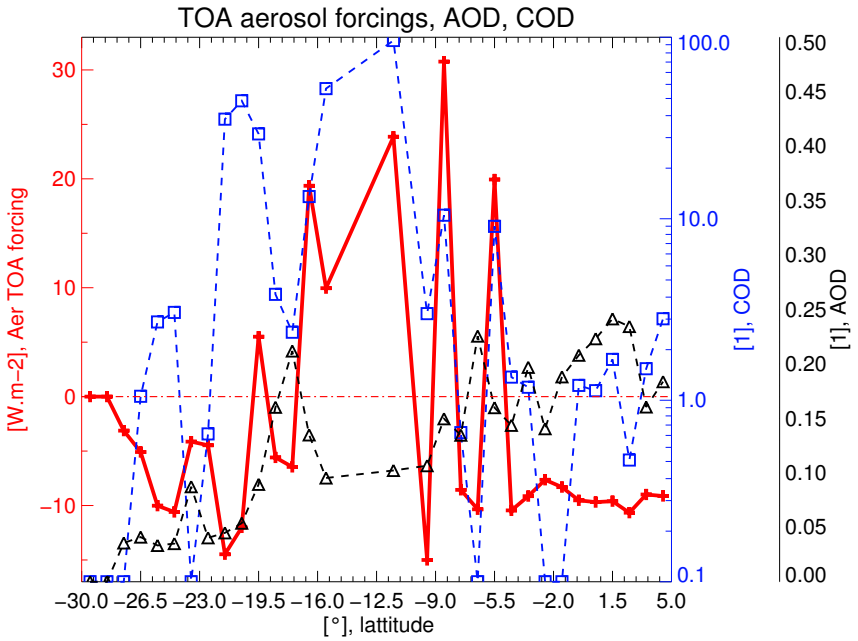

Figure 10.3.: TOA aerosol radiative forcing (red line) in $\mathrm{W m^{-2}}$ along the CALIPSO track, and complementary information: AOD (black dashed lines with triangles) and COD (blue dashed line with squares). These are instant radiative forcing for SZA = 30°.

(Chapter 8). The diversity of input data regarding the AOD and the COD observed here allowed to validate with concrete observed cases the theoretically study of Chapter 9 (influence of clouds below absorbing aerosols).

This study has 3 main limitations. The first limitation is that the aerosol is not so good characterized as in the case study of the TRAQA campaign (Chapter 8): The measurements from space in the Guinea Gulf are not combined with in-situ measurements of a measurement campaign. A solution that is planed is to enlarge the spatial synergy with POLDER data (Polarization and Directionality of the Earth's Reflectance), an instrument on board of the CNES satellite PARASOL (Polarisation et Anisotropie des Reflectances au sommet de l'Atmosphère, couples avec un Satellite d'Observation emportant un Lidar). The data of this instrument have been used by *Waquet et al.* 2009 for the remote sensing of aerosol above clouds. The use of POLDER will provide measurements for other wavelengths than the lidar one (POLDER has 4 channels devoted to aerosol characterization in visible and near infrared); this will allow to constraint the input macroscopic properties. POLDER

is also a polarized instrument, it can thus discriminate dust particles from spherical particles. This will also help to a better characterization of the kinds of aerosols that are observed. The data of the measurement campaign SAFARI (Southern African Regional Science Initiative) and AMMA (African Monsoon Multidisciplinary Analysis) should also help to the characterization of biomass burning aerosol especially for the calibration of the size distribution and refractive indexes given in input of MOMO. *Mallet et al.* 2008 have presented a similar study for the dry season in West Africa: The use of MODIS data has been combined to airborne in-situ measurements during the AMMA campaign and to observations of ground based lidar and spectrometers, this synergy of measurements allowed to estimate the daily radiative forcing of the aerosols with low uncertainties, because the aerosol microscopic properties have been characterized very finely.

The second limitation is that this study is only done on a '*1-D or 2-D*' scale (many 1-D cases all along a 7500 km lidar track). If we want to discuss the influence of the aerosols on the climate of the region, we need to extend this study to 3 dimensions. To this purpose, we have to characterize the clouds and aerosol spatial distribution for the whole region. Cloud spatial distribution can be easily provided by MSG. The knowledge of the aerosol spatial distribution is something more challenging. An outlook of this Ph-D work is to manage it for the Mediterranean region, and to estimate the regional influence on the climate of diverse aerosol types. The first ideas and methods are presented in Section 10.2.

The third limitation is that this study is restricted temporally: all computations have been done for the instant vertical profiles of the atmosphere as observed by the A-Train. Also, the radiative forcings that have been computed are instant radiative forcing for SZA = 30°. We could make the same radiative study, but at other times of the day than the one of the lidar observation. To this purpose, we should suppose the aerosol layer being at the same place, and only other parameters (SZA, COD, water vapor and temperature profile) varying. The cloud coverage variation can be observed with geostationary satellite MSG (Meteosat Second Generation). Water vapor and temperature variations can be taken from GMAO dataset. Note, that the aerosol properties (size distribution, refractive indexes) can change with the change of water vapor vertical distribution. A sensibility study of the influence of these changes on the aerosol radiative forcing should be taken into account for a time-extended study.

This study has been done in partnership with Damien Josset (SSAI/NASA Larc). I particularly thank Damien for providing the satellite input data. The radiative

transfer computation has been done by myself with the radiative transfer code MOMO. The radiative transfer scheme has been built by myself. I presented an oral presentation of this work at the IRS (International Radiation Symposium) in Berlin, in 2012: *Josset D., Doppler L., Waquet F., Seze G., Pelon J., Hu Y., Fischer J., Ravetta F., Tsamalis C., Zhai P. : Aerosol radiative forcing over liquid water clouds based on A-Train synergies and active/passive polarized observations. International Radiation Symposium 2012, Berlin*. D. Josset wrote the proceeding paper.

10.2. Generalization of the radiative study to a regional scale: outlook and preliminary study.

We want to simulate the radiative impact of aerosols on the regional climate of the Mediterranean Basin. The aerosols can be characterized type by type, with their different provenance (pollution aerosols from the Pô Valley, from Barcelona, and from Marseille, dust aerosol from the Sahara). The characterization of the diverse aerosols is possible by repeating 1-D case studies like the two ones presented in Chapter 8. On another side, the study of the influence on climate of these aerosols at a regional scale requires the knowledge of the spatial distributions of these aerosols in the Mediterranean basin and the temporal evolution of these spatial distributions.

10.2.1. Characterization of aerosol plumes and atmospheric stratification with spaceborne lidar and satellite measurements (CALIOP and A-Train).

A solution for the estimation of the regional radiative impact of the aerosols in the Mediterranean region, is to combine the instrumental synergy presented in Section 10.1 to the aerosol characterization presented Chapter 8: The different kinds of aerosols can be well characterized with case studies as presented in Chapter 8, and the evolution of the aerosol plumes can be followed with geostationary satellite MSG and with the A-train data: Lidar (CALIOP), radar (Cloudsat) and radiometers (IIR, POLDER, MODIS). The A-Train overflies the Mediterranean sea 3 or 4 times a day. A model of plume dynamics can thus be built, with the help of CALIOP data. If the plume dynamics is well described for each kind of aerosol characterized during the TRAQA campaign, than it is possible to evaluate the radiative impact of each aerosol plume individually with MOMO and estimate the temporal evolution of the

radiative forcing of each plume. At the end we can estimate the radiative effect of a kind of aerosol at a regional scale for a month or for a season in the Mediterranean basin.

10.2.2. Radiative impact of aerosols on the climate of Mediterranean region: an outlook.

For a future study, we plan to use a mesoscale model, namely the chemical-transport model WRF-Chem (Weather Research and Forecasting model coupled with Chemistry, *Skamarock et al.* 2008, *Grell et al.* 2005). The mesoscale model simulates the emission, transport, mixing, and chemical transformation of trace gases and aerosols and meteorology parameters. WRF-Chem will provide an estimation of the spatial distribution of the aerosols at different times. It will then be possible to divide the region of the Mediterranean basin in grid cells and to compute with MOMO for different times, the radiative forcing of the aerosols for each cell of the grid. The inputs of MOMO will be the WRF-chem spatial distribution for the aerosol amount and vertical distribution and the TRAQA data (from case studies like the ones presented in Chapter 8) for the microscopic properties of the aerosols.

WRF-Chem owns a radiative scheme that can, as does MOMO, compute the aerosol radiative forcings and the aerosol additional heating rates. Because WRF-Chem radiative scheme uses more approximations than MOMO does, it should be faster and less precise to make the radiative forcing study with WRF-Chem than with MOMO. Our next objective is therefore to validate or improve the radiative scheme of WRF-Chem by comparisons to MOMO for common inputs of the radiative schemes. Then we will use WRF-chem for the estimates of radiative forcings, but we will use MOMO simulations to control the WRF-Chem simulations, in order to find a resolution of the grid cells that is high enough so that the spatial averaging does not lead to mistakes.

The problem of averaging inside of the grid cells of a mesoscale model is a serious problem, because within a grid cell, there are different aerosol and cloud vertical structures. It is not always correct to take the average amount of clouds and aerosols as input of the radiative scheme. In order to anticipate this problem, next subsection presents the results of a preliminary study. This preliminary study quantifies the errors that can be done by averaging the aerosol and cloud vertical structures in input of the radiative transfer scheme.

10.2.3. Preliminary study: The problem of averaging the atmospheric stratification.

Simulating the radiative impact of aerosols or clouds at a regional or global scale suppose to define a grid, with grid cells, and to compute the radiative forcings in each cell. For each grid cell, a vertical profile of aerosols and clouds is given in input of the radiative scheme. The simplest approach is to average in each cell the vertical profiles of aerosols and the vertical profiles of clouds and to give these cell-averaged profiles in input of the radiative scheme that computes the radiative fluxes and the radiative forcings. This approach is valid only if one of the two following statements is correct:

- **#Statement 1:** The radiative forcing is linear in cloud and aerosol vertical distribution. This means that if we have two different vertical structures of aerosols and clouds (vertical structure A and vertical structure B), then: Forcing(vertical structure A + vertical structure B) = Forcing(vertical structure A) + Forcing(vertical structure B).

- **#Statement 2:** The cells of the grid are small enough so that the vertical structure of aerosols and clouds are is homogeneous inside of each grid cell.

Figure 10.4 presents the results of a theoretically study with radiative transfer code MOMO. The aim of this theoretically study is to test if the statement 1 is valid. 8 different vertical structures of aerosols and clouds are considered. The TOA radiative forcing is computed for each of the 8 structures, for a small and large amount of aerosols (AOD = 0.11 and AOD = 0.34). The values of the shortwave TOA aerosol radiative forcings for all 8 cases are displayed in the color boxes above the descriptions of the structures on Figure 10.4. The values that are displayed are the instant shortwave TOA radiative forcing for SZA = 30°. Note, that the aerosol that is used in this study is the model of biomass burning aerosol. The macroscopic properties (SSA, ext_norm, g) of this aerosol are displayed on Figure 9.5.

Statement 1 is valid only if the average of the 8 forcings computed separately for each case is equal to the forcing computed with MOMO with in input a mean vertical structure that corresponds to the average of the 8 vertical structures shown on Figure 10.4.

We assume the following description of the sky scenes in midlatitude region:

-> Presence of clouds: 1/3 of the cases are cloud free cases and for the 2/3 of cloud cases, each of the seven cloudy cases presented in Figure 10.4 has the same probability to occur.

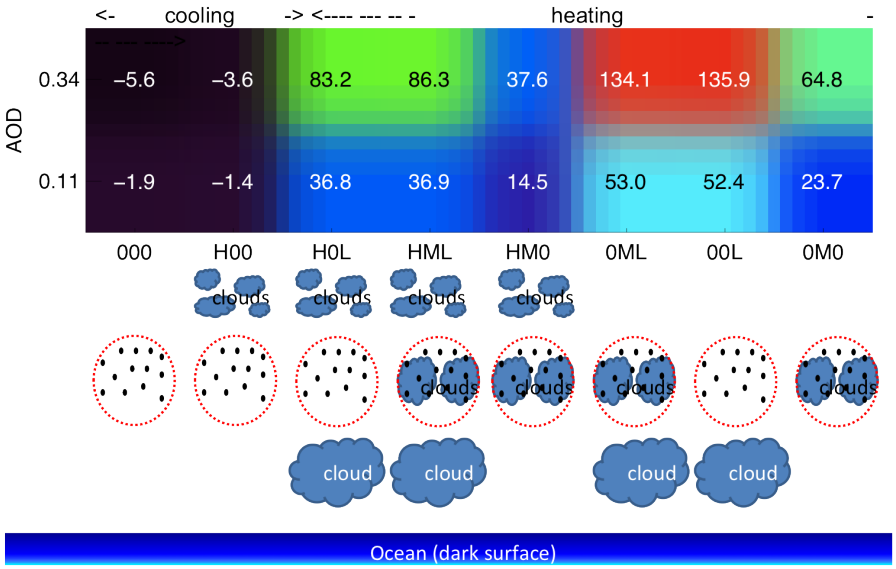

Figure 10.4.: Theoretical cases of vertical structures of aerosols and clouds. 8 different scenes are considered (bottom). The TOA shortwave aerosol radiative forcings for each scene and for 2 different AOD are displayed in color boxes just above each scene description.

-> Presence and amount of aerosols: 2/3 of the cases are aerosol-free and for the aerosol cases, in 2/3 of the cases the AOD is low (0.11) and in 1/3 of the cases the AOD is high (0.34).

With these probabilities of scene occurrences within a large grid cell, the average of the aerosol shortwave TOA radiative forcings for each case is 8.55 $\mathrm{W\,m^{-2}}$. This is the value obtained with the exact method. If we use the basic method (computing an average vertical structure of aerosols and clouds and then computing the radiative forcing for this average structure) the value of the shortwave TOA aerosol radiative forcing is 97.79 $\mathrm{W\,m^{-2}}$. One can see that doing the average on the vertical structure of aerosols and clouds in input of the radiative transfer scheme leads to huge error on the TOA forcing, because we totally underestimate the aerosol and cloud free cases that have insignificant or negative radiative forcing, and thus these aerosol-free and clouds-free cases considerably reduce the average value of the forcing within the grid cell.

The huge differences between the correct approach (to know the probability of

each structure and to average the forcing of each structure with probability weights) and the basic one (to define the average vertical structure of the clouds and aerosols and compute the aerosol forcing of the average structure) convince us that statement 1 is wrong, and that the TOA radiative forcing is not linear in the vertical structure of aerosols and clouds.

Therefore, for a future WRF-Chem study of aerosol radiative forcings, we must take care that grid cells of the model are small enough so that each cell individually, contains an homogenous vertical structure of aerosols and clouds (i.e. statement 2 must be valid). If not, we have to introduce a probability approach of the vertical structures of aerosols and clouds in the WRF-Chem radiative forcing computation.

Synthesis and Outlook

Within this chapter, we discussed the spatial extension of 1-D radiative case studies of Chapter 8. A spatial extension of the 1-D case study has been presented: the instant TOA radiative forcings of absorbing aerosols above low dense clouds in the Guinea Bay have been estimated for cases all along CALIPSO lidar track. The use of a synergy of spaceborne instruments with A-train satellites brought the input material necessary to a radiative forcing simulation with MOMO along the whole track of the lidar CALIOP. Contrary to 1-D studies of Chapter 8, the '2-D - 1-D' study presented in Section 10.1 allowed to analyse many different cases of aerosols above clouds, and to outline some general results: For COD < 6, the TOA radiative forcing of the aerosols is negative. For COD > 6, the TOA radiative forcing of the aerosols is positive and increases with COD and AOD.

We discussed outlook of this Ph-D work: A large spatial and temporal extension of the radiative forcing simulations for the estimate of aerosol radiative impact at a regional scale. For this study, the use of a mesoscale model (WRF-Chem) is intended. A preliminary study points out the problem that aerosol radiative forcing is not linear in vertical structure of clouds and aerosols. Thus we have to pay a special attention to the method used by the mesoscale model when it computes the aerosol radiative forcing: The grid cells in which the model computes the forcings have to be small enough to contain only homogeneous vertical structure of aerosols and clouds. An interesting outlook is a combination of the characterization of aerosols done for TRAQA case studies and of A-train measurements, because with A-train measurements (especially measurements of lidar CALIOP), it is possible to follow the aerosol plumes and thus to characterize the aerosol spatial distribution. With

the spatial distribution delivered by the A-Train method and the aerosols characterization done with TRAQA 1-D case studies, there is enough input material to compute the aerosol radiative forcing at a regional scale with MOMO.

Summary of Part III.

Radiative transfer code MOMO in its full range version is an efficient tool to compute the radiation budget and especially the aerosol radiative forcings and the vertical profiles of aerosol additional heating rates.

In Part III of this thesis, we first focused on the aerosol characterization, a critical step for precise estimates of the influence of aerosols on the radiation budget. During the TRAQA campaign in summer 2012 in the Mediterranean region, a synergy between in-situ and lidar measurements, provided a complete dataset that has allowed, for isolated case studies, to retrieve the aerosol size distribution and the [0.2 – 1 μm] spectrum of aerosol refractive index. This method presented in Chapter 8 is named optical closure. The optical closure method has been applied to the characterization of two kinds of aerosol: A Saharan dust aerosol and a pollution aerosol coming from the Pô Valley. A radiative study has been realized for these two kinds of aerosol.

The sensitivity study of chapter 9 points out the importance of the characterization of the size of large aerosols (e.g. dust aerosol) for the estimate of the aerosol radiative forcings. The real part of the aerosol refractive index is a less critical parameter than the imaginary part of aerosol refractive index. The imaginary part of aerosol refractive index governs the aerosol absorption and emission. Therefore, the TOA longwave aerosol radiative forcing and the atmosphere aerosol radiative forcing are very sensible to the value of the imaginary part of aerosol refractive index.

The AEROCOM experiment published in *Randles et al.* 2013, to which MOMO took part shows that the radiative scheme and the radiative transfer model are important source of diversity for the aerosol radiative forcing estimates: the dispersion between the results of different radiative transfer models can reach 15 %. For the most complicate simulation cases (scattering aerosols), it is especially recommended to use a radiative transfer code that is more advanced than a 2-streams method.

The environment of aerosol plumes is also a parameter of influence on aerosol radiative forcings: The presence of low dense clouds above absorbing aerosol plumes changes the sign of TOA aerosol radiative forcing (aerosol radiative cooling at the TOA for cloud-free cases, and radiative warming if there are clouds below aerosol plumes). This phenomenon has been studied for concrete cases, within a case study for biomass burning aerosols above low dense clouds in the Guinea Bay in summer

2007. The radiation budget has been computed all along a spaceborne lidar track. The conclusions of this case study are that for COD larger than 6, the aerosol radiative forcing is positive and its value increases with the value of AOD. When there are no cloud or few clouds (COD < 6) below the aerosols, the aerosol radiative forcing is negative. This case study shows also that the use of a synergy of spaceborne instruments (with the A-Train) allows a spatial extension of the case study.

Several ideas of outlook are proposed for a spatial and temporal extension of the aerosol radiative forcing study, in order to estimate the radiative influence of aerosols on the climate of the Mediterranean region. A method that is currently explored is to use the mesoscale model WRF-Chem. A preliminary study put forward the importance of the vertical structure of aerosols and clouds, for the choice of the grid cells' size of the mesoscale model. Another idea that should be explored is to characterize the spatial distribution of the aerosol plumes and their dynamics over the Mediterranean basin with the help of A-train (especially CALIOP) observations. This characterization, coupled with the aerosol characterization of TRAQA campaign will allow to estimate the aerosol plumes' radiative forcing at the scale of the Mediterranean basin during their whole residence time in the atmosphere.

General Conclusions

Synthesis

The objective of this PhD work was to contribute to a better understanding of the Earth and atmosphere radiation budget, by estimating the aerosol radiative impact at a regional scale. To this purpose, radiative transfer code MOMO has been improved (especially it has been extended to the thermal infrared) and was applied to radiative studies about aerosols, coupled to observations at a regional scale. The works presented in this thesis should answer 3 questions: What are the numerical developments realized for the improvement of MOMO and its extension to the thermal infrared? What brings the combination of MOMO and observations for the study of aerosol radiative impact? Is radiative transfer code MOMO convenient to fullfill the needs of radiation transfer tools at the LATMOS and the ISS (forward model for remote sensing inversions, radiative transfer simulations for very different issues, with various inputs/outputs and various user exygencies)?

As presented in Part II of this thesis, MOMO has been properly extended to the thermal infrared: The matrix operator method includes now the thermal infrared emission of radiation by gases, aerosols and clouds. A spectroscopy module CGASA has been developed. Thanks to CGASA, we overcome the difficulty of modeling the water vapor continuum of absorption in the thermal infrared. Full range high-resolution spectra of gas absorption can now be computed with accuracy. MOMO's k-distribution module KISS can be used in the thermal infrared, with the development of the K-IR method. K-IR allows the implementation of the emission of radiation by gases in the k-distribution. The extension of KISS to the thermal infrared was indispensable for radiative transfer simulations of large spectral bands in the thermal infrared.

MOMO has been used for applications to the estimation of aerosol radiative forcings based on observations at a regional scale. With the data of TRAQA campaign (a measurement campaign focused on aerosols in Mediterranean basin), we developed a method named optical closure that allows a characterization of aerosol microscopic properties (size distribution and refractive indexes). This method uses a synergy of in-situ and lidar measurements. Chapter 8 of this thesis presented the results of this method for the characterization of pollution aerosol of the Pô Valley and of dust aerosol of the Sahara that have both been transported over the Mediterranean basin, and analyzed between Marseille and the Corsica. Both observed aerosols are very scattering (SSA > 0.9 at 532 nm). The refractive indexes are different. The size distributions also are very different: The pollution aerosol

contains finer particles than the dust aerosol does. A radiative study with radiative transfer code MOMO showed a complete different radiative behavior from one aerosol to another: The fine pollution aerosol does not have any impact on the radiative fluxes for wavelengths larger than 1 μm. Dust aerosol leads to large values of longwave radiative forcings. The case studies of aerosol impact on the radiation budget that are presented in chapter 8 were restricted to 1-D column simulations. This study has been extended along a lidar track on a lattitude range of 35° in the tropics: Thanks to the combination of MOMO computations and a synergy of spaceborne measurements, it was possible to characterize the vertical profiles of aerosols and clouds all along the lidar track of CALIPSO. Then the radiation budget have been computed with the help of a radiation scheme based on MOMO for 200 km long pieces of the lidar track. This study demonstrates the importance of the presence of clouds below the aerosols for the sign and the order of magnitude of aerosol TOA radiative forcings: If the aerosols are above dense cloud layers (COD > 6), the value of aerosol instant radiative efficiency (SZA = 30 °) can reach 200 Wm^{-2} if the clouds are dense enough (COD > 10).

The validation of MOMO's extention to the thermal infrared (presented in articles *Doppler et al.* 2013a and 2013b in chapters 5 and 7 of this thesis) shows that MOMO in its full range version is precise enough to be used as a forward code for remote sensing inversion algorithms. The radiative transfer code and scheme that are used are decisive parameters for the estimates of aerosol radiative forcing: AEROCOM experiment (to which MOMO took part) assesses that the diversity of the results can reach 15 % for the estimates of the aerosol radiative forcings during an experiment comparing 31 radiative transfer scheme, and results for MOMO shown in this experiment prove that it obtains results close to the results of reference codes. Hence, MOMO is a convenient tool for broadband fluxes computations and aerosol radiative forcings estimates. The extension of MOMO to the thermal infrared has allowed to estimate also the radiative forcing of dust aerosol in the longwave. MOMO's versatility allowed to build a radiative scheme adapted to all the different inputs and outputs provided and required in the several studies of this PhD .

Outlook

This PhD work offers interesting outlook for the radiative transfer development, and for the estimation of aerosol radiative impact at a regional scale.

New developments of radiative transfer tools are always welcome. The spectroscopy module CGASA can still be improved regarding the modeling of other gases than water vapor: the VCLW method should be supplied by more relevant methods for some parts of the spectrum and some gases (ozone, carbon dioxide). Tests have to be managed and compare the results of CGASA to spaceborne measurements of high-resolution spectrometers (SCHIAMACHY, IASI). The rapidity of spectroscopy module CGASA can be improved. Methods like the convolution algorithm of LBLRTM (Clough et al. 1979) could be tested. A fast version of non-correlated k-distribution module KISS can be developed, with a first objective of rapidity and a second objective of accuracy (the opposite philosophy of the current version). Validation tests of the global package of MOMO should be done also for cases with scattering in the thermal infrared. CALIPSO-IIR radiometer has been the reference instrument for the comparison of MOMO to real measurements for clear air cases. A radiation transfer code comparison experiment can be organized, with restricted number of codes (FASDOM, RTTOV, MOMO, SPIRS). The objective of this experiment will be to simulate CALIPSO-IIR channels for atmospheric scenes with aerosols and clouds.

The study of the radiative impact of aerosols has also a wide field of outlook. First we can go further with the aerosol characterization using TRAQA dataset: we can apply the case study of Chapter 8 to other kinds of aerosols (e.g. pollution aerosols from Barcelona and from Marseille, sea salt aerosols) and then, by applying the radiative study of Chapter 8, characterize the radiative behavior of many different Mediterranean aerosols. These 1-D radiative studies can be validated with radiative closures: The fluxes computed for real cases with MOMO can be controlled by the flux measurements done by SAFIRE airborne instruments during TRAQA campaign or during future campaigns of the ChArMEx project.

We can also imagine methods for the spatial and temporal extension of these studies : The method presented in Chapter 10, Subsection 10.2.1 proposes to use A-train (especially CALIOP data) to characterize the evolution of aerosol plumes (spatial distribution, optical depth). It will then be possible with MOMO to characterize the radiative behavior of each aerosol plume all along the life time of the plume, and thus to estimate the aerosol radiative forcings of the Mediterranean basin over long times. We can also, as explained in Subsection 10.2.2, estimate the aerosol impact on the radiation budget with the help of mesoscale model WRF-Chem. This approach should allow long time estimation and evolution of the aerosol radiative

forcings over the whole Mediterranean region.

The combination of all these perspectives, concerning the pure radiative transfer modeling, the aerosol characterization and the strategies of measurements and modeling should be, in the continuity of this PhD work, a way to improve the understanding of the radiative impact of aerosols, by mixing the scientific cultures of the LATMOS and ISS.

References

Ackerman AS, Toon OB, Stevens DE, Heymsfield AJ, Ramanathan V, Welton EJ. Reduction of tropical cloudiness by soot. Science **2000**;288(5468):1042-47.

Albrecht BA. Aerosols, cloud microphysics, and fractional cloudiness. Science **1989**;245(4923):1227-30.

Allan RP, Slingo A, Milton SF, Brooks ME. Evaluation of the Met Office global forecast model using Geostationary Earth Radiation Budget (GERB) data. QJRMS **2007**;133(629):1993-2010.

Anderson GP, Clough SA, Kneizys FX, Chetwynd JH, Shettle EP. AFGL Atmospheric Constituent Profiles (0-120km). AFGL-TR-86-0110, Env Res Papers **1986**;984:1-43.

Ardanuy PE, Stowe LL, Gruber A, Weiss M. Shortwave, longwave, and net cloud-radiative forcing as determined from Nimbus 7 observations. J Geoph Res **1991**;96(D10):18537-49.

Barker HW, Kato S, Wehr T. Computation of Solar Radiative Fluxes by 1D and 3D Methods Using Cloudy Atmospheres Inferred from A-train Satellite Data. Surv Geoph, **2012**;33(3-4): 657-76.

Barkstrom BR. The earth radiation budget experiment (ERBE). Bull of Ame Met Soc **1984**;65(11): 1170-85.

Bennartz R, **Fischer** J. A modified k-distribution approach applied to narrow band water vapour and oxygen absorption estimates in the near infrared. J Quant Spectrosc Radiat Transfer **2000**;66:539–53.

Boucher O, Schwartz SO et al. Intercomparison of models representing direct shortwave radiative forcing by sulfate aerosols. J Geoph Res **1998**;103(D14):16979-16998.

Chandrasekar S. Radiative Transfer. Dover New York Inc, **1960**;393pp.

Clough SA, **Kneizys** FX. Convolution algorithm for the Lorentz function. Applied Optics **1979**;18(13): 2329-33.

Clough SA, Kneizys FX, Davies RW. Line Shape and the Water Vapor Continuum. Atmos Res **1989**;23:229-41.

Clough SA, Iacono MJ, Moncet JL. Line-by-line calculation of atmospheric fluxes and cooling rates: Application to water vapor. J Geophys Res **1992**;97:15761-85.

Clough SA, Shephard MW, Mlawer EJ, Delamere JS, Iacono MJ, Cady-Pereira K, Boukabara S, Brown PD. Atmospheric radiative transfer modeling: a summary of the AER codes, Short Communication. J Quant Spectrosc Radiat Transfer **2005**;91:233–44.

Coakley Jr JA, Cess RD, Yurevich FB. The effect of tropospheric aerosols on the earth's radiation budget: A parameterization for climate models. J Atm Sci **1983**;40:116-38.

d'Almeida GA, Koepke P, Shettle EP. Atmospheric aerosols: global climatology and radiative characteristics. Hampton: A. Deepak Pub 1991.

Deuzé JL, Herman M, Santer R. Fourier series expansion of the transfer equation in the atmosphere-ocean system. J of Quant Spect and Rad Trans 1989;41(6):483-94.

Di Biagio C, di Sarra A, Meloni D, Monteleone F, Piacentino S, Sferlazzo D. Measurements of Mediterranean aerosol radiative forcing and influence of the single scattering albedo. J Geoph Res **2009**;114(D6).

Di Biagio C, di Sarra A, Meloni D. Large atmospheric shortwave radiative forcing by Mediterranean aerosols derived from simultaneous ground-based and spaceborne observations and dependence on the aerosol type and single scattering albedo. Journal of Geophysical Res **2010**;115(D10).

Di Sarra A, Di Biagio C, Meloni D, Monteleone F, Pace G, Pugnaghi S, Sferlazzo D. Shortwave and longwave

radiative effects of the intense Saharan dust event of 25–26 March 2010 at Lampedusa (Mediterranean Sea). J Geoph Res **2011**;116(D23).

Dines WH. The heat balance of the atmosphere. QJRMS **1917;**43(182): 151-58.

Doppler L, Preusker R, Bennartz R, Fischer J. k-bin and k-IR: Improved non-correlated k-distribution methods for non-fixed instrument response function and extension to thermal infrared. Applications to satellite remote sensing. J of Quant Rad Transfer **2013**a, in revision.

Doppler L, Fischer J, Carbajal-Henken C, Pelon J, Ravetta F. Extension of radiative transfer code MOMO, Matrix-Operator Model to the thermal infrared. Clear air validation by comparison to RTTOV and application to CALIPSO-IIR. Submitted in Mai **2013b** in J of Quant Rad Transfer.

Dubovik O, Sinyuk A, Lapyonok T, Holben BN, Mishchenko M, Yang P et al. Application of spheroid models to account for aerosol particle nonsphericity in remote sensing of desert dust. J Geoph Res **2006**;111(D11).

Dubuisson P, Buriez JC, Fouquart Y. High spectral resolution solar radiative transfer in absorbing and scatteringmedia: application to the Satellite Simulation. J Quant Spectrosc Radiat Transfer **1996**;55(1):103–26.

Dubuisson P, Giraud V, Chomette O, Chepfer H, Pelon J. Fast Radiative transfer modeling for infrared imaging radiometry. J Quant Spectrosc Radiat Transfer **2005**;95:201–20.

Dubuisson P, Giraud V, Pelon J, Cadet B, Yang P. Sensitivity of thermal infrared radiation at the top of the atmosphere and the surface to ice cloud microphysics. J of App Met and Clim **2008**;47(10):2545-60.

Dufresne JL, Gautier C, Ricchiazzi P, Fouquart,Y. Longwave scattering effects of mineral aerosols. J Atm Sciences **2002**;59(12):1959-66.

Eddington AS. On the radiative equilibrium of the stars. Monthly Notices of the Royal Astronomical Society 1916;77:16-35.

Fell F, **Fischer** J. Numerical simulation of the light field in the atmosphere-ocean system using the matrix-operator method, J Quant Spectrosc and Radiat Transfer **2001**;69:351–88.

Ferrare RA, Melfi SH, Whiteman DN, Evans KD, Poellot M, Kaufman Y J. Raman lidar measurements of aerosol extinction and backscattering: 2. Derivation of aerosol real refractive index, single-scattering albedo, and humidification factor using Raman lidar and aircraft size distribution measurements. J Geoph Res **1998**;103(D16), 19673-19689.

Fischer J, **Grassl** H. Radiative transfer in an atmosphere-ocean system: an azimuthally dependent matrix-operator approach. Applied Optics **1984**;23(7):1031-39.

Fu Q, **Liou** KN: On the Correlated k-Distribution Method for Radiative Transfer in Nonhomogeneous Atmospheres. J Atm Sc **1992**;49(22):2139-56.

Garnier A, Pelon J, Dubuisson P, Faivre M, Chomette O, Pascal P, Kratz DP. Retrieval of Cloud Properties Using CALIPSO Imaging Infrared Radiometer. Part I: Effective Emissivity and Optical Depth. J App Met and Clim **2012**;51:1407-25.

Goody RM, Yung YL. Atmospheric Radiation, Theoretical Basis. Oxford University Press. Second Edition, **1989**; 519pp.

Goody R, West R, Chen L, Crisp D. The correlated-k method for radiation calculations in nonhomogeneous atmospheres. J of Quant Spectrosc and Radiat Transfer **1989**;42(6):539-550.

Grassl H. Strahlung in Getruebten Atmosphaeren und in Wolken. Hamburger Geophysikalische Einzelschriften **1978**;A(37):136pp.

Grell GA, Peckham SE, Schmitz R, McKeen SA, Frost G, Skamarock WC, Eder B. Fully coupled "online" chemistry within the WRF model. Atm Env **2005**;39(37):6957-6975.

Hänel G. The properties of atmospheric aerosol particles as functions of the relative humidity at thermodynamic equilibrium with the surrounding moist air. Adv Geoph **1976**;19(1):73-188.

Halthore RN, Crisp D, Schwartz SE, et al. Intercomparison of shortwave radiative transfer codes and measurements. J Geophys Res **2005**;110(D11):1984-2012.

Harries JE. et (42) al. others. The Geostationary Earth Radiation Budget (GERB) project. Bull of Am Met Soc **2005**;86:945-960.

Haywood J**, Boucher** O. Estimates of the direct and indirect radiative forcing due to tropospheric aerosols: A review. Rev Geoph **2001**;38(4):513-43.

Haywood JM, **Shine** KP. Multi-spectral calculations of the direct radiative forcing of tropospheric sulphate and soot aerosols using a column model. QJRMS **1997**;123(543):1907-1930.

Hess M, Koepke P, Schult I. Optical Properties of Aerosols and Clouds: The Software Package OPAC. Bull Am Met Soc **1998**;79(5):831-44.

Hu Y, Vaughan M, Liu Z, et al. The depolarization-attenuated backscatter relation: CALIPSO lidar measurements vs. theory. Opt Express **2007**;15(9):5327-32.

Huneeus N, Schulz M, Balkanski Y, Griesfeller J, Prospero J, Kinne S, et al. Global dust model intercomparison in AeroCom phase I. Atm Chem Phys **2011**;11(15):7781-7816.

Hunt GE, Kandel R, Mecherikunnel AT. A history of presatellite investigations of the earth's radiation budget. Revi Geoph 1986;24(2):351-356.

Intergovernmental Panel on Climate Change (IPCC): Solomon S, Qin D, Manning M, Chen Z, Marquis M, Averyt KB, Tignor M, Miller HL. Contribution of Working Group I to the Fourth Assessment Report of the Intergovernmental Panel on Climate Change. Cambridge University Press, Cambridge United Kingdom and New York, NY, USA **2007**; 996pp.

Jacquinet-Husson N, Crepeau L et al. The 2009 edition of the GEISA spectroscopic database. Journal of Quantitative Spectroscopy and Radiative Transfer **2011**;112(15):2395-445.

Joseph JH, Wiscombe WJ, Weinman JA. The delta-Eddington approximation for radiative flux transfer. Journal of the Atmospheric Sciences **1976**;33(12):2452-59.

Josset D, Pelon J, Protat A, Flamant C. New approach to determine aerosol optical depth from combined CALIPSO and CloudSat ocean surface echoes. Geoph Res Lett **200**8; 35(10).

Josset D, Doppler L, Waquet F, et al. Aerosol radiative forcing over liquid water clouds based on A-Train synergies and active/passive polarized observations. In International Radiation Symposium 2012.**Kandel** R, Viollier

M, Raberanto P et al. The ScaRaB earth radiation budget dataset. Bull of Am Met Soc **1998**;79(5):765-784.

Kato S, Sun-Mack S, Miller WF, Rose FG, Chen Y, Minnis P, Wielicki BA. Relationships among cloud occurrence frequency, overlap, and effective thickness derived from CALIPSO and CloudSat merged cloud vertical profiles. J of Geoph Res 2012;115(D4).

Kato S, Rose FG, Sun-Mack S, Miller WF et al. Improvements of top-of-atmosphere and surface irradiance computations with CALIPSO-, CloudSat-, and MODIS-derived cloud and aerosol properties. J of Geoph Res **2011**;116(D19).

Kato S, Loeb NG, Rutan DA, Rose FG, Sun-Mack S, Miller WF, Chen Y. Uncertainty estimate of surface irradiances computed with modis-, calipso-, and cloudsat-derived cloud and aerosol properties. Surv Geoph **2012**;33(3-4):395-412.

Kim D, **Ramanathan** V. Solar radiation budget and radiative forcing due to aerosols and clouds. J of Geoph Res 2008;113(D2).

Kiehl JT, Hack JJ, Briegleb BP. The simulated Earth radiation budget of the National Center for Atmospheric Research community climate model CCM2 and comparisons with the Earth Radiation Budget Experiment (ERBE). J Geoph Res 1994;99(D10):20815-27.

Kiehl JT, **Trenberth** KE. Earth's annual global mean energy budget. Bull of Am Met Soc **1997**;78(2):197-208.

Kinne S, Schulz M, Textor C, Guibert S. An AeroCom initial assessment–optical properties in aerosol component modules of global models. Atm Chem Phys **2006**;6(7).

King MD, Kaufman YJ, Menzel W, Tanre D. Remote sensing of cloud, aerosol, and water vapor properties from the Moderate Resolution Imaging Spectrometer (MODIS). Geosc and Rem Sens, IEEE Transactions **1992**;30(1):2-27.

King MD, Menzel WP, Kaufman YJ, Tanré et al.. Cloud and aerosol properties, precipitable water, and profiles of temperature and water vapor from MODIS. Geosc and Rem Sens, IEEE Transactions **2003**;41(2), 442-58.

Koch D et al. Evaluation of black carbon estimations in global aerosol models. Atm Chem Phys 2009;9(181):9001-9026.

Kurucz RL. New atlases for solar flux, irradiance, central intensity, and limb intensity. Mem Soc Astron Ita Supp **2005**;8(189).

Kyle H.L, Arking A, Hicke et al. The Nimbus earth radiation budget (ERB) experiment: 1975 to 1992. Bull of Am Met Soc **1993**;74(5):815-30.

Lacis AA, **Oinas** V. Nongray Gaseous Absorption, Thermal Emission, and Multiple Scattering in Vertically Inhomogeneous Atmospheres. J Geophys Res **1991**;96(D5):9027-63.

Lindstrot R, Preusker R, Ruhtz Th, Heese B, Wiegner M, Lindemann C, Fischer J. Validation of MERIS cloud top pressure using airborne lidar measurements. J of App Met Clim **2006**;45(12):1612-21**.**

Lindstrot R, Preusker R, Fischer J. Remote Sensing of Multilayer Cloud-Top Pressure Using Combined Measurements of MERIS and AATSR Onboard ENVISAT. J of Appl Meteor Climatol **2010**;49(6):1191-204.

Lindstrot R, Preusker R, Diedrich H, Doppler L, Bennartz R, Fischer J. 1D-Var retrieval of daytime total columnar water vapour from MERIS measurements. Atmos Meas Tech **2012**;5:631-46.

Loeb NG, Wielicki BA, Doelling DR, et al. Toward optimal closure of the Earth's top-of-atmosphere radiation budget. J of Climate **2009**;22(3):748-66.

London J. A study of the atmospheric heat balance. Report AFRC-TR-57-287, AFGL **1957**.

Macke A, Mishchenko MI, Muinonen K, Carlson BE. Scattering of light by large nonspherical particles: ray-tracing approximation versus T-matrix method. Optics letters **1995**;20(19):1934-1936.

Mallet M, Pont V, Liousse C, Gomes L, Pelon J, et al. Aerosol direct radiative forcing over Djougou (northern Benin) during the African Monsoon Multidisciplinary Analysis dry season experiment (Special Observation Period-0). J Geoph Res **2008**;113(D23).

Marchuk GI, Mikhailov GA, Nazaraliev MA. The Monte Carlo methods in atmospheric optics. Springer Series in Optical Sciences, Berlin: Springer **1980.**

McClatchey R, Fenn R, Selby J, Volz F, Garing J. Optical Properties of the Atmosphere. Air Force Cambridge Research Laboratories, 3rd edition 1972.

Mishchenko MI. Calculation of the amplitude matrix for a nonspherical particle in a fixed orientation. App Opt **2000**;39(6):1026-1031.

Mlawer EJ, Taubman SJ, Brown PD, Iacono MJ, Clough SA. Radiative transfer for inhomogeneous atmospheres: RRTM, a validated correlated-k model for the longwave. J Geophys Res **1997**;102(D14):16663-82.

Mlawer EJ, Payne VH, Moncet JL, Delamere JS, Alvarado MJ, Tobin DC. Development and recent evaluation of the MT_CKD model of continuum absorption. Phil. Trans R Soc **2012**;A370:2520-56.

Olesen FS, Grassl H. Cloud detection and classification over oceans at night with NOAA-7. Int J Remote Sensing **1985**;6(8):1435-44.

Perrone MR, Tafuro AM, Kinne S. Dust layer effects on the atmospheric radiative budget and heating rate profiles. Atm Env **2012**.

Petty GW. A First Course in Atmospheric Radiation. Second Edition. Sundog Publishing **2006**;458pp.

Plass GN, **Kattawar** GW. Radiative transfer in an atmosphere-ocean system. App Opt **1969**;8(2):455-466.

Plass G, Kattawar G, Catchings F. Matrix-operator theory of radiative transfer. 1: Rayleigh scattering. Applied Optics **1973**;12(2):314-29.

Preusker R, **Lindstrot** R. Remote Sensing of Cloud-Top Pressure Using Moderately Resolved Measurements within the Oxygen A Band - A Sensitivity Study. J App Met Clim **2009**;48:1562-74.

Ptashnik IV, Shine KP, Vigasin AA. Water vapour self-continuum and water dimers: 1. Analysis of recent work. J of Quant Spect and Rad Trans **2011**;112(8);1286-303.

Ramanathan V, Barkstrom BR, Harrison EF. Climate and the Earth's Radiation Budget. Physics Today **1989**;22,:22–32.

Ramanathan V, Crutzen PJ, Lelieveld J, Mitra AP, Althausen D, Anderson J, Valero FPJ. Indian Ocean Experiment: An integrated analysis of the climate forcing and effects of the great Indo-Asian haze. Journal of Geophysical Research: Atmospheres **2001**;106(D22):28371-98.

Randles CA, Kinne S, Myhre G, et al. Intercomparison of shortwave radiative transfer schemes in global aerosol

modeling: results from the AeroCom Radiative Transfer Experiment. Atm Chem Phys **2013**;3(5):1-74.

Raschke E. Multiple scattering calculation of the transfer of solar radiation in an atmosphereocean system. Contrib Atmos Phys Atmos 1972;45(1):1-19.

Rast M, Bezy JL, Bruzzi S. The ESA Medium Resolution Imaging Spectrometer MERIS - A review of the instrument and its mission. Int J Rem Sens **1999**;20:1681–702. **Raut** JC, **Chazette** P. Retrieval of aerosol complex refractive index from a synergy between lidar, sunphotometer and in situ measurements during LISAIR experiment. Atmos Chem Phys **2007**;7:2797-815.

Rathke C, **Fischer** J. Retrieval of cloud microphysical properties from thermal infrared observations by a fast iterative radiance fitting method. Journal of Atmospheric and Oceanic Technology **2000**;17(11):1509-1524.

Raut JC, **Chazette** P. Vertical profiles of urban aerosol complex refractive index in the frame of ESQUIF airborne measurements. Atm Chem Phys **2008**;8:901-919.

Raut JC. Synergie expérimentale impliquant la mesure lidar pour la caractérisation optique et microphysique de l'aérosol : applications à la qualité de l'air et au trasfert radiatif. Ph-D thesis of the Université Pierre et Marie Curie **2008**;265pp.

Rodgers C. Inverse Methods for Atmospheric Sounding: Theory and Practice. World Scientific, London **2000**.

Rosenfeld D. TRMM observed first direct evidence of smoke from forest fires inhibiting rainfall. Geoph Res Lett **1999**;26(20):3105-8.

Rosenfeld D, Lahav R, Khain A, Pinsky M. The role of sea spray in cleansing air pollution over ocean via cloud processes. Science **2002**;297(5587):1667-70.

Rossow WB, **Schiffer** RA. ISCCP cloud data products. Bull of Am Met Soc **1991**;72(1):2-20.

Rossow WB, **Zhang** YC. Calculation of surface and top of atmosphere radiative fluxes from physical quantities based on ISCCP data sets: 2. Validation and first results. J Geoph Res **1995**;100(D1):1167-97.

Rossow WB, **Duenas** EN. The international satellite cloud climatology project (ISCCP) web site: An online resource for research. Bulletin of the American Meteorological Society **2004**;85(2):167-72.

Rothman LS, Gordon IE, et al. The HITRAN 2008 molecular spectroscopic database. J of Quant Spectrosc and Radiat Transfer **2009**;110(9–10):533-72.

Saunders R, Matricardi M, Geer A. RTTOV9.1 users guide. NWP SAF report, Met. Office **2008**.

Seinfeld JH, Pandis SN. Atmospheric chemistry and physics: from air pollution to climate change. John Wiley & Sons Inc 1997.

Shine KP, Ptashnik IV, Raedel G. The Water Vapour Continuum: Brief History and Recents Developments. Surv Geophys **2012**;33:535-55.

Skamarock WC, Klemp JB. A time-split nonhydrostatic atmospheric model for weather research and forecasting applications. J of Comp Phys **2008**;227(7): 3465-85.

Slingo A, Ackerman TP, Allan RP, et al. Observations of the impact of a major Saharan dust storm on the atmospheric radiation balance. Geoph Res Lett **2006**;33(24).

Sokolik I, Andronova A, Johnson TC. Complex refractive index of atmospheric dust aerosols. Atm Env

1993;27(16):2495-2502.

Stamnes K, Tsay SC, Wiscombe W, Jayaweera K. Numerically stable algorithm for discrete-ordinate-method radiative transfer in multiple scattering and emitting layered media. Applied Optics **1988**;27(12).

Stamnes K, Tsay SC, Laszlo I. DISORT, a General-Purpose Fortran Program for Discrete-Ordinate-Method Radiative Transfer in Scattering and Emmiting Layered Media: Documentation of Methodology (version 1.1.). Goddard Flight Space Center **2000**.

Stephens GL, Vane DG, Boain RJ, et al. The CloudSat mission and the A-Train: A new dimension of space-based observations of clouds and precipitation. Bull of Am Met Soc **2002**;83(12),:1771-90.

Stevens B, **Schwartz** SE. Observing and modeling Earth's energy flows. Surv Geoph **2012**;33(3-4):779-816.

Takamura T, Sasano Y, Hayasaka T. Tropospheric aerosol optical properties derived from lidar, sun photometer, and optical particle counter measurements. App Opt **1994**;33(30):7132-7140.

Textor C, Schulz M, Guibert S, Kinne S, et al. Analysis and quantification of the diversities of aerosol life cycles within AeroCom. Atm Chem Phys **2006**;6(7): 1777-1813.

Toon OB, McKay CP, Ackerman TP. Rapid calculation of radiative heating rates and photodissociation rates in inhomogeneous multiple scattering atmospheres. J of Geophys Res **1989**;94(D13):16287-301.

Tran H, **Hartmann** JM. An improved O2 A band absorption model and its consequences for retrievals of photon paths and surface pressures. J Geoph Res **2008**;113(D18).

Trenberth KE, Fasullo JT, Kiehl J. Earth's global energy budget. Bull of Am Met Soc **2009**;90(3):311-323.

Twomey S. Pollution and the planetary albedo. Atm Env **1967**;8(12):1251-56.

Twomey S. The influence of pollution on the shortwave albedo of clouds. J Atm Sci **1977**;34(7):1149-52.

Volten H, Munoz O, Rol E, De Haan JF, Vassen Wet al. Scattering matrices of mineral aerosol particles at 441.6 nm and 632.8 nm. J Geoph Res **2001**;106(D15):17375-17.

Volz FE. Infrared refractive index of atmospheric aerosol substances. App Opt **1972**;11(4), 755-759.

Volz FE. Infrared optical constants of ammonium sulfate, Sahara dust, volcanic pumice, and flyash. App Opt **1973**;12(3):564-568.

Waquet F, Riedi J, Labonnote LC, Goloub P, Cairns B, Deuzé JL, Tanré D. Aerosol remote sensing over clouds using A-Train observations. J Atm Sciences **2009**;66(8):2468-80.

Waterman PC. Matrix formulation of electromagnetic scattering. Proc IEEE **1965**;53(8):805-812.

West R, Crisp D, Chen L. Mapping transformations for broadband atmospheric radiation calculations. J Quant Spectrosc and Radiat Transfer **1990**;43(3):191-199.

West R, Goody R, Chen L, Crisp D. The correlated-k method and related methods for broadband radiation calculations, J Quant Spectrosc Radiat Transfer **2010**;111:1672-73.

Wielicki BA, Barkstrom BR, Harrison EF, Lee III RB, Louis Smith G, Cooper JE. Clouds and the Earth's Radiant Energy System (CERES): An earth observing system experiment. Bull of Am Met Soc **1996**;77(5):853-68.

Winker DM, Pelon J, Coakley Jr JA et al. The CALIPSO mission, a Clobal 3D View of Aerosols and Clouds, Bull of Am Met Soc 2010;1211:29**.**

Wiscombe WJ. Improved Mie scattering algorithms. App Opt **1980**;19:15059.

Zhang Y, Rossow WB, Lacis AA, Oinas V, Mishchenko MI. Calculation of radiative fluxes from the surface to top of atmosphere based on ISCCP and other global data sets: Refinements of the radiative transfer model and the input data. J of Geoph Res **2004**;109(D19).

Appendixes: Lidar inversion and nomenclature

LIDAR: signal, equation and inversion.

Row lidar signal

The row signal measured by the telescope of a lidar is the backscattered radiation: A laser beam is emitted by the lidar. The laser radiation reaches a point of the atmosphere at a distance r of the lidar. The strength of the radiation when its reach this point is attenuated by: $\exp(-\tau(r))$; where $\tau(r)$ is the optical depth between the lidar and the point distant of r from the lidar. The air at distance r from the lidar scattered the light in all direction with respect of the phase function of the air's mixture. The backscattered light that can reach the lidar back is the light scattered with an angle $\theta = 180° \pm 0.5°$ compared to the incident direction ($\theta = 0°$). The quantity that quantifies the backscattered radiation is $\beta(z) = \beta_s(z) \cdot p_\pi$; with $p_\pi = p(\theta, \theta + \pi)$. Note, that the phase function is here written $p(\theta, \theta')$ and not $p(\Omega, \Omega')$ (like in Chapter 2 and 3), because we suppose a revolution symmetry over the azimuthal angle for the phase function p. θ is the zenithal angle defined with $\theta = 0$ for the incident direction of the radiation. Along the return way of the backscattered radiation, between the point r and the lidar, the radiation is attenuated by $\exp(-\tau(r))/r^2$. The lidar equation (Equation 10.1) describes the quantity of radiation that arrives on the telescope:

$$S(r) = C \cdot (\beta(r) \exp(-2\tau(r)))/r^2 + S_1 = (S_0(r))/r^2 + S_1 \tag{10.1}$$

S_1 is the sky radiation received by the lidar's telescope when the laser is switched of. C is a constant depending on the area of the telescope and of the strength of the laser beam. $\tau(r)$ is the integrated optical depth of the atmosphere between the lidar (r' $= 0$) and the point at distance r:

$$\tau(r) = \int_0^r \alpha(r')dr' \tag{10.2}$$

Where $\alpha(r') = \beta_e(r')$ is the extinction coefficient in the atmospheric layer at distance r' off the lidar. Equation 10.3 is a formulation of $S_0(r)$ using equations 10.1 and 10.2:

$$S_0(r) = C.\beta(r) \exp(-2 \int_0^r \alpha(r')dr') = C \cdot \beta_{\text{att}}(r) \tag{10.3}$$

$\beta_{\mathrm{att}}(r)$ is the row lidar signal before the lidar inversion. It is named by the lidarists: *attenuated beta*. In Figure 10.2, we show the profile of $C \cdot \beta_{\mathrm{att}}(r)$ for a measurement with the lidar LNG2 during the campaign TRAQA. Figure 10.2 represents a zenith measurement: The aircraft flew at 300 m of altitude and the lidar was oriented in direction of the top of the atmosphere. During the first 200 m over the aircraft, there is an area in which the signal starts from 0 and increases very quick with r. This is in contradiction with Equation 10.3 that suggests larger values for r close to 0. This area is named non-overlap area: close to the lidar, because of an optical phenomenon named *non-overlap*, the backscattered signal is not entirely catch by the telescope. We need to correct Equation 10.3. The signal that is actually measured by the telescope is described in Equation 10.4:

$$S_0(r) = C_0 \cdot O(r) \cdot \beta_{\mathrm{att}}(r) \tag{10.4}$$

Where $O(r)$ is the *overlap function*. The overlap function has the following properties: $O(r) \to 0$ for $r \to 0$, $O(r) \to 1$ for $r >$ overlap distance ($\approx$ 200 m). The overlap function $O(r)$ can be estimated experimentally. The signal is corrected before the lidar inversion algorithm. It is also possible to estimate C_0, with the help of the signal coming from a reference area (pure Rayleigh area, see Figure 10.2).

In a next step, we can extract the attenuated beta profile $\beta_{\mathrm{att}}(r)$ and put it in input of the inversion algorithm. $\beta_{\mathrm{att}}(r)$ is expressed in Equation 10.5:

$$\beta_{\mathrm{att}}(r) = (\beta_{\mathrm{ray}}(r) + \beta_{\mathrm{aer}}(r)) \cdot \exp(-2 \int_0^r \alpha_{\mathrm{aer}}(r')dr' - 2\tau_{\mathrm{ray}}(r)) \tag{10.5}$$

Where, β_{ray} is the Rayleigh backscattered (180°) coefficient, β_{aer} is the aerosol backscattered (180°) coefficient. Both parameters are expressed in $\mathrm{sr}^{-1}\mathrm{m}^{-1}$; α_{aer} is the aerosol extinction coefficient (in m^{-1}); τ_{ray} is the Rayleigh optical thickness. We need to know precisely the air pressure profile in order to estimate ($\beta_{\mathrm{ray}}(r)$, $\tau_{\mathrm{ray}}(r)$) properly. $\beta_{\mathrm{ray}}(r)$ and $\tau_{\mathrm{ray}}(r)$ are also inputs of the inversion algorithm.

Lidar inversion

From the row signal $\beta_{\mathrm{att}}(r)$, it is possible with an inversion algorithm (*Klett* 1981; 1985, *Sassano and Fernald* 1989) to extract the extinction coefficient and the backscattered (180°) coefficient of the aerosols: The inversion algorithm can invert ($\beta_{\mathrm{aer}}(r)$, $\alpha_{\mathrm{aer}}(r)$) from the inputs ($\beta_{\mathrm{att}}(r)$, $\beta_{\mathrm{ray}}(r)$, $\tau_{\mathrm{ray}}(r)$).

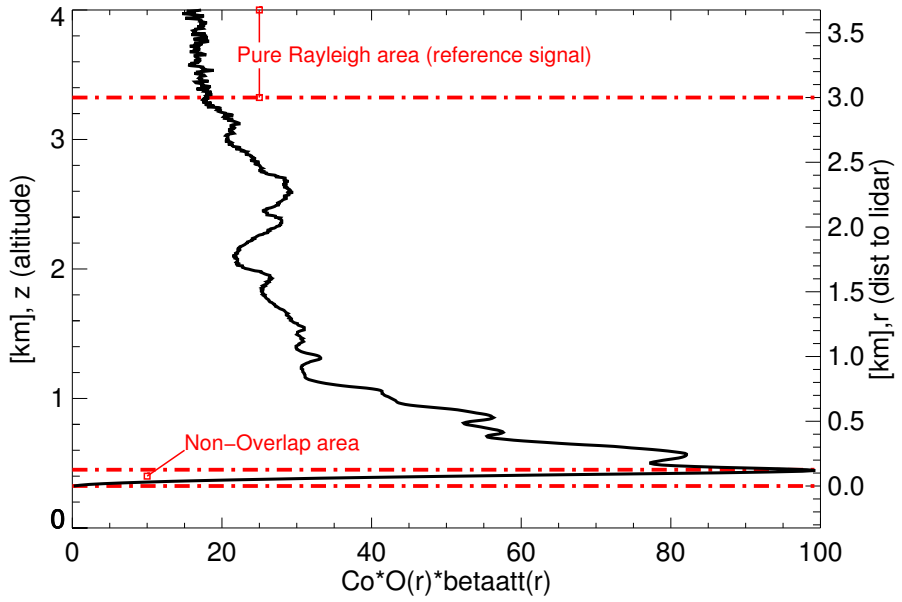

Figure 10.5.: Row lidar signal: $C_0 . O(r) . \beta_{\text{att}}(r)$, measured by the lidar LNG2 during the TRAQA campaign.

There is nevertheless a difficulty for the lidar inversion: The algorithm has 2 unknown quantities to invert ($\beta_{\text{aer}}(r)$, $\alpha_{\text{aer}}(r)$) with only one equation (the evolution of $\beta_{\text{att}}(r)$, along r). We need to inject one more equation in the lidar inversion algorithm. The basic idea is to introduce the quantity lidar ratio: $P = \alpha_{\text{aer}}(r)/\beta_{\text{aer}}(r)$, expressed in sr.

This quantity depends on the nature of the aerosol. Approximated values of the lidar ratio for different kinds of aerosols are listed in Table 4.1. The value of the lidar ratio can be computed with the phase function p of the aerosol and with its single scattering albedo ω_0:

$$P = 1/(\omega_0 . p_\pi);\ p_\pi = p(\theta, \theta + \pi) \tag{10.6}$$

The inversion algorithm can be constrained in P (an a-priori lidar radio is defined for all the aerosol layers). The input-parameters are therefore:($\beta_{\text{att}}(r)$, $\beta_{\text{ray}}(r)$, $\tau_{\text{ray}}(r)$, $P(r)$) and the outputs are ($\beta_{\text{aer}}(r)$, $\alpha_{\text{aer}}(r)$).

Another possibility is to constrain the lidar inversion algorithm in $\alpha_{\text{aer}}(r)$ instead of $P(r)$. In this case, the inputs are ($\beta_{\text{att}}(r)$, $\beta_{\text{ray}}(r)$, $\tau_{\text{ray}}(r)$, $\alpha_{\text{aer}}(r)$) and the outputs

are ($\beta_{\mathrm{aer}}(r)$, $P(r)$).

A third solution, when we have an estimation of the total aerosol optical depth τ_{aer} (photometer measurement) is to constraint the algorithm in τ_{aer} and to suppose the profile of lidar ratio constant ($P(r) = P$). Then a loop algorithm allows to obtain in output ($\beta_{\mathrm{aer}}(r)$, $\alpha_{\mathrm{aer}}(r)$,P), with the inputs: ($\beta_{\mathrm{att}}(r)$, $\beta_{\mathrm{ray}}(r)$, $\tau_{\mathrm{ray}}(r)$, τ_{aer}).

The input parameters chosen as constraint of the inversion depend on the information that we have (from measurements).

Nomenclature

AEROCOM **Aero**sol Model Inter**com**parison Initiatiative

AMMA **A**frican **M**onsoon **M**ultidisciplinary **A**nalysis

C3M **C**ALIPSO **C**loudsat **C**ERES **M**odis

CALIPSO **C**loud **A**erosol **L**idar and **I**nfrared **P**athfinder **S**atellite **O**bservations

CALIOP **C**loud-**A**erosol **Li**dar with **O**rthogonal **P**olarization

CAVIAR **C**ontinuum **A**bsorption at **V**isible and **I**nfrared Wavelengths and its **A**tmospheric **R**elevance

CERES **C**loud and the **E**arth's **R**adiant **E**nergy **S**ystem

CGASA **C**oefficients of **Gas** **A**borption

ChArMEx **Ch**emistry-**Aer**osol **M**editerranean **Ex**periment

CKD **C**lough **K**neizys **D**avies

CNES **C**entre **N**ational d'**E**tudes **S**patiales, French space agency

CPR **C**loud **P**rofiling **R**adar (on board of Cloudsat)

DISORT **Dis**crete **Or**dina**t**e Method

ERB **E**arth **R**adiation **B**udget

ERBE **E**arth **R**adiation **B**udget **E**xperiment

FASDOM **Fas**t Calculation with **D**iscrete **O**rdinate **M**ethod

FUB **F**reie **U**niversität **B**erlin

FWHM **F**ull **W**idth at **H**alf **M**aximum

GEISA **G**estion et **E**tude des **I**nformations **S**pectroscopiques **A**tmosphériques

GERB **G**eostationnary **E**arth **R**adiation **B**udget

GMAO **G**lobal **M**odeling and **A**ssimilation **O**ffice, NASA GSFC

GSFC NASA **G**oddard **S**pace **F**light **C**enter

HITRAN **Hi**gh-Resolution **Tran**smission Molecular Absorption Database

IIR **I**nfrared **I**maging **R**adiometer

IPCC **I**ntergovernmental **P**anel on **C**limate **C**hange

IPSL **I**nstitut **P**ierre **S**imon **L**aplace

IR **I**nfra-**R**ed

ISCCP **I**nternational **S**atellite **C**loud **C**limatology **P**roject

ISS **I**nstitute for **S**pace **S**ciences

KISS **k**-distribution of **I**nstitute for **S**pace **S**ciences

LATMOS **L**aboratoire **At**mospheres **M**ilieux et **O**bservations **S**patiales

LBLRTM **L**ine **b**y **L**ine **R**adiative **T**ransfer **M**odel

LEANDRE **L**idars Aéroportés pour l'**E**tude des **A**érosols, des **N**uages, de la **D**ynamique, du **R**ayonnement et du cycle de l'**E**au

LIDAR **Li**ght **D**etection **a**nd **R**anging

LIExI **L**idar **I**nversion with **Ex**tinction coefficient in **I**nput

LISA **L**aboratoire **I**nteruniversitaire des **S**ystèmes **A**tmospheriques

LNG **L**eandre **N**ouvelle **G**énération

MERIS **Me**dium **R**esolution **I**maging **S**pectrometer

MISTRALS **M**editerranean **I**ntegrated **St**udies at **R**egional **a**nd **L**ocal **S**cales)

MODIS **Mod**erate Resolution **I**maging **S**pectroradiometer

MOMO **M**atrix **O**perator **Mo**del

MSG **M**eteosat **S**econd **G**eneration

MT-CKD **M**lawer **T**obin **C**lough **K**neizys **D**avies

NASA **N**ational **A**eronautics and **S**pace **A**dministration, USA space agency

OPAC **O**ptical **P**roperties of **A**erosol and **C**louds.

PCASP **P**assive **C**avity **A**erosol **S**pectrometer **P**robe

PARASOL **P**olarisation et **A**nisotropie des **R**eflectances au sommet de l'**A**tmosphère, couplées avec un **S**atellite d'**O**bservation emportant un **L**idar

POLARCAT **Polar** study of **C**limate Chemistry **A**erosols and **T**ransport

POLDER **Pol**arization and **D**irectionality of the **E**arth's **R**eflectance (on board of PARASOL)

RADAR **Ra**dio **D**etection **a**nd **R**anging

RT **R**adiative **T**ransfer

RTE **R**adiative **T**ransfer **E**quation

RTTOV **R**adiative **T**ransfer for **TOV**S

SAFARI **S**outhern **Afric**a**n** **R**egional Science **I**nitiative

SAFIRE **S**ervice des **A**vions **F**rançais **I**nstrumentés pour la **R**echerche en **E**nvironement

SEVIRI **S**pinning **E**nhanced **V**isible **I**nfra-**R**ed **I**mager on board of MSG

SOS **S**uccessive **O**rders of **S**actering

SSA **S**ingle **S**cattering **A**lbedo

SZA **S**olar **Z**enith **A**ngle

TACT **T**ransport **A**érosol **C**himie dans la **T**roposphère

TIROS **T**elevision **I**nfra-**R**ed **O**bservation **S**atellite

TOA **T**op **o**f **A**tmosphere

TOVS **T**IROS **O**perational **V**ertical **S**ounders

TRAQA **Tra**nsport à longue distance et **qua**lité de l'air

UPMC **U**niversité **P**ierre et **M**arie **C**urie

UV **U**ltra-**V**iolet

VCLW **V**oigt **C**enter **L**orentz **W**ings

WRF-Chem **W**eather **R**esearch and **F**orecasting model coupled with **Chem**istry

XTRA E**x**tinction and **Tra**nsmission

Acknowledgements

First of all, I would like to thank my supervisors Prof. Jürgen Fischer, François Ravetta and Jacques Pelon for continued support and encouragement and the opportunity to work on this interesting topic. It was an enriching experiment to work with these three persons and to benefit of their qualities from a scientific and a human point of view.

I am much obliged to Prof. Philippe Dubuisson and Andreas Macke for agreeing to be the reviewers of my thesis.

I kindly thank the DAAD (Deutscher Akademischer Austauschdienst) for the financial support, that permits me to travel between Berlin and Paris and get accommodation without material problems.

I pay tribute to all my colleagues of the LATMOS in Paris and of the ISS in Berlin and thank them for their friendship. Especially I thank my poor colleagues Rasmus Lindstrot, Cintia Carbajal-Henken, Jean-Christophe Raut and Vincent Mariage that had to share a room with me at the office and had to bear my noise, bad jokes and songs during long times.

To all the coauthors of my papers: René Preusker, Ralph Bennartz, Jürgen Fischer, Cintia Carbajal-Henken, Jacques Pelon and François Ravetta, I address a special thanks for their scientific and linguistic help.

I would like to express my gratitude to my German colleagues and friends Rasmus Lindstrot (best neighbor and taxi driver ever), Ronny Leinweber, Kerstin Ebert and Stefan Stapelberg, for all their favors and tips that help me a lot to survive in another country.

Last but not least, I would like to thank my family and my friends for their support and for everything else, especially my parents Jean-Luc (other best taxi driver ever) and Marie Doppler, my brother Thiébaut, my flatmates Anthony and Benoît and my girlfriend Sabine.

Curriculum Vitae

Der Lebenslauf ist in der Online-Version aus Gründen des Datenschutzes nicht enthalten.